

Jordan Journal of Mechanical and Industrial Engineering (JJMIE)

JJMIE is a high-quality scientific journal devoted to fields of Mechanical and Industrial Engineering. It is published by The Hashemite University in corporation with the Jordanian Scientific Research Support Fund.

EDITORIAL BOARD

Editor-in-Chief

Prof. **Mousa S. Mohsen**

Editorial board

Prof. **Bilal A. Akash**
Hashemite University

Prof. **Adnan Z. Al-Kilany**
University of Jordan

Prof. **Ayman A. Al-Maaitah**
Mutah University

Prof. **Moh'd A. Al-Nimr**
Jordan University of Science and Technology

Prof. **Ali A. Badran**
University of Jordan

Prof. **Naseem M. Sawaqed**
Mutah University

Assistant Editor

Dr. **Ahmed Al-Ghandoor**
Hashemite University

THE INTERNATIONAL ADVISORY BOARD

Abu-Qudais, Mohammad
Jordan University of Science & Technology, Jordan

Abu-Mulaweh, Hosni
Purdue University at Fort Wayne, USA

Afaneh Abdul-Hafiz
Robert Bosch Corporation, USA

Afonso, Maria Dina
Institute Superior Tecnico, Portugal

Badiru, Adedji B.
The University of Tennessee, USA

Bejan, Adrian
Duke University, USA

Chalhoub, Nabil G.
Wayne State University, USA

Cho, Kyu-Kab
Pusan National University, South Korea

Dincer, Ibrahim
University of Ontario Institute of Technology,
Canada

Douglas, Roy
Queen's University, U. K

El Bassam, Nasir
International Research Center for Renewable
Energy, Germany

Haik, Yousef
United Arab Emirates University, UAE

Jaber, Jamal
Al- Balqa Applied University, Jordan

Jubran, Bassam
Ryerson University, Canada

Kakac, Sadik
University of Miami, USA

Khalil, Essam-Eddin
Cairo University, Egypt

Mutoh, Yoshiharu
Nagaoka University of Technology, Japan

Pant, Durbin
Iowa State University, USA

Riffat, Saffa
The University of Nottingham, U. K

Saghir, Ziad
Ryerson University, Canada

Sarkar, MD. Abdur Rashid
Bangladesh University of Engineering &
Technology, Bangladesh

Signer, Dennis
Wichita State University, USA

Sopian, Kamaruzzaman
University Kebangsaan Malaysia, Malaysia

Tzou, Gow-Yi
Yung-Ta Institute of Technology and Commerce,
Taiwan

EDITORIAL BOARD SUPPORT TEAM

Language Editor

Dr. Abdullah Jaradat

Publishing Layout

Eng. Hasan B. Al-Ba'ba'a

SUBMISSION ADDRESS:

Prof. **Mousa S. Mohsen**, Editor-in-Chief
Jordan Journal of Mechanical & Industrial Engineering,
Hashemite University,
PO Box 330127, Zarqa, 13133, Jordan
E-mail: jjmie@hu.edu.jo



Hashemite Kingdom of Jordan



Hashemite University

Jordan Journal of
Mechanical and Industrial Engineering

JJMIE

An International Peer-Reviewed Scientific Journal

<http://jjmie.hu.edu.jo/>

ISSN 1995-6665

Jordan Journal of Mechanical and Industrial Engineering (JJMIE)

JJMIE is a high-quality scientific journal devoted to fields of Mechanical and Industrial Engineering. It is published by The Jordanian Ministry of Higher Education and Scientific Research in corporation with the Hashemite University.

Introduction: The Editorial Board is very committed to build the Journal as one of the leading international journals in mechanical and industrial engineering sciences in the next few years. With the support of the Ministry of Higher Education and Scientific Research and Jordanian Universities, it is expected that a heavy resource to be channeled into the Journal to establish its international reputation. The Journal's reputation will be enhanced from arrangements with several organizers of international conferences in publishing selected best papers of the conference proceedings.

Aims and Scope: Jordan Journal of Mechanical and Industrial Engineering (JJMIE) is a refereed international journal to be of interest and use to all those concerned with research in various fields of, or closely related to, mechanical and industrial engineering disciplines. Jordan Journal of Mechanical and Industrial Engineering aims to provide a highly readable and valuable addition to the literature which will serve as an indispensable reference tool for years to come. The coverage of the journal includes all new theoretical and experimental findings in the fields of mechanical and industrial engineering or any closely related fields. The journal also encourages the submission of critical review articles covering advances in recent research of such fields as well as technical notes.

Guide for Authors

Manuscript Submission

High-quality submissions to this new journal are welcome now and manuscripts may be either submitted online or mail.

Online: For online submission upload one copy of the full paper including graphics and all figures at the online submission site, accessed via E-mail: jjmie@hu.edu.jo. The manuscript must be written in MS Word Format. All correspondence, including notification of the Editor's decision and requests for revision, takes place by e-mail and via the Author's homepage, removing the need for a hard-copy paper trail.

By Mail: Manuscripts (1 original and 3 copies) accompanied by a covering letter may be sent to the Editor-in-Chief. However, a copy of the original manuscript, including original figures, and the electronic files should be sent to the Editor-in-Chief. Authors should also submit electronic files on disk (one disk for text material and a separate disk for graphics), retaining a backup copy for reference and safety.

Note that contributions may be either submitted online or sent by mail. Please do NOT submit via both routes. This will cause confusion and may lead to delay in article publication. Online submission is preferred.

Submission address and contact:

Prof. **Mousa S. Mohsen**, Editor-in-Chief
Jordan Journal of Mechanical & Industrial Engineering,
Hashemite University,
PO Box 330127, Zarqa, 13115, Jordan
E-mail: jjmie@hu.edu.jo

Types of contributions: Original research papers

Corresponding author: Clearly indicate who is responsible for correspondence at all stages of refereeing and publication, including post-publication. Ensure that telephone and fax numbers (with country and area code) are provided in addition to the e-mail address and the complete postal address. Full postal addresses must be given for all co-authors.

Original material: Submission of an article implies that the work described has not been published previously (except in the form of an abstract or as part of a published lecture or academic thesis), that it is not under consideration for publication elsewhere, that its publication is approved by all authors and that, if accepted, it will not be published elsewhere in the same form, in English or in any other language, without the written consent of the Publisher. Authors found to be deliberately contravening the submission guidelines on originality and exclusivity shall not be considered for future publication in this journal.

Supplying Final Accepted Text on Disk: If online submission is not possible: Once the paper has been accepted by the editor, an electronic version of the text should be submitted together with the final hardcopy of the manuscript. The electronic version must match the hardcopy exactly. We accept MS Word format only. Always keep a backup copy of the electronic file for reference and safety. Label the disk with your name. Electronic files can be stored on CD.

Notification: Authors will be notified of the acceptance of their paper by the editor. The Publisher will also send a notification of receipt of the paper in production.

Copyright: All authors must sign the Transfer of Copyright agreement before the article can be published. This transfer agreement enables Jordan Journal of Mechanical and Industrial Engineering to protect the copyrighted material for the authors, but does not relinquish the authors' proprietary rights. The copyright transfer covers the exclusive rights to reproduce and distribute the article, including reprints, photographic reproductions, microfilm or any other reproductions of similar nature and translations.

PDF Proofs: One set of page proofs in PDF format will be sent by e-mail to the corresponding author, to be checked for typesetting/editing. The corrections should be returned within 48 hours. No changes in, or additions to, the accepted (and subsequently edited) manuscript will be allowed at this stage. Proofreading is solely the author's responsibility. Any queries should be answered in full. Please correct factual errors only, or errors introduced by typesetting. Please note that once your paper has been proofed we publish the identical paper online as in print.

Author Benefits

Page charge: Publication in this journal is free of charge.

Free off-prints: Three journal issues of which the article appears in along with twenty-five off-prints will be supplied free of charge to the corresponding author. Corresponding authors will be given the choice to buy extra off-prints before printing of the article.

Manuscript Preparation:

General: Editors reserve the right to adjust style to certain standards of uniformity. Original manuscripts are discarded after publication unless the Publisher is asked to return original material after use. If online submission is not possible, an electronic copy of the manuscript on disk should accompany the final accepted hardcopy version. Please use MS Word for the text of your manuscript.

Structure: Follow this order when typing manuscripts: Title, Authors, Affiliations, Abstract, Keywords, Introduction, Main text, Conclusions, Acknowledgements, Appendix, References, Figure Captions, Figures and then Tables. For submission in hardcopy, do not import figures into the text - see Illustrations. For online submission, please supply figures imported into the text AND also separately as original graphics files. Collate acknowledgements in a separate section at the end of the article and do not include them on the title page, as a footnote to the title or otherwise.

Text Layout: Use double spacing and wide (3 cm) margins. Ensure that each new paragraph is clearly indicated. Present tables and figure legends on separate pages at the end of the manuscript. If possible, consult a recent issue of the journal to become familiar with layout and conventions. All footnotes (except for table and corresponding author footnotes) should be identified with superscript Arabic numbers. To conserve space, authors are requested to mark the less important parts of the paper (such as records of experimental results) for printing in smaller type. For long papers (more than 4000 words) sections which could be deleted without destroying either the sense or the continuity of the paper should be indicated as a guide for the editor. Nomenclature should conform to that most frequently used in the scientific field concerned. Number all pages consecutively; use 12 or 10 pt font size and standard fonts. If submitting in hardcopy, print the entire manuscript on one side of the paper only.

Corresponding author: Clearly indicate who is responsible for correspondence at all stages of refereeing and publication, including post-publication. The corresponding author should be identified with an asterisk and footnote. Ensure that telephone and fax numbers (with country and area code) are provided in addition to the e-mail address and the complete postal address. Full postal addresses must be given for all co-authors. Please consult a recent journal paper for style if possible.

Abstract: A self-contained abstract outlining in a single paragraph the aims, scope and conclusions of the paper must be supplied.

Keywords: Immediately after the abstract, provide a maximum of six keywords (avoid, for example, 'and', 'of'). Be sparing with abbreviations: only abbreviations firmly established in the field may be eligible.

Symbols: All Greek letters and unusual symbols should be identified by name in the margin, the first time they are used.

Units: Follow internationally accepted rules and conventions: use the international system of units (SI). If other quantities are mentioned, give their equivalent in SI.

Maths: Number consecutively any equations that have to be displayed separately from the text (if referred to explicitly in the text).

References: All publications cited in the text should be presented in a list of references following the text of the manuscript.

Text: Indicate references by number(s) in square brackets in line with the text. The actual authors can be referred to, but the reference number(s) must always be given.

List: Number the references (numbers in square brackets) in the list in the order in which they appear in the text.

Examples:

Reference to a journal publication:

- [1] M.S. Mohsen, B.A. Akash, "Evaluation of domestic solar water heating system in Jordan using analytic hierarchy process". Energy Conversion & Management, Vol. 38, No. 9, 1997, 1815-1822.

Reference to a book:

- [2] Strunk Jr W, White EB. The elements of style. 3rd ed. New York: Macmillan; 1979.

Reference to a conference proceeding:

- [3] B. Akash, S. Odeh, S. Nijmeh, "Modeling of solar-assisted double-tube evaporator heat pump system under local climate conditions". 5th Jordanian International Mechanical Engineering Conference, Amman, Jordan, 2004.

Reference to a chapter in an edited book:

- [4] Mettam GR, Adams LB. How to prepare an electronic version of your article. In: Jones BS, Smith RZ, editors. Introduction to the electronic age, New York: E-Publishing Inc; 1999, p. 281-304

Free Online Color: If, together with your accepted article, you submit usable color and black/white figures then the journal will ensure that these figures will appear in color on the journal website electronic version.

Tables: Tables should be numbered consecutively and given suitable captions and each table should begin on a new page. No vertical rules should be used. Tables should not unnecessarily duplicate results presented elsewhere in the manuscript (for example, in graphs). Footnotes to tables should be typed below the table and should be referred to by superscript lowercase letters.

PAGES	PAPERS
383 – 387	Experimental Investigation of Forced Convective Heat Transfer in Rectangular Micro-channels <i>R.Kalaivanan, R.Rathnasamy</i>
389 – 401	The Effect of Alkaline Additives on the Operating Conditions of Kaolinitic Polymerization <i>Y. A. Mubarak, A. I. Al-Swalkah, F. K. Sweis</i>
403 – 406	The Effect of Thermal Barrier Coatings on Diesel Engine Performance of PZT Loaded Cyanate Modified Epoxy Coated Combustion Chamber <i>Vijaya Kumar K.R, Sundareswaran V.</i>
407– 417	Variable Structure Controller Schemes Based on Work and Energy Principle for SIMO Systems <i>M. Ababneh, A. Al-Jarrah, K. Al-Widyan, S. BaniHani</i>
419 – 423	MHD Heat and Mass Transfer Free Convection Flow near The Lower Stagnation Point of an Isothermal Cylinder Imbedded in Porous Domain with the Presence of Radiation <i>Ziya Uddin, Manoj Kumari</i>
425 – 432	Assessment of High Temperatures Sound Transmission Losses and Noise Reduction Factor for a DPF Using a Six-port Acoustic Model <i>S. M. Fayyad, M. N. Hamdan, S. Abdallah</i>
433 – 438	A Predictive Model for Surface Roughness in Turning Glass Fiber Reinforced Plastics by Carbide Tool (K-20) Using Soft Computing <i>S. A. Hussain, V. Pandurangadu, K.P. Kumar and V.V. Bharathi</i>
439 – 446	Modeling Stock Market Exchange Prices Using Artificial Neural Network: A Study of Amman Stock Exchange <i>S. M. Alhaj Ali, A. A. Abu Hammad, M. S. Samhoury, and A. Al-Ghandoor</i>
447 – 450	Densification and Deformation Behavior of Sintered P/M Zinc-Zinc Oxide Composite during Cold Upsetting <i>B. Selvam, A. P. Singh</i>
451 – 459	Selection of Temperature Measuring Sensors Using the Analytic Hierarchy Process <i>T. Al-Hawari, S. Al-Bo'ol, A. Momani</i>
461 – 470	Modeling of Weld Bead Geometry and Shape Relationships in Submerged Arc Welding using Developed Fluxes <i>Vinod Kumar</i>
471 – 477	Experimental Energy Study for Domestic Hot Water Storage Tanks <i>N. Beithou, M. Abu Hilal</i>

Experimental Investigation of Forced Convective Heat Transfer in Rectangular Micro-channels

R.Kalaivanan^a, R.Rathnasamy^{*a}

^aMechanical Engineering, Annamalai University, Annamalainagar, Tamilnadu, 608002, India

Abstract

This paper investigates the experimental program on the study of heat transfer characteristics in micro-channels. The two test sections used are of 47 and 50 micro-channels in rectangular cross-section of equivalent diameters 387 and 327 μm respectively. Each channel of length 192 mm is fabricated on a 304 stainless steel substrate (230 mm x 160 mm x 1.6 mm) by photo chemical etching process. Covering the top with another plate of 0.5 mm thickness forms the channels by vacuum brazing. Experiments cover laminar region using the fluids ethanol, methanol and an ethanol-methanol mixture. The heat transfer coefficient is evaluated based on the heat carried away by the coolant and an average wall to mean fluid temperature difference. The Nusselt number is correlated through empirical correlations involving Reynolds number and Prandtl number with length parameter, the hydraulic diameter.

© 2011 Jordan Journal of Mechanical and Industrial Engineering. All rights reserved

Keywords: Micro-channels; alcohols; alcohol mixture; forced convection; laminar

Nomenclature

Symbols

a	index
c_p	specific heat (J/kg K)
C	constant
d	diameter (m)
D_{eq}	equivalent diameter (m)
h	heat transfer coefficient ($\text{W}/\text{m}^2 \text{K}$)
H	channel height (m)
L	channel length (m)
m	mass flow rate (kg/s)
n	Prandtl index
q	heat transfer rate (W)
q_{spi}	electrical power input (W)
q	heat flux (W/m^2)
Re	Reynolds number ($=\rho v d/\mu$)
t	temperature ($^{\circ}\text{C}$)
v	velocity (m/s)
W	channel width (m)
x	mass fraction
y	mole fraction

Greek Letters

Δ	differential
λ	thermal conductivity ($\text{W}/\text{m K}$)
μ	dynamic viscosity, ($\text{N s}/\text{m}^2$ or Pa s)
ρ	fluid density (kg/m^3)

Subscripts

eq	equivalent
f	fluid
i	inlet
m	mean
mix	mixture
o	outlet
w	wall conditions
1	component 1
2	component 2

1. Introduction

The systematic research into micro-scale flow and heat transfer studies were in vogue for the past three decades, started by initiation of Tuckermann & Pease [1-2] on the thermal management of high heat dissipating electronic components both covering chip and board levels. As far as micro-scale flow passages are concerned, the literature sources are not more recent. The emergence of micro-electro-mechanical systems (MEMS) has generated significant interest in the area of micro scale heat transfer. Several investigations ensued those dealt with flow of gases [3] and liquids [4] through micro-geometries. Fluid flow through micro-scale flow geometries is encountered in numerous engineering systems such as cooling of electronic devices and compact heat exchangers. Micro-channel flows have been used for liquid dosing and flow measurement [5]. Non-circular geometries are often adopted because of their relative simplicity in fabrication as compared to circular channels. Issues pertaining to

* Corresponding author. e-mail: mecratz@yahoo.co.uk

micro-channel heat exchangers were dealt with by Peterson [6] and Ravigururajan et al [7]. Theoretical approaches to fluid flow and heat transfer as well were reported [8]. The substrates used were silicon, glass, copper and stainless steel. The test section geometries varied from a fraction of a μm to a few 100s of μm . There had been limited study with mixtures of fluids [9] and Rathnasamy et al [10] investigated flow of alcohols and its mixtures in long serpentine micro-channels. Steinke and Kandlikar [11] reviewed previous studies on the topic of fluid flow and heat transfer and tried to explain the deviation in data by conducting experiments. It is concluded that deviations came from the measurement uncertainty of micro-channel dimension in conjunction, with inlet and exit losses. Fluid flow and heat transfer experiments were conducted in rectangular micro-channels by Jung and Kwak [12]. There is general agreement in the literature that the high relative roughness of micro-channels reduces the critical Reynolds number for transition to turbulent flow. It is well known that roughness influences the transition to turbulent in Schlichting [13].

These studies provide substantial evidence to prove that flow and heat transfer in micro-channels need to be addressed differently compared to conventional channels. Wang et al [14] have attempted to provide some possible explanation to peculiarities of micro-channel heat transfer. It appears that the results quite good agreement with experimental data. Moreover Jung-Yeul Jung et al [15] have reported that the Nusselt number increases with increasing Reynolds number in laminar regime by doing experiments with nano fluids. There is a need for more experimental data on a variety of fluids and flow geometries (i.e; channel dimensions and relative roughness) so that some generalized conclusions can be evolved.

2. Test section

Micro-components are mostly fabricated using etching, deposition and photo-lithographic techniques. The EDM is considered to be a non-conventional machining technique. It was reported that with a precision EDM dimensional tolerances up to $0.5 \mu\text{m}$ could be obtained.

In the present case, two test sections herein after designated as MCP1 and MCP2 having common features; each channel of length 192 mm were fabricated on a 304 stainless steel substrate (230 mm x 160 mm x 1.6 mm) by photo chemical etching process as shown in Figure 1.

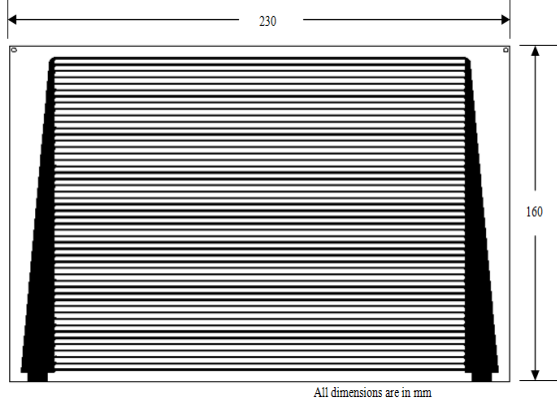


Figure 1: Details of micro-channel test section.

MCP1 and MCP2 have 47 and 50 micro-channels of rectangular cross-section 1000 by $240 \mu\text{m}$ and 900 by $200 \mu\text{m}$ in width and depth, respectively. The channel header portions were deepened after etching by EDM in order to have negligible pressure loss. The surface roughness (ϵ) of MCP1 and MCP2 was done to check the uniformity of the channel using a surface profilometer (Rank Taylor Hobson). The surface roughness measured have shown rms values of the order $1.11\text{-}6.90 \mu\text{m}$ for machined surface and $0.19\text{-}0.34 \mu\text{m}$ for cover plate. The flow passage is formed by vacuum brazing the machined plate, covering with another stainless steel plate of thickness 0.5 mm on top. Inlet and out conduits were attached together with the two plates and brazed in a vacuum furnace at $10\text{-}5$ torr and about 1000°C . The mating surfaces were coated with some plating technique to assist brazing.

3. Experimental Setup and Procedure

The experimental set-up, shown in Figure 2, consists of a liquid reservoir (capacity ~ 20 lit) to supply fluid to the test section. A diaphragm operated pump is used to pump fluid to the test section through a micro-filter (~ 50 micron) built-in in the main line to avoid any dirt that may enter into the test section. In the absence of micro-filter poor measurement data could be resulted due to blockage of the channels to the flowing fluid.

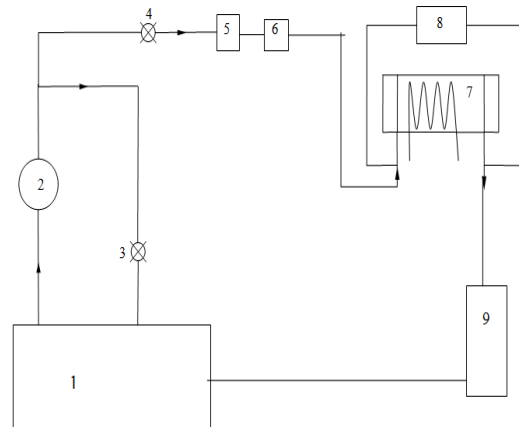


Figure 2: Schematic of experimental setup, Legend: 1 Sump 2 Pump 3 By-pass control valve 4 Flow control valve 5 Micro-filter 6 Flow meter 7 Test section 8 Differential pressure transducer 9 Temperature bath.

Experiments were conducted with liquids ethanol, methanol and a mixture 50%E-50%M by volume (i.e; 0.53E-0.47M by mole fraction). It consists of liquid reservoir/sump (capacity ~ 20 lit) to supply fluid to the test section. Further the test setup is provided with by-pass line and control valves to establish the required flow rate in the test section and as well the pressure drop, measured with the aid of differential pressure transducer (make: KELLER Druckmesstechnik; piezoresistive pressure transmitter, PD-23/ 5 bar/8666.1). Flow rate through the test section was measured by using the flow meter (make: DIGMESA; magnetic turbine flow meter). However, the flow meter was calibrated by measuring known volume of methanol manually with a maximum absolute deviation 4% over the measuring range 0.03- 8.00 lpm. Nichrome ribbon heaters wound on a mica sheet and encapsulated between a pair of mica sheets, were used as heat sources. Two identical

heaters were mounted on either side of the test section. This enabled application of equal heat inputs from both sides of the test module. The entire test section was adequately insulated with 2-mm thick asbestos sheet followed by 75-mm thick glass wool and 20-mm thick polystyrene foam on each side and at the edges. The fluid coming out of the channel was passed through a cooling coil and then in to the sump. The cooling coil was submerged in a temperature bath. The flow rates were varied with a corresponding variation of heat inputs. Thermocouples (T-type) and few Platinum resistance thermometers were affixed to the surface at 15 designated locations on the each side of the test section. A few thermocouples were used for measuring the inlet and outlet temperatures of conduits of the micro-channel test section. A digital display unit is used with a resolution of 0.1°C. in the measurement.

The flow medium used to test is filled in the reservoir. To start the experiment all the required precautions are taken into consideration. The pump is switched on while keeping the by-pass valve in open position and control valves to test section closed. The required discharge flow rate of the pump is obtained through stroke adjustment in the pump system. Control valve is somewhat opened allowing the flow to take place in the test section. Later, the control valve is tuned to set the required flow rate indicated by the display unit connected. Pressure drop at the test section for the corresponding flow rate indicated by the display unit is noted. The steady value of flow rate is taken to reduce the measurement uncertainty. Several trials are carried out and the average value is taken to evaluate flow rate in terms of cc/min basis. The primary data were heat flux, flow rate, pressure drop, and temperatures at various locations on the test section. Each experiment is continued till the steady state conditions had stabilised, which took about one hour after the commencement of a test. The experiment was continued for a further period of 10-15 minutes before switching to the next run. In the present case of heat transfer experiments the Reynolds number covered the laminar region ($30 \leq Re \leq 500$). All tests were conducted with the test section in a horizontal plane.

4. Data Reduction

The Reynolds number is defined in the conventional way, $Re = \rho v d / \mu$. The velocity v (average) is calculated from flow rate based on the cross-sectional area of the channel. The velocity is evaluated using the mass flow rate and the equivalent diameter ($D_{eq} = 2 WH / (W+H)$). The mass flow rate was evaluated based on the density at inlet condition.

4.1. Property evaluation:

Thermophysical properties required for the heat transfer calculations were evaluated at the mean fluid temperature, defined as

$$t_{fm} = \frac{(t_{fi} + t_{fo})}{2} \quad (1)$$

The linear mixing rules for specific volume were used for evaluating the density, specific heat and thermal conductivity of the mixtures. The logarithmic mixing rule

was used for viscosity of liquid mixed mixtures [16]. Temperature-dependent pure property data used were taken from reference [17].

4.2. Heat transfer coefficient:

There is an uncertainty over the amount of heat transferred to the fluid. Because of the inevitable losses from the test section, all the electrical power given to the heaters is not transferred to the fluid. Thus, the actual heat transferred to the fluid was calculated from the enthalpy change. The heat flux was calculated based on energy balance of the fluid.

$$q = \dot{m} c_p (t_{fo} - t_{fi}) \quad (2)$$

$$q''_m = \frac{q}{2L(W+H)} \quad (3)$$

The average heat transfer coefficient is defined as

$$h_m = \frac{q''_m}{\Delta t_m} \quad (4)$$

Where

$$\Delta t_m = (t_{wm} - t_{fm}) \quad (5)$$

The mean wall temperature (t_{wm}) was based on the measurements at 15 locations. The Nusselt number is correspondingly defined as

$$Nu = \frac{h_m D_{eq}}{\lambda_{fm}} \quad (6)$$

This is procedure is similar to the one used by other researchers also [18,19].

Table 1 shows the electrical heat input, velocity, fluid inlet and outlet temperatures, mean wall temperature and heat transfer rate for ethanol flow in MCP1. The last column indicates the percent of heat transfer to the fluid with respect to electrical power supplied to the heater. Similar data for experiments with methanol and one liquid mixture were generated for both channels. It is seen that about 10% of the input power is lost to the ambient in experiments.

Table 1: Raw data for ethanol flow in micro-channel.

Exp.	q _{epi} (W)	v (m/s)	t _{fi} (°C)	t _{fo} (°C)	t _{wm} (°C)	q (W)	q/q _{epi} (%)
1	2	0.136	24.1	52	41.7	1.83	91.4
2	2.5	0.165	24.5	53	42	2.28	91.1
3	2.7	0.185	24.3	52	42.4	2.47	91.4
4	3.2	0.208	24.1	54.2	44.2	3.03	94.8
5	3.8	0.232	24.3	57	46.9	3.69	97
6	4	0.248	24.3	54.7	45	3.66	91.5
7	4.5	0.278	24.3	54.6	46.3	4.07	90.6
8	5.25	0.324	24.8	56.2	48.8	4.93	93.9
9	5.5	0.306	24.8	58.5	49.1	5.03	91.4
10	5.8	0.377	25.2	54.4	49.7	5.33	91.9
11	6	0.428	25	52	47	5.58	93.1
12	6.6	0.467	25	53.3	48.3	6.39	96.8
13	7	0.443	24.2	54.5	49.2	6.49	92.8
14	7.5	0.502	24	54	51.2	7.29	97.1
15	8	0.829	24.6	43.5	48.1	7.3	91.3
16	8.5	0.916	25.1	43.5	47.1	8.07	94.9
17	9	0.798	24.8	46.4	50.1	8.17	90.8
18	10	0.572	25	57.9	55.2	9.18	91.8
19	10	0.689	25.2	53.4	54	9.39	93.9
20	10	0.73	24.2	51.2	51.9	9.49	94.9
21	10.2	0.764	24.2	49.1	51.1	9.13	89.5
22	11	0.66	25.2	58	55.5	10.56	96
23	11	1.086	25.3	44.8	49.8	10.01	91
24	12	1.21	25.1	44.8	50.4	11.15	92.9
25	12	1.507	25.3	42	52.2	11.82	98.5
26	12.4	1.285	25.2	43.7	51	11.16	90
27	12.5	1.42	25.1	42.5	51.6	11.47	91.7
28	14.2	1.831	25.2	41	54	13.47	94.8
29	14.5	1.754	25.5	42	53.4	13.76	94.9
30	14.6	1.67	25.2	43	52.8	13.91	95.3

5. Results and discussion

The Nusselt number data obtained from previous section are shown in Figure 3 as a plot of Nusselt number versus Reynolds number. These include all the experiments with liquids. These data show a perceptible fluid species dependence. Several researchers [8,19,20,21] have brought out that the transition to turbulent regime occurs at lower Reynolds numbers in micro-channels than in normal channels. These transitions have been identified in the present fluid flow work also communicated [22]. The experimental data from the present work had been fitted to relation as in figure 4 with the following relation:

$$Nu = C Re^a Pr^n \quad (7)$$

The values in eq. (7) for correlation coefficient 'C' and indices a and n are obtained.

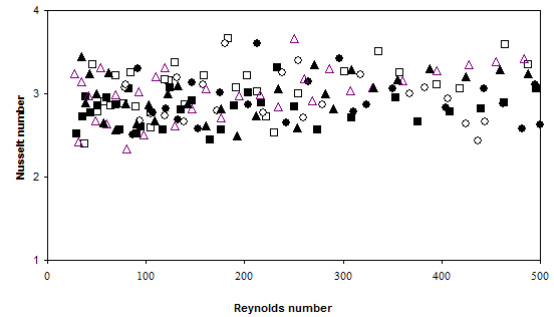


Figure 3: Nusslet number versus Reynolds plots for all liquids in micro-channels, Legend: □ MCP1 ethanol, ■ MCP2 ethanol, ○ MCP1 methanol, ● MCP2 methanol, △ MCP1 0.53E-0.47M mixture, ▲ MCP2 0.53E-0.47M mixture.

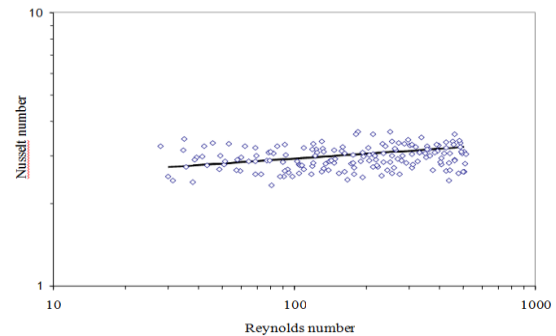


Figure 4: Nusselt number versus Reynolds number plot for all liquids in micro-channels with fit to equation (7) as solid line.

6. Conclusion

An experimental setup was devised to study the characteristics of single phase forced convective heat transfer in micro-channels. The two test sections MCP1 and MCP2 employed has equivalent diameter of 387 and 327 μm on 230 x 160 mm² steel plate. The flow media studied were alcohols and their mixture. The measured flow rate and temperatures data were used to evaluate the Nusselt number. An empirical correlation is obtained for Nusselt number in terms of Reynolds number and Prandtl number for laminar region as below:

$$Nu = 0.949 Re^{0.06} Pr^{0.4} \quad (8)$$

More experiments on different channel dimensions, surface roughness and fluids are needed to evolve a generalised correlation for heat transfer at micro-scale length. These experimental data could set off the ongoing efforts on micro-channel studies. The dependence of Nusselt number on Reynolds number and Prandtl number in micro-channel is quite different from that of normal channels.

Acknowledgment

The test modules used in this paper are financially supported by Department of mechanical engineering, Indian Institute of Science, Bangalore. The authours are grateful to Liquid Propulsion Systems Centre, Indian Space Research Organisation, Bangalore for deploying their expertise in the fabrication of test sections.

References

- [1] Tuckermann, D.B., and RFW. Pease, 1982. Optimized convective cooling using micro machined structures. *J. Electro Chem. Soc.* 129, (3) C98.
- [2] Tuckermann, D.B., 1984. Ph. D. Thesis, Department of Electrical Engineering, Stanford University, Alto, CA.
- [3] Wu, P., and W.A. Little, 1983. "Measurement of friction factors for the flow of gases in very fine channels used for micro-miniature Joule-Thomson refrigerators", *Cryogenics* 23, (5) : pp.273-277.
- [4] Adams, T.M., S.L. Abdel-Khalik, S.M. Jeter, and Z.H. Qureshi, 1997. "An experimental investigation of single-phase forced convection in micro-channels", *AIChE Symposium series., Heat transfer-Baltimore.* pp: 87-94.
- [5] Richter, M., P. Woias, and D. Weiß, 1997. Micro-channels for applications in liquid dosing and flow-rate measurement. *Sensors and Actuators A Physical* 62, pp: 480-483.
- [6] Peterson, G.P.,(1992). Overview of micro heat pipe research and development. *Appl. Mech. Rev.* 45, (5) pp :175-189.
- [7] Ravigururajan, T.S., J. Cuta, C.E. McDonald, and M.K. Drost, 1996. Single-phase flow thermal performance characteristics of a parallel micro-channel heat exchanger. *HTD-329, National Heat Transfer Conference, 7 ASME,* pp: 157-166.
- [8] Mala, G. M., D. Li, and J.D. Dale, 1997. Heat transfer and fluid flow in micro- channels. *Int. J. Heat Mass Transfer* 40, (13) pp : 3079-3088.
- [9] Peng, X.F., and G.P. Peterson, 1996. Convective heat transfer and flow friction for water flow in micro channel structures, *Int. J. Heat Mass Transfer* 39, pp: 2599-2608.
- [10] Rathnasamy, R., J.H. Arakeri, and K. Srinivasan, 2005. Experimental investigation of fluid flow in long rectangular micro-channels. *Proc. IMechE Part E: J. Process Mechanical Engineering*, 219, pp: 227-235.
- [11] Steinke, M.E. and S.G. Kandlikar, 2006. Single- phase liquid friction factors in micro-channels. *Int. J. Heat Mass Transfer* 45, pp: 1073-1083.
- [12] Jung, J.Y., and H.Y. Kwak, 2008. Fluid flow and heat transfer in micro-channels with rectangular cross section. *Int. J. Heat Mass Transfer* 44, pp: 1041-1049.
- [13] Schlichting, H., 1979. *Boundary Layer Theory*, McGraw-Hill Book Company, New York.
- [14] Wang, B. X., and X. F. Peng, 1994. Experimental investigation on liquid forced convection heat transfer through micro-channels. *Int. J. Heat mass Transfer* 37, pp: 73-82.
- [15] Jung-Yeul Jung., Hoo-Suk Oh, and Ho-Young Kwak, 2009. Forced convective heat transfer of nanofluids in micro-channels. *Int. J. Heat Mass Transfer* 52, pp: 466-472.
- [16] Heide, R., 1980. An instrument for measuring viscosity of refrigerants and refrigerant mixtures. *Proc. Int. Inst. of Refrig., Comm. B1,B2,E1,E2, Mons.Belgium.*
- [17] Beaton, C. F., and G.F. Hewitt, 1989. *Physical Property Data for the Design Engineers.* Hemisphere publishers, New York.
- [18] Peng, X. F., and Wang, B. X, 1994. Liquid flow and heat transfer in micro-channels with / without phase change heat transfer. In *proceedings of the 10th International Heat Transfer Conference, Brighton, UK, 1,* pp: 159-177.
- [19] Wu, P., and W.A. Little, 1984. Measurement of heat transfer characteristics of gas flow in fine channel heat exchangers used for micro-miniature refrigerators. *Cryogenics*, 24, pp: 415- 420.
- [20] Pfahler, J. N., J. Harley, H.H. Bau, and J. Zemel, 1990. Liquid transport in micron and submicron channels. *Sensors and Actuators.*, 38 pp: 431- 434
- [21] Harely, J., Y. Huang, H.H. Bau, and J. N. Zemel, 1995. Gas flow in micro-channels. *J. Fluid Mech.*, 284, pp: 257-274.
- [22] Kalaivanan, R., and R. Rathnasamy, 2009. Investigation of low density fluid flow through parallel micro-channels, Paper communicated.

The Effect of Alkaline Additives on the Operating Conditions of Kaolinitic Polymerization

Y. A. Mubarak^{*a}, A. I. Al-Swalkah^a, F. K. Sweis^a

^aDepartment of Chemical Engineering, Faculty of Engineering and Technology, University of Jordan, Amman 11942, Jordan

Abstract

Jordanian kaolinite polymerization has been studied to determine the effect of using different alkaline materials such as NaOH, KOH, and Ca(OH)₂, and sand as a filler on the compressive strength, durability under wet and dry conditions, and water absorption of the produced specimens. The studied parameters were mixing proportions such as; alkaline materials to kaolinite ratios, filler to kaolinite ratios, water to kaolinite ratios, and filler particles size. The polymerization step was carried out by mixing the kaolinitic and the filler with the alkaline solution in the case of NaOH and KOH before molding the specimens. In the case of Ca(OH)₂, the kaolinitic, fillers, and powder of Ca(OH)₂ were dry mixed together before water is added. The moulding step was carried out using a stainless steel mould at a pressure of about 15 MPa, the curing temperature was 80°C. Twenty four hours was the curing time for specimens containing NaOH or KOH, while 7 days was the curing time for Ca(OH)₂ specimens. The obtained results indicate that using NaOH as an alkaline material has the best compressive strength of 45.45 MPa under dry condition, 20.38 MPa under wet condition, and the lowest water absorption of 9.41 %. The composition of the specimens with optimum values consist of 42.37 % kaolinite, 5.93 % NaOH, 42.37 % sand, and 9.32 % water, with sand particles size of (180-355) µm. The specimens of NaOH and sand as a filler showed highest durability under dry cycling condition compared with KOH specimens. While the specimens of KOH and sand as a filler showed highest durability under immersion, and wet cycling condition.

© 2011 Jordan Journal of Mechanical and Industrial Engineering. All rights reserved

Keywords: Kaolinite; geopolymerization; alkaline; durability; compressive strength

1. Introduction

One of the basic demands for development of any society is the availability of construction materials. These materials are mainly obtained from cement industry. Cement manufacturing is one of the largest carbon emitting industrial sectors with carbon dioxide emitted as a result of both fuel combustion and process-related emissions. The production of one tone of cement generates 0.55 tons of chemical CO₂ and 0.40 tons as combustion product [1], also consumes high energy. High cost of energy and transportation has made it an expensive industry. Therefore it becomes necessary to look for other sources of construction materials that consider both economical and environmental factors. These new materials should be characterized by low production cost, low energy consumption, and low CO₂ emission. Soil is the most common building material world-wide, because it is available almost everywhere on earth. The use of soil as a construction material is a need for improvement to achieve stable, reliable, and high quality materials.

Mineral polymerization techniques offer possibilities for soil improvement. It refers to reactions between alkalis and minerals such as kaolinite which will be hardened and transformed into useful construction materials. Kaolinite is the main clay minerals that have been widely used as a raw material in several industrial sectors such as paper,

ceramics, paint and cement. The Natural Resources Authority (NRA) of Jordan has published a geological survey indicating the availability of kaolinite in commercial amounts so that it can become a main economic resource to the industrial sector [2]. This encourages researchers to study the use of the Jordanian kaolin as a raw material to produce mineral polymers that are suitable for use as construction materials.

The objectives of this work described here are to evaluate the suitability of using different alkaline additives such as NaOH, KOH and Ca(OH)₂ with silica sand as a filler in Jordanian kaolinite polymerization to produce mineral polymers that are suitable for use as construction materials, and to determine some physical and mechanical properties of the produced specimens with respect to filler particles size and mix proportions, such as alkaline material to kaolinite ratio, filler to kaolinite ratio, and water to kaolinite ratio. The property determination will cover compressive strength, durability under wet and dry conditions and water absorption degree.

2. Theoretical background

Earth soil is the oldest and most widely used building material in the world, because it is cheap and abundant. The use of soil as a constructional material is limited by low strength, volume stability and durability, so there is a need for soil improvement. Alkaline addition is a

* Corresponding author. e-mail: ymubarak@ju.edu.jo

chemical technique for the soil improvement refers to the addition of alkali hydroxide or silicate to the soil. Davidovits [3] defined the chemical reactions of aluminate and silicate species that originate from the dissolution of silicon and aluminum containing materials under highly alkaline conditions as geopolymerization process that yield geopolymer which is an amorphous to semi-crystalline three dimensional alumino-silicate polymer produced at temperature lower than 100°C.

Various sources of silicon and aluminum are used as raw material for geopolymerization process such as kaolinite and bentonite. The common activators are NaOH, Na₂SO₄, Na₂CO₃, K₂CO₃, KOH, and K₂SO₄ [4]. Xu and Deventer [5] used fifteen natural Al-Si materials in geopolymerization with sodium and potassium hydroxide, the potassium hydroxide based geopolymer showed highest strength. Borbosa et al. [6] synthesized geopolymer of metakaolinite and sodium silicate with a maximum compressive strength of 48.1 MPa. Cioffi et al. [7] reported that geopolymers of kaoline with potassium silicate have better strength than geopolymer of kaolin with sodium silicate. Wang et al. [8] concluded that strength of metakaolinite and sodium hydroxide geopolymer increased with increasing of sodium hydroxide content.

Gogo [9] has evaluated the stabilization of soil from Ghana for building and construction purposes by mixing and curing the soil with various additives; Na₂CO₃, KOH, NaOH, Ca(OH)₂ and a mixture of K₂CO₃ and Ca(OH)₂. Soil stabilized with the K₂CO₃ and Ca(OH)₂ system as a solid additive have shown the best resistance to failure in the dry state while the NaOH system has shown the best resistance to failure in the wet state. A study by Al shaaer [10] evaluated the quality and suitability of different kaolinitic soils from Jordan for construction purposes using inorganic polymerization technique. The results showed that red brownish portion of Jordanian soil produce stable and good quality construction materials with compressive strength of 22 MPa and 50 MPa under wet and dry conditions, while gray portion of Jordanian soil has low quality to produce construction materials since it could not attain an acceptable compressive strength after immersion or cycling process. Linh [11] concluded that kaolinitic soil from Vietnam can be stabilized successfully with NaOH and sand to form strong and durable construction material. Fai [12] studied the possibilities of using the inorganic polymerization technique for the kaolinitic soils from Cameroon with NaOH for the aim of making them more suitable for construction purposes.

Esaifan [13] study was to evaluate the quality and suitability of kaolinitic soils from the southern Jordan desert to use it in the future work as a raw material for build up an in-situ water harvesting system after applying the technology of inorganic polymerization technique using NaOH. Khoury et al. [14] studied the production of a new construction material using kaolinitic clay, sand, sodium, potassium and calcium hydroxide by mineral polymerization.

3. Experimental

3.1. Materials:

In the present study Jordanian Hiswa kaolinite, supplied by the Public Mining Company (Jordan), was used as a raw material. It has a particle size less than 425 µm and a density of 2.8 g/cm³. Analytical grade of sodium hydroxide NaOH was used as an alkaline additive in the form of pellets, it was obtained from Merck with ≥ 99 % purity and a density of 2.1 g/cm³. Analytical grade of potassium hydroxide KOH was used as an alkaline additive in the form of pellets, it was obtained from Scharlau with ≥ 85 % purity and a density of 2.0 g/cm³. Synthesis grade of calcium hydroxide Ca(OH)₂ was used as an alkaline additive in the form of powder, it was obtained from Scharlau with 90 % purity and a density of 2.2 g/cm³. Jordanian silica sand, supplied by the International Silica Industries Company (Jordan), was used as a filler, with particle size of 45 <d ≤ 500 µm and a density of 2.1 g/cm³. Distilled water was used in the preparation of sodium, potassium hydroxide solutions or was added to calcium hydroxide-kaolinite-silica sand mixture.

3.2. Determination of materials properties:

3.2.1. Plastic limit determination:

The consistency of kaolinite depends on the water content. Using water content in the mixing process equals to the plastic limit was proposed to improve the quality of produced polymer. Plastic limit is defined as the water content below which the soil is nonplastic [15]. The plastic limit was determined for kaolinite sample after dried at 105 °C for 24 h to remove all moisture content using Shel Lab oven (model CE3). The kaolinite sample is mixed with water, then the mixture was divided into several smaller samples. These smaller samples were rolled between the fingers into a thread with a diameter of about 3 mm without breaking or sticking to the fingers until its water content is reduced to a point at which the thread just crumbles and is no longer is able to be rerolled. The wet threads were put into a weighed can and the weight of wet threads plus the can was recorded. Using KERN EG/EW electronic balance (model 3000-2M) the weights of the threads before and after drying at 105 °C for 24 hr were recorded, the difference between the two weights is the plastic limit. A value of 21.9 ml of water was obtained for the kaolinite sample used in the present work.

3.2.2. Chemical and mineral analyses:

X-Ray Fluorescence (XRF) analysis was performed to identify the chemical composition of kaolinite, while X-Ray diffraction (XRD) analysis was performed to identify the major mineralogical components of samples. The XRF and XRD analyses were carried out at the Natural Resources Authority laboratories using X ray fluorescence spectrometer, and Philips X ray diffractometer (model PW 3040 with Co K_α radiation) respectively. Table 1 shows the chemical composition of the kaolinite used in the present study that was identified using XRF analysis.

Table 1: Chemical composition of the raw materials used in the present study.

Material	SiO ₂ %	TiO ₂ %	Al ₂ O ₃ %	Fe ₂ O ₃ %	MnO %	MgO %	CaO %	Na ₂ O %	K ₂ O %	P ₂ O ₅ %	SO ₃ %	L.O.I %
Kaolinite	48.94	0.86	25.17	7.53	0.01	0.21	0.68	0.21	1.37	0.15	2.94	11.89

The XRD diffractions of materials were obtained as graphical output in the form of (2θ) angle diffraction within 2 to 60. These data were analyzed for the reflection angle and was compared to the tables of interplanar spacing (d-value) to identify possible peaks. Figure 1 shows an X-ray diffraction of a representative sample of kaolinite. The most abundant minerals are kaolinite and quartz, there are trace amounts of muscovite and hematite.

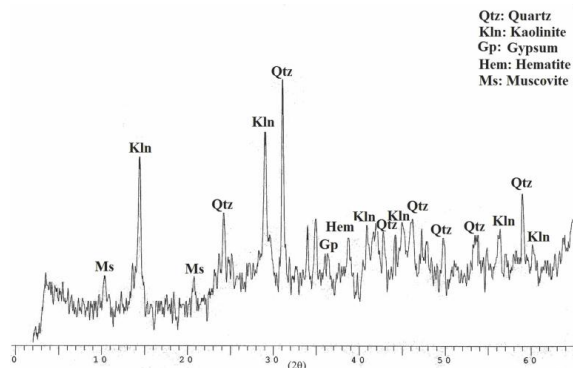


Figure 1: X-ray diffraction of kaolinite.

3.3. Polymerization of kaolinite:

3.3.1. Polymerization mixtures:

Throughout this study the components of a mixture were prepared by considering the kaolinite ratio to be 1, while the ratios of the other components are presented with respect to this ratio. For example, using silica sand as twice as kaolinite by weight, then we consider the silica sand to kaolinite ratio to be 2.

3.3.1.1. Polymerization of kaolinite using NaOH and silica sand.

Fourteen batches of kaolinite, NaOH, silica sand and distilled water were prepared. Eleven batches NaOH1 to NaOH11 (Table 2) were prepared with silica sand size range of (45 < d ≤ 500) μm. Three batches of (NaOH4) (Table 2) were prepared by using the silica sand size range as (45 < d ≤ 180), (180 < d ≤ 355) and (355 < d ≤ 500) μm.

Table 2: Ratio, mass fraction and weight of batch components for kaolinite polymerization with NaOH and silica sand.

Batch Name	Kaolinite			NaOH			Silica Sand				Water		
	R _i	X _i	W _i (g)	R _i	X _i	W _i (g)	R _i	X _i	W _i (g)	Particles size	R _i	X _i	W _i (g)
NaOH 1	1	41.67	250	0.18	7.5	45	1	41.67	250	45 < d ≤ 500	0.22	9.17	55
NaOH 2	1	42.02	252.1	0.16	6.72	40.34	1	42.02	252.1	45 < d ≤ 500	0.22	9.24	55.46
NaOH 3	1	42.19	253.16	0.15	6.33	37.97	1	42.19	253.16	45 < d ≤ 500	0.22	9.28	55.7
NaOH 4	1	42.37	254.24	0.14	5.93	35.59	1	42.37	254.24	45 < d ≤ 500	0.22	9.32	55.93
NaOH 5	1	42.74	256.41	0.12	5.13	30.77	1	42.74	256.41	45 < d ≤ 500	0.22	9.4	56.41
NaOH 6	1	43.1	258.62	0.1	4.31	25.86	1	43.1	258.62	45 < d ≤ 500	0.22	9.48	56.9
NaOH 7	1	34.97	209.79	0.14	4.9	29.37	1.5	52.45	314.69	45 < d ≤ 500	0.22	7.69	46.15
NaOH 8	1	38.31	229.89	0.14	5.36	32.18	1.25	47.89	287.36	45 < d ≤ 500	0.22	8.43	50.57
NaOH 9	1	47.39	284.36	0.14	6.64	39.81	0.75	35.55	213.27	45 < d ≤ 500	0.22	10.43	62.56
NaOH 10	1	42.92	257.51	0.14	6.01	36.05	1	42.92	257.51	45 < d ≤ 500	0.19	8.15	48.93
NaOH 11	1	41.84	251.05	0.14	5.86	35.15	1	41.84	251.05	45 < d ≤ 500	0.25	10.46	62.76
NaOH4-1	1	42.37	254.24	0.14	5.93	35.59	1	42.37	254.24	45 < d ≤ 180	0.22	9.32	55.93
NaOH4-2	1	42.37	254.24	0.14	5.93	35.59	1	42.37	254.24	180 < d ≤ 355	0.22	9.32	55.93
NaOH4-3	1	42.37	254.24	0.14	5.93	35.59	1	42.37	254.24	355 < d ≤ 500	0.22	9.32	55.93

3.3.1.2. Polymerization of kaolinite using KOH and silica sand:

Twelve batches of kaolinite, KOH, silica sand and distilled water were prepared. Ten batches KOH1 to

KOH10 (Table 3) were prepared with silica sand size range of (45 < d ≤ 500) μm. Three batches of (KOH2) (Table 3) were prepared by using the silica sand size range as (45 < d ≤ 180), (180 < d ≤ 355) and (355 < d ≤ 500) μm.

Table 3: Ratio, mass fraction and weight of batch components for kaolinite polymerization with KOH and silica sand.

Batch Name	Kaolinite			KOH			Silica Sand				Water		
	R _i	X _i	W _i (g)	R _i	X _i	W _i (g)	R _i	X _i	W _i (g)	Particles size	R _i	X _i	W _i (g)
KOH 1	1	40.49	242.91	0.25	10.12	60.73	1	40.49	242.91	45 < d ≤ 500	0.22	8.91	53.44
KOH 2	1	41.67	250	0.18	7.5	45	1	41.67	250	45 < d ≤ 500	0.22	9.17	55
KOH 3	1	42.02	252.1	0.16	6.72	40.34	1	42.02	252.1	45 < d ≤ 500	0.22	9.24	55.46
KOH 4	1	42.37	254.24	0.14	5.93	35.59	1	42.37	254.24	45 < d ≤ 500	0.22	9.32	55.93
KOH 5	1	42.74	256.41	0.12	5.13	30.77	1	42.74	256.41	45 < d ≤ 500	0.22	9.4	56.41
KOH 6	1	34.48	206.9	0.18	6.21	37.24	1.5	51.72	310.34	45 < d ≤ 500	0.22	7.59	45.52
KOH 7	1	37.74	226.42	0.18	6.79	40.75	1.25	47.17	283.02	45 < d ≤ 500	0.22	8.3	49.81
KOH 8	1	46.51	279.07	0.18	8.37	50.23	0.75	34.88	209.3	45 < d ≤ 500	0.22	10.23	61.4
KOH 9	1	42.19	253.16	0.18	7.59	45.57	1	42.19	253.16	45 < d ≤ 500	0.19	8.02	48.1
KOH 10	1	41.15	246.91	0.18	7.41	44.44	1	41.15	246.91	45 < d ≤ 500	0.25	10.29	61.73
KOH 2	1	41.67	250	0.18	7.5	45	1	41.67	250	45 < d ≤ 180	0.22	9.17	55
KOH 2	1	41.67	250	0.18	7.5	45	1	41.67	250	180 < d ≤ 355	0.22	9.17	55
KOH 2	1	41.67	250	0.18	7.5	45	1	41.67	250	355 < d ≤ 500	0.22	9.17	55

Ca(OH)₂5 (Table 4) were prepared with silica sand size range of (180 < d ≤ 355) μm.

3.3.1.3. Polymerization of kaolinite using Ca(OH)₂ and silica sand:

Five batches of kaolinite, Ca(OH)₂, silica sand and distilled water were prepared. These batches Ca(OH)₂1 to

Table 4: Ratio, mass fraction and weight of batch components for kaolinite polymerization with Ca(OH)₂ and silica sand.

Batch Name	Kaolinite			Ca(OH) ₂			Sand				Water		
	R _i	X _i	W _i (g)	R _i	X _i	W _i (g)	R _i	X _i	W _i (g)	Particles size	R _i	X _i	W _i (g)
Ca(OH) ₂ 1	1	40.49	242.91	0.25	10.12	60.73	1	40.49	242.91	180 < d ≤ 355	0.22	8.91	53.44
Ca(OH) ₂ 2	1	42.37	254.24	0.14	5.93	35.59	1	42.37	254.24	180 < d ≤ 355	0.22	9.32	55.93
Ca(OH) ₂ 3	1	43.1	258.62	0.1	4.31	25.86	1	43.1	258.62	180 < d ≤ 355	0.22	9.48	56.9
Ca(OH) ₂ 4	1	43.86	263.16	0.06	2.63	15.79	1	43.86	263.16	180 < d ≤ 355	0.22	9.65	57.89
Ca(OH) ₂ 5	1	44.64	267.86	0.02	0.89	5.36	1	44.64	267.86	180 < d ≤ 355	0.22	9.82	58.93

3.3.2. Specimens Preparation:

3.3.2.1. Components Preparation:

The components of each mixture; the kaolinite, alkaline additives, silica sand and distilled water were accurately weighed. Several batches of specimens were prepared with different materials and mass fractions with a total weight of 600 g. The mass fraction of each component was calculated according to the following equation:

$$x_i = \left(\frac{R_i}{\sum_{i=1}^n R_i} \right) * 100\% \quad (1)$$

Where x_i is the mass fraction of component i, R_i is the ratio of component i to kaolinite and n is the number of components.

The weight of each component was calculated according to the following equation:

$$W_i = \left(\frac{x_i}{100} \right) * 600 \quad (2)$$

Where W_i is the weight of component i (g) and x_i is the mass fraction of component i.

3.3.2.2. Solutions preparation:

Sodium and potassium hydroxide solutions were prepared by adding a weighed amount of distilled water to a weighed amount of hydroxide pellets in plastic bottles; the bottles were closed to avoid evaporation then were shaken. As these solutions become hot, they were placed in a water bath to allow the solution cool down.

3.3.2.3. Constituents mixing:

Mixing of the weighed kaolinite, silica sand, alkaline and distilled water was done using a Kitchen Aid Artisan mixer (model 5KSM150PS). Two methods were used to carry on the mixing step; liquid method where kaolinite and silica sand were mixed at speed 1 for 2 minute then solutions of sodium or potassium hydroxides were added to the mixture before mixing was continued at speed 2 for 10 minutes and solid method where kaolinite, silica sand and calcium hydroxide in a powder form were mixed at speed 1 for 2 minutes then distilled water was added to the dry mixture before mixing was continued at speed 2 for 10 minutes. At several time intervals of 4 minutes mixing was stopped to remove any materials stuck on the rotating shaft or on the body of the mixing bowl.

3.3.2.4. Specimens moulding:

The mixture of each batch with total weight of 600 g was divided into ten equal specimens by weight (60 g). The specimens were immediately moulded after weighing to avoid both drying and decrease of the workability of the mixture. They were moulded using a stainless steel cylindrical mould with dimensions of 50 mm length and 26 mm diameter under a pressure of 15 MPa using a manually SHOP hydraulic press (model GARG-501-9). Then the moulded specimens were extruded using CARVER laboratory press (model C), before they were weighted and given numbers.



Figure 2: Extruded and numbered samples.

3.3.2.5. Specimens curing:

The extruded specimens were cured by placing them for 24 hours in BINDER oven (model ED 115) at a temperature of 80°C. In the case of Ca(OH)₂ curing was done under enclosed curing condition (closed in sealed container) at 80°C for 7 days in the oven, this variation in curing conditions was recommended to avoid the premature dehydration of the specimens and formation of CaCO₃ by absorbing CO₂ from atmosphere, which had a negative effect on the development of strength [10]. After this period of time the specimens were removed from the oven and they were allowed to cool down under laboratory conditions. The cured specimens were then weighed and the dimensions (length and diameter) were measured using KERN EG/EW electronic balance (model 3000-2M) and OXFORD digital caliper (model 331-3120K) respectively.

3.3.2.6. Pre-test treatment:

Specimens of each batch were variously treated; they were divided into four groups. The first group consists of 3 specimens where they were dried in SHEL lab oven (model CE3) at 40 °C for 7 days then their density, uniaxial compressive strength and durability under dry conditions were measured. The second group consists of 3 specimens where they were immersed in plastic containers filled with tap water for 7 days and after that their water absorption, their uniaxial compressive strength and durability under wet conditions were measured. The third group consists of 2 specimens where they were subjected to five cycles of drying and wetting, that means specimens were immersed in tap water for one day and then dried in an oven at a temperature of 40 °C for a day; this was repeated five times, before they were immersed in water for another day and after that uniaxial compressive strength and durability were measured. Finally the fourth group consists of 2 specimens, which were subjected to five cycles of drying and wetting, that means specimens were immersed one day and then dried in an oven at a temperature of 40 °C for a day; this was repeated five times before they were put in an oven at a temperature of 40 °C for another day before determining their uniaxial compressive strength and durability [10].

3.3.3. Testing of specimens:

3.3.3.1. Determination of water absorption:

Water absorption is the property of a material to be saturated with water [16]. It was determined for specimens soaked by total submergence in tap water for 7 days using the following equation [9, 10]:

$$A\% = \left(\frac{W_w - W_d}{W_d} \right) * 100\% \quad (3)$$

Where A% is the percentage of water absorbed by the specimen, W_w is the weight of the immersed specimen after drying with a paper towel (g), W_d is the weight of the specimen after curing at 80 °C (g).

3.3.3.2. Uniaxial compression test:

Uniaxial compression strength is a mechanical property which refers to the capacity of a material to withstand axially directed pushing forces. It is that value of uniaxial compressive stress reached when the material fails completely. The uniaxial compression test was performed using the CONTROLS CBR testing machine (model SBA-5T). The uniaxial compressive strength was determined [9, 10] using the following equation:

$$S = \frac{L}{A} \quad (4)$$

Where S is the uniaxial Compressive strength (N/m² or Pa), L is the maximum load applied before failure (N), A is the cross section area of the specimens (m²).

Compressive strength was measured for specimens treated in different ways. S1 is the dry compressive strength of specimens that dried for 7 days at a temperature of 40 °C, S2 is the immersed specimens compressive

strength of specimens that immersed for 7 days in a tap water, S4 is the cycling dry compressive strength of the specimens that immersed in tap water for one day and then dried in an oven at a temperature of 40 °C for a day; this was repeated five times, then they were dried in an oven at a temperature of 40 °C for one day. S3 is the wet cycling compressive strength of the specimens that immersed in tap water for one day and then dried in an oven at a temperature of 40 °C for a day, this was repeated five times, then they were immersed in water for one day.

The stability and durability of produced specimens was evaluated by calculating the differences between the compressive strength under different conditions. L1 is the loss of compressive strength due to immersion process. L2 and L3 is the loss of compressive strength due to cycling process under dry and wet conditions. The loss of compressive strength was calculated by using equations ((5)-(7)) [10].

$$L1 = \left(1 - \frac{S_2}{S_1}\right) * 100\% \quad (5)$$

$$L2 = \left(1 - \frac{S_3}{S_1}\right) * 100\% \quad (6)$$

$$L3 = \left(1 - \frac{S_4}{S_1}\right) * 100\% \quad (7)$$

3.3.3.3. Chemical and mineral analyses:

XRF analysis was performed to identify the chemical composition of the produced specimens, and XRD analysis was employed to identify the major mineralogical components of the produced specimens. The analysis was carried out at the NRA laboratories for those produced specimens that give optimum compressive strength.

4. Results and Discussion

4.1. Effect of NaOH and silica sand on kaolinite polymerization:

4.1.1. Effect of varying the ratio of NaOH to kaolinite:

In order to study the effect of sodium hydroxide content on the produced specimens. Several NaOH to kaolinite ratios of 0.18, 0.16, 0.15, 0.14, 0.12, and 0.10 were used with silica sand of particles size range of ($45 < d \leq 500$) μm . All the produced specimens were stable, no swelling or shrinking was observed. Figure 3 shows the water absorption as a function of NaOH to kaolinite ratio. Water absorption decreases with increasing NaOH to kaolinite ratio from 10.28 to 9.44 %. This may be attributed to the fact that higher alkali content in the mixture gives better reactivity, since NaOH having an affinity for water and readily dissolving in water, then more Al and Si species dissolve, resulting in denser microstructure, which means fewer surfaces for water to absorb on [17].

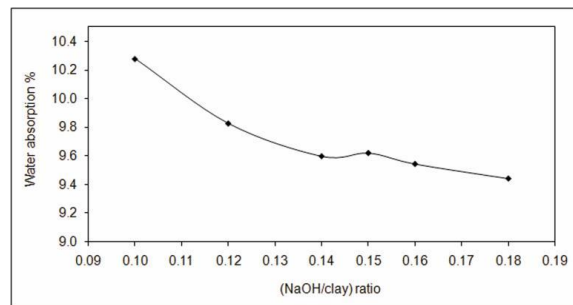


Figure 3: Water absorption as a function of NaOH to kaolinite ratio.

Figure 4 shows the variation of the specimens compressive strength as a function of NaOH to kaolinite ratio. A maximum compressive strength of 44.01 MPa was obtained for dry specimens (S1) containing NaOH to kaolinite ratio of 0.14. Similarly, the compressive strength of the immersed specimens (S2), the compressive strength of the dry cycling specimens (S3), and the compressive strength of the wet cycling specimens (S4) show a maximum value of 18.68, 39.08, and 20.12 MPa respectively. As a result NaOH to kaolinite ratio of 0.14 was considered as the optimum ratio which was used for all the next stages.

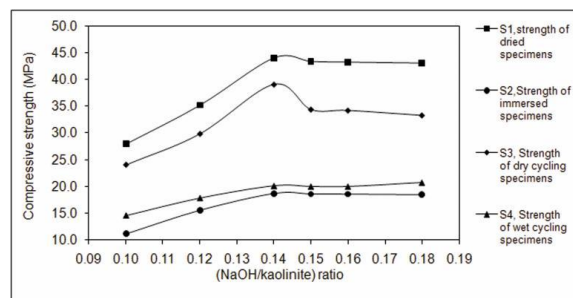


Figure 4: Variation of the specimen's compressive strength as a function of NaOH to kaolinite ratio.

The compressive strength of the specimens under different conditions increases with the increase of NaOH to kaolinite ratio from 0.10 up to 0.14 and then the compressive strength starts to decrease for specimens prepared with NaOH to kaolinite ratio greater than 0.14. This is probably due to the fact that with increasing the NaOH content affects the dissolution of Al and Si from kaolinite and more monomers will liberate into the solution ready for polymerization. Increasing the amount of sodium hydroxide within the specimens can be beneficial until certain limit. Beyond which excess sodium content can form Na_2CO_3 as a result of CO_2 absorption from the atmosphere may disrupt the polymerization process [6]. This salt will dissolve in water and even in the presence of the humidity. Salt dissolution causes a reduction in the strength and stability of the end products [13].

It is noticed that the loss of compressive strength values varied from 55.80 to 60.12 % due to immersion in water (L1), from 11.20 to 22.73 % due to cycling under dry condition (L2), and from 47.71 to 54.28 % due to cycling under wet condition (L3).

4.1.2. Effect of varying the ratio of silica sand to kaolinite:

The use of silica sand as a filler material in kaolinite polymerization process has two advantages; the first is to make the mixing process easier by reducing the cohesion between particles, and the second is to give strength to the end product by improving the grain packing within the specimens [13]. In order to study the effect of the silica sand content of particles size range of (45-500) μm on the produced specimens, four batches were prepared by varying the ratio of the silica sand to kaolinite as 1, 1.50, 1.25, and 0.75.

Figure 5 shows the water absorption as a function of silica sand to kaolinite ratio. Water absorption decreases from 9.85 to 9.60 % by increasing silica sand to kaolinite ratio from 0.75 to 1, then increases from 9.60 to 9.97 % by increasing silica sand to kaolinite ratio from 1 to 1.5. This indicates that increasing silica sand to kaolinite ratio from 0.75 to 1 causes much better grain packing, and thus a dense and strong structure with a reduction in water absorption, then any increment in the silica sand content to a constant kaolinite content will produce cohesionless grain packing with an increase of water absorption.

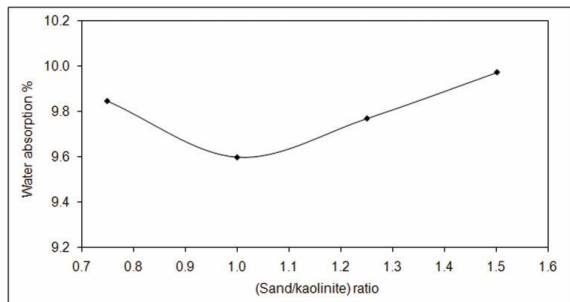


Figure 5: Variation of water absorption with the variation of silica sand to kaolinite ratio.

Figure 6 shows the variation of the specimens compressive strength as a function of silica sand to kaolinite ratio. A maximum compressive strength of 44.01 MPa was obtained for the dried specimens (S1) with silica sand to kaolinite ratio of 1. Similarly, maximum values of 18.68, 39.08, and 20.12 MPa were obtained for immersed (S2), dry cycling (S3), and wet cycling specimens (S4), respectively with a silica sand to kaolinite ratio of 1. As a result this silica sand to kaolinite ratio is considered as the optimum ratio used for all the next stages.

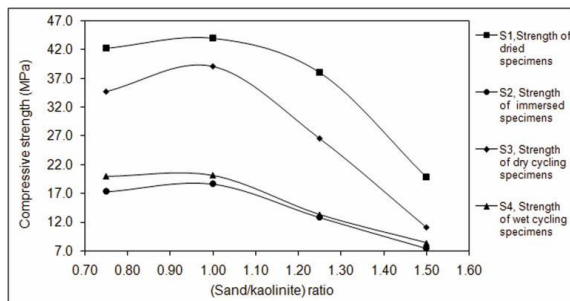


Figure 6: Variation of the specimen's compressive strength as a function of silica sand to kaolinite ratio.

One possible explanation for the increase of the specimens compressive strength as a result of increment of silica sand to kaolinite ratio from 0.75 up to 1 is the improvement of the grain packing of the specimens by reduction of pores, and thus a dense and strong structure is

formed. Beyond the silica sand to kaolinite ratio of 1, an observable reduction in the specimens compressive strength due to the cohesionless grain packing with increment of pores and less is geopolymerization [18].

The loss of compressive strength values range from 57.56 to 66.30 % due to immersion process (L1), from 11.204 to 44.028 % due to cycling under dry condition (L2), and from 52.81 to 65.04 % due to cycling under wet condition (L3).

4.1.3. Effect of varying the ratio of water to kaolinite:

To reveal the effect of water content on the produced specimens, three batches were prepared using ratio of water to kaolinite of 0.19, 0.22 and 0.25, respectively. It is observed that using water to kaolinite ratio of 0.19 showed low workability. The mixture was cohesionless, the compaction and extruding of the specimens from the mould was very difficult. The workability of the mixture was improved by increasing the water to kaolinite ratio to 0.22, but again, the workability of mixing becomes very low by using 0.25 water to kaolinite ratio because at this ratio the excess amount of water made cohesive mixture, difficult to compact and to extrude. Figure 7 shows the water absorption as a function of water to kaolinite ratio. The percentage of absorbed water decreased from 9.98 to 7.99 % as the ratio of water to kaolinite increased. This may be referred to the tendency of mineral polymerization mixtures to form larger crystals when the total amount of water in the reaction mixture is increased. This increment in the water content will lead to a decrease in the specific surface area for each specimens so decrease in the water absorption [18].

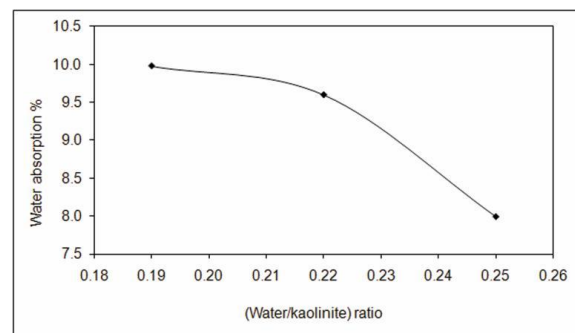


Figure 7: Water absorption as a function of water to kaolinite ratio.

Figure 8 shows the variation of the specimens compressive strength with the variation of water to kaolinite ratio. A maximum compressive strength value of 44.01 MPa was obtained for the dried specimens (S1) with water to kaolinite ratio of 0.22. Similarly maximum values of 18.68, 39.08, and 20.12 MPa were obtained for immersed (S2), dry cycling (S3), and wet cycling specimens (S4), respectively. As a result water to kaolinite ratio of 0.22 was considered as the optimum ratio and used in all the next stages.

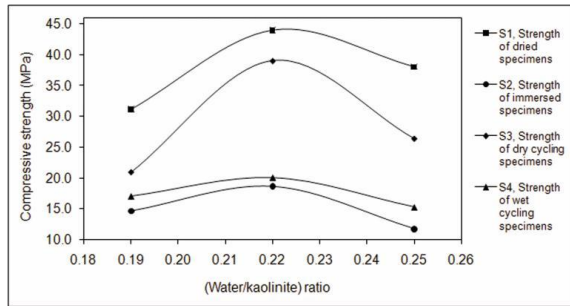


Figure 8: Variation of the specimen's compressive strength with the variation of water to kaolinite ratio.

Increasing the water to kaolinite ratio above 0.22 causes a reduction in the compressive strength. This may be attributed to two possibilities; the first is the evaporation of the water leaving large voids with fragile microstructure with low compressive strength for the end products. The second possibility is that the dilution effect of excess water that lowers the hydroxide ion concentration in the solution, which could decrease the dissolution of Al and Si from kaolinite during the polymerization process [6, 13].

For these samples the loss of compressive strength values varied from 52.88 to 69.08 % due to immersion process (L1), from 11.20 to 32.61 % due to cycling under dry condition (L2), and from 45.13 to 59.81 % due to cycling under wet condition (L3).

4.1.4. Effect of varying silica sand particles size:

To investigate the effect of silica sand particles size range on the produced specimens, three batches were prepared by varying the silica sand particles size range as ($45 < d \leq 180$), ($180 < d \leq 355$), and ($355 < d \leq 500$) μm . The absorbed water by the specimens as a function of silica sand particles size is shown in Figure 9. The absorbed water decreased from 9.72 % to 8.86 % as the silica sand particles size increased. This may be referred to the reduction of surface area as the particles size increase.

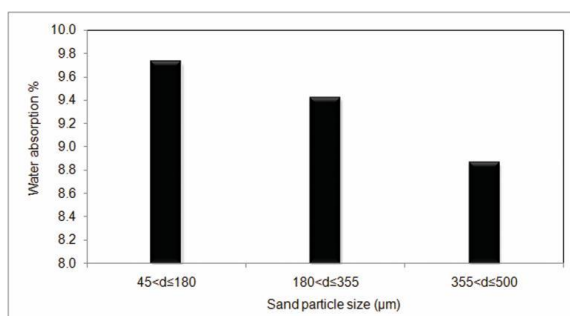


Figure 9: The absorbed water by the specimens as a function of silica sand particles size.

The specimen's compressive strength as a function of silica sand particles size is presented in Figure 10. A maximum compressive strength value of 45.45 MPa was obtained for the dried specimens (S1) for specimens produced with silica sand particles size range of ($180 < d \leq 355$) μm . Similarly, the immersed (S2), the dry cycling (S3), and the wet cycling specimens (S4) show maximum values of 20.38, 40.38, and 22.72 MPa, respectively.

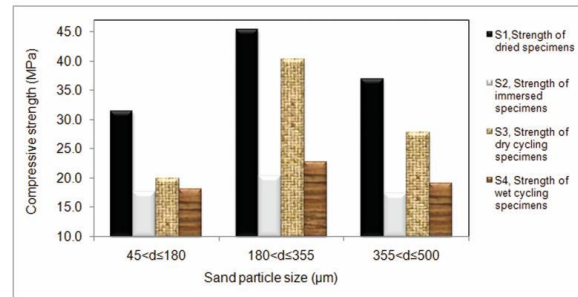


Figure 10: The specimen's compressive strength as a function of silica sand particles size.

The addition of NaOH to the polymerize kaolinite produced specimens with improved strength compared to reference specimens (kaolinite, NaOH, silica sand, and water ratios are 1, 0, 1, and 0.22 respectively) which have (S1) value of 2.53 MPa, and disintegrated completely immediately after immersed in water. The compressive strength of the dried specimens (S1), the immersed (S2), show maximum values of 45.45, and 20.38 MPa, respectively, and a water absorption of 9.41 % were obtained for specimens produced with kaolinite: NaOH: silica sand: and water ratios fixed at 1: 0.14: 1: and 0.22, respectively, and silica sand particles silica sand range of ($180 < d \leq 355$) μm .

The loss of compressive strength values varied from 43.44 to 55.16 % due to immersion process (L1), from 11.17 to 24.75 % due to cycling under dry condition (L2), and from 42.39 to 50.01 % due to cycling under wet condition (L3).

4.2. Effect of KOH and silica sand on kaolinite polymerization:

4.2.1. Effect of varying the ratio of KOH to kaolinite:

To study the effect of potassium hydroxide content on the produced specimens, five batches were prepared by varying the ratio of KOH to kaolinite as 0.25, 0.18, 0.16, 0.14, and 0.12, the silica sand particles size range was fixed at ($45 < d \leq 500$) μm . Using KOH to kaolinite ratio less than 0.12 produced unstable specimens in water, this may be referred to the low percentage of KOH to polymerize kaolinite. All produced specimens were stable. The variation of water absorption as a function of KOH to kaolinite ratio is presented in Figure 11. Water absorption decreased from 10.29 to 8.80 % as the KOH to kaolinite ratio increased from 0.12 to 0.25 %. This may be attributed to the fact that higher alkali content in the mixture gives better reactivity resulting in denser microstructure, which means fewer surfaces for water absorption [17].

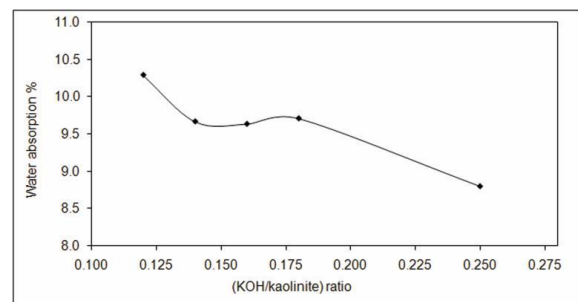


Figure 11: Variation of water absorption as a function of KOH to kaolinite ratio.

Figure 12 shows the specimens compressive strength as a function of KOH to kaolinite ratio. The specimens compressive strength increased by increasing the KOH to kaolinite ratio, a maximum compressive strength of 26.00 MPa was obtained for the dried specimens (S1) using KOH to kaolinite ratio of 0.25. Similarly, the immersed (S2), the dry cycling (S3), and the wet cycling specimens (S4) show maximum values of 10.87, 15.09, and 13.58 MPa, respectively.

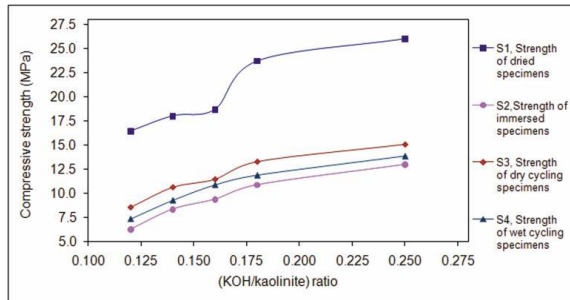


Figure 12: The specimen's compressive strength as a function of KOH to kaolinite ratio.

The compressive strength of the specimens under different conditions increased as the KOH to kaolinite ratio increased. This is probably due to the fact that increasing the KOH content will result in more dissolution of Al and Si from kaolinite and more monomers liberated into the solution ready for polymerization [6].

The tests show that the loss of compressive strength values varied from 38.68 to 48.10 % due to immersion process (L1), from 11.20 to 32.61 % due to cycling under dry condition (L2), and from 41.79 to 55.20 % due to cycling under wet condition (L3).

4.2.2. Effect of varying the ratio of silica sand to kaolinite:

In order to study the effect of silica sand content of particles size range of ($45 < d \leq 500$) μm on the produced specimens, four batches were prepared by varying the ratio of silica sand to kaolinite of 1, 1.50, 1.25, and 0.75.

The absorbed water percentage as a function of silica sand to kaolinite ratio is shown in Figure 13. Water absorption decreased from 10.86 to 9.71 % by increasing the silica sand to kaolinite ratio from 0.75 to 1, and then increased from 9.71 to 10.63 % by increasing the silica sand to kaolinite ratio from 1 to 1.5. This indicates that increasing the silica sand to kaolinite ratio from 0.75 to 1 caused much better grain packing, and thus a dense and strong structure which reduced the amount of absorbed water, increasing the silica sand to kaolinite ratio above 1 produced specimens with cohesionless grain packing, which absorbed more water as a result of the poor grain packing.

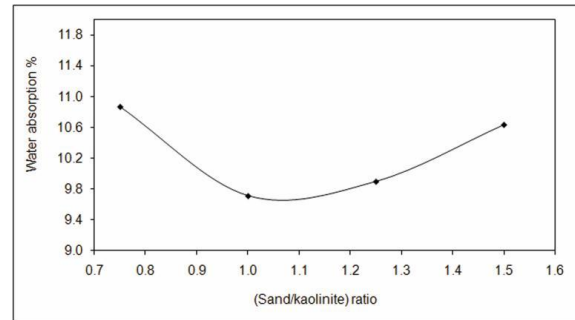


Figure 13: The percentage of absorbed water as a function of silica sand to kaolinite ratio.

Figure 14 presents the variation of the specimens compressive strength with the variation of the silica sand to kaolinite ratio. A maximum compressive strength (S1) of 23.71 MPa was obtained for the dried specimens with silica sand to kaolinite ratio of 1. Similarly, (S2), (S3), and (S4) show maximum values of 10.87, 13.29, and 11.18 MPa respectively using silica sand to kaolinite ratio of 1. Silica sand to kaolinite ratio of 1 was considered as optimum ratio and used in all the next stage.

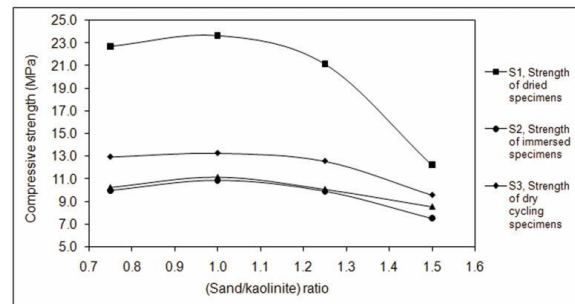


Figure 14: Variation of the specimen's compressive strength with the variation of silica sand to kaolinite ratio.

One possible explanation for the increase in the specimens compressive strength as a result of silica sand to kaolinite ratio increment from 0.75 up to 1 is the improvement achieved in the grain packing of the specimens by reduction of the pores number. Then, as the silica sand to kaolinite ratio increased from 1 up to 1.5 a reduction in the specimens compressive strength was observed due to the cohesionless grain packing and increment of pores number [18].

The variation of the loss of compressive strength values was from 38.71 to 56.10 % due to immersion process (L1), from 21.83 to 43.92 % due to cycling under dry condition (L2), and from 29.99 to 54.81 % due to cycling under wet condition (L3).

4.2.3. The Effect of varying the ratio of water to kaolinite

Three batches were prepared to investigate the effect of water content on the produced specimens. The absorbed water by the specimens as a function of water to kaolinite ratio is presented in Figure 15. The absorbed water decreased from 10.29 % to 8.60 % as the water to kaolinite ratio increased from 0.18 to 0.25. This may be explained by the tendency of mineral polymerization mixtures to form larger crystals when the total amount of water in the reaction mixture, this lead to a decrease in the specific surface area for each specimens and hence a decrease in the amount of absorbed water [19].

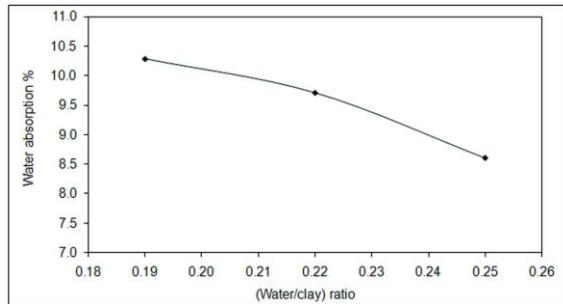


Figure 15: The absorbed water by the specimens as a function of water to kaolinite ratio.

The variation of the specimens compressive strength with the variation of water to kaolinite ratio is shown in Figure 16. A maximum compressive strength value of 23.707 MPa was obtained for the dried specimens (S1) for specimens prepared with water to kaolinite ratio of 0.22. Similarly, the immersed (S2), dry cycling (S3), and wet cycling (S4) show maximum compressive strength values of 10.87, 13.29, and 11.18 MPa respectively at the same water to kaolinite ratio of 0.22. Water to kaolinite ratio of 0.22 was considered as the optimum ratio and used in all the next stages.

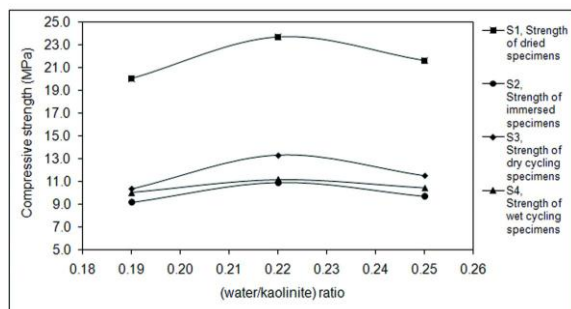


Figure 16: Variation of the specimen's compressive strength with variation of water to kaolinite ratio.

The compressive strength increased as the water to kaolinite ratio increased up to 0.22, then it decreased as the water to kaolinite ratio increased above 0.22. This may be explained by the evaporation of the water, which leaves large voids with fragile microstructure with low compressive strength for the end products. It also may be related to the dilution effect of excess water that lowering the hydroxide ion concentration in the solution, which could decrease the dissolution of Al and Si from kaolinite during the polymerization process [6, 13].

The loss of compressive strength for specimens prepared with the addition of KOH varied from 54.13 to 55.24 % due to immersion process (L1), from 43.92 to 48.39 % due to cycling under dry condition (L2), and from 50.00 to 52.82 % due to cycling under wet condition (L3).

4.2.4. The Effect of varying the ratio of water to kaolinite:

In order to study the effect of silica sand particles size range on the end product, three batches were prepared by varying the silica sand particles size range as ($45 < d \leq 180$), ($180 < d \leq 355$), and ($355 < d \leq 500$) μm .

The absorbed water by the specimens as a function of silica sand particles size is presented in Figure 17. Water absorption decreased from 10.82 to 9.28 % by increasing the silica sand particles size range from ($45 < d \leq 180$) to

($355 < d \leq 500$) μm . The reduction of the absorbed water may be attributed to the decrease of surface area as the particles size increase.

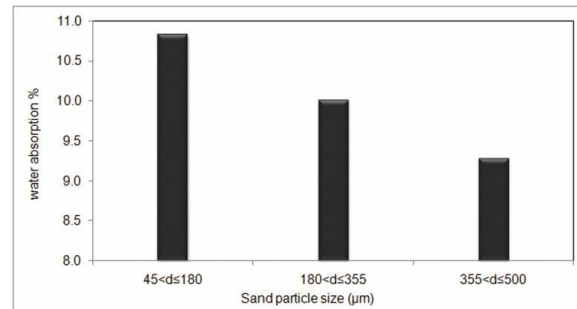


Figure 17: The absorbed water by the specimens as a function of silica sand particles size.

Figure 17 shows the variation of the specimens compressive strength with the variation of silica sand particles size. A maximum compressive strength value of 26.53 MPa was obtained for the dried specimens (S1) for specimens prepared with silica sand particles range of (180-355) μm . Similarly, the immersed (S2), dry cycling (S3), and wet cycling (S4) show maximum compressive strength values of 11.98, 14.21, and 12.04 MPa respectively at the same silica sand particles range of (180-355) μm . Silica sand particles range of (180-355) μm was considered as the optimum silica sand size range and used in all the next stages.

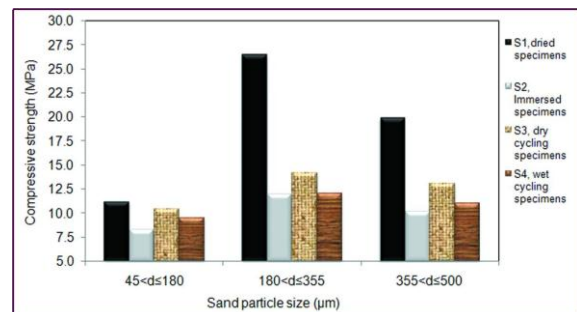


Figure 18: Variation of the specimen's compressive strength with the variation of silica sand particles size.

The loss of compressive strength values varied from 26.34 to 54.84 % due to immersion process (L1), from 7.38 to 46.44 % due to cycling under dry condition (L2), and from 8.79 to 15.77% due to cycling under wet condition (L3).

It should be noted that specimens that were prepared with the addition of NaOH exhibit significantly higher compressive strength values compared to the other specimens which were prepared with the addition of KOH, this may related to the fact that a higher extent of dissolution in NaOH than in KOH medium where Na^+ compared with K^+ enhances the dissolution of aluminum and silicate species [20]. As Na^+ and K^+ have the same electric charge, their different effects are a result of their different ionic sizes, the cation-anion pair interaction becomes less significant as the cation size increases. Cations with smaller sizes favour the ion-pair reaction with the smaller silicate monomers, dimers and trimers. Hence, it is expected that Na^+ with the smaller size will be more active in the reactions compared with K^+ , this should result in a higher extent of dissolution of minerals in the NaOH solution [5].

4.3. Effect of Ca(OH)₂ and silica sand on kaolinite polymerization:

To reveal the effect of calcium hydroxide content on the produced specimens, five batches were prepared by varying the ratio of Ca(OH)₂ to kaolinite as 0.25, 0.14, 0.10, 0.06, and 0.02, and silica sand of particles size range of (180 < d ≤ 355) μm. The produced specimens were stable and there were no observed swelling or shrinking.

The variation of water absorption as a function of Ca(OH)₂ to kaolinite ratio is shown in Figure 19. The absorbed water decreased from 18.00 to 12.80 % as the ratio of Ca(OH)₂ to kaolinite increased from 0.02 to 0.25. This may be attributed to the fact that higher alkali content in the mixture gives better reactivity resulting in denser microstructure, which means fewer surfaces for water absorption [5].

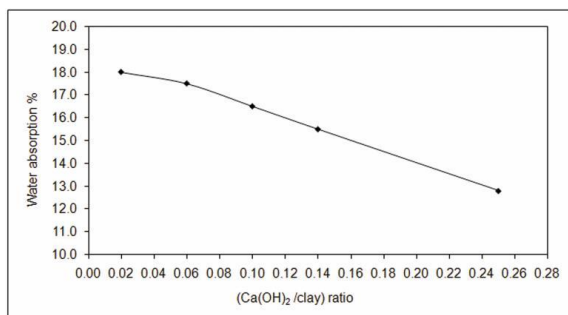


Figure 19: The variation of water absorption with the variation of Ca(OH)₂ to kaolinite ratio.

Figure 20 shows the variation of the specimens compressive strength with as a function of Ca(OH)₂ to kaolinite ratio. Compressive strength increases by increasing Ca(OH)₂ to kaolinite ratio. A maximum compressive strength value of 22.66 MPa was obtained for the dried specimens (S1) for specimens prepared with Ca(OH)₂ to kaolinite ratio of 0.25. Similarly, the immersed (S2), dry cycling (S3), and wet cycling (S4) show maximum compressive strength values of 7.89, 11.35, and 8.47 MPa respectively. The compressive strength of the specimens under different conditions increases with increasing the Ca(OH)₂ to kaolinite ratio. This is probably due to the fact that with increasing the Ca(OH)₂ content will lead to more dissolution of Al and Si from kaolinite and more monomers liberated into solution ready for polymerization [6].

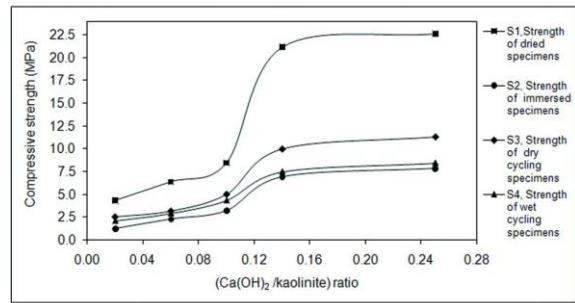


Figure 20: The variation of the specimens compressive strength with the variation of Ca(OH)₂ to kaolinite ratio.

Ca(OH)₂ specimens show the lowest compressive strengths values compared to that of NaOH and KOH specimens, and that was consistent with the low reactivity of Ca(OH)₂, the ageing of this specimens may increase the strength of it [9].

The loss of compressive strength values for specimens prepared with Ca(OH)₂ as the alkali material varied from 61.83 to 70.98 % due to immersion process (L1), from 41.47 to 52.69 % due to cycling under dry condition (L2), and from 48.36 to 64.54 % due to cycling under wet condition (L3).

4.4. Specimens Characterization:

For all produced specimens in the present work, the reduction (loss) in the compressive strength on soaking maybe due to several factors; one of these factors is the hydration process of the produced specimens. The liberation of water they hold acts to reduce the binder strength. Another factor that may lead to the reduction is the loss of some additives in the water and this leaves pores which act to decrease the compressive strength [9].

4.4.1. Chemical and mineral analyses results:

Table 5 shows the chemical composition of the produced specimens that give the optimum compressive strength after drying for 7 days at a temperature of 40 °C. This data was obtained by X-ray Fluorescence XRF analysis. The data show that the major components are SiO₂ and Al₂O₃. Ca(OH)₂ specimens have the minimum SiO₂ and Al₂O₃ compared with other specimens, and the highest loss on ignition, this may be explained by the lowest kaolinite and sand weight when using highest Ca(OH)₂ to kaolinite ratio as shown in Table 5.

Table 5: Chemical composition of the produced specimens that produced optimum strength the present study.

Specimens	SiO ₂ %	TiO ₂ %	Al ₂ O ₃ %	Fe ₂ O ₃ %	MgO %	CaO %	Na ₂ O %	K ₂ O %	P ₂ O ₅ %	L.O.I %
NaOH4	75.28	0.54	11.93	4.73	0.29	0.81	4.76	0.71	0.08	2.37
KOH1	74.71	0.52	10.85	4.65	0.39	0.79	0.43	5.65	0.1	2.54
Ca(OH) ₂ 5	66.21	0.43	10.18	3.51	0.15	10.54	0.6	0.47	0.06	7.41

The results of the mineral identification by XRD for the produced specimens that give the optimum compressive strength after drying are shown in Figures from (21 to 23). The XRD patterns show that there are undissolvable ingredients of quartz and kaolinite remain in all the produced specimens. This referred to the partially dissolved of Si and Al by the alkali solution then forming

the units of geopolymers. There are also traces of undissolvable amounts of muscovite and hematite.

Figure 21 shows the X-ray diffractogram pattern of the NaOH4 specimens, it shows new peaks of sodalite (sodium aluminum silicate hydrate, Na₅7Al₅7Si₁₀3O₃₂12H₂O) compared to the original kaolinite XRD pattern that was presented in Figure 1. This material is a zeolite mineral which are hydrated aluminosilicates and consist of three-dimensional

frameworks of AlO_4 and SiO_4 tetrahedra linked to each other by sharing all oxygen, these are more stable and have higher strengths than the kaolinite sheets. Zeolite has porous structure, inner and outer charged surfaces, suitable for ion exchange [21].

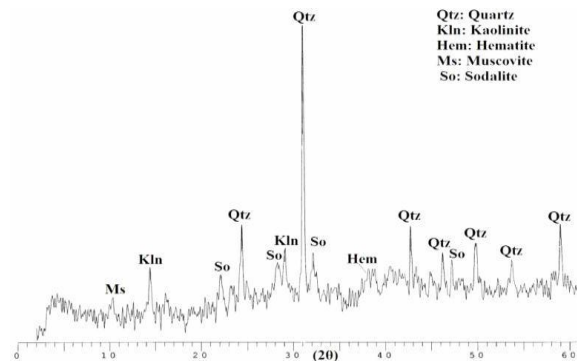


Figure 21: X-ray diffractogram of NaOH4 specimens.

Figure 22 shows X-ray diffractogram pattern of the KOH1 specimens, it shows new peaks of a zeolite mineral; phillipsite (potassium calcium aluminum silicate hydrate, $\text{KCaAl}_3\text{Si}_5\text{O}_{16}\cdot 6\text{H}_2\text{O}$) [3].

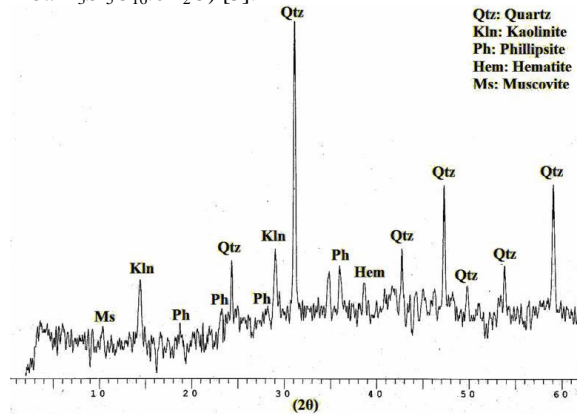


Figure 22: X-ray diffractogram of KOH1 specimens.

The X-ray diffractogram pattern of the $\text{Ca}(\text{OH})_2$ 5 specimens is shown in Figure 23, the figure shows new peaks of a [zeolite](#) mineral; gismondine (calcium aluminum silicate hydrate, $\text{CaAl}_2\text{Si}_2\text{O}_8\cdot 4\text{H}_2\text{O}$).

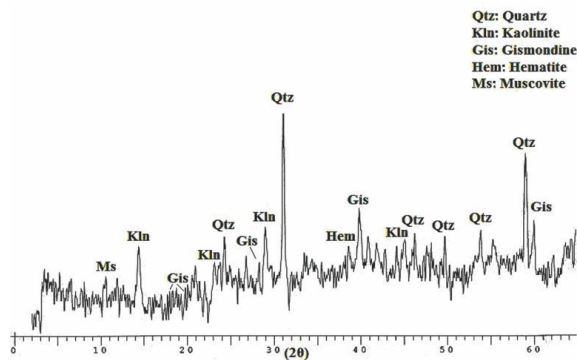


Figure 23: X-ray diffractogram of $\text{Ca}(\text{OH})_2$ 5 specimens.

5. Conclusion

- The optimum specimens were obtained using NaOH to kaolinite ratio of 0.14, water to kaolinite ratio of 0.22, and silica sand to kaolinite ratio of 1 with silica sand particle size of ($180 < d \leq 355$) μm . The values of water absorption, compressive strength under dry and wet condition was 9.41 %, 45.45, and 20.38 MPa respectively.
- Water absorption determination showed a decrease trend as alkaline content, and water content increased, on the other hand a minimum value was obtained when using silica sand to kaolinite ratio of 1.0.
- Compressive strength under different conditions showed a maximum value when using NaOH to kaolinite ratio of 0.14, on the other hand it showed increase trend by increasing KOH, and $\text{Ca}(\text{OH})_2$ content. A maximum value obtained when using silica sand to kaolinite ratio 1, and water to kaolinite ratio of 0.22.
- Variation of silica sand particle size shows an effect on the water absorption, and compressive strength of the produced specimens. This is a result of the changes in the grain packing of this material. Using silica sand particle size range of ($45 < d \leq 180$), ($180 < d \leq 355$), and ($355 < d \leq 500$) μm produce specimens of optimum compressive strength, with moderate density and water absorption.
- The acceptable specification for kaolinite based construction materials are hard to obtain. The standard requirement of 7 days compressive strength for ordinary Portland cement to be used in the general concrete construction has the specification limit of 12 MPa according to (ASTM C 150), while the ordinary Portland cement in Jordan have the 7 days dry compressive strength of 25 MPa. Comparison of this values with the obtained dry compressive strength values of the produced specimens in the present work show acceptable values using NaOH (45.45 MPa), and KOH (26.53 MPa) as alkaline additives with silica sand as a filler.
- Durability of produced specimens was evaluated by calculating the differences between the compressive strength under different conditions. The specimens of NaOH and silica sand as a filler showed the highest durability under dry cycling condition than KOH specimens. While the specimens of KOH and silica sand as a filler showed the highest durability under immersion, and wet cycling condition. The specimens of $\text{Ca}(\text{OH})_2$ and silica sand as a filler were showed the lowest durability.

References

- [1] J. Davidovits, "Properties of geopolymer cements". First International Conference on Alkaline Cements and Concretes, Vol. 1, Kiev State Technical University, Kiev, Ukraine, 1994, 131-149.
- [2] Yasin S, Ghannam A. Kaolin. Internal Report, NRA, Amman, Jordan; 2006.
- [3] J. Davidovits, "Inorganic polymeric new materials". Journal of Thermal Analysis, Vol. 37, No. 8, 1991, 1633-1656.
- [4] D. Khale, R. Chaudhary, "Mechanism of geopolymerization and factors influencing its development: a review". Journal of Materials Science, Vol. 42, No. 3, 2007, 729-746.
- [5] H. Xu, V. Deventer, "The geopolymerisation of aluminosilicate minerals". International Journal of Mineral Processing, Vol. 59, No. 3, 2000, 247-266.
- [6] V. Barbosa, K. MacKenzie, C. Thaumaturgo, "Synthesis and characterisation of materials based on inorganic polymers of alumina and silica: sodium polysialate polymers". International Journal of Inorganic Materials, Vol. 2, No. 4, 2000, 309-317.
- [7] R. Cioffi, L. Maffucci, L. Santoro, "Optimization of geopolymer synthesis by calcinations and polycondensation of a kaolinitic residue". Resources, Conservation and Recycling, Vol. 40, No. 1, 2003, 27-38.
- [8] H. Wang, H. Li, F. Yan, "Synthesis and mechanical properties of metakaolinite based geopolymer". Colloids and Surfaces A: Physicochemical and Engineering Aspects, Vol. 268, No. 1-3, 2005, 1-6.
- [9] Gogo J. Geological and geotechnical evaluation of latosols from Ghana, and their improvement for construction. PhD Thesis. Vrije Universiteit Brussel, Belgium; 1990.
- [10] Al shaaer M. Stabilization of kaolinitic soil from Jordan for construction purposes. MSc Thesis. Vrije Universiteit Brussel, Belgium; 2000.
- [11] Linh N. Stabilization of kaolinitic soil from viet nam for construction purposes. MSc Thesis. Vrije Universiteit Brussel, Belgium; 2002.
- [12] Fai N. Stabilization of soils from Cameroon for construction purposes. MSc Thesis. Vrije Universiteit Brussel, Belgium; 2007.
- [13] Esaifan M. Stabilization of Jordanian soils for water harvesting purposes. MSc Thesis. Vrije Universiteit Brussel, Belgium; 2007.
- [14] Khoury H, Hodali H, Hourani M, Mubarak Y, Faqir N, Hanayneh B, Esaifan M. Mineral polymerization of some industrial rocks and minerals in Jordan. Internal Report. University of Jordan, Amman, Jordan; 2008.
- [15] Bowles J. Engineering Properties of Soil and Their Measurement. 4th ed. Singapore: McGraw-Hill Inc; 1992.
- [16] A. Okunade, "The effect of wood ash and sawdust admixtures on the engineering properties of a burnt laterite clay brick". Journal of Applied Sciences, Vol. 8, No. 6, 2008, 1042-1048.
- [17] S. Thokchom, P. Ghosh, S. Ghosh, "Effect of water absorption, porosity and sorptivity on durability of geopolymer mortars". Journal of Engineering and Applied Sciences, Vol. 4, No. 7, 2009, 28-32.
- [18] H. Shu-guang, W. Jing, W. Yang, H. Yong-jia, W. Fa-zhou, D. Qing-jun, "Preparation and properties of geopolymer lightweight aggregate refractory concrete". Journal of Central South University of Technology, Vol. 16, No. 6, 2009, 914-918.
- [19] V. Jaarsveld, V. Deventer, G. Lukey, "The effect of composition and temperature on the properties of fly ash and kaolinite based geopolymers". Chemical Engineering Journal, Vol. 89, No. 1-3, 2002, 63-73.
- [20] H. Xu, V. Deventer, G. Lukey, "Effect of Alkali Metals on the Preferential Geopolymerization of Stilbite/Kaolinite Mixtures". Industrial and Engineering Chemistry Research, Vol. 40, No. 17, 2001, 3749-3756.
- [21] R. Yousef, B. El-Eswed, M. Alshaaer, F. Khalili, H. Khoury, "The influence of using Jordanian natural zeolite on the adsorption, physical, and mechanical properties of geopolymers products". Journal of Hazardous Materials Science, Vol. 165, No. 1-3, 2009, 379-387.

The Effect of Thermal Barrier Coatings on Diesel Engine Performance of PZT Loaded Cyanate Modified Epoxy Coated Combustion Chamber

Vijaya Kumar K.R^{*a}, Sundareswaran V.^a

^aDepartment of Mechanical engineering, Anna University, Chennai-25, India.

Abstract

The performance of internal combustion engines should be improved depending on some technological requirements and rapid increase in the fuel expenses. On the other hand, the improvements in engine materials are forced by using alternative fuels and environmental requirements. Therefore, the performances of engine materials become increasingly important. The purpose of PZT loaded cyanate modified epoxy system (60EPCY 20PI) is to focus on developing binder systems with low thermal conductivity and improve the coating durability under high load condition. The coating material is made up of 20% Lead Zirconate Titanate (PZT) in 60% Cyanate modified Epoxy system. The triazine ring of cyanate ester offers better thermal resistance characteristics to the epoxy system. Experimental investigation is carried out under different load condition on a single cylinder diesel engine with PZT loaded cyanate modified epoxy resin system of 0.5 mm thickness to the piston, cylinder head with valves and cylinder liner. The result showed 15.89 % of reduced specific fuel consumption. Emissions of unburnt hydrocarbon, carbon monoxide are reduced whereas NOx is increased.

© 2011 Jordan Journal of Mechanical and Industrial Engineering. All rights reserved

Keywords: 60EPCY 20PI; triazine ring; Diesel engine; Emissions; Thermal Resistance

1. Introduction

Diesel engine has become the most fuel efficient power plant sustainable for mobile application. It has assumed a leading role in both transport and agricultural sector because of its outstanding fuel economy and its lower running cost. Even in diesel engine the coolant and exhaust gases carry substantial amount of fuel energy away from the combustion chamber [1]By using PZT loaded cyanate modified epoxy system (60EPCY 20PI) coated combustion chamber there is reduction in heat transfer to the coolant and an improvement in power output along with an increase in exhaust energy.

The transfer of heat is conducted through the combustion chamber elements, like valves, piston surfaces and liners. Ceramic of this element by a composite with low thermal conductivity keeps the heat in the chamber and hence increases the temperature [2]. The requirement for more efficient engines in the future will also require even higher operating temperatures. Ceramic with their high temperature resistance, may offer an excellent coating surface to reduce the amount of degradation and to extend the life. Composite coating absorbs thermal shocks and protects the substrate.

The primary purposes of high temperature structural coatings are to enable high temperature components to operate at even high temperature, to improve component durability of engines [3]. 60EPCY 20PI are characterized by excellent mechanical and low thermal conductivity

properties, high chemical and corrosion resistance, low shrinkage on curing and the ability to be processed under a variety of conditions.

In this paper main emphasis is placed on investigating the effect of 60EPCY 20PI coated combustion chamber on the engine fuel consumption and thermal efficiency. Emission measurement of unburned hydrocarbon, carbon monoxide and NOx were also conducted.

Figure 1 shows the 60EPCY 20PI coated piston, cylinder head with valves and liner.



Figure 1: Photographic view of 60EPCY 20PI coated piston, cylinder head with valves and liner.

* Corresponding author. e-mail: priyadarshan02@yahoo.co.in

2. 60EPCY 20PI Material

Epoxy resin LY556 (diglycidyl ether of bis phenol A), curing agent HT972 (DDM - diamino diphenyl methane), Arocy b10 (bis phenol dicyanate), E-glass fibre and lead zirconate titanate (PZT).

The composites are fabricated from E-glass fiber and commercial epoxy resin/cyanate modified epoxy resin. The glass fiber with an aerial density of 200 g/m² was used as the reinforcement for composite laminate. The liquid epoxy was taken in a beaker, which was heated to 90°C to lower the resin viscosity and desired amount of cyanate was added into resin. The Cyanate loading is 60% and 20% PZT loading by weight of epoxy resin. The mixture was degassed in a vacuum oven followed by addition of DDM (curing agent) in 27% by weight of epoxy and stirred for 3 minutes at 90°C. It is coated on the combustion chamber which has high temperature phases like tetragonal and cubic structures.

The mechanical properties are investigated by using universal Testing Machine (Model H50K-S, Hounsfield Test Equipment Ltd, UK). The cross head speed was 1mm / min The span length of the specimen was 150mm .Tensile modulus studies were evaluated as per ASTM D 3039. The flexural strength and flexural modulus of the composites were studied as per ASTM – D790. The crosshead speed was 1.0 mm / min. The double cantilever beam (DCB) test samples for GIC fracture toughness measurements were prepared according to the ASTM D 5528 (dimension 125 x 25 x 3mm) with a preinitiated crack of 50mm. Aluminium hinges were attached to the surfaces of the specimens to facilitate crack propagation. Measurements of load and crack displacement were taken at the initial crack propagation, at 1mm intervals for first 5mm, then at 5 mm interval up to a total crack length of 45 mm and at 1mm intervals for the last 5 mm giving a total of 19 readings. Three methods of data reduction were applied, using software programs, the data quoted being those obtained by compliance method at peak load. The displacement of crack was observed using a camera and the test was carried out in universal testing machine .Table 1 shows the mechanical properties of 60EPCY 20PI.

Table 1: Mechanical Properties of 60EPCY 20PI.

Properties	60EPCY 20PI
Tensile Strength (MPa)	355
Tensile Modulus (GPa)	7.98
Flexural Strength (MPa)	465
Flexural Modulus (GPa)	9.5
Fracture Toughness (kJ/m ² s)	0.9
Damping Factor	0.10029
Stiffness (N/mm)	62.97

3. Test Engine

Tests were carried out on a Kirloskar, single cylinder, water cooled, direct injection, four stroke stationary diesel engine. Once the steady state condition was reached after loading then the readings such as time taken for 10cc fuel consumption, exhaust gas temperature, HC, CO and NOx were taken. The air flow rate was measured by a U tube manometer. The pollutant emissions such as unburnt hydrocarbon, carbon monoxide, carbon dioxide, oxides of nitrogen and oxygen concentrations were measured by AVL 444 exhaust gas analyzer. The analyzer consists of an electrochemical sensor, which converts the concentration

of different species in the exhaust gas into corresponding electrical signals. The exhaust gas temperature was measured by using a k- type thermocouple.

The following Figure shows a photographic view of the Experimental set up.



Figure 2: Photographic view of Experimental set-up.

The Technical specifications of the engine used in the experiments are illustrated in table 2.

Table 2: Technical specification of the engine used in the experiments.

Engine Type	Kirloskar, Vertical, Four stroke diesel engine
Bore Diameter	80mm
Stroke Length	110mm
Brake Power	3.68kW
Compression Ratio	16:01
Speed	1500rpm
Injection Type	Direct Injection
Cooling	Water
Fuel Injection	23°bTDC
No.of.Cylinder	1
Injection Pressure	210 bar

4. Results and Discussion

The performance and Emission characteristics of 60EPCY 20PI material coated combustion chamber diesel engine was investigated and compared with standard engine. 60EPCY 20PI material acts as a thermal barrier coating which can improve BSFC and increase thermal efficiency. UBHC and carbon monoxide emission are reduced compared to standard engine. The results obtained from the experiments conducted on the engine are presented in Figure3 to Figure 8.

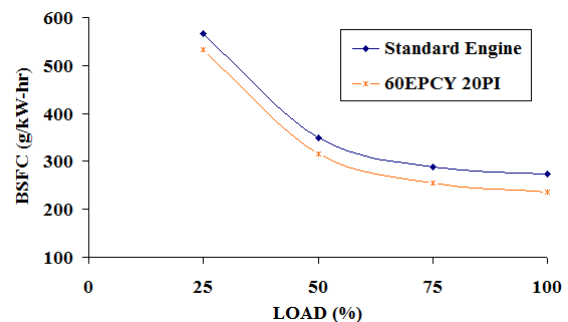


Figure 3: Comparison of Brake Specific Fuel Consumption for different loads.

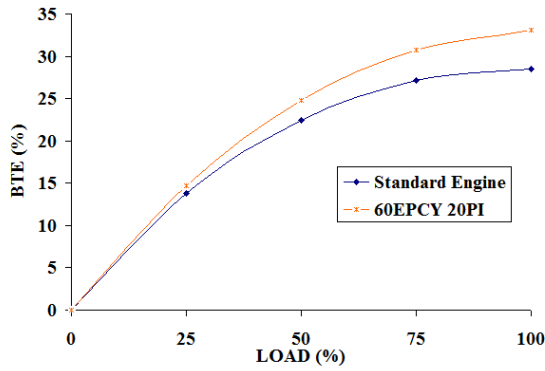


Figure 4: Comparison of Brake Thermal Efficiency for different loads.

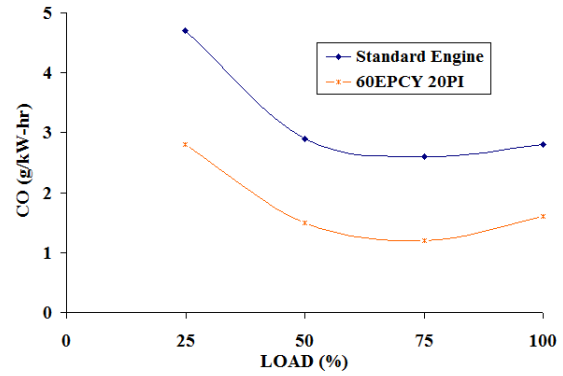


Figure 8. Comparison of carbon monoxide emission for different loads.

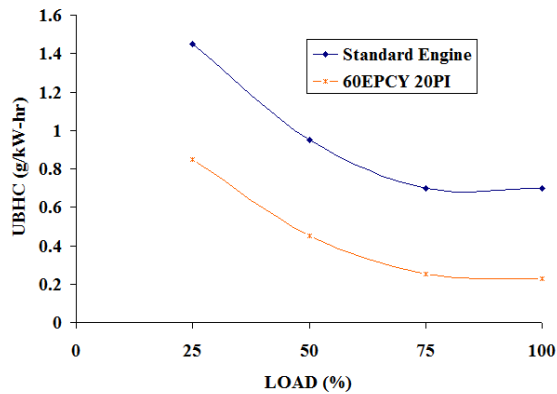


Figure 5: Comparison of Hydrocarbon emission for different loads.

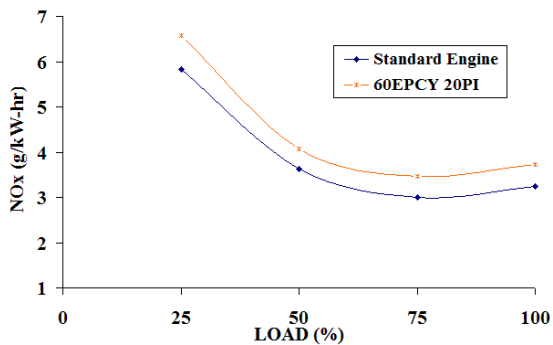


Figure 6: Comparison of Oxides of Nitrogen emission for different loads.

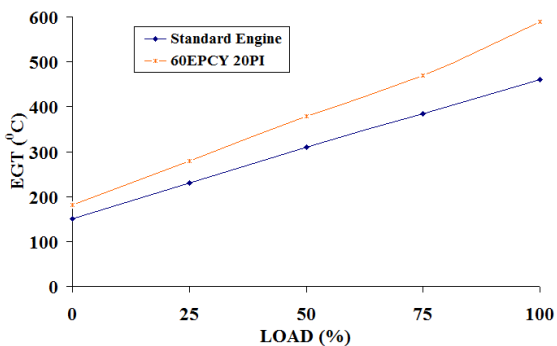


Figure 7: Comparison of Exhaust Gas Temperature for different loads.

Figure 3 shows the variations of brake specific fuel consumption of standard engine and compared with 60EPCY 20PI coated combustion chamber. The specific fuel consumption is reduced by 15.89% for resin-PZT coated combustion chamber compare to standard engine. This may be due to increased temperature of the combustion chamber walls, which increases the temperature of the fuel issuing from the heated nozzle orifice resulting in the reduced fuel viscosity.

The variation of brake thermal efficiency with load for engine operating on 60EPCY 20PI coated combustion chamber and standard engine are shown in figure 4. It is significant that modified combustion chamber has higher efficiency than that of base line. This may be due to thermal resistance on the walls which cannot allow the heat energy to the coolant. The maximum brake thermal efficiency obtained for engine operating on 60EPCY 20PI coated combustion chamber and standard engine are 33.05 % and 28.49 %.

Figure 5 shows the comparison of Hydrocarbon emission for different loads. Formation of sac volume is not possible because of high compression temperature at the end of compression stroke so the fuel droplets stored in the tip of the nozzle also enhance the combustion in the 60EPCY 20PI coated combustion chamber which reduces hydrocarbon emission compared to standard engine. For modified combustion chamber and standard engine HC emissions are 0.23 g/kW-hr and 0.7 g/kW-hr at full load condition.

Figure 6 indicated the variation of oxides of nitrogen with load for 60EPCY 20PI coated combustion chamber and standard engine. NOx is generated mostly from nitrogen present in air and also from fuel. The inherent availability of nitrogen and oxygen in the fuel accelerates the formation of NOx. While observing the trends of modified combustion chamber, it is noticed that higher the combustion and maximum temperature in the combustion chamber which in turn results in higher NOx. With 60EPCY 20PI coated combustion chamber, the NOx level varies from 6.57 g/kWh at no load and 3.72 g/kWh at full load condition.

Figure 7 depicts the variation of exhaust gas temperature with load for 60EPCY 20PI coated combustion chamber and standard engine. It can be observed that when the combustion chamber is 60EPCY 20PI coated the combustion temperature is high which increases exhaust temperature. The increase in temperature is due to the better combustion of oxygenated fuels. The exhaust gas temperature for standard engine is 150°C at no load and 460°C at full load. With 60EPCY 20PI coated

combustion chamber, the exhaust gas temperature increases to 181°C to 590°C.

The measured CO emissions for 60EPCY 20PI coated combustion chamber and standard engine are shown in Figure 8. The reduction in CO emission is due to complete combustion and on local rich region found in the 60EPCY 20PI coated combustion chamber. With 60EPCY 20PI coated combustion chamber, the CO level varies from 2.8 g/kWh at no load and 1.6 g/kWh at full load condition.

5. Conclusion

A conventional contemporary diesel engine was converted to a 60EPCY 20PI coated combustion chamber diesel engine. The BSFC and emission were measured to

determine the performance and emission characteristics of the engine. The following conclusions can be drawn from the experimental results.

60EPCY 20PI coated combustion chamber diesel engine shows better BSFC compared to conventional diesel engine. It is 15.89% reduced specific fuel consumption than the standard engine. NO_x and Exhaust Gas Temperature are so high for 60EPCY 20PI coated combustion chamber diesel engine. Hydrocarbon emission was reduced drastically in 60EPCY 20PI coated combustion chamber diesel engine.

References

- [1] P. Tamilporai, S. Jaichandar, "The Status Of Experimental Investigation On Low Heat Rejection Engines". 2004, SAE Transaction, 2004, Paper No. 2004-01-1453.
- [2] S. Venkatesh, "Surface treatment of Pistons and their effect on engine performance". *Wear*, Vol.25, 1973, 65-71.
- [3] Cengiz Oner, Hanbey Hazar, Mustafa Nursoy, "Surface Properties of CrN Coated Engine Cylinders". *Material and Design*, Vol.30, 2009, 914 -920.
- [4] B.P. Krishnan, N. Raman, K. Narayanaswamy, K.P Rohatgi, "Performance of an AL-SI-GRAPHITE Particle Composite Piston in a Diesel Engine". *Wear*, Vol.60, 1980, 205-215.
- [5] R. Prasad, N. Samria, "Heat transfer and stress fields in the inlet and exhaust valves of a semi-adiabatic diesel engine". *Comput Struct*, Vol.34, 1990, 765-777.
- [6] T. Hejwowski, A. Weronki, "The Effect of Thermal Barrier Coatings on Diesel Engine Performance". *Vacuum*, Vol.65, 2002, 427-432.
- [7] D.J. Godfrey, "The Use of Ceramic for Engines". *Material Design*, Vol. 4, 1983, 759-765.
- [8] B. Hwang, S. Lee, J. Ahn, "Effect of oxides on wear resistance and surface roughness of ferrous coated layers fabricated by atmospheric plasma spraying, *Material Science Engineering*". Vol. 335, 2002, 268-280.
- [9] N. Ganesan, Ravikiran Kadoli, "Buckling and Dynamic Analysis of Piezothermoelastic Composite Cylindrical Shell", *Composite Structure*, Vol. 59, 2003, 45-60.
- [10] Mallick P.K. *Composite Engineering Handbook*. Newyork: Marcel Dekker; 1997.

Variable Structure Controller Schemes Based on Work and Energy Principle for SIMO Systems

M. Ababneh^{*,a}, A. Al-Jarrah^a, K. Al-Widyan^a, S. BaniHani^a

^aMechatronics Engineering Department, Hashemite University, P.O.Box 150459, Zarqa, 13115, Jordan

Abstract

This paper presents a reasoned methodology for designing variable structure controllers (VSC), also known as sliding mode controllers (SMC), for Single- Input-Multi-output (SIMO) systems. The approach is explicitly based on the assessment of a system total energy, and the realization of a VSC that minimizes that energy. A relationship between controller gains and the slope of the sliding surface is explicitly formulated. The practical implementation of the proposed approach is exemplified on an inverted pendulum system where the system has two independent sliding surfaces representing the two system states. A VSC with hyper sliding surface is also introduced. Since the pendulum system has no dissipative viscous load to absorb energy, a VSC for pure inertial systems is proposed.

© 2011 Jordan Journal of Mechanical and Industrial Engineering. All rights reserved

Keywords: Work and Energy; Variable Structure Controller; Hyper; SIMO; Inertial system; Optimal

1. Introduction

VSCs or SMCs are based on the theory of Variable Structure Systems (VSS) which first appeared in the late fifties in Russia as a special class of nonlinear systems [1-2]. A VSC is characterized by a discontinuous action whereby upon reaching a switching, or sliding, surface in the state space the structure of the controller changes to another which is a member of a set of possible continuous functions of the state [2]. This approach can result in a very robust control action that is superior to any of the members of the set of controller it is allowed to switch among taken alone.

The realization of a VSC involves two distinct stages; 1) the equation of the sliding surface or the manifold is designed to meet the desired dynamics of the sliding motion in accordance with some performance specifications, 2) the switching or discontinuous feedback control law is designed such that the locus of the system state would reach the manifold and that the sliding mode exists on this manifold. The design of linear sliding mode surfaces for linear systems was studied and developed extensively [3-9]. The design of the sliding surface for more general nonlinear systems remains largely an open problem [1]. This paper focuses exclusively on linear sliding mode surfaces.

Design theory and procedures outlined in [3-9] and other literature dealing with VSCs and SMCs tend to be specific to a narrow class of plant structures. To overcome this drawback, methods developed in other publications [10- 13] involve integrating the classical theories used for designing the sliding mode surface and the switching control law with other computational intelligence-based systems such as Fuzzy Logic (FL), Neural Networks (NN),

and Genetic Algorithms (GA). However, despite its simplicity of realization and advantages, the lack of a general systematic design approach that is mathematically lucid have hindered its widespread use. Since all the reported VSC design approaches are specific to the specific system under consideration and tend to exploit its characteristics, rather than being general, the need for such a methodology provided the motivation for this work. Furthermore, literature on the subject does not provide an understanding of the link between the control law parameters suitable for VSCs and the sliding surface parameters.

This paper provides a mathematically clear link between the action of a VSC and the work and energy of the system. This link is used to tie the control law parameters to those of the sliding surface. The stability of a designed system using the proposed methodology is provided. The design methodology is suitable for Single-Input-Single-Output (SISO) as well as Single-Input-Multiple-Output (SIMO) control systems. An inverted pendulum system is selected to test the new design methodology is a SIMO system. The system is a special case of Multi-Input-Multi-output (MIMO) control systems and is acknowledged to be difficult one to control. In order to study the performance of the controller, different VSC schemes are proposed and applied to the pendulum system. Simulation results and comparisons between the designed controllers and classical ones are provided to show the performance of the proposed VSC schemes.

2. VSCs and the Principle of Work and Energy

A phase plane portrait of a system relates a system state to its derivative. For a physical system, the axes of the phase plane are typically the displacement and the

* Corresponding author. e-mail: ababneh@hu.edu.jo

velocity. Consider a conservative spring-mass system subjected to a step input displacement. Upon release, the potential energy is gradually converted to kinetic energy as the body accelerates. The continual interchange between potential and kinetic energy cause the body to oscillate. The ordinate of the system phase portrait being velocity can be viewed as a proxy of the kinetic energy and the abscissa being displacement can be viewed as a proxy of the potential energy. With reference to Figure 1, the total energy, E , of the system is given by:

$$E = \frac{1}{2}kx^2 + \frac{1}{2}m\dot{x}^2 \tag{1}$$

where m is the system mass and k is the spring constant. Rearranging Equation 1 and using $a = \sqrt{2E/k}$ and $b = \sqrt{2E/m}$ gives:

$$\frac{x^2}{a^2} + \frac{\dot{x}^2}{b^2} = 1 \tag{2}$$

Equation 2 is that of an ellipse. Figure 1 (b) shows a scaled phase portrait of the system where the abscissa is scaled by $1/a^2$ and the ordinate by $1/b^2$. The ellipses correspond to different initial levels E_i . The phase portrait in the figure shows that the system has no dissipative element since its energy level remains constant. A phase plane portrait that converge to the origin indicates a stable system with decreasing energy level and a phase portrait diverging to infinity indicates an unstable system with increasing energy level as shown in Figure 2 (a) and (b) respectively.

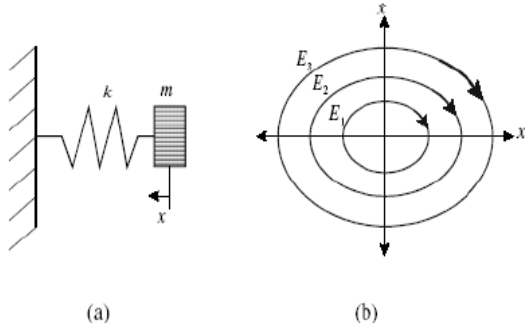


Figure 1: Spring-mass system phase portrait. a) System b) Phase portrait.

A dynamic system converges towards stability if its total energy decreases asymptotically with time to its minimum value at the equilibrium state. Lyapunov criteria exploits this fact by requiring the time derivative of the Lyapunov energy function, be it a true representation of the energy of the system or a proxy for it, to be negative definite.

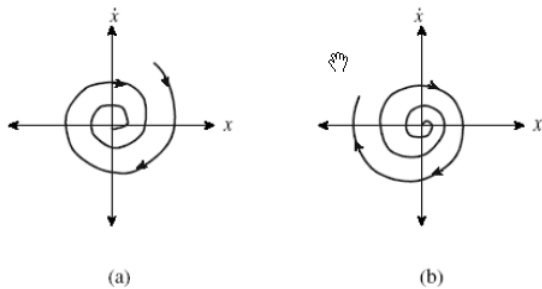


Figure 2: Phase portrait of linear systems. a) Stable b) Unstable.

For a control system, a change in the set point is tantamount to shifting the stability state from 0 on the phase plane portrait to A as shown in Figure 3 (a). 0 now represents the minimum energy level of the system required for stability. It follows that the controller action will appear like it will have to dissipate energy equivalent to that between A and 0.

The locus of the system state due to the controller action can not be strictly along the x-axis. While an infinite number of possible paths can lead the system from state A to 0, those that remain exclusively in the upper left quadrant, Figure 3 (a), correspond to overdamped responses and those that traverse the x-axis, Figure 3 (b), correspond to underdamped responses.

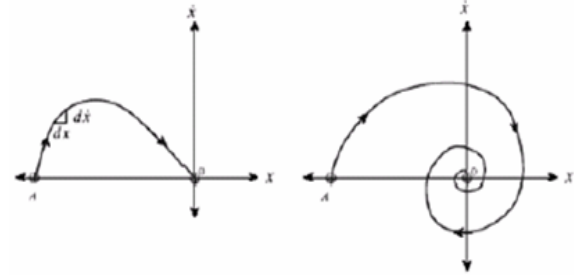


Figure 3: Control system with possible phase plane portrait a) Overdamped phase portrait b) Underdamped phase portrait.

A single structure conventional controller can be designed to allow energy to flow in one direction only resulting in an overdamped system. The system state in this case will remain in the second quadrant of the phase plane. Such a controller will not be optimal. Utkin [2] showed that a variable structure controller can be designed such that the phase plane portrait of the system will have a higher x yet remains entirely in the second quadrant. The energy based design methodology of such a controller is the subject of the next section.

3. Work and Energy Based VSC Design Methodology

With reference to Figure 4, the controller is required to move the system from (1) to (2) in the presence of a dissipative load. The work done by the controller less than that consumed by the dissipative load is related to the energy of the system as follows:

$$T_1 + V_1 + U_{1 \rightarrow 2} = T_2 + V_2 + U_{R(1 \rightarrow 2)} \tag{3}$$

where,

T_1, V_1 are the kinetic and potential energy at position (1).

T_2, V_2 are the kinetic and potential energy at position (2).

$U_{1 \rightarrow 2}$ is the work done by the controller between the two positions.

$U_{R(1 \rightarrow 2)}$ is the work lost due to the viscous damper between the two positions.

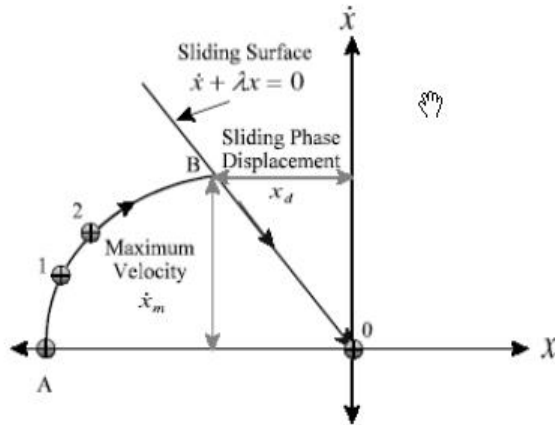


Figure 4: Phase plane portrait showing VSC action.

For a general system, Equation 3 becomes:

$$\frac{1}{2}\beta(\dot{x}_2^2 - \dot{x}_1^2) + \frac{1}{2}\alpha(x_2^2 - x_1^2) - \Gamma(\dot{x}_2x_2 - \dot{x}_1x_1) - k(x_2^2 - x_1^2) = 0 \quad (5)$$

β is the inertial energy storage element constant,
 α is the potential energy storage element constant,
 Γ is the linear dissipative element constant,
 k is the controller gain.

As an example, consider a mechanical system given by the classical differential form:

$$m\ddot{x} + b\dot{x} + k_sx = u$$

Where m , b , and k_s are the mass, damping coefficient, and spring constant respectively. u is the controller force. The work done by the controller between (1) and (2) is given by:

$$\int_1^2 m\ddot{x} dx + \int_1^2 b\dot{x} dx + \int_1^2 k_sx dx = \int_1^2 u dx \quad (6)$$

Substituting $\ddot{x} = \dot{x}d\dot{x}/dx$, $u = kx$ and integrating gives:

$$\frac{1}{2}m(\dot{x}_2^2 - \dot{x}_1^2) + \frac{1}{2}k_s(x_2^2 - x_1^2) - b(\dot{x}_2x_2 - \dot{x}_1x_1) = \frac{1}{2}k(x_2^2 - x_1^2) \quad (7)$$

Comparing equation 4 and 7 shows that:

$$\beta = m, \alpha = k_s, \text{ and } \Gamma = b$$

The energy balance at any point along the trajectory of the VSC phase portrait is given by:

$$\frac{1}{2}\beta\dot{x}^2 + \frac{1}{2}\alpha x^2 - \Gamma\dot{x}x - kx^2 = 0 \quad (8)$$

For the linear sliding surface shown in Figure 4, $x = -\dot{x} / \lambda$, substituting for x into equation 8 gives:

$$\frac{1}{2}\beta\dot{x}^2 + \frac{1}{2\lambda^2}\alpha\dot{x}^2 - \frac{1}{\lambda}\Gamma\dot{x}^2 = \frac{1}{\lambda}k\dot{x}^2 \quad (9)$$

Equation 9 relates the controller gain to the slope of the sliding surface as follows:

$$k = \frac{1}{2}(\beta\lambda^2 + \alpha) + \Gamma\alpha \quad (10)$$

Equation 10 can be used for SISO control systems. An extended design methodology can be achieved to include

SIMO control systems. If a four-state-variables system with a single input is considered, two sliding surfaces can be designed as follows:

$$s_1 = \lambda_1x_1 + x_2 \quad (11)$$

$$s_2 = \lambda_2x_3 + x_4 \quad (12)$$

where x_1, x_2, x_3 , and x_4 are the states of the system and $x_2 = \dot{x}_1$, and $x_4 = \dot{x}_3$.

The input control signal is a relay type signal and is given by:

$$u = k_1x_1 + k_2x_2 \quad (13)$$

where

$$k_1 = \begin{cases} +\eta_1, & sx_1 > 0 \\ -\eta_1, & sx_1 < 0 \end{cases} \quad (14)$$

and

$$k_2 = \begin{cases} +\eta_2, & sx_3 > 0 \\ -\eta_2, & sx_3 < 0 \end{cases} \quad (15)$$

λ_1, λ_2 are the slopes of the sliding surfaces

k_1, k_2 are the controller gains,

η_1, η_2 are the magnitudes of the controller gains.

Equation 10 can be used to find the magnitudes of the controller gains as well as the sliding surfaces slopes as follows:

$$k_1 = \frac{1}{2}(\beta_1\lambda_1^2 + \alpha_1) + \Gamma_1\alpha_1 \quad (16)$$

$$k_2 = \frac{1}{2}(\beta_2\lambda_2^2 + \alpha_2) + \Gamma_2\alpha_2 \quad (17)$$

The same methodology used before for finding the coefficient β, α , and Γ for both k_1 and k_2 is used as it will be shown later. Equations 16 and 17 show that the ranges of the VSC parameters ($\lambda_1, \lambda_2, k_1, k_2$) are very wide such that additional constraints have to be imposed on the choice of the parameters. Sensitivity analysis [14] is introduced to find such constraints as it will be shown in the coming sections.

4. Inverted Pendulum System and VSCSCHEMES

Figure 5 shows an inverted pendulum system. Such systems are popular test cases and examples in many control literature because of the many practical applications they can model, particularly in the field of robotics and rockets [15]. The system is also found to be very informative for performance evaluation and comparison for various types of controllers. The goal for this system is to keep the pendulum always upright by controlling the input force applied to the cart.

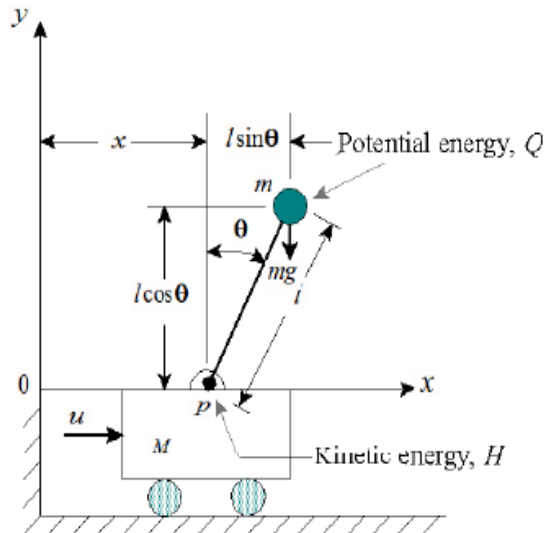


Figure 5: Inverted pendulum system.

With reference to Figure 5, the system has one input, the force u , and two outputs, the pendulum angle and the cart position x . The state space representation of the system dynamics, subject to the assumptions that the pendulum angular displacement is small and the angular velocity is negligible, is given as follows [16]:

$$\begin{bmatrix} \dot{x}_1 \\ \dot{x}_2 \\ \dot{x}_3 \\ \dot{x}_4 \end{bmatrix} = \begin{bmatrix} 0 & 1 & 0 & 0 \\ -\frac{m}{M}g & 0 & 0 & 0 \\ 0 & 0 & 0 & 1 \\ \frac{M+m}{MI}g & 0 & 0 & 0 \end{bmatrix} \begin{bmatrix} x_1 \\ x_2 \\ x_3 \\ x_4 \end{bmatrix} + \begin{bmatrix} 0 \\ \frac{1}{M} \\ 0 \\ -\frac{m}{MI} \end{bmatrix} u \quad (18)$$

4.1. Controller Design Using Decoupled Sliding Surfaces:

The controller is designed such that motion along the sliding surfaces occurs independently as mention in Section 3. To bring the system back to stability at after a disturbance is difficult since only one control input is available. However, to guarantee this control task, two different sliding mode surfaces corresponding to the two desired system outputs and are used with one control signal u . Equations 11-17 can be used where and s are the sliding surfaces

In order to find the coefficients and for both and the methodology introduced in Section 3 is used, i.e., comparing Equations 16 and 17 to the system dynamics given by Equation 18 gives:

$$k_1 = \frac{1}{2} M \lambda_1^2 \quad (19)$$

$$k_2 = \frac{1}{2} MI \lambda_2^2 + \frac{1}{2} (M + m)g \quad (20)$$

Equations 19 and 20 show that choosing the values of the slopes and hence the corresponding control switching gains is difficult especially with the existence of cross coupling between the dynamics of the cart and that of the pendulum. The equations also show that for each of the two parts the value of one of the parameters λ_1 or k_1 has to be assumed. The ranges of the VSC variables are very wide as mentioned in Section 3. The system sensitivity to

parameters variations is introduced to find parameter limitations. The condition $\dot{s} = 0$ is necessary to keep the system state on the sliding surface. Combining the system sensitivity with $\dot{s}_1 = 0$ and $\dot{s}_2 = 0$ for both sliding surfaces result in the following cases:

Case I: Sliding surface of the cart:

Since $s_1 = \lambda_1 x + \dot{x}$, the rate of change of sliding surface equation \dot{s}_1 is given by:

$$\lambda_1 \dot{x} + \ddot{x} = 0 \quad (21)$$

Substituting for u and x from Equations 13 and 18 into Equation 21 respectively results in the following:

$$\lambda_1 \dot{x} + \frac{1}{M} k_1 x + \left(\frac{1}{M} k_2 - \frac{mg}{M} \right) \theta = 0 \quad (22)$$

The change in the angular position θ of the inverted pendulum system, and hence its stability, to changes in the cart velocity \dot{x} is obtained from the partial derivative of θ with respect to x as follows:

$$\frac{\partial \theta}{\partial \dot{x}} = -\frac{M \lambda_1}{k_2 - mg} \quad (23)$$

For the pendulum position θ to be rendered insensitive to the cart velocity \dot{x} , the magnitude of the denominator of Equation 23 must be much larger than that of the numerator. This implies $\lambda_1 \ll (k_2 - mg)/M$.

Substituting for λ_1 and then for k_2 from Equations 19 and 20 respectively into Equation 23 gives the following two

$$k_1 \ll \frac{(k_2 - mg)^2}{2M} \quad (24)$$

$$\lambda_1 \ll \frac{1}{2} l \lambda_2^2 + \frac{1}{2M} (M - m)g \quad (25)$$

Case II: Sliding surface of the cart:

Since $s_2 = \lambda_2 \theta + \dot{\theta}$ and the rate of change of sliding surface equation \dot{s}_2 is given by:

$$\lambda_2 \dot{\theta} + \ddot{\theta} = 0 \quad (26)$$

Substituting Equations 13 and 18 into Equation 26 for u and $\ddot{\theta}$ gives:

$$\lambda_2 \dot{\theta} + \left[\frac{(M + m)g}{MI} - \frac{k_2}{MI} \right] \theta - \frac{k_1}{MI} x = 0 \quad (27)$$

It can be seen that Equation 27 provides no significant information. Also, it is not possible to carry out the sensitivity analysis since the equation does not include the cart velocity.

4.1.1. Simulation Results and Comparisons:

In this section, a proportional controller and a VSC based on the new design methodology are applied to the inverted pendulum system for comparison. Table 1 shows the values of the system parameters used.

Table 1: Inverted pendulum numerical values.

m	0.1 kg
M	2 kg
I	0.5 m
g	9.81 m/sec ²

Substituting the parameters of Table 1 into Equations 19 and 20 gives:

$$k_1 = \lambda_1^2 \tag{28}$$

$$k_2 = \frac{1}{2}\lambda_2^2 + 10.3 \tag{29}$$

With reference to Figure 5, in order to find the optimal limits of Equations 28 and 29, the pendulum is disturbed by applying an initial input angle. The pendulum at this inclination has a maximum potential energy Q that must be compensated for by the kinetic energy H in order to keep the system at that inclination stable, hence;

$$Q = H \tag{30}$$

$$mgl = \frac{1}{2}(M + m)\dot{x}^2$$

For a maximum initial disturbance angle $\theta = -0.1 \text{ rad}$ (5.73°) and the parameters of Table 1, Equation 30 results in $\dot{x} = 0.683 \text{ m/sec}$; consequently, $\dot{\theta} = 1.366 \text{ rad/sec}$ and the slope of the sliding surface becomes:

$$\lambda_2 = \frac{\dot{\theta}}{\dot{x}} = \frac{1.336}{0.1} = 13.66 \text{ sec}^{-1} \tag{31}$$

Equations 28 and 29 are used with the constraints found from the sensitivity analysis to design the VSC. The slope of the cart sliding surface λ_1 must satisfy the condition of Equation 25. For $\lambda_2 = 13.66 \text{ sec}^{-1}$, $\lambda_1 \ll 51.3 \text{ sec}^{-1}$, λ_1 is selected to be 0.7 and result in the corresponding controller gains $k_1 = \pm 0.49$ and $k_2 = \pm 103.6$. These values do satisfy the constraint set forth by Equation 24. The responses of the pendulum and cart with respect to time for this design case are shown in Figures 6 and 8 respectively. The corresponding phase portraits are shown in Figures 7 and 9 respectively.

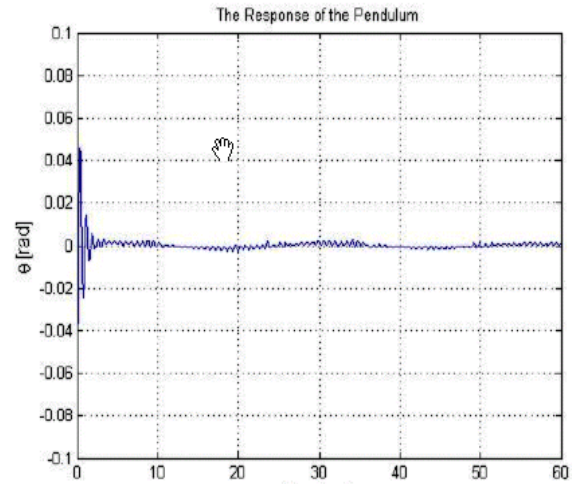


Figure 6: Pendulum response for VSC.

The system state crosses the sliding surface at relatively high speed such that it leaves the sliding surface as shown in Figure 7. Since the structure of the controller is unable to brake the system, the system circles around the origin and intercepts the sliding surface in the lower right quadrant. In Figure 6, this is manifested by the oscillations of the pendulum around the set point. With reference to the cart, when the pendulum is disturbed by the initial input angle, the cart tries to compensate by moving in the same direction of the input angle as shown in Figure 9.

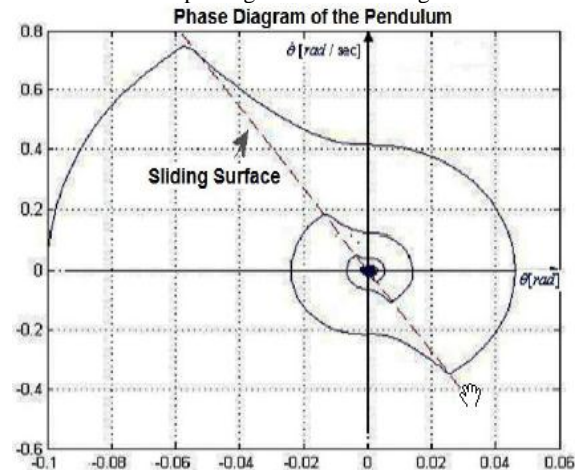


Figure 7: Pendulum phase portrait for the VSC.

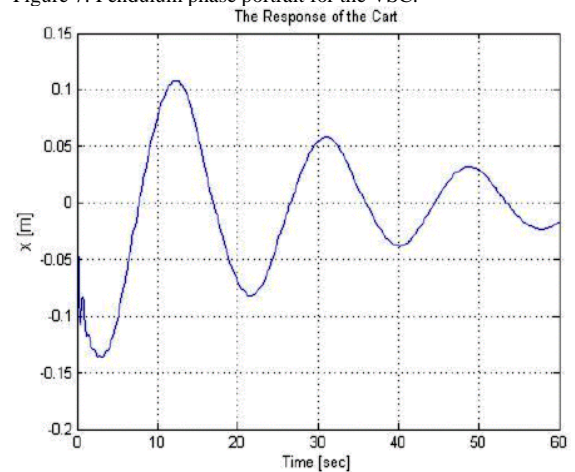


Figure 8: Cart response for the VSC.

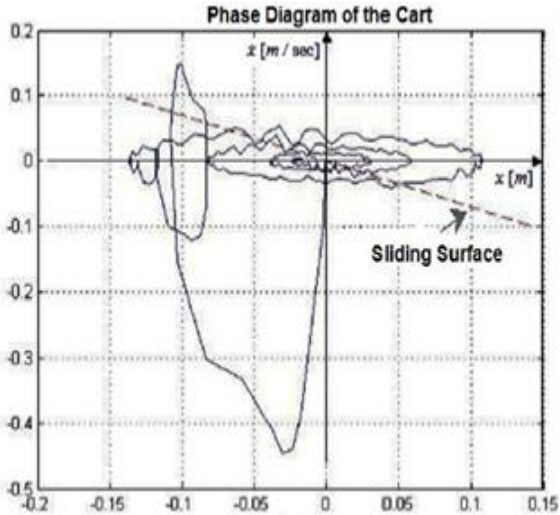


Figure 9: Cart phase portrait for the VSC.

While returning back to its original position, the cart oscillates around the origin in response to the oscillatory behavior of the pendulum in order to keep it stable upright as shown in Figure 8. This is manifested on the phase diagram whereby its response leaves the sliding surface of the cart while stabilizing the pendulum and returning back to the original position represented by the origin of the plot.

Reducing the slopes of the cart and the pendulum sliding surfaces to respectively results in the responses and the phase portraits shown in the Figures 10-13. In this case, the response of the pendulum is marginally underdamped, and the pendulum will keep oscillating with a small magnitude around the equilibrium point. The response of the cart in this case is overdamped. Reducing the slopes implies reducing the kinetic energy when the system state intercept the sliding surfaces for the pendulum and the cart. The system state do not leave the sliding surface as shown in Figures 11 and 13.

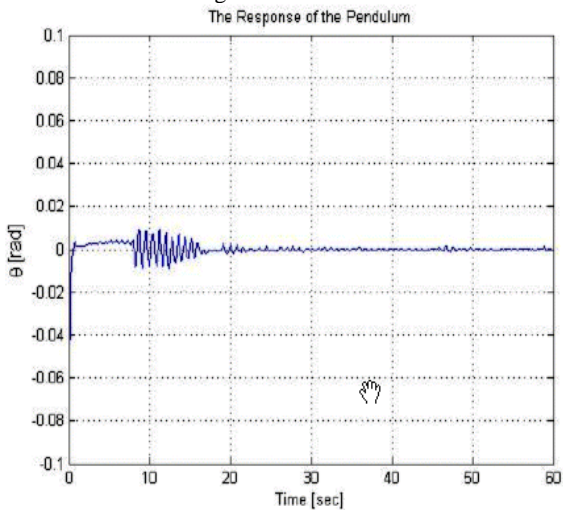


Figure 10: Pendulum response for the VSC.

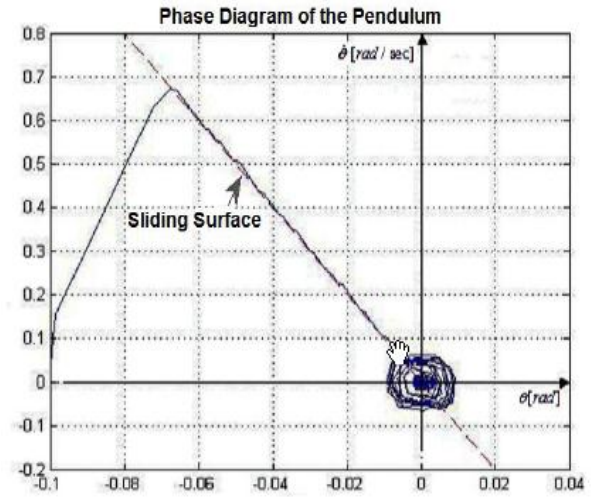


Figure 11: Pendulum phase portrait.

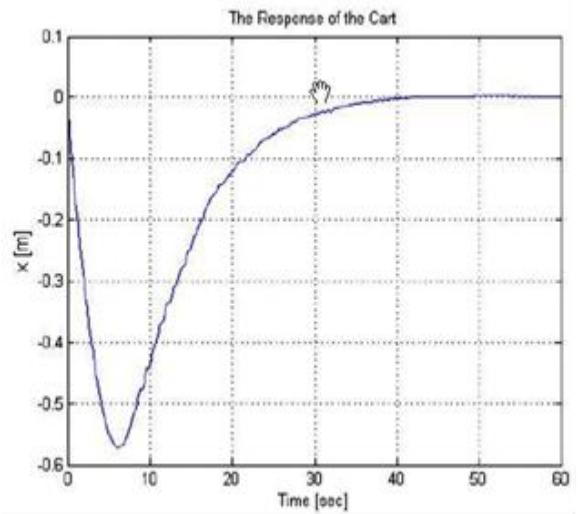


Figure 12: Cart response for the VSC.

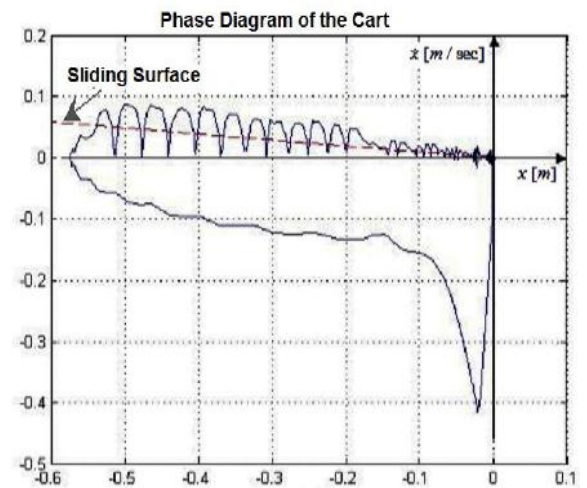


Figure 13: Cart portrait for the VSC.

Since the system is a single-input-two-output, a possible proportional control law can be constructed as follows:

$$u = k_1x + k_2\theta \tag{32}$$

where k_1 and k_2 are the controller gains.

If the proportional controller gains are selected to be where $k_1 = 0.49$ and $k_2 = 103.6$ are the responses of the pendulum and the cart for the same step input used earlier are shown in Figures 14 and 16 respectively. The corresponding phase portraits are shown in Figures 15 and 17 respectively. The figures show critically stable undamped responses. The performance of the VSC and the proportional controller based on the simulation results clearly show how the energy is absorbed by VSC as it asymptotically brings the system to stability, while it is not the case when the proportional controller is used.

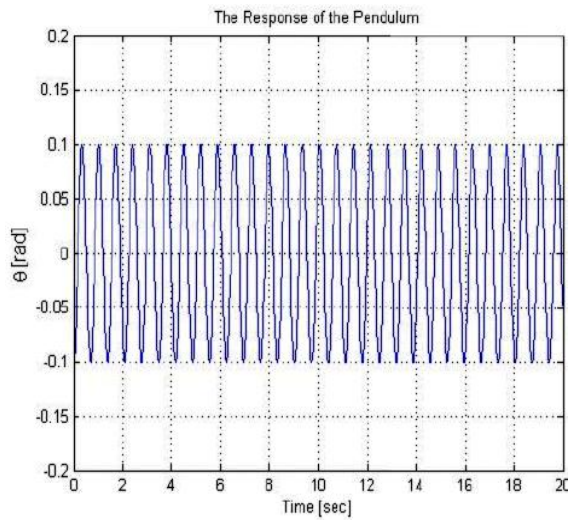


Figure 14: Pendulum response for the P-controller.

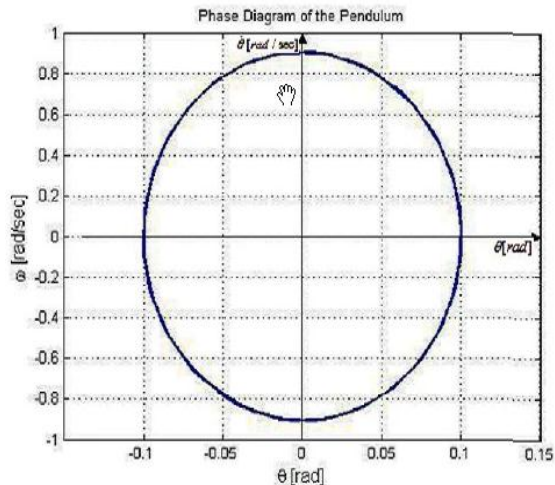


Figure 15: Pendulum phase portrait for the P-controller.

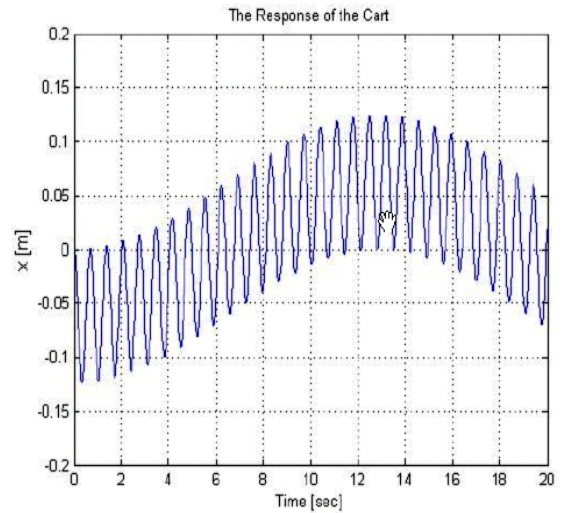


Figure 16: Cart response for the P-controller.

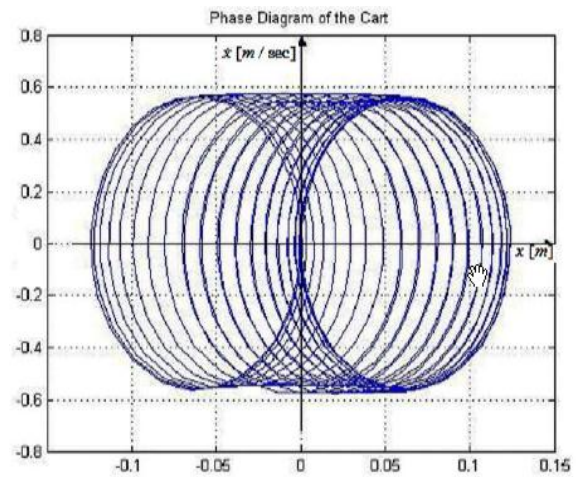


Figure 17: Cart phase portrait for the P-controller.

4.2. Controller Design Using Hyper Sliding Surface:

The sliding mode controller in this section is designed such that the sliding surfaces of the pendulum and the cart are coupled together to form a hyper sliding surface. The hyper sliding surface has the following form:

$$s = s_1 + s_2 \tag{33}$$

where s_1 and s_2 are the sliding surfaces of the pendulum and the cart respectively. Substituting Equations 11 and 12 for s_1 and s_2 in to Equation 33 gives:

$$s = \lambda_1x + \dot{x} + \lambda_2\theta + \dot{\theta} \tag{34}$$

The input force applied to the cart u is a relay type signal and is given by:

$$u = \begin{cases} +v, & s > 0 \\ -v, & s < 0 \end{cases} \tag{35}$$

where the values of $+v$ and $-v$ are chosen based on the system capability.

4.2.1. Simulation Results and Comparisons:

If a DC motor is used to provide the desired input force u to the cart, the selection of the values and is based on the motor torque limits. The rated torque of the motor can be chosen to be 0.28 N.m. [16] and a gear ratio of 1:16. If the cart wheel connected to the motor has a radius of 5cm, the controller force will have switching gains ± 90 . For the same sliding surfaces used in Section 3.1, , Figures 18 and 19 show the responses of the pendulum and cart respectively. The performance of this controller is much better than those of the previous controller. The pendulum response is faster than the one shown in Section 4.1 and is marginally underdamped (around the critical damping state). The cart response shows an underdamped response with a small overshoot; however, it is faster than the one of Section 4.1.

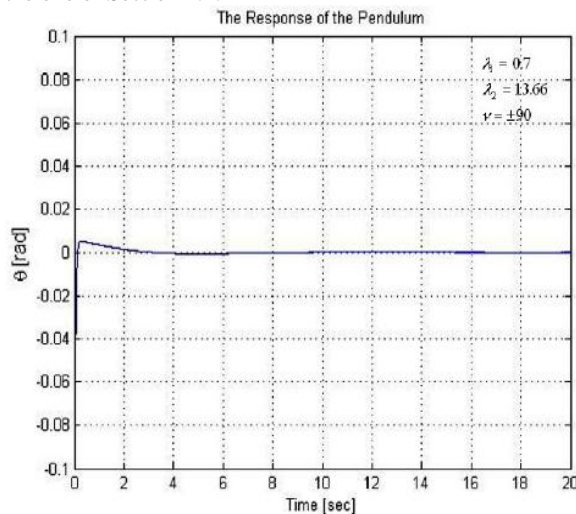


Figure 18: Pendulum response for the Hyper VSC.

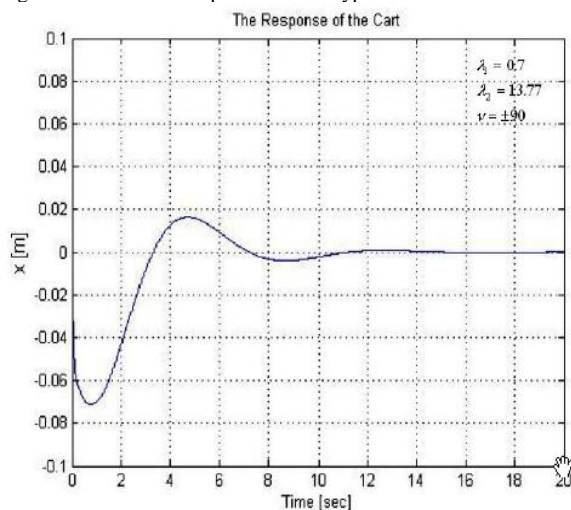


Figure 19: Cart response for the Hyper VSC.

4.3. Controller Design of Pure Inertial System:

The inverted pendulum system has no dissipative viscous load to absorb energy. This can be seen in the dynamic equations of the system. The controller design used in Section 3 also does not include any damping terms in the control law to compensate for the lack of damping. Hence, adding a damping terms in the control law is advisable. This can be accomplished by modifying the control law of Equation 13 as follows:

$$u = k_1 x + k_2 \theta + k_3 \dot{x} + k_4 \dot{\theta} \quad (36)$$

where k_1 and k_2 are the same controller gains given by Equations 14 and 15. k_3 and k_4 are the damping controller gains, and chosen to be always positive. In order to select suitable values for k_3 and k_4 the system sensitivity analysis is carried out as follows:

$$\left(\lambda_1 + \frac{k_3}{M} \right) \dot{x} + \frac{k_1}{M} x + \frac{k_3 - mg}{m} \theta + \frac{k_4}{M} \dot{\theta} = 0 \quad (37)$$

Taking the partial derivative of the pendulum angle with respect to the cart velocity in Equation 37 gives:

$$\frac{\partial \theta}{\partial \dot{x}} = \frac{M \lambda_1 + k_3}{k_2 - mg} \quad (38)$$

Case I: Sliding surface of the pendulum:

Substituting Equations 18 and 36 into Equation 26 for $\ddot{\theta}$ and u respectively gives:

$$-\frac{k_1}{Ml} x - \frac{k_3}{Ml} \dot{x} + \frac{(M+m)g - k_2}{Ml} \theta + \left(\lambda_2 - \frac{k_4}{M} \right) \dot{\theta} = 0 \quad (39)$$

Taking the partial derivative of the pendulum angle with respect to the cart velocity in Equation 39 gives:

$$\frac{\partial \theta}{\partial \dot{x}} = \frac{k_3}{k_2 - (M+m)g} \quad (40)$$

In order for the system to be rendered insensitive to the cart velocity, the magnitude of the denominators of Equations 38 and 40 must be much larger than that of the numerators, hence:

$$k_3 \ll k_2 - mg - M \lambda_1 \quad (41)$$

$$k_3 \ll k_2 - (M+m)g \quad (42)$$

If the partial derivative of the pendulum angular velocity is taken with respect to the cart velocity in Equations 37 and 39, the following can be achieved:

$$\frac{\partial \dot{\theta}}{\partial \dot{x}} = \frac{M \lambda_1 + k_3}{k_4} \quad (43)$$

$$\frac{\partial \dot{\theta}}{\partial \dot{x}} = \frac{k_3}{k_3 - \lambda_1 M l} \quad (44)$$

With reference to Figure 5, the following equation is also valid:

$$\frac{\partial \dot{\theta}}{\partial \dot{x}} = \frac{1}{l} \quad (45)$$

Equating Equation 43 and 44 to Equation 45 respectively gives

$$k_4 = -(lk_3 + Ml \lambda_1) \quad (46)$$

$$k_4 = lk_3 + MI\lambda_2 \tag{47}$$

Equation 46 can be ignored since k_4 is chosen to be always positive.

4.3.1. Simulation Results and Comparisons:

In order to use the control law of Equation 36, the controller gains $k_1, k_2, k_3,$ and k_4 must be selected based on the sensitivity analysis of the system. With reference to Section 4.1, the slope of the cart sliding surface must satisfy the condition of Equation 25. Substituting and into Equations 28 and 29 result in the corresponding controller gains $k_1 = \pm 4$ and $k_2 = \pm 103.6$ respectively. The damping controller gains k_3 and k_4 must satisfy the conditions of Equations 41, 42, and 47. Since $k_3 \ll 82.7,$ k_3 is selected to be 9. Substituting the parameters in Table 1 into Equation 47 with $k_3 = 9$ results in $k_4 = 18.16.$ Figures 20 and 21 show the responses of the pendulum and the cart respectively. The response of the cart is overdamped and the response of the pendulum is marginally underdamped.

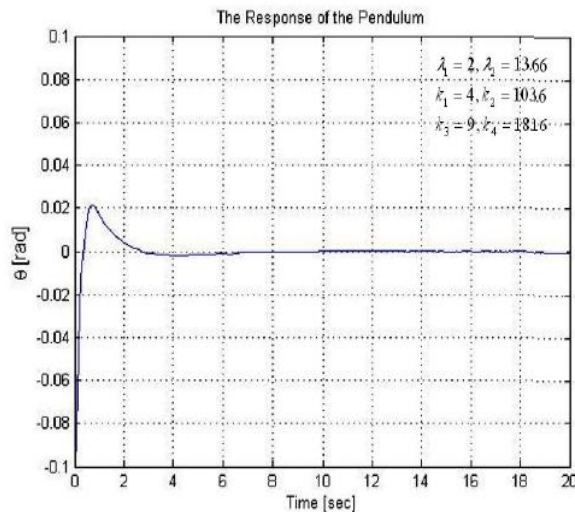


Figure 20: Pendulum response for the modified VSC of pure inertial systems.

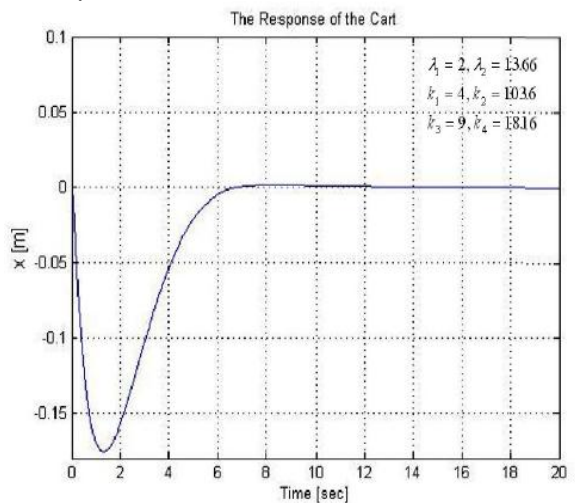


Figure 21: Cart response for modified VSC of pure inertial systems.

For comparison purposes, a Proportional-Derivative (PD) controller design that has the following form is used [16]:

$$u = 163.1x + 73.4\dot{x} + 298.15\theta + 60.7\dot{\theta} = 0 \tag{48}$$

The PD-controller gains of Equation 48 are chosen based on the pole placement tuning method where the closed loop pole locations are selected to meet a given desired performance specifications. The closed-loop pole locations are chosen to give a 2 sec settling time [16]. The responses of the pendulum and the cart when using this controllers are shown in Figures 22 and 23. The figures show that both responses are underdamped. The 2 sec settling time results in 0.5 damping ratio and 70% overshoot as shown in Figure 22.

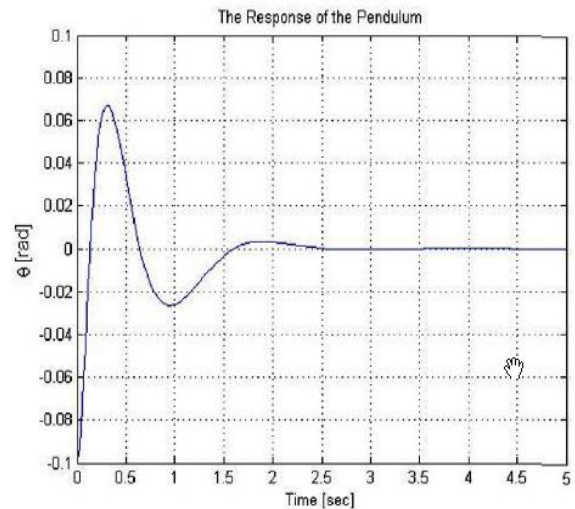


Figure 22: Pendulum response of PD-controller [16].

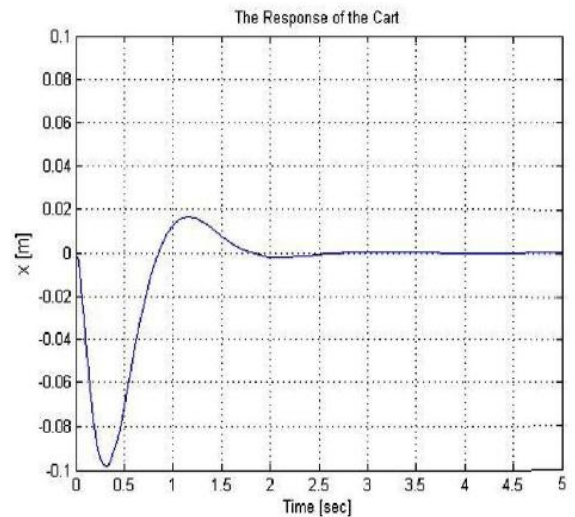


Figure 23: Cart response for the PD-controller [16].

A faster response of the pendulum alone ignoring completely the cart can be obtained if the choice of the PD-controller gains of the pendulum are selected based on Ziegler-Nichols method of tuning [16]. The control law in this case is given by:

$$u = 210\theta + 10.5\dot{\theta} \tag{49}$$

Figure 24 shows the response of the pendulum in this case. Figure 25 shows the cart response to continually

move away from the desired equilibrium state since there is no contribution of the cart state in the control law. If the control law (Equation 49) is modified to include the cart state, and the gains of these state are tuned using the MATLAB Control System Toolbox, the following control law is obtained:

$$u = 15x + 5\dot{x} + 210\theta + 10.5\dot{\theta} \quad (50)$$

Figure 24 also shows the pendulum response when using this modified PD-controller. The figure shows the response to be more oscillatory, however, with reference to Figure 25 the cart response is shown to be stable but slightly underdamped. When MATLAB Control System Toolbox is used to tune the PD-controller gains of both cart and pendulum together, the following control law results:

$$u = 80x + 100\dot{x} + 550\theta + 82\dot{\theta} \quad (51)$$

The response of the pendulum using the control law of Equation 51 is underdamped as shown in Figure 24. The cart response in this case however, is overdamped as shown in Figure 25.

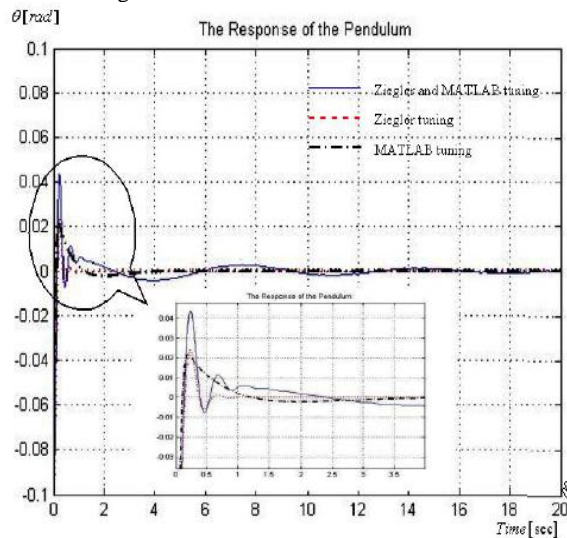


Figure 24: Pendulum response using different PD tuning.

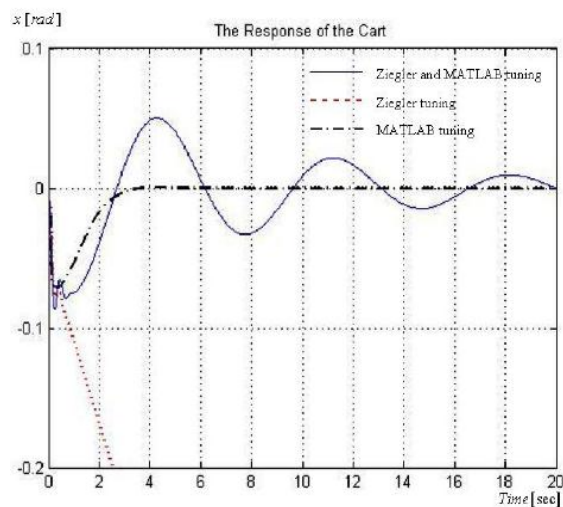


Figure 25: Cart responses using different tuning methods for PD-controllers.

Comparing the responses of the different controllers used so far shows that the PD-controller of Equation 48 has the fastest response for the cart; however, the response has an overshoot. The response of the system when using the VSC with the hyper sliding surface shows ideal performance for the pendulum where the response is almost at the critical damping state, and is faster than for all the other types of controllers. Comparing the responses of the cart and the pendulum for the original VSC of Equation 13 with that of the modified VSC of Equation 36 shows that the modified VSC has a better performance and a faster response. The response of the cart for the modified VSC also shows a faster response and a better performance than that of the VSC with a hyper sliding surface.

Among the four PD-controllers, that of Equation 49 results in the best performance of the pendulum, least overshoot and the fastest response. Comparing this performance to that of the VSC with the hyper sliding surface shows that the latter is still the best among all controllers. The cart response when using the controller of Equation 51 is faster than those resulting from using other controllers, and has no overshoot.

5. Conclusion

This paper presents the derivation and the proof of the relationship between a system's work and energy and a VSC to control it. The relationship between the slope of the linear sliding surface and the controller gains is then used to develop a simple systematic design methodology suitable for SISO systems. This new design methodology is then extended to SIMO systems. An inverted pendulum system is used to test this new design methodology. The results show that the proposed approach produces a controller with very good performance. In order to enhance further the performance, a hyper VSC was applied; where the sliding surfaces of the pendulum and cart are coupled together. Since the pendulum systems is a pure inertial system, the control law was improved upon by introducing artificial damping terms. The VSC schemes simulation results were compared to those of a proportional and a PD-controller. The comparison shows that the performance of the VSC with the hyper sliding surface is the best among all controllers.

References

- [1] Yu-Fing Li, "High Precision Motion Control Based on Discrete Time Sliding Mode Approach", Doctoral Thesis, Royal Institute of Technology, Stockholm, Sweden, 2001.
- [2] Jeen Lin, Ruey-Jing Lian, "Enhanced fuzzy sliding mode controller for active suspension systems", IEEE Transactions on Automatic Control, Volume 19, Issue 7, Pages 1178-1190, 2009.
- [3] J. Slotine, W. Li, "Applied Nonlinear Control", Prentice Hall Englewood Cliffs, New Jersey, 1992.
- [4] Qinglei Hu, "Variable structure maneuvering control with time-varying sliding surface and active vibration damping of flexible spacecraft with input saturation", Acta Astronautica, Volume 64, Issues 11-12, June-July 2009.
- [5] M.Ö. Efe, "MIMO variable structure controller design for a bioreactor benchmark process", ISA Transactions, Volume 46, Issue 4, Pages 459-469, 2007.
- [6] J. Ackermann, V. Utkin, "Sliding Mode Control Design Based on Ackermann's Formula", IEEE Transactions on Automatic Control, Vol. 43, Issue 2, pp. 234-237, Feb. 1998.
- [7] K. Young, V. Utkin, U. Ozguner, "Sliding mode control for a class of non-affine nonlinear systems", Nonlinear Analysis: Theory, Methods & Applications, Volume 71, Issue 12, Pages e1589-e1597, 15 December 2009.
- [8] Tai-Zu Wu, Jinn-Der Wang, Yau-Tarng Juang, "Decoupled integral variable structure control for MIMO systems", Journal of the Franklin Institute, Volume 344, Issue 7, Pages 1006-1020, October 2007.
- [9] İlyas Eker, "Sliding mode control with PID sliding surface and experimental application to an electromechanical plant", ISA Transactions, Volume 45, Issue 1, Pages 109-118, January 2006.
- [10] J. Wang, A. B. Rad, P. T. Chan, "Indirect Adaptive Fuzzy Sliding Mode Control: Part I: Fuzzy Switching", Journal of Fuzzy Sets and Systems, Vol. 122, Issue 1, pp.21-30, 2001.
- [11] H.F. Ho, Y.K. Wong, A.B. Rad "Adaptive fuzzy sliding mode control with chattering elimination for nonlinear SISO systems", Simulation Modelling Practice and Theory, Volume 17, Issue 7, Pages 1199-1210, August 2009.
- [12] S.M. Gadoue, D. Giaouris, J.W. Finch, "Artificial intelligence-based speed control of DTC induction motor drives—A comparative study", Electric Power Systems Research, Volume 79, Issue 1, Pages 210-219, January 2009.
- [13] J. Javadi Moghaddam, M.H. Farahani, N. Amanifard, "A neural network-based sliding-mode control for rotating stall and surge in axial compressors", Applied Soft Computing, In Press, Corrected Proof, Available online 11 February 2010.
- [14] R. C. Dorf, Robert H. Bishop, "Modern Control Systems", 11th Edition, Prentice Hall, New Jersey 2008.
- [15] E. Doskocz, Y. Shtessel, "MIMO Sliding Mode Control of a Robotic 'Pick and Place' System Modeled as an Inverted Pendulum on a moving Car", IEEE Proceedings of the Southeastern Symposium of System theory, 1998.
- [16] K. Ogata, "Modern Control Engineering", 5th Edition, Prince Hall, New Jersey, 2010.

MHD Heat and Mass Transfer Free Convection Flow near The Lower Stagnation Point of an Isothermal Cylinder Imbedded in Porous Domain with the Presence of Radiation

Ziya Uddin^{*a}, Manoj Kumari^b

^aDepartment of Applied Sciences and Humanities ITM University, Gurgaon, India

^bDepartment of Mathematics, Statistics and Computer Science G. B. Pant University of Agriculture and Technology, Pantnagar – 263 145, Uttarkhand, India

Abstract

Heat and mass transfer characteristics and the flow behavior on MHD flow near the lower stagnation point of a porous isothermal horizontal circular cylinder have been studied. The equations of conservation of mass, momentum, energy and concentration which govern the case study of heat and mass transfer flow have been obtained. These equations have been transformed into a system of non-dimensional coupled non-linear ordinary differential equations by using similarity transformations and finally solved by Runge-Kutta and shooting method. It has been assumed that the fluid is incompressible, absorbing-emitting radiation and viscous, with temperature dependent viscosity and temperature dependent thermal conductivity in the presence of radiation. Velocity profiles, temperature distributions and concentration distributions for the flow have been presented for various values of radiation parameter, viscosity variation parameter, thermal conductivity variation parameter, Prandtl number and Schmidt number. The skin friction factor, local Nusselt number and Sherwood number are also calculated for all the parameters involved in the problem. It has been observed that with the increase in Schmidt number skin friction and Nusselt number decrease, while Sherwood number increases.

© 2011 Jordan Journal of Mechanical and Industrial Engineering. All rights reserved

Keywords: MHD heat mass transfer; free convection; isothermal circular cylinder; radiation effect; variable thermal conductivity and viscosity; Runge-Kutta shooting technique

Nomenclature

a	Curvature
b	Inertial drag coefficient
B_0	Magnetic intensity
C	Concentration
C_f	Skin friction
C_p	Specific heat at constant pressure
D	Mass diffusivity
f	Non-dimensional reduced stream function
Gm	Modified Grashoff number
Gr	Grashoff number
K	Porosity parameter
k	Thermal conductivity
k'	Permeability of porous media
M	Magnetic parameter
N	radiation parameter
Nf	Forchheimer inertial porous parameter
Nu	Nusselt number
O	Stagnation point
Pr	Prandtl number
q_r	Radiative heat flux
q_w	Rate of heat transfer
Sc	Schmidt number
Sh	Sherwood number
So	Soret number
s_w	Rate of mass transfer

T	Temperature
u, v	Velocity components along X, Y directions
X, Y	distances along and perpendicular to the surface

Greek symbols

μ	Viscosity of the fluid
k_1	Mean absorption coefficient
β	Coefficient of thermal expansion
ε	Variable viscosity parameter
η	Dimensionless distance
θ	Non-dimensional temperature
ν	kinematic viscosity of the fluid
ρ	Density of the fluid
σ	Electrical conductivity
σ_1	Stefan Boltzmann constant
Φ	Non-dimensional concentration
ψ	Stream function
ω	Variable thermal conductivity parameter

Subscripts

w	wall of cylinder
∞	Distance far away from the surface

Superscript

'	Differentiation with respect to η
---	--

*Corresponding Author. email: ziya_dd@rediffmail.com

1. Introduction

The study of flow problems which involve the interaction of several phenomena, has a wide range of applications in the field of Science and Technology. One such study is related to the effect of free convection MHD flow, which plays an important role in Agriculture, Engineering and Petroleum industries. The problem of free convection under the influence of magnetic field has attracted many researchers in view of its application in Geophysics, Astrophysics, geological formations, thermal recovery of oil, and in assessment of aquifers, geothermal reservoirs and underground nuclear waste storage site, etc. The heat transfer in porous media has great practical importance in geophysics and energy related engineering problems. These include the utilization of geothermal energy, the control of pollutants in ground water, solar power collectors, high performance insulations of buildings, food processing, casting and welding of a manufacturing process, etc.

The effect of temperature dependent viscosity on natural convection of fluid from heated vertical wavy surface was studied by [1]. In case of vertical cone, this effect was studied by [2]. Nazar et al. [3] studied the free convection boundary layer on an isothermal horizontal circular cylinder in a micropolar fluid. In case of horizontal cylinder the radiation-conduction interaction on mixed convection was investigated by [4]. Kafoussius et al. [5] studied the combined free and forced convection laminar boundary layer past a vertical isothermal flat plate with temperature dependent viscosity. In porous media the effect of viscosity variation was considered by [6] and [7]. Free convection boundary layer on cylinders of elliptic cross section was studied by [8]. Harris et al. [9] studied the transient free convection near the lower stagnation point of a cylindrical surface subjected to a sudden change in surface temperature. Effect of aligned magnetic field on steady viscous flow past a circular cylinder was studied by [10]. Free convection and mixed convection about a circular cylinder was studied by the authors [11] and [12] respectively. The effect of variable viscosity on the fluid flow past a horizontal cylinder was also investigated by [13]. The combined heat and mass transfer along a vertical moving cylinder was studied by [14]. In this analysis both uniform wall temperature and uniform heat flux cases have been included. Bhargava et al. [15] found the finite element solution for non-newtonian pulsatile flow in a non-darcian porous medium conduit, they used the Darcy-Forchheimer model to formulate the problem. Transient analysis of heat and mass transfer by natural convection in power law fluid past a vertical plate immersed in a porous medium is studied by [16]. Rashad [17] studied the effect of thermal radiation on the steady laminar flow past a vertical plate immersed in a porous medium. He used the Rosseland approximation to incorporate the effect of radiation, in the mathematical model of the problem.

It is observed that MHD heat and mass transfer free convection flow near the lower stagnation point of an isothermal horizontal circular cylinder in presence of radiation and temperature dependent fluid properties has given a very scant attention in the literature. Hence in the present study the effect of radiation with temperature dependent thermal conductivity and temperature dependent viscosity on MHD heat and mass transfer free convection flow near the lower stagnation point of a porous, isothermal horizontal circular cylinder has been considered.

2. Formulation

Consider a two dimensional MHD free convection flow of a viscous, incompressible, electrically conducting fluid absorbing-emitting radiation, over a uniformly heated circular cylinder of radius "r". It is assumed that the surface temperature of the porous cylinder is T_w and T_∞ is the ambient temperature of the fluid. A uniform radial magnetic field of strength B_0 is applied perpendicular to the surface of the cylinder. A locally orthogonal coordinate system is chosen with origin O, at lower stagnation point and X and Y denoting the distances measured along and perpendicular to the surface respectively. If "a" is the curvature of the body surface, then by the choice of axes, "a" is the principal curvature at O. The physical model and coordinate system is shown in the fig. 1.

We assume that (i) the fluid has constant kinematic viscosity and the Boussinesq approximation may be adopted for the steady laminar boundary layer flow, (ii) the magnetic Reynolds number is assumed to be small so that the induced magnetic field is negligible in comparison to the applied magnetic field, (iii) the cylinder is considered to be non-electrically conducting and the hall effect has been neglected, (iv) the joule heating effect has been neglected, and (v) the fluid is considered to be gray absorbing-emitting radiations but non scattering medium and the Rosseland approximation is used to describe the radiative heat flux in the x-direction is considered negligible in comparison to y-direction. This approximation is valid at points far from the boundary surface, and is good for intensive absorption, that is, for an optically thick boundary layer. The Darcy-Forchheimer model is used to describe the flow in porous media. Under the usual Boussinesq approximation, the equations that govern the flow are:

Equation of Continuity:

$$\frac{\partial u}{\partial x} + \frac{\partial v}{\partial y} = 0 \quad (1)$$

Equation of Momentum:

$$u \frac{\partial u}{\partial x} + v \frac{\partial u}{\partial y} = g\beta(T - T_\infty)ax + g\beta_c(C - C_\infty)ax + \frac{1}{\rho} \frac{\partial}{\partial y} \left(\mu(T) \frac{\partial u}{\partial y} \right) - \frac{\sigma B_0^2 u}{\rho} - \frac{\mu u}{\rho k'} - bu^2 \quad (2)$$

Equation of Energy:

$$\rho C_p \left(u \frac{\partial T}{\partial x} + v \frac{\partial T}{\partial y} \right) = \frac{\partial}{\partial y} \left(k(T) \frac{\partial T}{\partial y} \right) - \left(\frac{\partial q_r}{\partial y} \right) \quad (3)$$

Equation of Diffusion:

$$\left(u \frac{\partial C}{\partial x} + v \frac{\partial C}{\partial y} \right) = D \frac{\partial^2 C}{\partial y^2} \quad (4)$$

where u and v denote the fluid velocity components in the x and y directions respectively, T is the fluid temperature, C is fluid concentration, g is the magnitude of acceleration due to gravity, β is the coefficient of thermal expansion, ρ is the density of the fluid, σ is the fluid electrical conductivity, B_0 is the strength of applied magnetic field, k' is the permeability of porous medium, b is the Forchheimer geometrical (inertial drag) coefficient, C_p is specific heat at constant pressure, $\mu(T)$ is the

temperature dependent viscosity of the fluid, $k(T)$ is the temperature dependent thermal conductivity and D is mass diffusivity. The term $g\beta(T-T_\infty)ax$ in the momentum equation arises from the component of buoyancy force in the x direction in the vicinity of O and the last term qr in the energy equation represent the radiative heat flux in y direction.

The radiative heat flux qr under Rosseland approximation by Brewster [18] has the form:

$$q_r = -\frac{4\sigma_1}{3k_1} \frac{\partial T^4}{\partial y} \tag{5}$$

where σ_1 is Stefan-Boltzmann constant and k_1 is the mean absorption coefficient.

We assume that the temperature differences within the flow are so small that T^4 can be expressed as a linear function of T_∞ . This is obtained by expanding T^4 in a Taylor series about T_∞ and neglecting the higher order terms. Thus we get:

$$T^4 \cong 4T_\infty^3 T - 3T_\infty^4 \tag{6}$$

The initial and boundary conditions are:

$$u=0, v=0, T=T_w, C=C_w \text{ at } y=0 \tag{7a}$$

$$u \rightarrow 0, T \rightarrow T_\infty, C \rightarrow C_\infty, \text{ as } y \rightarrow \infty \tag{7b}$$

It is assumed that the viscosity $\mu(T)$ and thermal conductivity $k(T)$ varies with temperature as follows:

$$\mu(T) = \frac{\mu_\infty}{1+\gamma(T-T_\infty)} \tag{8}$$

$$k(T) = k_\infty(1 + b(T - T_\infty)) \tag{9}$$

The system of partial differential equations (1)-(4) and initial and boundary conditions (7) after introducing equations (5-6) and (8-9) can be reduced to a system of semi-similar equations by employing the following transformations:

$$\psi = Gr^{1/2}avxf(\eta), \quad \eta = Gr^{1/2}ay, \quad \theta(\eta) = \frac{T-T_w}{T_w-T_\infty} \tag{10a}$$

$$\phi(\eta) = \frac{C-C_w}{C_w-C_\infty}, \quad Gr = \frac{g\beta(T_w-T_\infty)}{a^3\nu^2}, \quad Gm = \frac{g\beta_c(C_w-C_\infty)}{a^3\nu^2} \tag{10b}$$

where ψ is the stream function, f is non-dimensional reduced stream function, θ is non-dimensional reduced temperature, C is non-dimensional reduced concentration, Gr is Grashoff number and Gm is modified Grashoff number.

Thus, the reduced equations in non-dimensional are:

$$f''' = (1 + \epsilon\theta) \left[(1 - Nf)f'^2 - ff'' + \frac{\epsilon}{(1+\epsilon\theta)^2} \theta' f'' \right] + \frac{1}{\sqrt{Gr}} \left\{ M + \left(\frac{1}{(1+\epsilon\theta)K} \right) \right\} f' - \theta - \frac{Gm}{Gr} \phi \tag{11}$$

$$\theta'' = -\frac{3N}{4+3N(1+\omega\theta)} [Pr \cdot f \cdot \theta' + \omega\theta'^2] \tag{12}$$

$$\phi'' = -Sc \cdot f \cdot \phi' \tag{13}$$

Here, $\epsilon = \gamma(T_w - T_\infty)$ is variable viscosity parameter, $\omega = b(T_w - T_\infty)$ is variable thermal conductivity parameter, $N = \frac{k_1 k_\infty}{4\sigma_1 T_\infty^3}$ is radiation parameter, $M = \frac{\sigma B_0^2 a^2}{\mu_\infty}$ is magnetic parameter, $K = k'a^2$ is porosity parameter, $Nf = bx$ is Forchhiemer inertial porous parameter, $Pr = \frac{k_\infty}{\mu_\infty C_p}$ is Prandtl number, $Sc = \frac{\nu}{D}$ is Schmidt number and prime (') denote the differentiation with respect to η .

The corresponding initial and boundary conditions are:

$$f(0) = 0, f'(0) = 0, \theta(0) = 1, \phi(0) = 1 \tag{14a}$$

$$f'(\infty) \rightarrow 0, \theta'(\infty) \rightarrow 0, \phi'(\infty) \rightarrow 0 \tag{14b}$$

In the absence of magnetic field, radiation and porosity and at $Gm=0$, eq. (11) and eq.(12) reduce to the equations given by Md. Mamun Molla et al. [13] as follows:

$$f''' = (1 + \epsilon\theta) \left[f'^2 - ff'' + \frac{\epsilon}{(1+\epsilon\theta)^2} \theta' f'' - \theta \right] \tag{15a}$$

$$\theta'' = -Pr \cdot f \cdot \theta' \tag{15b}$$

Keeping in view of engineering aspects, the most important characteristics of the flow are local surface heat flux (Nusselt number), local surface mass flux (Sherwood number) and skin-friction, which can be written as

$$Nu = \frac{Gr^{-1/4}}{ak_\infty(T_w-T_\infty)} q_w, \quad Mu = \frac{Gr^{-1/4}}{aD(C_w-C_\infty)} S_w, \quad C_f = \frac{Gr^{-3/4}}{a^3\nu^2} \tau_w \tag{15}$$

Where

$$q_w = -\left(k \frac{\partial T}{\partial y}\right)_{y=0} \text{ is rate of heat transfer,}$$

$$S_w = -\left(D \frac{\partial C}{\partial y}\right)_{y=0} \text{ is rate of mass transfer and,}$$

$$\tau_w = \left(\mu \frac{\partial u}{\partial y}\right)_{y=0} \text{ is local wall shear stress.}$$

Using the variables equations (8)-(10) and initial and boundary conditions (14a, 14b), we get the following expressions for the Nusselt number, Sherwood number and skin-friction:

$$Nu = -(1 + \omega)\theta'(0), \quad Sh = -\Phi'(0), \quad C_f = \frac{1}{(1+\epsilon)} f''(0) \tag{16}$$

3. Results and Discussion

The equations (11-13) with initial and boundary conditions (14) have been solved using Runge-Kutta and Shooting method. Taking $\Delta\eta=0.05$ shooting technique has been applied for getting missing boundary conditions. The value of dependent variable is calculated at the terminal point by adopting fourth-order Runge-Kutta method within an admissible tolerance viz., of order 10^{-6} .

In the absence of magnetic field, porosity and radiation and at $Gm=0$, $\epsilon=0$ and $Nf=0$ the value of $-\theta'(0)$ is 0.4212, the value of $-\theta'(0)$ found by Merkin [10] was 0.4214, by Nazar [14] it was found to be 0.4214 and by Md. Mamun Molla [10] it has been calculated to 0.4241. This shows

that our results are in good agreement with these three solutions.

For several values of the dimensionless parameters, values of dimensionless velocity $f'(\eta)$ and dimensionless temperature $\theta(\eta)$ have been computed and are presented in figures (2)-(7). Figures (2) and (3) show the effects of variable viscosity parameter and radiation parameter on velocity and temperature respectively. It is seen from the figure (2) that the velocity increases with the increase in viscosity parameter, but after a certain distance from the surface of cylinder it decreases. It is also noticed that temperature decreases uniformly with an increase in viscosity parameter. Figure (3) depicts the effect of radiation parameter and results that velocity and temperature both decrease with the increase in radiation parameter. The effects of thermal conductivity parameter and Schmidt number on velocity as well as temperature are shown in figures (4) and (5). It is noticed that velocity and temperature both increase with the increase in thermal conductivity parameter. This is because as thermal conductivity parameter ω increases, the thermal conductivity of the fluid increases. This increase in the fluid thermal conductivity increases the fluid temperature and accordingly its velocity. Moreover, it is obvious that neglecting the variation of fluid thermal conductivity for high temperature differences introduces a substantial error. This error has been shown by plotting the dimensionless velocity and temperature for $\omega=0$. On increasing the Schmidt number the velocity decreases but temperature increases. The effects of Prandtl number on dimensionless velocity and temperature have been shown in figure (6). It is clear that thermal boundary layer thickness decreases sharply with the increase in Prandtl number. Also the momentum boundary layer thickness decreases with the increase in Prandtl number from $Pr=0.71$ to $Pr=7.0$, but for $Pr=70.0$ the velocity is smaller than in the case of $Pr=7.0$ in the neighborhood of the cylinder and afterwards it increases. Figure (7) shows the velocity distribution for various values of Nf i.e. Forchheimer parameter. A rise in Nf increases the velocity near the surface of the cylinder, but if we move longitudinally far away from the cylinder a rise in Nf depresses the velocity slightly and there is a slight depression in temperature for an increase in the Nf value for all the distances.

The effects of various dimensionless parameters on dimensionless concentration $\Phi(\eta)$ are shown in figures (8)-(10). From all these figures it is clear that the concentration decreases sharply as we move away from the surface. The effects of Prandtl number and thermal conductivity parameter are shown in figure (8), which depicts that the concentration boundary layer thickness increases with the increase in Prandtl number and there is a slight decrease in the concentration with the increase in thermal conductivity parameter. The variation of concentration with the change in the values of Schmidt number and viscosity parameter has been shown in figure (9). It is seen that with the increase in Schmidt number concentration boundary layer thickness decreases. Also it depicts that the dimensionless concentration decreases with an increase in viscosity parameter. Figure (10) shows the effect of radiation parameter and Forchheimer parameter on concentration distribution and results that concentration increases with the increase in radiation parameter, and there is a slight depression with with the increase in Nf , but this depression is negligible.

The numerical values of $f'(0)$, $-\theta'(0)$ and $-\Phi'(0)$ have been presented in tabular form in table 1 for different

values of various dimensionless parameters ϵ , M , K , ω , N , Sc , Nf and Pr at $Gr=Gm=1.0$. It is observed that dimensionless wall velocity gradient $f'(0)$ increases as ϵ , K , Nf and ω increase, while it decreases with the increase in M , N , Sc and Pr . Moreover, the value of $-\theta'(0)$ decreases with the increase in M , Sc and ω , while it increases with the increase in K , ϵ , N , Nf and Pr . Also it is seen that the value of $-\Phi'(0)$ increases with the increase in ϵ , ω , K , Nf and Sc and it decreases with the increase in N , M and Pr .

4. Conclusion

In this work we used darcy Forchheimer model to formulate the problem. The effect of Radiation, Porosity, Variable thermal conductivity, Variable Viscosity, Magnetic field and Prandtl number has been included in this analysis. The governing nonlinear equations have been solved by using Runge-Kutta and Shooting method. It was found that:

- Skin friction factor increases with the increasing porosity and thermal conductivity, while this is reduced with the increase in applied magnetic field, viscosity and radiation.
- Rate of heat transfer (Nusselt number) increases with the increase in the porosity, radiation and Prandtl number, while it decreases with the increase in Magnetic field, viscosity and thermal conductivity.
- Rate of mass transfer (Sherwood number) increases with the increase in thermal conductivity and porosity, while it decreases with the increase in viscosity, applied magnetic field and radiation.

Acknowledgment

We would like to thank to the reviewers for their encouraging comments and constructive suggestions to improve the manuscript.

References

- [1] M. A. Hossain, S. Kabir and D. A. S. Rees, "Natural convection of fluid with temperature dependent viscosity from heated vertical wavy surface". ZAMP, Vol. 53, 2002, 48-52.
- [2] M. A. Hossain, M. S. Munir and I. Pop, "Natural convection flow of viscous fluid with viscosity inversely proportional to linear function of temperature from a vertical cone". Int J Thermal Sci, Vol. 40, 2001, 366-371.
- [3] R. Nazar, N. Amin and I. Pop, "Free convection boundary layer on an isothermal horizontal circular cylinder in a micro-polar fluid". 12th international conference Heat Transfer. In., 2002.
- [4] M. A. Hossain, M. Kutubuddin and I. Pop, "Radiation-conduction interaction on mixed convection past a horizontal circular cylinder". Int J Heat Mass transfer, Vol. 35, 1999, 307-314.
- [5] N. G. Kafoussius and D. A. S. Rees, "Numerical study of the combined free and forced convective laminar boundary layer flow past a vertical isothermal flat plate with temperature dependent viscosity". Acta Mech, Vol. 127, 1998, 39-50.
- [6] J. Gray, D. R. Kassory and H. Tadjeran, "The effect of significant viscosity variation on convective heat transport in water saturated porous media". J Fluid Mech, Vol. 117, 1982, 233-248.
- [7] N. K. Mehta and S. Sood, "Transient free convection flow with temperature dependent viscosity in a fluid saturated porous media". Int J Eng Sci, Vol. 30, 1992, 1083-1087.
- [8] J. H. Merkin, "Free convection boundary layer on cylinders of elliptic cross section". ASME J Heat Transfer, Vol. 99, 1977, 453-457.
- [9] S. D. Harris and D. B. Ingham, "Transient free convection near the lower stagnation point of a cylindrical surface subjected to a sudden change in surface temperature". Int Comm. Heat Transfer, Vol. 27, 2000, 1091-1100.
- [10] T. V. S. Sekhar, R. Sivakumar, H. Kumar and T. V. R. Ravikumar, "Effect of aligned magnetic field on the steady viscous flow past a circular cylinder". App Math Model, Vol. 31, 2007, 130-139.
- [11] J. H. Merkin, "Free convection boundary layer on an isothermal horizontal circular cylinder". ASME/AIChE, heat transfer conference, St. Louis, MO, 9-11 August, 1976.
- [12] J. H. Merkin, "Mixed convection a horizontal circular cylinder". Int J Heat Mass Transfer, Vol. 20, 1977, 73-77.
- [13] Md. M. Molla, Md. Anwar Hossain and Gorla Rama Subba Reddy, "Natural convection flow from an isothermal horizontal circular cylinder with temperature dependent viscosity". Heat Mass Transfer, Vol. 41, 2005, 594-598.
- [14] H. S. Takhar, A. J. Chamka and G. Nath, "Combined heat and mass transfer along a vertical moving cylinder with a free stream". Heat Mass Transfer, Vol. 36, 2000, 237-246.
- [15] R. Bhargava, H. S. Takhar, S. Rawat, Tasveer A. Beg and O. anwar beg, "Finite element solutions for non-Newtonaian pulsatile flow in a non-darcian porous medium conduit". Nonlinear Analysis: Modelling and Control, Vol. 12, No. 3, 2007, 317-327.
- [16] Naseer S. Elgazery, "Transient analysis of heat and mass transfer by natural convection in power law fluid past a vertical plate immersed in a porous medium (numerical study)". Applications and Applied Mathematics, Vol. 3, No. 2, 2008, 267-285.
- [17] Rashad, A. M., "Perturbation analysis of radiative effect on free convection flow in the presence of pressure work and viscous dissipation". Communication in nonlinear sciences and numerical simulation, Vol. 14, 2009, 140-153.
- [18] Brewster, M. Q. Thermal Radiative Transfer and Properties. 2nd ed. New York: John Wiley and Sons; 1992.

Assessment of High Temperatures Sound Transmission Losses and Noise Reduction Factor for a DPF Using a Six-port Acoustic Model

S. M. Fayyad^a, M. N. Hamdan^{*b}, S. Abdallah^c

^aDepartment of Mechatronics, Al-Balqa applied university, Alsalt, Jordan

^bMechanical Engineering Department, University of Jordan, Amman 11942, Jordan

^cDepartment of Aerospace Engineering, University of Cincinnati, Cincinnati, OH, 45221, USA

Abstract

We construct a 2-D field model as a modified version of the 1-D model formulated in [1] for the study of sound propagation in a diesel particulate filter (DPF) unit. The modified model is used to evaluate both sound transmission losses and noise reduction factors of a typical DPF unit at high temperatures. The 2-D model is formulated using linearized field Navier-Stocks, energy, and continuity equations but retains the normal as well as transverse component of gas velocity. The temperature, pressure, density, and velocities of gas profiles in the 2-D space and variation with time are assumed to be harmonic. By substituting the differentials of the assumed forms of these variables with respect to both space and time in the governing field equations, a set of three coupled linear 2-D field variation equations for pressure, axial and transverse velocities is obtained. The obtained reduced model is solved analytically using Fourier series approximations for the obtained field variable functions in the reduced model. The approximate solution is used to build a 2-D acoustic model for the exhaust gases emission which accounts for both attenuation and phase shift defining the propagation wave constant. Also the obtained approximate solution is used to determine the acoustics impedance of the DPF unit, soot loading, noise and vibration damping, in addition to calculating the noise reduction factors (NRF). In the present study, unlike previous ones, six, rather than four, roots for wave propagation constant are obtained corresponding to the obtained six port acoustic DPF model. The results obtained using the present six-port model, for selected system parameters are graphically displayed and compared with those available in the open literature using a four-port model. The present model results show, in general, similar qualitative behavior and a significant quantitative improvement of the available results in the open literature obtained using a four port model.

© 2011 Jordan Journal of Mechanical and Industrial Engineering. All rights reserved

Keywords: Acoustic model; Porous media; Darcy law; Wave propagation Constant; Acoustic Transmission Losses

1. Introduction

One of the leading technologies for meeting future particulate matter (PM) emission strict standards is the diesel particulate filter (DPF). These devices generally consist of a wall-flow type filter positioned in the exhaust stream of diesel engine vehicles. As the exhaust gases pass through the exhaust system, particulate emissions are collected and stored in the DPF. Because the volume of diesel particulates collected by the system will eventually fill up and even plug the DP filter, a method for controlling trapped particulate matter and regenerating the filter is necessary. The DPF is a superior system in the reduction of particulate matters because it can reduce about 70% of the generated PM. A typical DPF system contains a large number of thin tubes or cavities with a diameter of about (1-2 mm), and (0.15-0.5 cm) length. It is available in several types such as: electric heater, burner (ceramic filter), and fuel additive type; the latter is a honey-comb ceramic. The honey-comb type constitutes an additive supply and an electronic system. In this type Fe is used as

an additive whereby iron oxide is formed which reacts with carbon and then it is converted to iron. The DPF is connected at a suitable intervening location along the exhaust gases path through the main exhaust pipe. Thus the noise and vibration characteristics of exhaust system are expected to change and consequently affect the performance of the engine by developing back pressure, changing temperature and velocity of the exhaust gases...etc. Hence building an acoustic model for the DPF is valuable in predicting its effect on the overall performance of the DPF unit.

The acoustic characteristics of the DPF systems have been the subject of many theoretical and experimental investigations, e.g [1-15]. Greevesm et. al [1] studied theoretically the origin of hydrocarbons emission from diesel engines. Their results indicate that a DPF can eliminate some of PM and is a very promising as an after-treatment technique. Yu and Shahed [2] studied the effects of injection timing and exhaust gas recirculation on emissions from a diesel engine. They classified a DPF action as filtration and regenerative processes. Konstandopoulous et al. [3] studied the DPF wall-flow, pressure drop and cooling efficiency. They used Darcy's

* Corresponding author. e-mail: naderhamdan@hotmail.com

law to describe the coupling between neighboring channels of the DPF and to predict system variable changes in the fluctuating fields between the neighboring DPF channels. Peat [4] studied sound propagation in capillary tubes using FEM solutions of simplified wave equations for a visco-thermal fluid flow. Also, Astley and Cumings [5] presented FEM solutions to the axial flow through porous medium, based on simplified wave equation in a visco-thermal fluid. They presented an analysis for the laminar flow with a parabolic velocity distribution and a quadratic flow cross-section. They simplified the governing equations by assuming that the axial gradients to be significantly smaller than the gradients over the cross-section. Employing a simplified analysis presented in [4,6], Dokumaci [7] obtained an exact solution for the case of a plug flow and a circular cross-section. He also presented an acoustic two-port model for a catalytic converter unit, which takes into account the presence of a mean flow, assuming a uniform velocity profile, and the presence of a mean pressure gradient [8]. Ih et al. [9] have developed analytical solutions for sound propagation in capillary cylindrical tubes which assumes a parabolic mean axial flow, and neglects the radial component of the particle velocity. Jeong and Ih [10] presented numerical solutions of the basic governing flow field equations taking into account the radial particle velocity. Their results showed that the radial velocity has a small but noticeable effect on the DPF acoustic behavior. Dokumaci [11] extended his earlier work in [7] to the case of rectangular narrow tubes with a plug flow. His analysis was based on approximate double Fourier sine series expansions for the field variables over the channel cross-section.

Allam and Abom [12,13] presented an approximate 1-D, two-ports discrete acoustic model for predicting sound transmission losses for an entire diesel particulate filter (DPF) unit. Their model was based on an approximate treatment of the viscous and thermal losses along the narrow channels of the DPF. Also in this model the steady flow resistance was used to calculate equivalent lumped acoustic impedance. To include the wave propagation effects the monolith was described using coupled wave guide model, where coupling is via the porous walls of monolith. Darcy's law was used to describe the pressure drop in the porous walls. This 1-D wave propagation model yielded a constant, frequency independent, transmission loss and agreed within 1 dB with measured data on a typical hot filter but for low frequencies (<300Hz).

Allam and Abom [14] modified their 1D model in [13] using the classical (exact) Kirchhoff solution for a plane wave propagation in a homogeneous, visco-thermal fluid in a rigid narrow tube [15]. The modified model includes a more detailed account for viscous and thermal losses by solving the convective acoustic wave equations for two neighboring channels using Zwikker and Kosten theory. It also uses and modifies the analysis followed by Dokumaci [8] to account for the effect of wall permeability. They used a straightforward linearization and segmentation approach to convert the obtained 1-D model to a 4-th order (4-port) eigenvalue problem whose four eigenvalues are the wave propagation constants. The presented results showed a fair agreement with measured

ones for frequencies up to 1000 Hz for a typical filter at operating (hot) conditions. It is noted that the above Allam and Abom [14] model assumes the fields to be constant with respect to space but vary harmonically with time. Fayyad [16], and Hamdan et al. [17] built, respectively, a four-port and a six-port acoustic models for the DPF following the analysis approach presented in [13, 14] but taking into account the transverse component of gas velocity. They used their models to find transmission losses and noise reduction factor at relatively low temperatures and presented results which showed good agreement with those presented in [14].

In the present work, the analysis developed by Allam and Abom [14] is modified by considering the effect of transverse velocity and is employed to build a 2-D, six-port acoustic model for the entire DPF unit. The presented model takes into account field variations both with respect to time and the 2-D space which, to the authors' best knowledge, has been ignored in previous models found in the open literature. The calculated results for the acoustic transmission losses in a typical hot DPF obtained using the present six-port model, for selected system parameters are compared with those presented in [14] using a four-port model.

2. Problem Formulation and solution

Following the analyses in [13,14], the DPF is divided into five parts, as shown in Fig. 1. These parts are: the inlet (IN), narrow pipes with impermeable walls (1) and (3), the ceramic section (2), and the outlet section (OUT). The DPF may be manufactured from different materials (Cordierite or Silicon Carbide for example) and in its most common form consists of a substrate of narrow channels. Each channel is approximately square in the cross-section with a width about (1-2) mm and is blocked at one end. Adjacent channels have this blockage at alternating ends. With this construction exhaust gas may enter at one end, but must pass through the wall of a channel before exiting and is thus termed a wall flow device [13,14]. It is clear from the above description of the DPF construction that the flow in y-direction affects the operation of the DPF, i.e. the transverse velocity can have a significant effect on the flow characteristics and the 1-D flow approximation may not be a realistic one. Therefore, in order to explore this affect the present work considers the flow as 2-D by taking into account the effect of the transverse velocity which was ignored in [13,14].

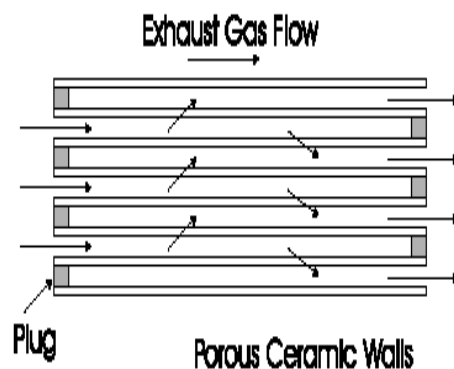


Figure 1: DPF sections and the 2D flow of gases.

3. Derivation of the Governing Equations

In deriving the acoustic model for the above described DPF unit the following assumptions, as in [13,14], are made:

- The DPF unit is partially a porous media,
- The transverse “normal” component of velocity, unlike the models in [13,14], will not be neglected: i.e. the flow is treated as a 2-D one.
- The flow is considered as viscous- thermal, incompressible, laminar, steady and a Newtonian ideal gas.
- Chemical reactions are neglected, and pressure, temperature, velocities, and density variations are considered to vary harmonically in both time and the 2-D space.

By considering the field to be 2-D instead of 1-D, the describing field Navier – stocks (momentum), continuity, energy and state equations used in [14], become:

A. Navier Stocks equations:

$$\rho_{0j} \left[\frac{\partial u}{\partial t} + u \cdot \nabla U_{0j} \right] = -[\nabla P]_j + \mu [\nabla^2 u_{sj}] \quad (1)$$

which, respectively, in x and y directions take the form:

$$\rho_{0j} \left[\frac{\partial u_{sj}}{\partial t} + u_{sj} \frac{\partial U_{0j}}{\partial x} + v_{sj} \frac{\partial U_{0j}}{\partial y} + w_{sj} \frac{\partial U_{0j}}{\partial z} \right] + \rho_{0j} U_{0j} \frac{\partial u_{sj}}{\partial x} = -\frac{\partial P_j}{\partial x} + \mu_j \left(\frac{\partial^2 u_{sj}}{\partial x^2} + \frac{\partial^2 u_{sj}}{\partial y^2} + \frac{\partial^2 u_{sj}}{\partial z^2} \right) \quad (2)$$

$$\rho_{0j} \left[\frac{\partial v_{sj}}{\partial t} + u_{sj} \frac{\partial v_{sj}}{\partial x} + v_{sj} \frac{\partial v_{sj}}{\partial y} + w_{sj} \frac{\partial v_{sj}}{\partial z} \right] + \rho_{0j} v_{sj} \frac{\partial v_{sj}}{\partial y} = -\frac{\partial P_j}{\partial y} + \mu_j \left(\frac{\partial^2 v_{sj}}{\partial x^2} + \frac{\partial^2 v_{sj}}{\partial y^2} + \frac{\partial^2 v_{sj}}{\partial z^2} \right) \quad (3)$$

B. Continuity equation:

$$\frac{\partial \rho_j}{\partial t} + u_{sj} \frac{\partial \rho_{0j}}{\partial x} + U_{0j} \frac{\partial \rho_j}{\partial x} + \rho_j \frac{\partial U_{0j}}{\partial x} + \rho_{0j} \nabla \cdot u_j = 0 \quad (4)$$

C. Energy equation

$$\rho_{0j} C_p \left[\frac{\partial T_j}{\partial t} + U_{0j} \frac{\partial T_j}{\partial x} + u_{sj} \frac{\partial T_{0j}}{\partial x} \right] + \rho_j C_p U_{0j} \frac{\partial T_{0j}}{\partial x} = -\frac{\partial P_j}{\partial t} + U_{0j} \frac{\partial P_j}{\partial x} + \frac{\partial P_{0j}}{\partial x} u_{sj} + K_{0j} \nabla^2 T_j \quad (5)$$

D. State equation:

With the assumption of ideal gas, the linearized state equation (linearized ideal gas law) takes the form [14]:

$$\rho_j = \left(\frac{P_j}{R_j T_{0j}} \right) - \left(\frac{\rho_{0j} T_j}{T_{0j}} \right), \quad (6)$$

where

$$\rho_j = \rho_j(x, y, t) \quad (7)$$

$$T_j = T_j(x, y, t)$$

$$P_j = P_j(x, y, t)$$

x, y denote, respectively, the longitudinal and transverse channel axes, u, v are the acoustic particle velocities in, respectively, the x and y directions, and j = 1, 2 represent the inlet and outlet pipes, respectively. Also p, T and ρ are the acoustic pressure, temperature and density, respectively, μ is the shear viscosity coefficient, k_{th} is the thermal conductivity of the fluid, R is the gas constant, Cp is the specific heat coefficient at constant pressure, P₀, T₀ and ρ₀ denote the ambient pressure, temperature and density, respectively, U₀, V₀ denote the axial mean flow velocity and transverse velocity respectively, and ∇_s² denotes the Laplacian over the channel cross-section.

To describe the coupling between neighboring channels (which describes the porosity of diesel particulate filter) Darcy’s law is applied to the fluctuating fields [14]:

$$P_1 - P_2 = R_w u_w \quad (8)$$

where a subscript w refers to wall, u_w is the acoustic velocity through the wall, R_w is the wall resistance, which is given by R_w = μ_wh_t/σ_w, μ_w is the dynamic viscosity, h_t is the wall thickness, and σ_w is the wall permeability.

4. Approximate Solution

In order to convert the above nonlinear model into an analytically tractable one, the linearization and segmentation approach presented in [14] is closely followed. Accordingly, and noting that the present model is a 2-D one, the following time and 2-D space harmonic variations for the fields are assumed:

$$u_{sj} = A_0 e^{i\omega t} \quad (9)$$

$$v_j = B_0 e^{i\omega t} \quad (10)$$

$$\rho_j = \rho_0 e^{i\omega t}, \quad P_j = P_0 e^{-i\omega t}, \quad T_j = T_0 e^{i\omega t} \quad (11)$$

$$u_{sj} = -D'(A_0 e^{\Gamma_{k_1} x} - B_0 e^{-\Gamma_{k_1} x}) \quad (12)$$

$$v_{sj} = -D'(A_0 e^{\Gamma_{k_1} y} - B_0 e^{-\Gamma_{k_1} y}) \quad (13)$$

$$P_{jy} = A_0 e^{\Gamma_{k_1} y} + B_0 e^{-\Gamma_{k_1} y} \quad (14)$$

$$P_{jx} = A_0 e^{\Gamma_{k_1} x} + B_0 e^{-\Gamma_{k_1} x} \quad (15)$$

$$\rho_{jx} = A_0 e^{\Gamma_{k_1} x} + B_0 e^{-\Gamma_{k_1} x} \quad (16)$$

$$\rho_{jy} = A_0 e^{\Gamma_{k_1} y} + B_0 e^{-\Gamma_{k_1} y} \quad (17)$$

$$T_{jx} = A_0 e^{\Gamma_{k_1} x} + B_0 e^{-\Gamma_{k_1} x} \quad (18)$$

$$T_{jy} = A_0 e^{\Gamma_{k_1} y} + B_0 e^{-\Gamma_{k_1} y} \quad (19)$$

Upon substituting equations (9)-(11) into equations (2)-(5), using equation (6) and noting that the assumed equations (12)-(19) are linear, the governing field equations (2)-(5) take the linear form

$$\rho_{0j} \left[i\omega + \frac{\partial U_{0j}}{\partial x} \right] u_{sj} + \rho_{0j} \frac{\partial U_{0j}}{\partial y} v_{sj} + (D_{0j} U_{0j} + \frac{\partial}{\partial x}) P_{jx} = \mu_j \left(\frac{\partial^2 u_{sj}}{\partial x^2} + \frac{\partial^2 u_{sj}}{\partial y^2} + \frac{\partial^2 u_{sj}}{\partial z^2} \right) \quad (20)$$

$$\rho_{0j} \left[i\omega + \frac{\partial V_{0j}}{\partial y} \right] v_{sj} + \rho_{0j} \frac{\partial V_{0j}}{\partial x} u_{sj} + (D_{0j} V_{0j} + \frac{\partial}{\partial y}) P_{jy} = \mu_j \left(\frac{\partial^2 v_{sj}}{\partial x^2} + \frac{\partial^2 v_{sj}}{\partial y^2} + \frac{\partial^2 v_{sj}}{\partial z^2} \right) \quad (21)$$

$$(i\omega + \frac{\partial U_{0j}}{\partial x}) \rho_j + (\frac{\partial \rho_{0j}}{\partial x} + D_{0j} U_{0j}) u_{sj} + \rho_{0j} \nabla \cdot u_j = 0 \quad (22)$$

$$(\rho_{0j}Cp_jiw - K_{thj}\nabla_s^2)T_j + \rho_{0j}Cp_ju_{sj}\frac{\partial T_{0j}}{\partial x} + Cp_jU_{0j}\frac{\partial T_{0j}}{\partial x}\rho_{0j} = (iw + U_{0j}\frac{\partial}{\partial x})P_j + (\frac{\partial P_{0j}}{\partial x} - U_{0j}D_{0jj}\rho_{0j})u_{sj} \tag{23}$$

It is noted that by setting to zero in the above equations (e.g by neglecting the transverse velocity) the above model in equations (21)-(24) reduces to the 1-D developed by Allam and Abom [14].

In order to develop an acoustic model for the DPF unit, and to find acoustic impedance, transmission losses, and other needed parameters such as noise reduction factor, equations (21) to (23) must be solved for the variables and These four, homogenous, coupled linear equations with four variables constitute an eigenvalue problem. The condition of a non-trivial solution to these equations leads to a characteristic frequency equation and associated eigenvectors. The eigenvalue problem is obtained as follows, (for more details, see [13,14]. First one assumes

$$\begin{aligned} P_j &= A_j \exp(-i\Gamma k_1 x), \\ u_{sj} &= H_j(x, y, z)P_j, \\ T_j &= F_j(x, y, z)P_j, \\ v_{sj} &= B_j \exp(-i\Gamma k_1 y) \end{aligned} \tag{24}$$

where A_j, H_j, F_j and B_j are constant coefficients. Next substituting the expressions in equation (24) into equations (21)-(23) one obtains

$$\frac{\partial^2 H_j}{\partial x^2} + \frac{\partial^2 H_j}{\partial y^2} + \frac{\partial^2 H_j}{\partial z^2} - i\beta_{sj}^2 H_j = \frac{D_{0j}CM_j}{\mu_j} - \frac{-i\Gamma k_1}{\mu_j} \tag{25}$$

$$\frac{\partial^2 H_j}{\partial x^2} + \frac{\partial^2 H_j}{\partial y^2} + \frac{\partial^2 H_j}{\partial z^2} - i\beta_{sj}^2 H_j = \frac{D_{0j}CM_j}{\mu_j} - \frac{-i\Gamma k_1}{\mu_j} \tag{26}$$

$$\frac{\partial^2 F_j}{\partial x^2} + \frac{\partial^2 F_j}{\partial y^2} + \frac{\partial^2 F_j}{\partial z^2} - \sigma_{jx}^2 F_j = \sigma_{0j}^2 + \sigma_{1j}^2 H_j \tag{27}$$

where

$$\begin{aligned} \beta_{sj}^2 &= (-\Gamma k_1 + \frac{1}{w} \frac{\partial U_{0j}}{\partial x} + \frac{1}{w} \frac{\partial U_{0j}}{\partial y})S_j^2 \\ \beta_{sj}^2 &= (-\Gamma k_1 + \frac{1}{w} \frac{\partial V_{0j}}{\partial x} + \frac{1}{w} \frac{\partial V_{0j}}{\partial y})S_j^2 \\ \sigma_{jx}^2 &= S_j^2 \text{Pr}(i - \frac{U_{0j}}{wT_{0j}} \frac{\partial T_{0j}}{\partial x}), \\ \sigma_{0j}^2 &= (\frac{\text{Pr}S_j^2}{w} \frac{\partial T_{0j}}{\partial x} - \frac{1}{K_{thj}} \frac{\partial P_{0j}}{\partial x} + \frac{S_j^2 MU_{0j}}{wK_{thj}} D), \\ \sigma_{jx}^2 &= \frac{1}{K_{thj}} (iw - iU_{0j}\Gamma Mw - \frac{Cp_j U_{0j}}{R_j T_{0j}} \frac{\partial T_{0j}}{\partial x}), \\ \text{Pr} &= \sqrt{\frac{\mu_j Cp_j}{K_{thj}}} \end{aligned}$$

Next, following Allam and Abom [14], the following Fourier sine series for the field variables H and F are assumed:

$$H(x, y, z) = \sum_{m,n} a_{mn} \sin \frac{m\pi y}{2a_j} \sin \frac{n\pi z}{2a_j} \tag{28}$$

$$F(x, y, z) = \sum_{m,n} b_{mn} \sin \frac{m\pi y}{2a_j} \sin \frac{n\pi z}{2a_j} \tag{29}$$

Then upon substituting equations (28) and (29) into equations (25)-(27), and, as in [1], averaging the mass conservation equation (22), one obtains the following eigenvalue problem:

$$\begin{aligned} &\left[\frac{1}{R_j T_{0j}} (iw + \frac{\partial U_{0j}}{\partial x})(1 - \rho_{0j}R_j < F_j >) + (\frac{\partial \rho_{0j}}{\partial x} + DU_{0j} - 2ik_1\Gamma\rho_{0j}) < H_j > \right] A_j \\ &+ (-1)^{j-1} \frac{2\rho_{0j}(A_1 - A_2)}{a_j R_w} = 0 \end{aligned} \tag{30}$$

which can be written in matrix form ,using the notation in [14], as follows:

$$\begin{bmatrix} K11 + K21 & -K12 \\ K21 & K12 - K22 \end{bmatrix} \begin{bmatrix} A_1 \\ A_2 \end{bmatrix} = \begin{bmatrix} 0 \\ 0 \end{bmatrix} \tag{31}$$

where

$$K_{1j} = \begin{bmatrix} \frac{R_w a_j}{2\rho_{0j} R_j T_{0j}} (iw + \frac{\partial U_{0j}}{\partial x})(1 - \rho_{0j}R_j < F_j >) + \\ \frac{R_w a_j}{2\rho_{0j}} (\frac{\partial \rho_{0j}}{\partial x} + DU_{0j} - 2ik_1\Gamma\rho_{0j}) < H_j > \end{bmatrix} \tag{32}$$

And

$$K_{2j} = (-1)^{j-1} \tag{33}$$

For a non trivial solution the determinant of the coefficients matrix in equation (31)

$$\begin{vmatrix} K11 + K21 & -K12 \\ K21 & K12 - K22 \end{vmatrix} \tag{34}$$

is set to zero, whereby one obtains the following system characteristic frequency equation:

$$(K11 + K21)(K12 - K22) + K12K21 = 0 \tag{35}$$

The above frequency equation is a 6th order equation for the propagation constant Γ which can only be solved numerically. A specially constructed MATLAB program was used to solve for the six roots of equation (35) for selected values of system parameters. The wave propagation constants, which is dependent on all field parameters, represent two types of waves: one along the positive (forward) and the other is along the negative (backward) directions of the pipe axis and are denoted, respectively ,as usual, by $\Gamma+$, and Γ [13,14]. See figures (1) – (4).

Note that the roots (eigenvalues) of equation (35) are complex. The real parts of these wave propagation constants represent the attenuation while the imaginary parts represent the phase shift. The corresponding three complex eigenvectors are given by

$$\begin{pmatrix} \hat{p}_1(x) \\ \hat{p}_2(x) \\ \hat{p}_3(x) \end{pmatrix} = \sum_{n=1}^6 \hat{a}_n e^{-ik_1\Gamma_n x} e_{j,n} \tag{36}$$

where $\hat{p}(x)$ is the acoustics pressure. , \hat{a}_n is the modal amplitude, Γ_n is the calculated wave propagation

constant (eigenvalue) and $e_{j,n}$, $j=1,2$, are the corresponding components of the 2-D eigenvector, with $j=1$ corresponds to the inlet and $j=2$ corresponds to outlet. Note that equation (36) represents the sound field (pressure fluctuation) in filter section. In addition to equation (36) one needs the field volume pressure velocities to calculate the sound transmission losses in the filter. The corresponding volume pressure velocities $\hat{q}_n(x)$ are obtained, as in [14], by dividing equation (36) by the characteristic wave impedance Z , where $Z = \frac{\rho c}{A}$, c = speed

of sound, ρ = mass density of the medium, and A is the cross sectional area of the DPF part. This leads to the following expression for the volume pressure velocities $\hat{q}_n(x)$:

$$\begin{pmatrix} \hat{q}_1(x) \\ \hat{q}_2(x) \\ \hat{q}_3(x) \end{pmatrix} = \sum_{n=1}^6 \hat{a}_n e^{-ik_2 \Gamma_n x} e'_{j,n} \quad (37)$$

where $e'_{j,n} = 4a_j^2 < H_{j,n} > e_{j,n}$, $k_2 = k_1 \sqrt{1 - 8i\beta/k_1}$,

$$\beta = C_j \rho_w / dh_j R_w$$

$<H_j> = 4a_{j1}/\Pi^2$. Finally, to calculate the acoustic

transmission losses in the DPF unit, one uses equation (36) and (37) to formulate the so called the transformation matrix T_{DPF} ,

$$[\hat{q}] = [T_{DPF}] [\hat{P}] \quad (38)$$

where the T_{DPF} is a 6×6 matrix, which is formed as a product of the individual 2- port transfer matrices corresponding to the five segments of the DPF, and takes the form [14].

$$T_{DPF} = T_{IN} T_1 T_2 T_3 T_{out} \quad (39)$$

The acoustic transmission losses TL are then calculated using the relation [14]

$$TL = 20 \log |T_{DPF}/2| \quad (40)$$

In addition, the noise reduction factor NRF can be calculated by using the following equation:

$$NRF = LP_2 - LP_1 = 20 \log \frac{P_2}{P_1} \quad (41)$$

5. Results and Discussion

The wave propagation constant Γ_n , transmission losses TL and the noise reduction factor NRF were calculated, for selected system parameters, using equations

(35), (40) and (41). A MATLAB program was used to carry out all needed calculations. The results obtained were for the cases: hot at $500^0 C$ and at $1000 C$. For the two cases the frequency was varied over the range $400 - 1000$ Hz. Also results were obtained for two cases: one with soot layer and the other with no soot layer. Samples of the obtained for different types of DPF are displayed in figures (2) – (14).

From these figures the following points are made:

- Both transmission losses and noise reduction factor for the typical filter and other types of DPFs tend to increase as frequency increases.
- Figures (2)-(5) show that the wave propagation through the DPF unit suffers both attenuation and phasing shift, and both attenuation and phase shift decrease as the shear wave number increases.
- Transmission losses for the case of soot layer formation are significantly higher than those with no soot layer formation.
- The present six-port model show similar trends concerning transmission losses as those presented in [14] using a four-port model. However the present six-port model result, which takes into account the effect of the field transverse velocity, are in closer agreement with the experimental ones presented in [14] than the analytical four-port model results presented obtained in [14] which ignore this effect. Therefore one may conclude that ignoring the transverse velocity can have a significant effect on the evaluation of acoustic transmission losses for a DPF unit.

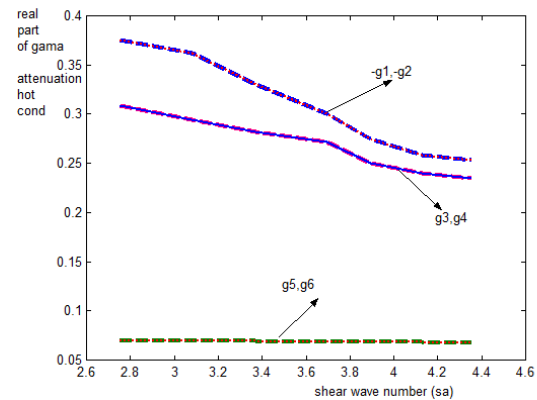


Figure 2: Real part of wave propagation constant Γ , denoted here as g , vs. shear wave number (phase shift), Γ_1 and Γ_2 propagation constants for uncoupled waves, Γ_3 and Γ_4 propagation constants for coupled waves, Γ_5 and Γ_6 represent the interfering parts, time and 2-D space harmonic variation, and under hot conditions ($T=500^0 C$).

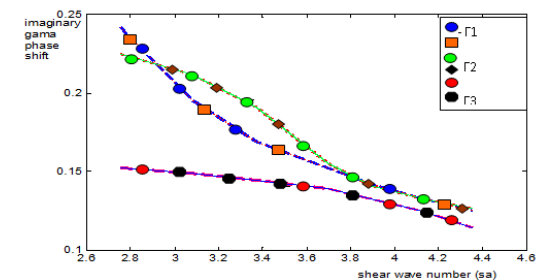


Figure 3: Imaginary part of Γ vs. shear wave number (phase shift), Γ_1 and Γ_2 propagation constants for uncoupled waves, Γ_3 and Γ_4 propagation constants for coupled waves, Γ_5 and Γ_6 represent the interfering parts, under hot conditions ($T=500^0 C$).

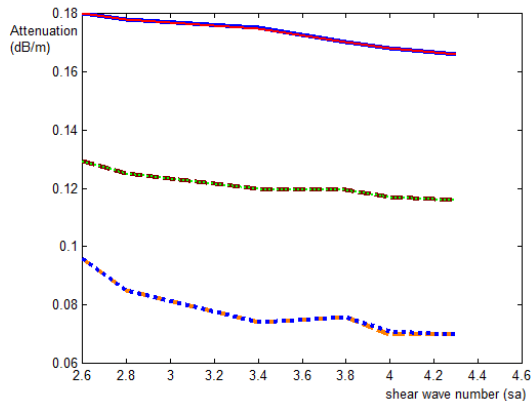


Figure 4: Real part of Γ vs. shear wave number, ... Γ_1 , and--- Γ_2 are propagation constants represent uncoupled waves, Γ_3 , and - Γ_4 propagation constants for coupled waves, Γ_5 , and ---- Γ_6 under hot conditions ($T=1000^\circ\text{C}$).

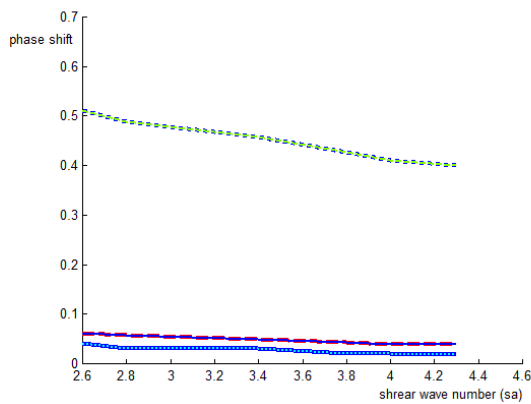


Figure 5: Imaginary part of Γ against shear wave number, ---- Γ_1 , and--- Γ_2 are propagation constants represent uncoupled waves, Γ_3 , and ---- Γ_4 propagation constants for coupled waves, Γ_5 , and Γ_6 , under hot conditions ($T=1000^\circ\text{C}$).

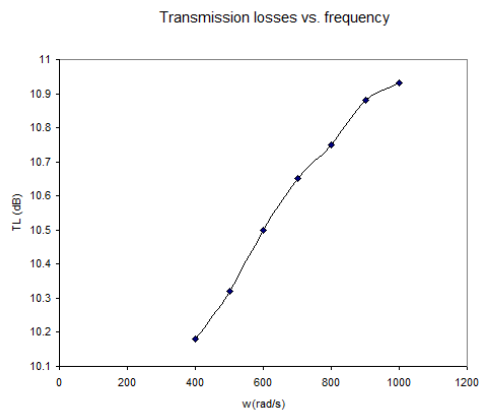


Figure 6: transmission losses vs. frequency in the case of hot conditions ($T=500\text{ C}$) for typical filter for the case of no soot layer, Mach=0.02 and space and time variation case.

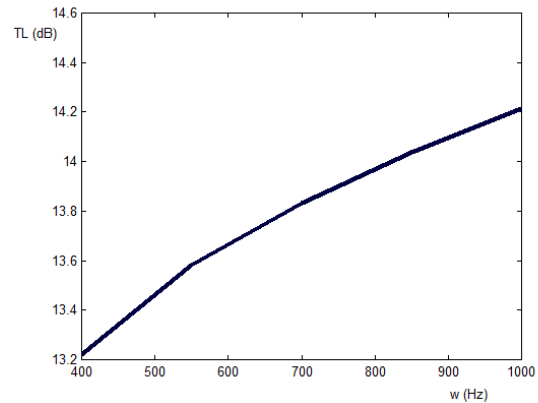


Figure 7: Transmission losses vs. frequency in the case of hot conditions ($T=500\text{C}$) for typical filter for the case of with soot layer, Mach=0.02, and Plane and time variation case.

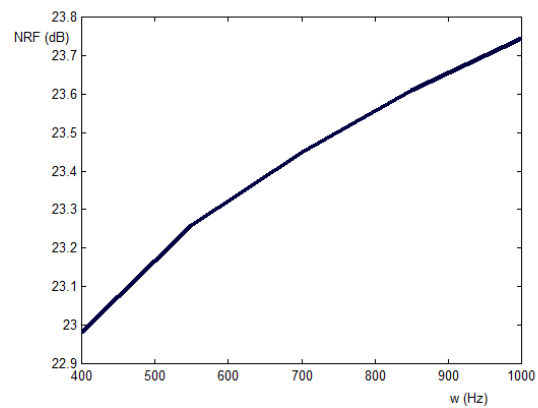


Figure 8: NRF vs. frequency for typical DPF in the case of hot conditions, (With no soot layer). Mach=0.02, in the case of plane and time variation.

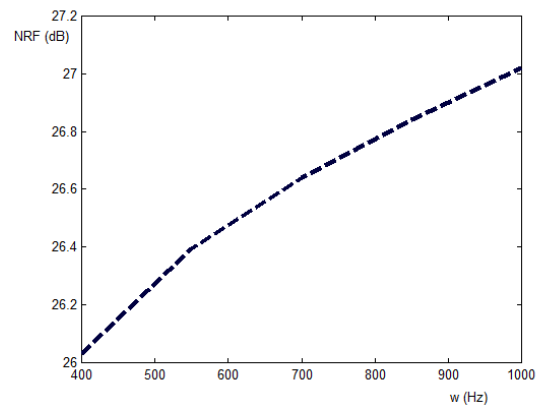


Figure 9: NRF vs. frequency for typical DPF in the case of hot conditions, (With soot layer). Mach=0.02, in the case of plane and time variation.

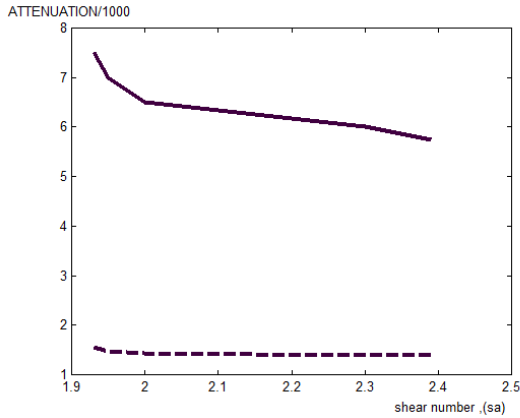


Figure (10): Attenuation against shear number comparison: **—** present study, **- - -** results in [14]. Hot conditions.

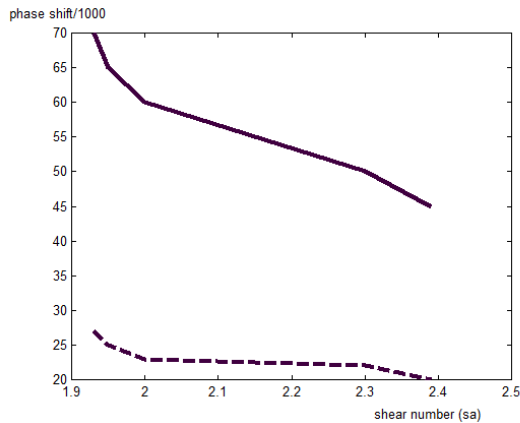


Figure (11): Phase shift against shear number comparison: **—** present study, **- - -** results in [14]. Hot conditions

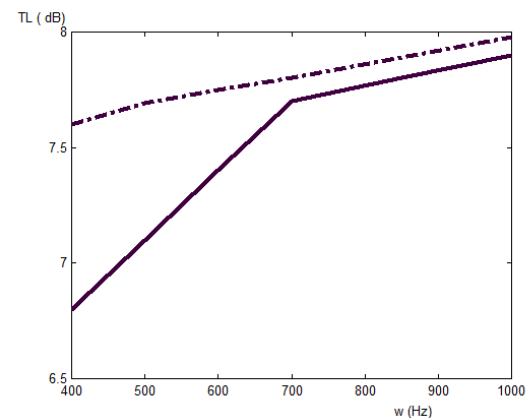


Figure (12): transmission losses against frequency for RC: 200/12 DPF unit type under the case of hot conditions compared with experimental results in [14], **—** present study, **- - -** Experimental results [14]; (with no soot layer), and Mach=0.02.

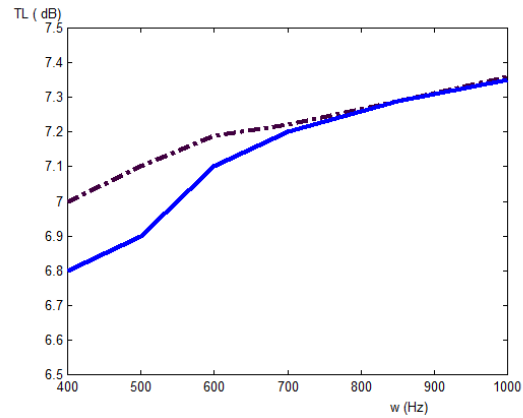


Figure (13): transmission losses against frequency for EX: 100/17 DPF unit type under the case of hot conditions compared with experimental results in [14]. **—** Present study, **- - -** experimental results [14]; (with no soot layer), and Mach number=0.02.

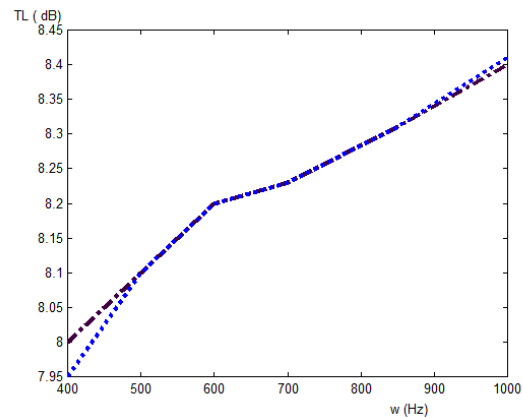


Figure 14: Transmission losses against frequency for EX80: 200/14 DPF unit type under the case of hot conditions compared with experimental results in [14]. **—** Present study, **- - -** experimental results [14]; (with no soot layer and March number =.02.

6. Conclusion

An approximate analytical 2-D, six-port acoustic model for a DPF unit is presented. The development of this approximate model follows closely the 1-D, four-ports analysis by Allam and Abom by taking into account the effect of transverse velocity. The results of the present study show similar qualitative behavior and a significant quantitative agreement improvement of the available experimental results for a clean (no soot formation) in the open literature than a four-port model and at room temperature only. Further validation of this model is required by comparing its predictions to those obtained using numerical analysis of the full governing nonlinear field equations and to results of tests on filter connected to running real engines to ensure hot conditions and soot layer formation.

References

- [1] G. Greevesm, I. M. Khan, C. H. T. Wang, I. Fenne, "Origins of hydrocarbon emission from diesel engines". Society of Automotive Engineering, SAE Paper No. 770259, 1977, 02-01.
- [2] R. Yu, Yu, S. M. Shahed, "Effects of injection timing and exhaust gas recirculation on emissions from a DI diesel engine". Society of Automotive Engineering, SAE Paper No. 811234, 1981.
- [3] A. G. Konstandopoulos, J. H. Johnson, "Wall-flow diesel particulate filters - their pressure drop and collection efficiency", Society of Automotive Engineering, SAE Paper No. 890405, 1989.
- [4] K. S. Peat, "A first approximation to the effects of mean flow on sound propagation in capillary tubes", *Journal of Sound and Vibration* Vol. 175, 1994, 475-489.
- [5] R. J. Astley, A. Cummings, A., "Wave propagation in catalytic converter formulation of the problem and finite element scheme". *Journal of Sound and vibration*, Vol.188 , No. 5, 1995, 635-657.
- [6] P. Davies, "Practical flow duct acoustics". *Journal of Sound and Vibration*, Vol. 124 , 1988, 91-115.
- [7] Dokumaci, "An approximate dispersion equation for sound waves in a narrow pipe with ambient gradients". *Journal of Sound and Vibration*, Vol. 240, No. 4, 2001, 637-646.
- [8] Dokumaci, "Sound transmission in narrow pipes with superimposed uniform mean flow and acoustic modeling of automobile catalytic converters", *Journal of Sound and Vibration*, Vol. 182 , 799-808, 1995.
- [9] J.-G. Ih, C. M. Park, H.-J. Kim , " A model for sound propagation in capillary ducts with mean flow". *Journal of Sound and Vibration* Vol. 190, No.2, 163-175, 1996.
- [10] K.-W. Joeng, J.-G. Ih, (1996). "A numerical study on the propagation of sound through capillary tubes with mean flow", *Journal of Sound and Vibration*, Vol. 198, No. 1, 67-79, 1996.
- [11] E. Dokumaci, "On transmission of sound in circular and rectangular narrow pipes with superimposed mean flow". *Journal of sound and vibration*, Vol. 210, No. 3, 1998, 375-389, 1998.
- [12] S. Allam, M. Abom, "On Acoustic modeling and testing of diesel particulate filters." *Proceedings of Inter. Noise Conference*, Paper No. 250, 2002 .
- [13] S. Allam, S. M. Abom, "Acoustic modeling and testing of diesel particulate filters ." *Journal of Sound and Vibration*, Vol. 288 (1/2) , 255-273, 2005.
- [14] S. Allam, S. M. Abom, "Sound propagation in an array of narrow porous channels with application to diesel particulate filters". *Journal of Sound and Vibration*, Vol. 291, 882-901, 2006.
- [15] D. H. Keefe, " Acoustical wave propagation in cylindrical ducts: transmission line parameter approximations for isothermal and non-isothermal boundary conditions." *Journal of the Acoustical Society of America*, Vol.75, No. 1, 58-62, 1984.
- [16] S. Fayyad, "Sound propagation in porous media with application to diesel" particulate filters." PhD Thesis, University of Jordan, 2006.
- [17] M. N. Hamdan, S. Fayyad, S., M. A. Hamdan, "Six-port model for sound propagation in a porous media with applications to diesel particulate filters", *AMME-13 Conference , Cairo-Egypt- Paper No. 62*, 2008.

A Predictive Model for Surface Roughness in Turning Glass Fiber Reinforced Plastics by Carbide Tool (K-20) Using Soft Computing

S. A. Hussain^{*a}, V. Pandurangadu^b, K.P. Kumar^c and V.V. Bharathi^d

^aDepartment of Mechanical Engineering, R.G.M.College of Engg &Technology, Nandyal-508501, A.P, India.

^bDepartment of Mechanical Engineering, J.N.T. University, Anantapur-515002, A.P, India

^cDepartment of Mechanical Engineering, Sri Sai Ram Institute of Technology, Chennai-44, India

^dDepartment of Mechanical Engineering, S.K.D Engineering College, Guty, Andhra Pradesh, India

Abstract

Glass fiber reinforced plastics are finding its increased applications in various engineering fields such as aerospace, automobile, electronics and other industries. This paper discusses the use of fuzzy logic for modeling turning parameters in turning of glass fiber reinforced plastics by carbide tool (K-20). Experiments were conducted based on the established Taguchi's Design of Experiments (DOE) L25 orthogonal array on an all geared lathe. The cutting parameters considered were cutting speed, feed, depth of cut, and work piece (fiber orientation). Fuzzy based model is developed for correlating the cutting parameters with surface roughness (Ra). The results indicated that the model can be effectively used for predicting the surface roughness (Ra) in turning of GFRP composites.

© 2011 Jordan Journal of Mechanical and Industrial Engineering. All rights reserved

Keywords: GFRP composites; turning; Surface roughness (Ra); Fuzzy logic; Model

1. Introduction

Composite materials are continuously replacing traditional materials due to their excellent properties. A single large part made of composites can replace many metal parts. Composite materials can be embedded with sensors, which can monitor fatigue and performance. They have high stiffness to density ratio thereby providing greater strength at lighter weights. The use of light-weight materials means an increase in the fuel efficiency of automobiles and airplanes. Also the endurance limit of some composites is higher than that of aluminum and steel. Most composites are made up of plastics or resins and hence provide a high level of resistance to corrosion, while aluminum and iron need special treatments like alloying to protect them from corrosion. Composites have a low coefficient of thermal expansion, which can provide a greater dimensional stability when required. Despite recent developments in near-net shape processing, composite parts often require post-mould turning and drilling to meet dimensional tolerance, surface quality and other functional aspects [1] Experimental studies on traditional turning of FRP were first reported by A. Koplev et al and K.Sakuma et al [2-3]. Koing et al [4] investigated the turning of fiber reinforced plastics (FRP) using different processes like drilling, routing, milling, water jet cutting and laser cutting. Santhanakrishnan et al.[5] analyzed the surface roughness and morphology. It is known that during turning of FRP composites, the mechanism of cutting is associated with the combination of plastic deformation, shearing and rupturing of fibers along with turning matrix material.

Eriksen [6] has enumerated guidelines for the turning of short fiber reinforced thermoplastics (SF RTP). The turning of FRP is different from that of metal working in many aspects because, the FRP behavior is not only inhomogeneous, but also dependent on fiber and matrix properties, fiber orientation, and type of weave. During the turning of fiber reinforced plastics fiber, which intermittently come into contact with tool produces poor surface finish. The studies carried out on FRP composites shows that minimizing the surface roughness is very difficult and is to be controlled. Taguchi's parameters design is used for conducting the experiments [7]. Taguchi's approach extensively uses statistical design of experiments [8]. By applying this approach this technique one can significantly reduce the number of experiments and time required for experimentation. In turning of GFRP composites, hard and abrasive glass fibers results in high tool wear.

Artificial intelligence tools are playing an important role in modeling and analysis. Fuzzy logic is relatively easier to develop and require less hardware and software resources. Fuzzy logic controller is the successful application of fuzzy set theory and was introduced by zadeh[9] in 1965 it is a mathematical theory of inexact reasoning that allows modeling of the reasoning process in human linguistic terms. This theory proved to be an effective means for dealing with objectives that are linguistically specified. Linguistic terms such as low, medium and high may be defined by fuzzy sets [10]. Fuzzy logic has been applied successfully for turning process such as cutting force evaluation by Suleyman et al [11], surface roughness prediction by Yue Jiao et al [12]. In the present study arithmetic average height (Ra) in

* Corresponding author. e-mail: s_a_hussain1@rediffmail.com

turning of GFRP composites by carbide (K-20) tool is modeled and analyzed. The results indicate that fuzzy logic modeling technique can be successfully applied for the prediction of surface roughness parameters in turning GFRP composites.

2. Experimental Work

The work material used for the present investigation is glass fiber reinforced plastics (GFRP) pipes. The inner diameter of the pipe is 30mm; outer diameter is 60mm and length 500mm respectively shown in figure 1. The pipes used in the study are manufactured by filament winding process. The orientation of the fibers on the works piece has been set during the manufacture of pipes. The fiber used in the pipe is E-glass and resin used is epoxy. The specification of the material used in this work is given in Table 1.

Table 1: Specifications of fiber and resin.

Fiber: E-glass – R099 1200 P556	Resin: Epoxy
Manufacturer: Saint Gobain vetrotex India Ltd.	Manufacturer: CIBA GEIGY
R099- Multi filament Roving	Product: ARALDITE MY 740 IN
1200-Linear Density, Tex	110KG Q2
P556- Sizing reference for vetrotex	Hardener: HT 972

The experiments are planned using Taguchi's orthogonal array L25 [13] in the design of experiments (DoE), which helps in reducing the number of experiments. The experiments were conducted according to orthogonal array. The four cutting parameters selected for the present investigation is cutting speed (v)/m/min, feed (f)mm/rev, depth of cut (d)mm and work piece (fiber orientation ' Φ ') in degrees. Since the considered factors are multi-level variables and their outcome effects are not linearly related. The studies related to the GFRP composites indicated that the higher cutting conditions leads to high tool wear and poor surface finish [14].

The turning parameter used and their levels chosen are given in Table 2. All the GFRP pipes are turned in a BHARAT all-g geared lathe of model NAGMATI-175 with a maximum speed of 1200 rpm and power of 2.25KW. The ISO specification of the tool holder used for the turning operation is a WIDAX tool holder PC LNR 2020 K12 and the tool insert used for the study is solid carbide (K-20)120408 sandvik make.



Figure 1: GFRP Composite Pipe Specimens.

Table 2: Cutting parameters, their notations and their limits.

Process parameters With units	Notation	Variable	Levels				
			-2	-1	0	1	2
Speed, m/min	v	x_1	40	60	95	145	225
Feed, mm/rev	f	x_2	0.048	0.096	0.143	0.191	0.238
Depth of cut, mm	d	x_3	0.25	0.5	0.75	1	1.25
Fiber orientation angle, deg	Φ	x_4	30	45	60	75	90

The average surface roughness (R_a), which is mostly used in industrial environments, is taken-up for this study. The machined surface was measured by using surface roughness tester (FORM TALY SURF) manufactured by Taylor Hobson, U.K. The mean response table for surface roughness (R_a) is presented in Table 3.

Table 3. Response table for surface roughness.

Level	Cutting speed (v),m/min	Feed (f), mm/rev	Depth of cut (d), mm	Fiber orientation angle (Φ) degrees
1	3.847	2.876	3.625	3.109
2	3.731	3.203	3.540	3.301
3	3.403	3.569	3.368	3.487
4	3.041	3.758	3.254	3.612
5	3.198	3.815	3.434	3.711
Delta	0.806	0.939	0.371	0.602
Rank	2	1	4	3

3. Fuzzy Model for evaluation of surface roughness

The studies on turning of GFRP composites shows that minimizing the surface roughness is a serious task. In order to know the surface quality and dimensional

properties, it is necessary to employ theoretical models for prediction purposes. The structure of fuzzy logic system consists of three conceptual components:

- Fuzzification : formation of member ship functions
- Selection of proper shape and definition of expert rules
- Selection of proper defuzzification method

The fuzzifier uses membership functions to fuzzify the input and output values. The inference engine is used for fuzzy reasoning on fuzzy rules to generate a fuzzy value.

Finally, the defuzzifier converts the fuzzy in to crisp output [15-16]. Cutting speed, feed, depth of cut, and work piece (fiber orientation) are chosen as input parameters. Surface roughness parameters R_a is chosen as output response in the system. In fuzzy system, membership function is used. Membership functions characterize the fuzziness in a fuzzy set whether the elements in the set are discrete or continuous in graphical form for eventual use in the mathematical formalism of fuzzy set theory [17]. The input and output variables are fuzzified and represented by means of membership functions (MF). The shapes of the membership function depend on the form of horizon approach function. In this

study, triangle membership function is considered. Triangular membership function has gradually increasing and decreasing characteristics and only one definite value and is generally used. The relationship between the input and outputs in a fuzzy model is characterized linguistic statements called fuzzy rules. Linguistic variables low, low medium, Medium, High medium, and High for cutting speed, feed, depth of cut and work piece (fiber orientation) were taken to represent the input numerical values. The number of membership functions used for the output response is nine such as Lowest, Lower, Low, Low medium, medium, High medium, High, Higher, and Highest. More precise results can be obtained by using more number of membership functions and hence 9-membership functions were selected for the present work. The expressions used for cutting speed, feed, depth of cut, fiber orientation and cutting force (F_z) is given in Table 4. Membership functions and their ranges of input parameters are shown in Fig 2-5. Similarly the membership function used for the output response surface roughness is presented in Fig 6. The fuzzy rules were developed based on experimental results and expertise. 25 fuzzy rules were developed for 25 experimental results by taking the max-min compositional operation. The output response of the fuzzy process is available only in fuzzy values and is to be defuzzified. For defuzzifying the values defuzzification is used. Defuzzification is the conversion process and it converts fuzzy quantity into precise quantity. There are several methods of defuzzification is used. Centroid of area defuzzification method is a general method and it gives more reliable results than other methods and it calculate the centroid of the area under the membership function. The non fuzzy value gives the output value in numerical form. The relationship between the output value and the experimental values are plotted and are shown in Figs. 7. The figures indicate a very close correlation between the experimental values and fuzzy predicted values, which shows that fuzzy logic can be effectively utilized for prediction of surface roughness parameters in turning of GFRP composites.

Table 4: Fuzzy expressions of input and output parameters.

Inputs				Output
Cutting speed (v)	Feed (f)	Depth of cut (mm)	Fiber orientation angle (Φ)	Surface roughness (Ra)
Low	Low	Low	Low	Lowest
Low medium	Low medium	Low medium	Low medium	Lower
Medium	Medium	Medium	Medium	Low
High medium	High medium	High medium	High medium	Low medium
High	High	High	High	Medium
				High medium
				High
				Higher
				Highest

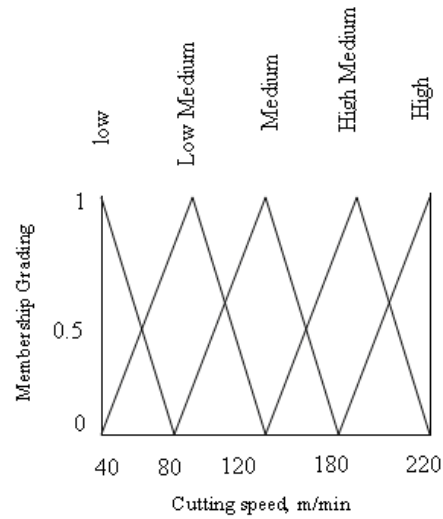


Figure 2: Membership function and their ranges for cutting speed.

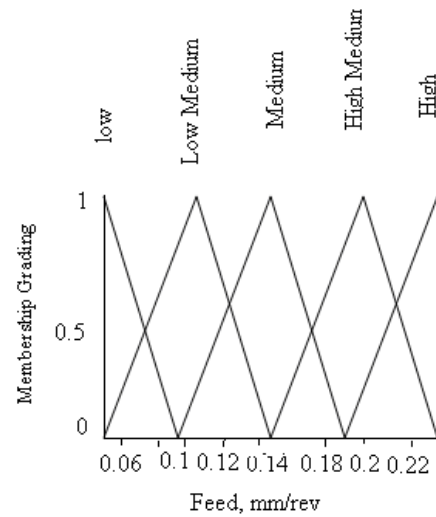


Figure 3: Membership function and their ranges for feed.

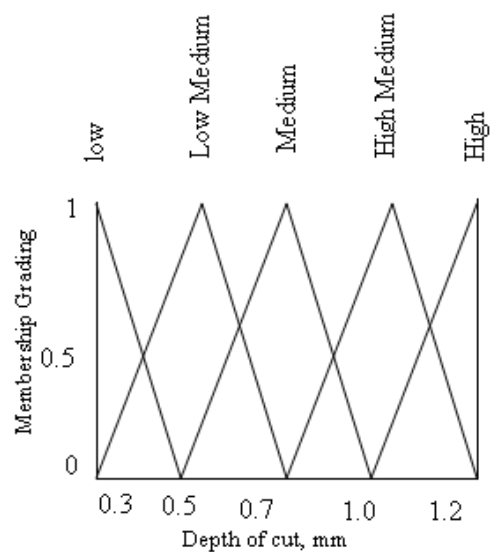


Figure 4: Membership function and their ranges for depth of cut.

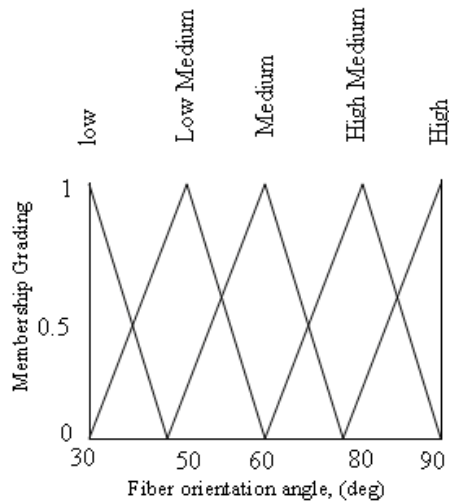


Figure 5: Membership function and their ranges for fiber orientation angle.

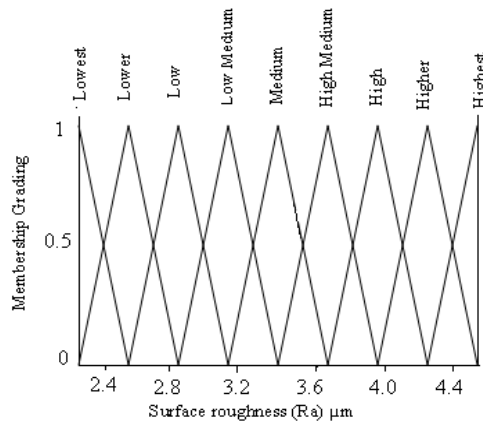


Figure 6: Membership function and their ranges for output response surface roughness.

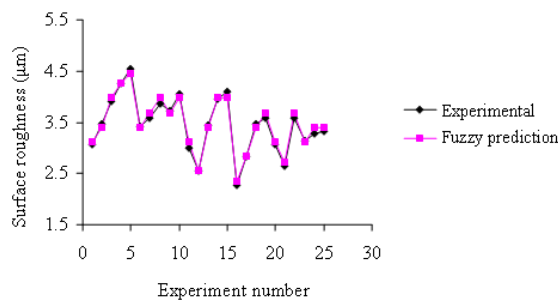


Figure 7: Comparison of experimental results and fuzzy output for Ra.

4. Results and Discussion

Surface roughness plays a predominant role in determining the turning accuracy. The study of surface roughness characteristics of GFRP composites dependent on many factors, it is more influenced by the cutting parameters like cutting speed, feed, depth of cut, etc., for a given machine tool and work piece set-up. The influence

of different cutting parameters on turning of GFRP composites can be studied by using response graph and response table. Figure 8 shows the influence of cutting parameters on surfaces roughness. The observed surface roughness at high cutting speed is low as compared to low cutting speed. The experimental results indicated that the surface roughness parameter is low at low feed as compared to the high feed. The effect of depth of cut on turning of GFRP composite indicated that the surface roughness reduces with increase of depth of cut. The experimental results indicated that low surface roughness is observed for low fiber orientation angle as compared to high fiber orientation angle. The response table for surface roughness, table 3 shows the effect of different cutting parameters. From the response table, it can be asserted that feed is the main parameters which affect the surface roughness.

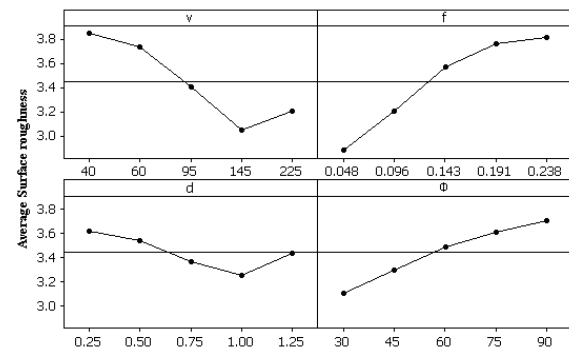


Figure 8: Effect plot for surface roughness.

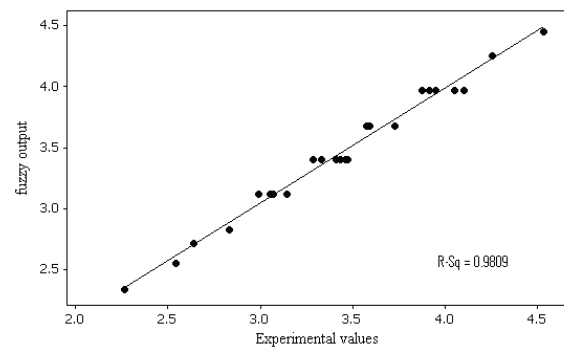


Figure 9: Correlation graph for Ra.

The modeling of machining parameters for surface roughness in turning of GFRP composites is carried out by fuzzy logic. Fig. 9 shows the correlation graph for experimental values and observed values. The adequacies of the developed models have been verified through R-Sq values, which are presented in the figures. The quantity R-Sq is called as coefficient of determination and is used to judge the adequacy of the models developed. In the present case the coefficient of determination is 0.9809 for Ra which shows high correlation that exists between the models and experimental results and hence fuzzy logic can be effectively used for the prediction of surface roughness in turning of GFRP composites. Fig 10 (a) - (e) shows the microstructure of machined GFRP composite specimen in which the distribution of fibers in the polymer matrix can be seen.

For confirmation of the fuzzy logic rule based modeling technique, verification tests were conducted at three different selected conditions. Fig 11 shows the test results for surface roughness (Ra), from the results it can be inferred that the variation between experimental results and model are within the limit and are very close to each other and hence fuzzy modeling technique can be effectively used for prediction of surface roughness parameters in turning of GFRP composites.

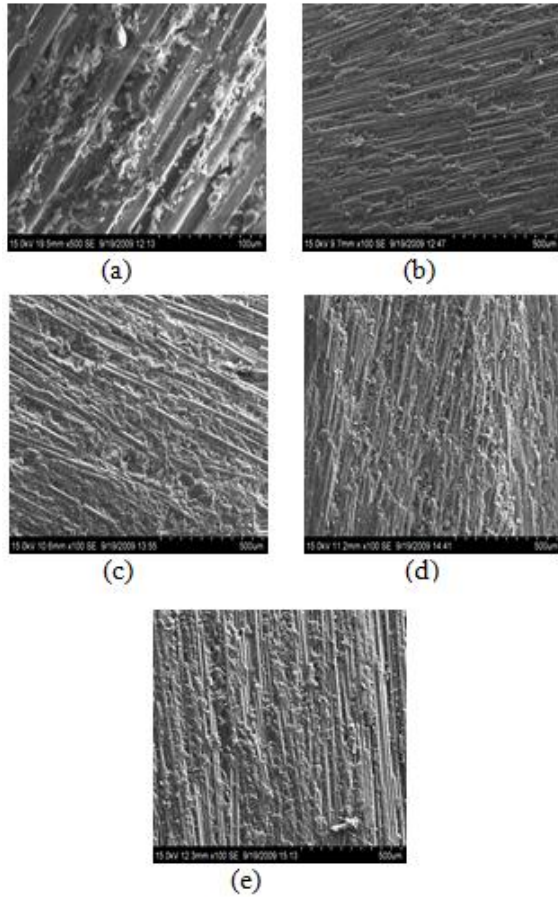


Figure 10: (a) – (e): Microstructure of machined GFRP composite.

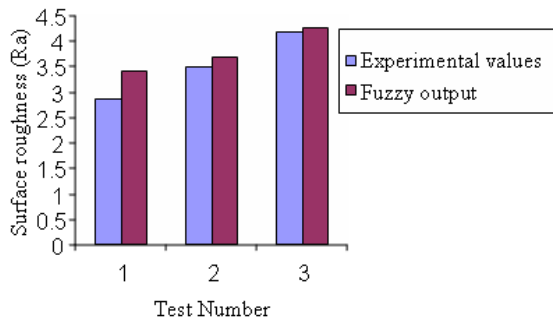


Figure 11: Verification Test Results for Surface roughness (Ra).

5. Conclusions

Experiments are conducted for modeling the surface roughness parameter Ra in turning of GFRP composites. Taguchi’s orthogonal array L25 design of experiments has been used for experimentation. Fuzzy rule based model has been developed for predicting the surface roughness in turning of GFRP composites. Based on the experimental and fuzzy modeling results, the following conclusions are drawn.

- Rule based fuzzy logic model for surface roughness is developed from the experimental data. The predicted fuzzy output values and measured values are fairly close to each other, which indicate that the fuzzy logic model can be effectively used to predict the surface roughness in turning of GFRP Composites.
- In machining of GFRP composites, increase in cutting speed and depth of cut reduces the surface roughness, where as the increase in feed and fiber orientation angle increases the surface roughness
- The feed is the dominant parameter which affects the surface roughness of GFRP composites, followed by cutting speed, fiber orientation angle. Depth of cut shows a minimal effect on surface roughness compared to other parameters.
- The confirmation experiment reveals that the developed model can be effectively used for predicting the surface roughness (Ra) in turning of GFRP composites.
- The accuracy of prediction by fuzzy model can be further improved by increasing the number of membership functions.
- Further improvement of model can be possible by introducing more number of variables and wider range of cutting conditions.
- The technique used is simple and can be used as an on-line monitoring tool, if proper equipments are used. This model can reduce the tedious model making, computational cost and time.

Acknowledgements

The authors are highly thankful to M/s ICP India (P) Limited, Bangalore for supplying the GFRP pipes used in this work.

References

- [1] D.H Wang, M. Ramulu and D.Arola. Orthogonal cutting mechanisms of graphite / epoxy composites. Part I: Unidirectional laminate. *Int. J. Mach. Tools Manufact*: 35 (12), 1995,1623-1638.
- [2] A. Koplev, A. Lystrup, T. Vorm The cutting process, chips and cutting forces in CFRP composites, 14(4): 1983, 371-376.
- [3] K.Sakuma and M.Seto 'Tool-Wear in cutting glass-fiber – reinforced –plastics (the relation between fiber orientation and tool wear)' *Bulletin of the JSME*, 26(218): 1983, 1420-1427.
- [4] W. Koning, Ch. Wulf, P. Grab, H.Willerscheid turning of fiber reinforced plastics, *Annals of the CIRP*, 34: 1985, 537-548.
- [5] Santhana krishanan .G. Krishnamoorthy R, Malhotra. S.K, "Machinability Characteristics of fiber reinforced plastics . Composites", *Journal of Mechanical Working Technology*, 17, 1988 195-204.
- [7] Else Eriksen Influence from production parameters on the surface roughness of machined short fiber reinforced plastics composites, *Int. J. Mach. Tools Manufact*, Vol.39, 1999,1611-1688.
- [8] M.S. Phadke, *Quality engineering using robust design*, Prentice-hall. Englewood Cliffs, NJ, 1989.
- [9] S.H. park, *Robust design and Analysis for quality engineering*, Chapman & Hall, London, 1996.
- [10] L.Zadeh "Fuzzy sets, information and control" Vol.8, 1965,338-353.
- [11] K.Hasmi, I.D. Graham and B. Mills fuzzy logic based data selection for the drilling process, *Journal of Material Processing Technology*108: 2000, 55-61.
- [12] Suleyman yaldiz, Faruk Unsacar and Hasi Saglam, Comparison of experimental results obtained by designed dynamometer to fuzzy model for predicting cutting forces in turning, *Materials & Design* 27, 2006, 1139-1147.
- [13] Yue Jiao, Shuting Lei,Z.I. Pci and F.S. Leo Fuzzy adaptive networks in turning process modeling: Surface roughness prediction for turning operations. *International Journal of Machine Tool & Manufacture*, 44: 2004, 1043-1651.
- [14] Ross PJ Taguchi techniques for quality engineering. Mc Graw- Hill, New yark., 1996.
- [15] K. Palanikumar, Cutting parameters optimization for surface roughness in turning of GFRP composites using Taguchi's method, *Journal of Reinforced Plastics and Composites*, 25 (16): 1739-1751.
- [16] Oguzhan Yilmaz, Omer Eyericioglu, and Nabil, N.Z Gindy, "A user-friendly fuzzy-based system for the selection of electro discharge turning process parameters, " *Journal of Material processing Technology*" vol.172, 2006, 363-371.
- [17] J. Sr. Jang, C.T. Sun, and E. Mizutani, "Neuro-fuzzy and soft computing- a computational approach to learning and machine intelligence", person Education, 2005.
- [18] J.L Lin, K.S. Wang, B.H.yan and Tarnq, "Optimization of the electrical discharge turning process based on the Taguchi method with fuzzy logic, " *Journal of materials Processing Technology*, vol.102, 2000, 48-55.

Modeling Stock Market Exchange Prices Using Artificial Neural Network: A Study of Amman Stock Exchange

S. M. Alhaj Ali^{*a}, A. A. Abu Hammad^b, M. S. Samhouri^a, and A. Al-Ghandoor^a

^aIndustrial Engineering Department, Faculty of Engineering, Hashemite University, Zarqa 13115, Jordan

^bCivil engineering Department, College of Engineering, Applied Science University, Amman 11931, Jordan

Abstract

Stock market represents an essential part of the economy in the Middle East, it is significant for shareholders and investors to estimate the stock price and select the best trading opportunity accurately in advance. This paper utilizes artificial neural network in the modeling of stock market exchange prices. The network was trained using supervised learning. Simulation was conducted for seven case study companies from Amman Stock Exchange representing both the service and manufacturing sectors. The case study companies were selected from different categories varies according to the degree of stock market stability. The model was evaluated by stock market brokers through the use of a questionnaire that was distributed in Amman Stock Exchange, the majority of the participants found the results acceptable. The use of ANN provides fast convergence; high precision, and strong forecasting ability for real stock prices which it turn will bring high return and reduce potential loss to stock brokers.

© 2011 Jordan Journal of Mechanical and Industrial Engineering. All rights reserved

Keywords: Artificial Neural Network; Supervised Learning; Simulation; Stock Market; Amman Stock Exchange; Prediction

1. Introduction

Stock market is the market involved with the issuance and trade of shares either through exchanges or over-the-counter which is also known as equity market, it provides companies with access to capital and investors with a segment of ownership in the company and the prospective of gains based on the company's future performance [1-2].

Stock market represents an essential part of the economy in the Middle East; however, stock markets in the Middle East are usually small and deeply regulated. Lack of reliable information, insider trading, accounting practices, and governments interference are among the problems that are encountered by investors. Some Middle East markets have limit foreigners to invest in the stock market except in some bourses, as those of Egypt, Lebanon, and Israel [3].

Apparently, it is significant for shareholders and investors to estimate the stock price and select the best trading opportunity accurately in advance. This will bring high return and reduce potential loss to investors. Traditional methods for stock price forecasting are based on the statistical methods, intuition, or on experts' judgment. Time series analysis, Autoregressive Moving Average (ARMA) models, Autoregressive Conditional Heteroskedasticity (ARCH) models, and Autoregressive Integrated Moving Average (ARIMA) models [4] are usually used for forecasting the stock market prices, however, their performance depends on the stability of the prices (i. e. if the prices time-series exhibits memory), as more political, economical and psychological impact

factors get into the picture, the problem becomes non linear, and need a more heuristic or nonlinear methods like ANN, Fuzzy logic and Genetic Algorithms [5-6].

Jordanian stock market faces continuous fluctuating values due to political and economical factors; it also witnesses a noticeable sharp growth in the last few years. Thus, it is imperative for the Jordanian stock brokers to employ new analysis tools. The motivation of this research was to introduce the concept of ANN into the Jordanian business sector and utilize it in forecasting the Jordanian stock market prices.

A lot of research had been conducted for using ANN in stock market prices forecasting, Hassoun [7] defines ANN as "parallel computational models comprised of densely interconnected adaptive processing units, they are viable computational models for a wide range of problems including pattern classification

, speech synthesis and recognition, adaptive interfaces, function approximation, image compression, associative memory, clustering, forecasting and prediction, combinatorial optimization, nonlinear system modeling, and control". ANN can outperform other methods of forecasting due to its remarkable ability to derive meaning from complicated or imprecise data, it had been used successfully to extract complex patterns and trends [8]. Literature shows that ANN can be used in prediction, classification, data association, data conceptualization, and data filtering [9].

Steiner and Wittkemper [10] had developed a portfolio optimization model embedded in the nonlinear dynamic capital market model based on ANN. An economic approach to the analysis of highly integrated financial markets and econometric methods had been developed by

* Corresponding author. e-mail: souma@hu.edu.jo

Poddig and Rehkugler [11]. Donaldson and Kamstra [12] proposed a methodology for forecasting future stock prices and return volatilities for fundamentally valuing assets such as stocks and stock options.

2. Amman Stock Exchange

Amman Stock Exchange (ASE) is a private non-profit institution with administrative and financial autonomy that was established in March 1999 and authorized to function as an exchange for the trading of securities by a board of directors. It includes in its membership 70 Jordanian brokerage firms. The ASE is an active member of the Union of Arab Stock Exchanges, Federation of Euro-Asian Stock Exchanges, World Federation of Exchanges, and an affiliate member of the International Organization for Securities Commissions [13].

3. ANN Mathematical Model

The neuron can be modeled mathematically as shown in Fig. 1, where:

The cell inputs are $x_1(t), \dots, x_n(t)$

The cell output is $y(t)$

The dendrite or input weights are v_1, \dots, v_n

The firing threshold or bias weight is v_0

The cell function or activation function is f

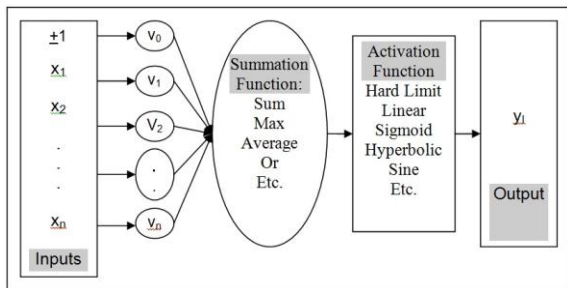


Figure 1: Neuron mathematical model.

The output can be expressed as [14]:

$$y(t) = f\left(\sum_{j=1}^n v_j x_j(t) + v_0\right). \tag{1}$$

Eq. (1) can be streamlined by defining the augmented column vector of the cell inputs $\bar{x}(t) \in \mathfrak{R}^{n+1}$ and the input weights $\bar{v}(t) \in \mathfrak{R}^{n+1}$ as [14]:

$$\bar{x}(t) = [1 \quad x_1 \quad x_2 \quad \dots \quad x_n]^T, \quad \bar{v}(t) = [v_0 \quad v_1 \quad v_2 \quad \dots \quad v_n]^T \tag{2}$$

Then Eq. (1) can be written in matrix notation as [14]:

$$y = f(v^T x). \tag{2}$$

One layer ANN is commonly used which has L cells, all fed by the same input signals $x_j(t)$, and producing one

output per neuron $y_l(t)$. This network can be modeled as [14]:

$$y_l = f\left(\sum_{j=1}^n v_{lj} x_j + v_{l0}\right); l = 1, 2, \dots, L. \tag{4}$$

However, most of the ANN consists of more than one layer, where the second layer input is the first layer output and so on. The cases presented in this paper needed two and three layers, the output for the network consists of three layers can be written based on Eq. (4) as follows:

$$y_l = f_3\left(\sum_{k=1}^{n_3} v_{kl} f_2\left(\sum_{o=1}^{n_2} v_{ko} f_1\left(\sum_{p=1}^{n_1} v_{op} x_p + v_{jo}\right) + v_{k0}\right) + v_{l0}\right) \tag{5}$$

Where:

f_1, f_2, f_3 : are the activation functions for layer 1, layer 2, and layer 3 respectively.

n_1, n_2, n_3 : are the number of input signals for layer 1, layer 2, and layer 3 respectively.

L: is the number of outputs for layer.

$v_{n_2 n_1}, v_{n_3 n_2}, v_{L n_3}$: are the input weights for layer 1, layer 2, and layer 3 respectively.

$v_{n_2 0}, v_{n_3 0}, v_{L 0}$: are the bias weights for layer 1, layer 2, and layer 3 respectively.

$l = 1, 2, \dots, L$.

The network used for stock market prices forecasting model build from two or three layers, 13 inputs and only one output; the variables of Eq. (5) were set as follows:

y : The price in JD's for the 14th working day of the month.

$x_1 - x_{13}$: The stock market prices for the first 13th days of the month.

The other variables were set according to the case study.

4. Training an ANN

Once a network has been structured for a particular application, that network is ready to be trained. To start this process the initial weights are chosen randomly. Then, the training, or learning, begins.

There are three approaches to training or learning: Supervised learning, unsupervised learning, and reinforcement learning. The vast bulk of networks utilize supervised learning. Unsupervised and reinforcement learning are used to perform some initial characterization on inputs. However, in the full blown sense of being truly self learning, it is still just a shining promise that is not fully understood and in need for further research.

4.1. Supervised Learning:

Supervised learning, or learning with a teacher, or associative learning is where the network is supplied with a training data set that includes a set of inputs and its corresponding output or target, ANN adjusts their weights using one observation at a time. Learning is achieved by

minimizing a criterion function which is the average square error between the network outputs and the target.

4.2. Reinforcement Learning:

The learning process in reinforcement learning is designed to maximize the expected value of a criterion function by using trial and error. That is if the action improves the state of affairs then the tendency to produce this action is reinforced while if it deteriorate the state of affairs, then the tendency to produce it is weakened [7]. The training data does not includes a target; instead, it includes a performance judge or a utility function that reports how good the current network output [15].

4.3. Unsupervised learning:

In this case the network is adapted without giving it any kind of directive feed back, in other words there are no target information in the training data or a performance judge, rather the learning objective is to find out the features inherent in the training data [16-18].

Stock market forecasting is done by approximating the function or the relationship between inputs and output, thus supervised learning is more appropriate for our application compared to the other two, furthermore, supervised learning is more mature and accurate than the other two learning approaches.

5. Simulation Results

To test the efficiency and effectiveness of the model a Software program was developed using MATLAB for this purpose. The weights and biases of the network were automatically initialized to small random numbers by the software. Seven Jordanian companies from different sectors were used as case studies. For each company, a full year was used for training the network; each month was used as a different pattern. The data starting from February and ending with January were used for the training; the validation was done by using the next year prices starting from February and ending with January.

Different training functions, activation functions, number of layer, and number of neurons were tried till the error converged to the set value which is 10^{-6} . The performance function used was the mean square error (MSE). MSE is the average squared error between the network outputs and the target.

5.1. Case 1: Arab Engineering Industry

The training was done using one step secant backpropagation, a two layers network was used with Hyperbolic tangent sigmoid activation function for the first layer and hard limit activation function for the second layers, the first layers consists with 14 neurons and 1 neuron for the second layer. The stock market prices for this company during the year in Jordanian Dinars (JD) are shown in Fig. 2, after entering these data into the simulation software, the error resulting during the training is shown in Fig. 3. As shown in the figure the network was able to train the data with 9.7245×10^{-7} in only 11 epochs. To put things into perspective, the output of the network is plotted against the target as shown in Fig. 4, after the network passed the validation stage, the network was used

to forecast the prices for the next year starting from February till January, Fig. 5 reveals the forecasted prices against the actual prices, as shown in the figure the forecasted price is very close to the actual one.

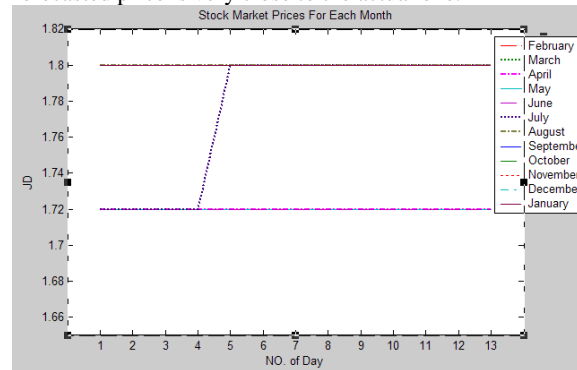


Figure 2: Stock market prices for Arab Engineering Industry Company.

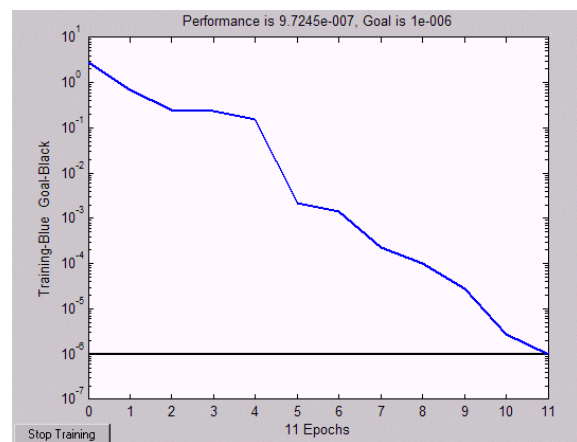


Figure 3: Training error for Arab Engineering Industry Company.

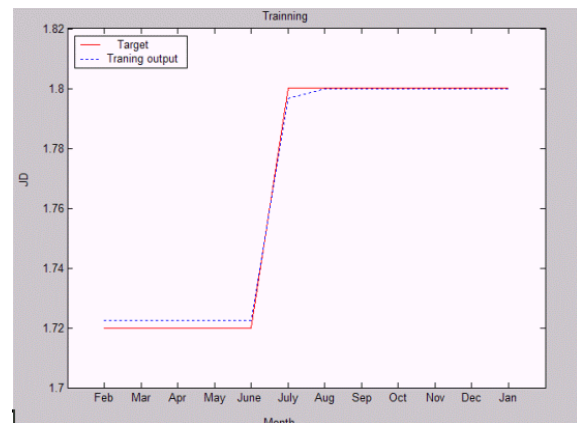


Figure 4: Training output against the target for Arab Engineering Industry Company.

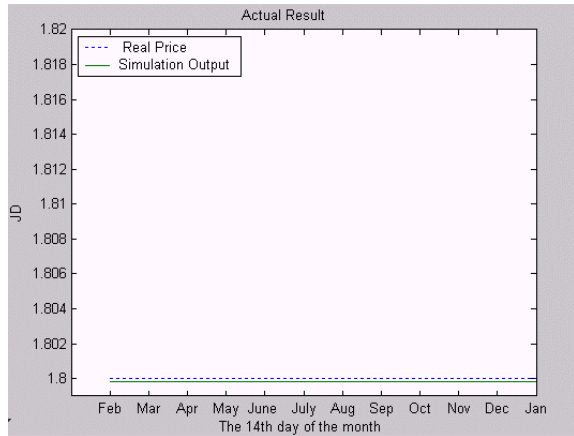


Figure 5: Forecasted prices against the actual prices for the Arab Engineering Industry Company.

5.2. Case 2: Nutriadar: Jordanian Drug Company:

The same training function was used, however, this time three layers contain (14,10,1) neurons respectively was needed to converge to a small training error, the first and second layers used positive linear transfer activation function, while the third layer used a hard limit transfer activation function. The stock market prices for this company are shown in Fig. 6, as revealed from the figure this company exhibit a noticeable variation of the prices among days in each month, which make the forecasting job more difficult, after entering these data into the simulation software, the error resulting during training is shown in Fig. 7. As shown in the figure the network was able to train the data in 1000 epochs that took only 30 seconds. The output of the network is plotted against the target as shown in Fig. 8, the figure prove that the network output matches the actual prices, after the network passed the validation stage, the network was used to forecast the prices for the next year, Fig. 9 reveals the forecasted prices against the actual prices. This time the forecasted price was slightly different than the actual prices, however, the gap did not exceed .08 JD (1 JD=\$1.40).

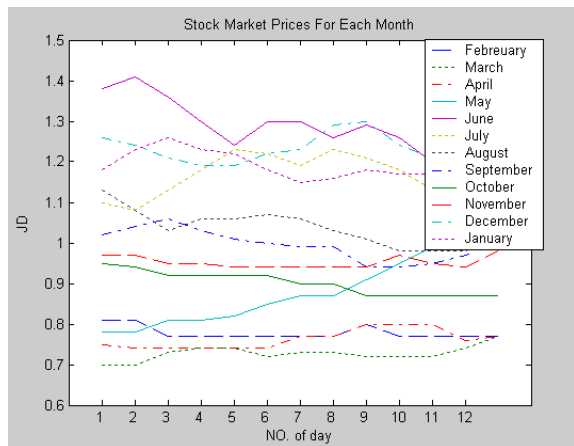


Figure 6: Stock market prices for the Nutriadar Company.

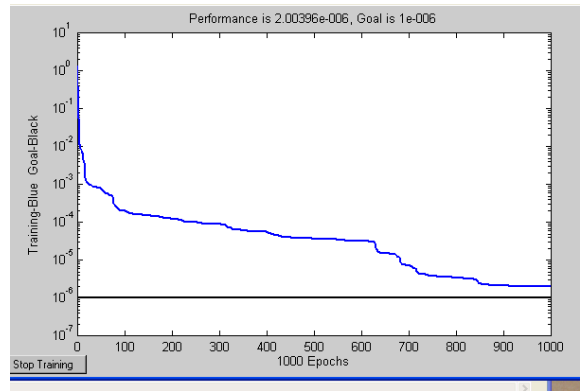


Figure 7: Training error for the Nutriadar Company.

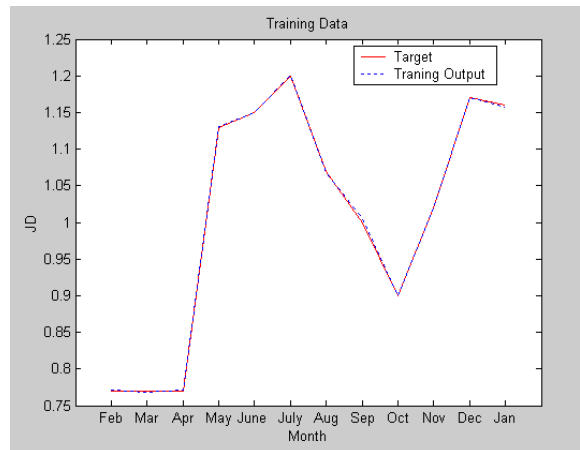


Figure 8: Training output against the target for the Nutriadar Company.

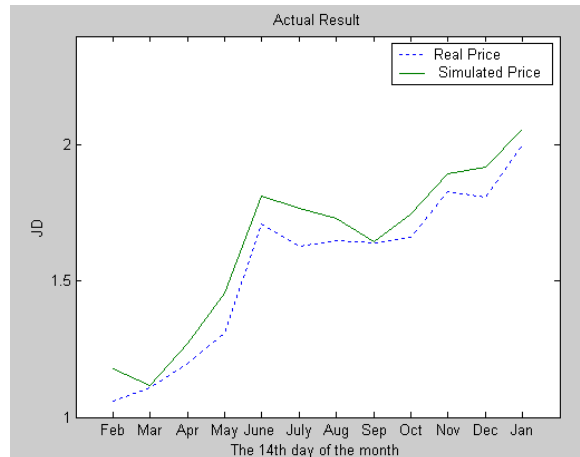


Figure 9: Forecasted prices against the actual prices for the Nutriadar Company.

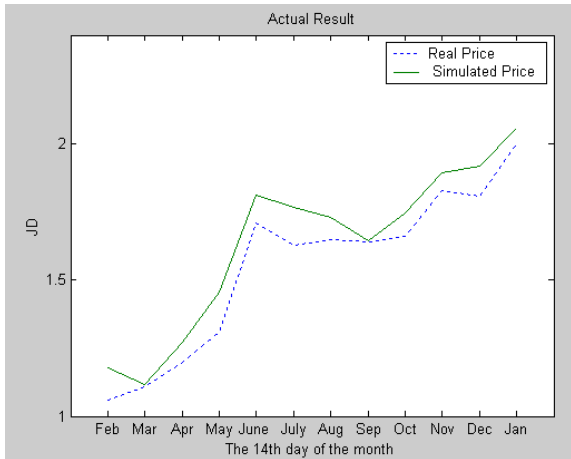


Figure 9: Forecasted prices against the actual prices for the Nutriadar Company.

5.3. Case 3: Jerusalem Insurance Company:

The training was done using one step secant backpropagation, two layers contain (14,1) neurons respectively was needed to converge to a small training error, the first layer used positive linear transfer activation function, while the third layer used a hard limit transfer activation function. The stock market prices for this company are shown in Fig. 10, as revealed from figure, the stock prices vary during the months, its also varies from month to another, after entering these data into the simulation software, the error resulting during the training is shown in Fig. 11. As shown in the figure the network took 174 epochs and 20 second to reach a performance level of 10^{-8} . The output of the network is plotted against the target as shown in Fig. 12, the network output is very close to the actual prices, after the network passed the validation stage, the network was used to forecast the prices for the next year, Fig. 13 reveals the forecasted prices against the actual prices. This time the forecasted prices are close to the actual prices.

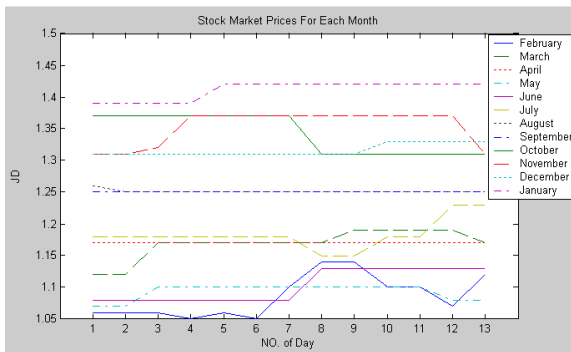


Figure 10: Stock market prices for Jerusalem Insurance Company.

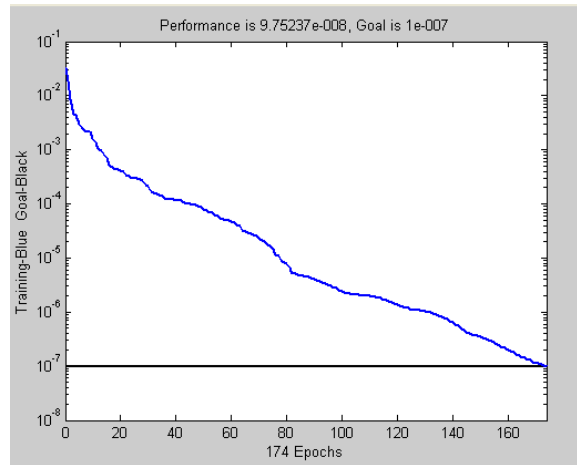


Figure 11: Training error for Jerusalem Insurance Company.

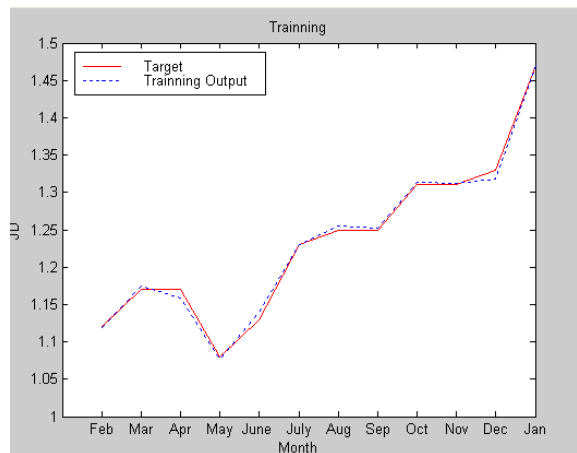


Figure 12: Training output against the target for Jerusalem Insurance Company.

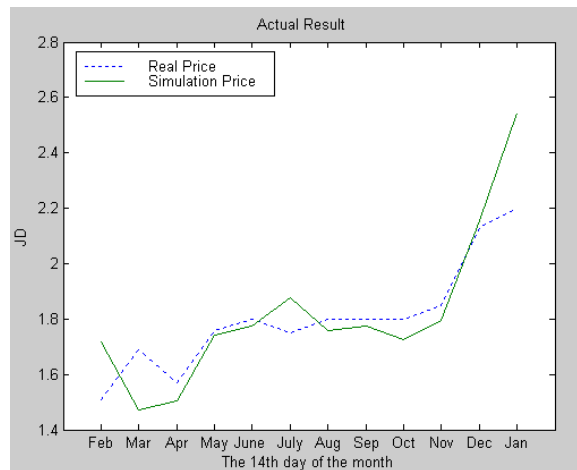


Figure 13: Forecasted prices against the actual prices for Jerusalem Insurance Company.

5.4. Case 4: United Glass Industries:

The training was done using one step secant backpropagation, two layers contain (14, 1) neurons respectively was needed to converge to a small training error, a two layers network was used with Hyperbolic tangent sigmoid activation function for the first layer and hard limit activation function for the second layers. The stock market prices for this company during the year is shown in Fig. 14, which shows that the stock prices are very stable, its varies from month to another but in very small amount (maximum change was 0.050 JD), entering these data into the simulation software resulted in an error of 10-7 in only 10 epochs as shown in Fig. 15. The output of the network is plotted against the target as shown in Fig. 16, the network output matches exactly the actual prices, after the network passed the validation stage, the network was used to forecast the prices for the next year, Fig. 17 reveals the forecasted prices against the actual prices. The forecasted prices are very close to the actual prices except for the last month (January) where the actual price has a small drop.

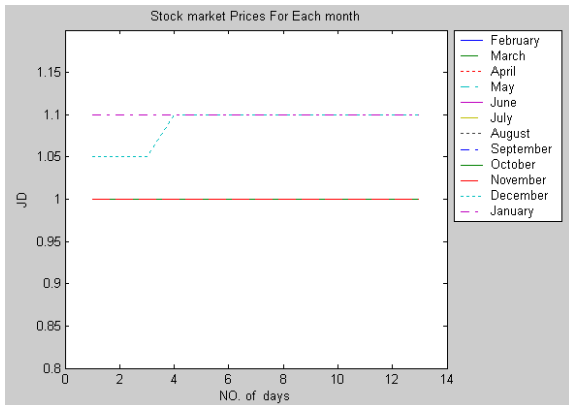


Figure 14: Stock market prices for United Glass Industries Company.

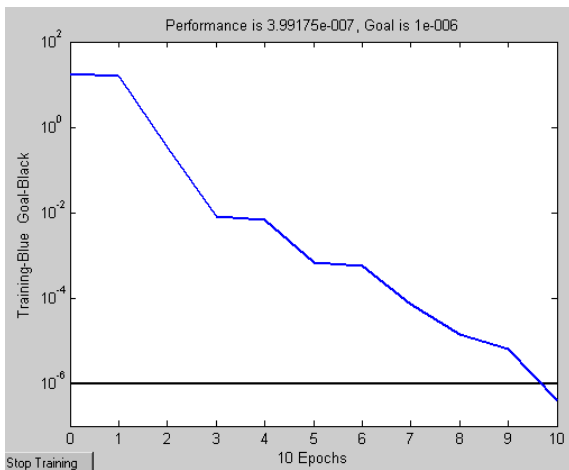


Figure 15: Training error for United Glass Industries Company.

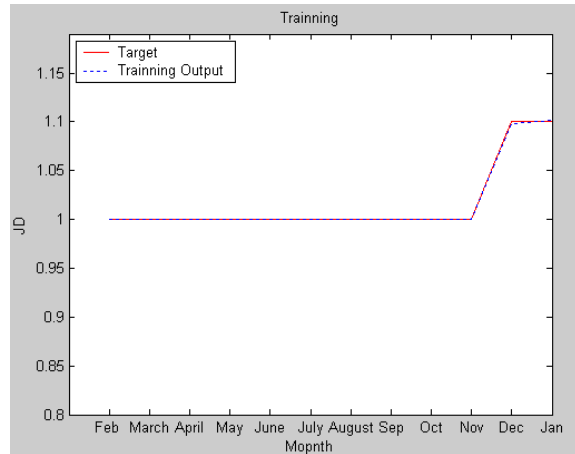


Figure 16: Training output against the target for United Glass Industries Company.

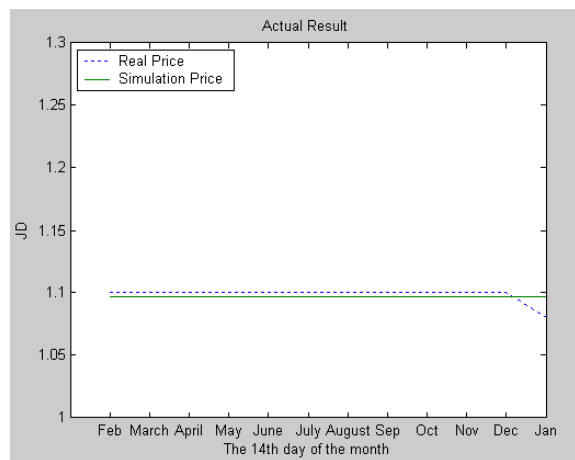


Figure 17: Forecasted prices against the actual prices for United Glass Industries Company.

The rest of the seven case studies were very close to the ones presented before where the network was able to train very quickly the data and produce a very good forecast, except for one case that will be presented next.

5.5. Case 7: Jordan Petroleum Refinery:

A three layers ANN was used in this case of (14,7,1) neurons on the three layers, the training was done using one step secant backpropagation, the first and second layers used positive linear activation function, while the third layer used hard limit activation function. The stock market prices for this company during the year are very volatile and vary substantially from month to month or even during the same month as shown in Fig. 18. The performance level could reach 10-3 within 90 second through 1000 epochs.

After 1000 epochs, the training mean square error was 10-3 which is far from the specified error of 10-6 as shown in Fig. 19. The output of the network is plotted against the target as shown in Fig. 20, this time the network output slightly differs from the target, although it exhibits the same pattern, finally, using the network to forecast the prices of the next year resulted in very good forecast for the first four months (February-June) as shown in Fig. 21, after June the actual prices jumps from 15 JD's to 4 JD's, the forecasted prices jumps too at the same time but with different amplitude (from 14 to 1 JD) then it follow the

same pattern of the actual price but with a gap that is less than 2 JD's. Further investigation into this case reveals that the company broke the shares in order to increase the supplied quantity of them which caused the prices to drop to 3 JD's.

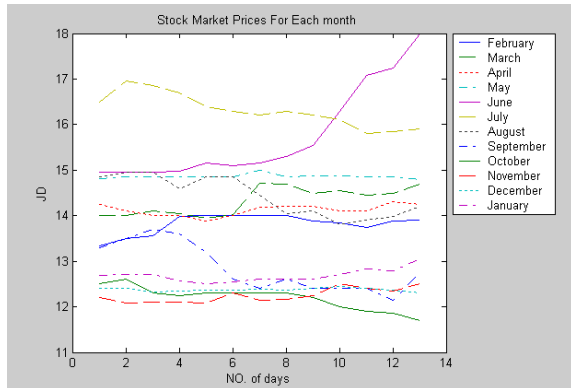


Figure 18: Stock market prices for Jordan Petroleum Refinery Company.

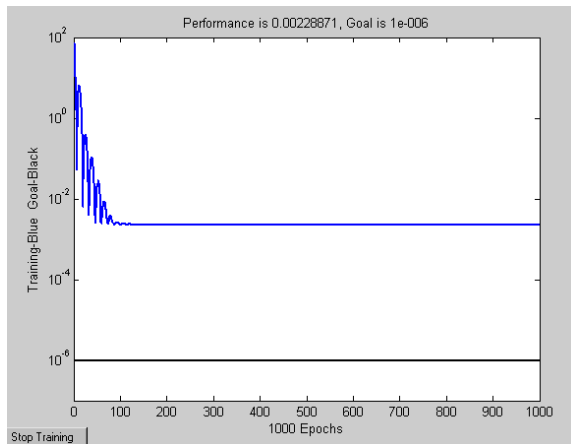


Figure 19: Training error for Jordan Petroleum Refinery Company.

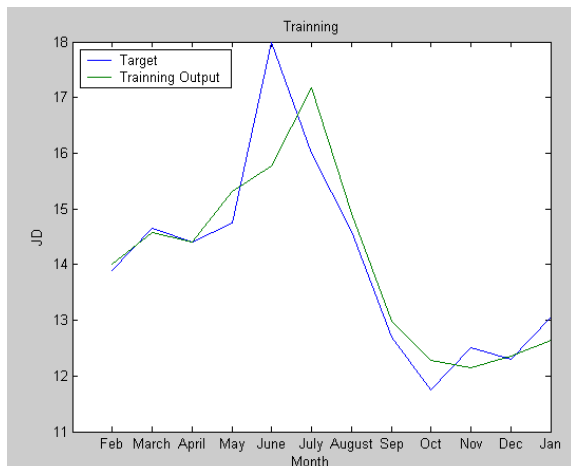


Figure 20: Training output against the target for Jordan Petroleum Refinery Company.

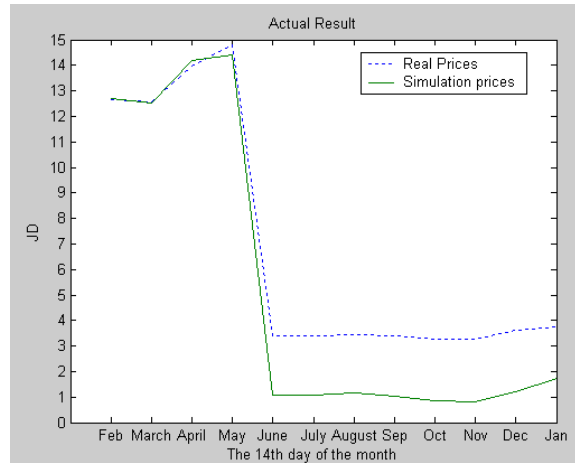


Figure 21: Forecasted prices against the actual prices for Jordan Petroleum Refinery Company.

6. Discussion

The results obtained from the software were very accurate for six out of seven cases, which prove that this is a valid technique for stock market price forecasting.

In the last case the results shows that although the network did not give a good forecast due to the significant drop in the actual Stock market prices but it followed the same pattern of the actual price, which means that even when the actual stock prices change dramatically for any assignable cause, the network was able to catch up and the forecast change at the same month and even with the same pattern as the actual data. This proves that this method can give a very good indication about market trends.

7. Model Evaluation by Stock market brokers

The model was evaluated by stock market brokers through the use of a questionnaire that was distributed in Amman Stock Market, the questionnaire was designed so that it can be filled in no more than two minutes, it first presents the forecasting results obtained from the network and then asked the participant to answer seven multiple choice questions, focus on the techniques currently used by the broker, and whether he want to use the network in the future, only seven questionnaires were returned.

In response to a question asking “Would you depend on the ANN technique for forecasting Amman Stock Market prices?”, five out of the seven participants who answered the questionnaires stated that they would depend on ANN technique, while two of them stated that they would partially depend on ANN technique.

In response to another question “Do you believe that this technique will be applicable to all categories of companies (volatile, stable)?”, six participants decided that the ANN technique will be applicable to all companies categories, while one participants believed that it is not applicable to all categories of companies.

8. Conclusions

This paper utilizes artificial neural network in the modeling of stock market exchange prices. The model was developed using a feed forward neural network with two to three layers; the network was trained using one step secant backpropagation, the activation functions used were hyperbolic tangent sigmoid, positive linear and hard limit transfer function. Simulation software developed by MATLAB was used to evaluate the network performance for seven Jordanian companies selected from service and manufacturing sectors. The companies have different degree of stock prices stability. The network was trained on a whole year data; the network was able to produce the output within a MSE of 0.0023×10^{-8} from the target. The network performance was evaluated using the stock market prices of the following year, the network output

was very close to the actual data, except for one case, for which the company broke its shares in the middle of the year, however, even in that case the network output drops dramatically to values close but not exactly the same as the ones of the actual data. The results of the network were further evaluated by stock brokers from Amman stock market; the majority of the responses stated that they may depend on ANN technique and that they believe that the technique is applicable to all categories of companies.

The model is significant in view of the fact that stock market represents an essential part of the economy in the Middle East. Using the developed ANN model can help shareholders and investors to estimate the stock price and select the trading chance that will maximize their profits more accurately in advance compared to the currently used methods.

References

- [1] Hagstrom R G, Miller B. *The Essential Buffett: Timeless Principles for the New Economy*. 1st ed. John Wiley & Sons Incorporated; 2002.
- [2] Investopedia ULC. *Investopedia Dictionary*. Investopedia a Forbes digital company; 2009; <http://www.investopedia.com/terms/s/stockmarket.asp>.
- [3] Mattar Ph. *Encyclopedia of the Modern Middle East and North Africa*. 2nd ed. USA: Macmillan Library Reference; 2004.
- [4] Mills T C. *Time Series Techniques for Economists*. Cambridge University Press, 1997.
- [5] Greene W H. *Econometric Analysis*. 5th ed. Prentice Hall; 2003.
- [6] InvestorWords. InvestorGuide.com, Inc. 2005; <http://www.investorwords.com>.
- [7] Hassoun M H. *Fundamentals of Artificial Neural Networks*. USA: Massachusetts Institute of Technology Press; 1995.
- [8] C. Stergiou, D. Siganos, "Neural networks". *Surprise Journal*, Vol. 14, 1996.
- [9] Anderson D, McNeil G. *Artificial Neural Networks Technology*. NY: Rome NY, Rome Laboratory; 1992.
- [10] M. Steiner and H. G. Wittkemper, "Theory and Methodology: Portfolio optimization with a neural network implementation of the coherent market hypothesis". *European Journal of Operational Research*, Vol. 100, 1997, pp. 27-40.
- [11] T. Poddig and H. Rehkugler, "A 'world' model of integrated financial markets using artificial neural network". *Neurocomputing*, Vol. 10, 1996, pp. 251-273.
- [12] Donaldson R G, Kamstra M. *Forecasting Fundamental Stock Price Distributions*. Canada: University of British Columbia; 2000.
- [13] Amman Stock Exchange, About ASE, <http://www.ammanstockexchange.net/>, 2008.
- [14] Lewis F L, Jagannathan S, Yesildirek A. *Neural Network Control of Robot Manipulators and Nonlinear Systems*. Padstow, UK: Taylor and Francis Ltd, T. J. International Ltd; 1999.
- [15] Sethi K, Jain A K. *Artificial Neural Networks and statistical Pattern Recognition: Old and New Connections*. Amsterdam, Netherlands: Elsevier Science Publishers B. V.; 1991.
- [16] Hassoun M H. *Associative Neural Memories: Theory and Implementation*. New York, USA: Oxford University Press, Inc.; 1993.
- [17] Kohonen T. *Self-Organization and Associative Memory*. 2nd ed. Berlin Heidelberg, Germany: Springer-Verlag; 1988.
- [18] Micheli-Tzanakou E. *Supervised and Unsupervised Pattern Recognition: Feature Extraction and Computational Intelligence*. USA: CRC Press LLC; 2000.

Densification and Deformation Behavior of Sintered P/M Zinc-Zinc Oxide Composite during Cold Upsetting

B. Selvam^{*,a}, A. P. Singh^a

^aDepartment of Mechanical Engineering, Eritrea Institute of Technology, 12344, Mai-Nefhi, Asmara, The State of Eritrea, N.E. Africa

Abstract

Studies were carried out to evaluate the initially preformed density and initial aspect ratio on the densification behavior of sintered Zinc and Zinc Oxide composite. The preform possessed 0.85 is the initial density. Aspect ratio for three different oxidizing temperatures (at 150°C, 200°C and 250°C) varied from 0.4 to 0.85. Properties of Zinc-Zinc Oxide composites with respect to linear strain, lateral strain and true stress were evaluated and plotted. Studies revealed that higher stress and higher strain values are obtained in composite when compared to the Zinc dust. The composite of Zinc-Zinc Oxide obtained at 150°C possessed the highest stress and strain when compared to the composites obtained at others two temperatures (200°C and 250°C).

© 2011 Jordan Journal of Mechanical and Industrial Engineering. All rights reserved

Keywords: Densification; Metal Matrix Composite; Zinc Oxide; Powder Metallurgy; Aspect Ratio; Sintering; Cold Upsetting; Preforms

1. Introduction

The term “composite” broadly refers to a material system which is composed of discrete constituents (the reinforcement) distributed in a continuous phase (the matrix). It derives its distinguishing characteristics from the properties of its constituents, from the geometry and architecture, and also from the properties of the boundaries (interfaces) of its different constituents. Composite materials are usually classified on the basis of physical or chemical nature of their matrix phase, like polymer matrix, metal-matrix and ceramic composites etc. Among the materials that are developed to an increasing extent metal matrix composites.

The space industry was the first sector interested in the usage of these materials. Another sector of even greater economic importance for the development of new metal matrix composites (MMC's) is the automotive industry [1]. The flexibility associated

with MMC's in tailoring their physical and mechanical properties as required by the users have made them suitable candidates for a spectrum of applications related to automobile and aeronautical sectors [2]. The introduction of fine dispersed particles into the metal matrix has significant reinforcing effects when maintained at elevated temperatures [3-7].

Many composites that are used today are at the leading edge of material technology, with performance and costs appropriate to ultra demanding applications such as spacecraft. But heterogeneous materials combining the best aspects of dissimilar constituents are available in nature and are being used as such for millions of years. Powder forging technique is accepted as the most economical and efficient technique leading to pore

elimination and superior mechanical strength. Although several processes are available for producing MMC's, the powder metallurgy technique was found to be the most suitable because it yields better mechanical properties. Zinc Oxide is an amorphous white powder used as a pigment in plastics, paints and primers etc. It is also reported to be the best ultraviolet light absorber of all commercially available pigments.

Research on dispersion strengthened materials points out the significance of the properties of the starting metallic powders and also the importance of the starting structure in preserving the structure of the final product [8]. A very important aspect of dispersion strengthening is the even distribution of oxide particles, their fine dispersion, especially in nanometer scale, and the introduction of a possible amount of dispersed particles into the volume of the base metal.

The powder metallurgy sintered parts possesses 10-30% porosity which can be advantageously used, but the mechanical properties of the component are adversely effected by the presence of porosity [9, 10]. Therefore, the parts intended for dynamic applications, the final compaction should be close (up to about 1-2%) to that of fully dense material. Forging of the sintered preforms result in a precision component with the reduction or elimination of porosity. The reduction in porosity during forging, results in a decrease in preform volume. The yielding of porous materials, thus, does not follow the laws of volume constancy. Further, the ‘material parameters’ (such as, modulus of elasticity and modulus of rigidity) are functions of density of the deforming body and as such the ‘material parameters’ also undergo a variation along with a change in porosity (density).

Initially, there had been some experimental, semi-experimental or analytical approaches using slab method for obtaining the density of porous formed metal parts [11-

* Corresponding author. e-mail: bselvam_spt@yahoo.co.in

16]. Thereafter, several researchers studied the forging of porous materials and billet by using finite element method taking material to be rigidly plastic. An attempt to use numerical method for the analysis of powder metal forging operation has also been studied by various researchers using a rigid plastic approach [17]. Rigid plastic approach could be acceptable for large deformation by excluding the effect of elastic behaviour of the material. Subsequently, there have been some attempts to develop elastic-plastic approach to study the deformation of porous materials [18, 19].

The aim of the present work is to study the mechanics of cold forging of powder metal preforms taking into account its plastic strains as the work material which undergoes deformation. The model developed was applied to study the forging of an axis symmetric short solid cylindrical part under simple upsetting. The analysis was carried out for the press forging with slow rates of deformation where inertia and temperature effects were negligible. The computed results predicted the densification pattern of the work material and the loads required to produce the desired deformation.

2. Problem Formulation

Present investigation focused on the densification behavior of sintered Zinc-Zinc Oxide powders when taken in varying quantities. Frictionless compression tests are used to find out the fundamental plastic flow characteristics of porous metals. Studies reveal that the deformation was uniform with barreling of cylindrical surfaces. The proposed study also carries out to evaluate the initial preformed density and initial aspect ratio on the densification behavior of sintered Zinc-Zinc Oxide composites. The preform possessed 0.85 as initial density and the aspect ratio for three different oxidizing temperatures (150°C, 200°C and 250°C) varied from 0.4 to 0.85. Four preforms, each of different aspect ratio were taken for each temperature.

A critical literature survey reveals that several attempts has been made in producing components through powder metallurgy route, which may contain one or the other type of impurifier. These perhaps could not be verified during the course of several investigations as the fine dispersion of self oxidized material in the component perhaps induced improved properties. A wide variety of research in the area of elemental powder and its own oxide composite has been carried out. But earlier investigations have shown that extruding the sintered preform containing the self oxidized dispersions in different proportions on extrusion may induce improved mechanical properties.

It is well established that in the metal forming operations the deformation is never strictly homogeneous and therefore pores present on the surface of the component can never be closed either due to the predominance of tensile forces or due to hydrostatic forces present in the dead metal zones. Therefore, it is more likely that the particulate structure will be prevalent at the surface of the component irrespective of preform design for any upsetting test.

For studying the behavior of Zinc-Zinc Oxide composite during cold upsetting, mechanical properties should be given priority. In most of the methods adapted for studying the strengthening of the composite, strengthening metal must have higher melting point than matrix metal. In this method, we have developed Zinc

Oxide as a strengthening component, but it possesses higher melting temperature than Zinc (matrix metal). The basic advantage of dispersion strengthened materials is that it does not improve yield strength at ambient temperature or work hardening rate. The present investigation on composite carried out at three different oxidizing temperatures (150°C, 200°C, and 250°C). Duration of treatment was three hours and a single preform density was taken for four different aspect ratios in cold compression test.

3. Experimental Procedure

3.1. Materials Required:

The materials required for this investigation are: Zinc dust for composite preparation, graphite/molebdenum-disulphide for using as lubricant, high carbon-high chromium die steel punch and die, two flat plates heat treated to Rc 52 to 55 and tempered to Rc 45 to 48, a stainless steel tray, and an electric muffle furnace.

3.2. Preparation of Zinc-Zinc Oxide Composite:

For obtaining self oxidizing Zinc-Zinc Oxide powder, the Zinc powder was taken in a steel tray, which was placed in an electric furnace maintained at 150°C for three hours. Thereafter on cooling, the oxidized powder was removed from the furnace and stored carefully. Similarly, the same procedure was followed for making composites at 200°C and 250°C. During this process some portion of the Zinc powder normally gets partially oxidized.

3.3. Grinding of Oxidized Powder:

In oxidized zinc powder, some parts of the Zinc normally contains Zinc Oxide. Generally, the oxide layer possesses an irregular surface; which needs to be changed to regular surface. To shape this irregular layer of oxide, the composite was taken in a clean ceramic bowl and grounded continuously for six hours.

3.4. Compaction of Zinc-Zinc Oxide Powder :

Cold compacts of Zinc-Zinc Oxide are prepared by using high carbon-high chromium steel dies. To avoid sticking of the metal powder to the surface and also to reduce co-efficient of friction due to its high density, graphite was used as lubricant. A known amount of metal powder was poured into the die and the punch was introduced into the die from the top. Thereafter, the whole setup was transferred to 0.60 MN capacities universal testing machine (UTM) for compaction. A load of 18 ton, 20 ton, and 22 ton was gradually applied to get the compacts, thereafter, the compacts were ejected out by removing the butt.

3.5. Aluminium Coating of Samples and Sintering of Coated Samples:

During sintering operation, the sample surface gets changed to oxide. To avoid getting it changed to oxide before sintering aluminium paint was used as an anti-corrosive agent. A total of three consecutive coats applied

each, after drying for minimum 12 hours at room temperature. Sintering was carried out at 390°C for ninety minutes and compacts were allowed to cool in the furnace itself.

3.6. Cold Deformation on Sintered Zinc-Zinc Oxide Composite:

Initial height (H) and diameter (D) of all the composite samples were taken. From initial dimension, H/D ratios were calculated. In UTM, 50 kgf least count was set. Before the deformations were done, graphite was applied as lubricant on both the flat plates as well as on the sample contact surfaces to reduce friction. Samples were deformed starting with 250 kgf and then at subsequent intervals of 250 kgf till cracks on the surface appears. The compressive loads at which fine cracks appeared at the free surfaces of the preforms were recorded. The application of compressive load continued till the cracks became predominant at the top, bottom, bulge and height. Dimensional changes on the compacts due to deformation were measured by means of digital vernier caliper.

4. Results and Discussions

The sintered P/M Zinc-Zinc Oxide composite was made under three different oxidizing temperatures (150°C, 200°C, and 250°C). Cylindrical preforms of four different aspect ratios for each temperature was employed in the compression tests.

Plots were drawn for pure zinc between the hoop strain and the axial strain to compare with composite (Figure 1) and zinc-zinc oxide composite (Figures 2, 3, and 4). The rate of change of hoop strain with respect to axial strain was not the same for all aspect ratios. This indicates that each aspect ratio had different slope and the hoop strain increased with axial strain. Among the three different oxidizing temperatures, sintered preforms oxidized at 150°C had more strain values. Similarly, the aspect ratio of 0.55 also had high strain values when compared with others. From the plots it was also evident that the strain increased with higher aspect ratios. The deformation of the composites is less. Due to the low value of hoop and axial strain, composites have the low ductile property. This composite is more suitable for the compressive load applications.

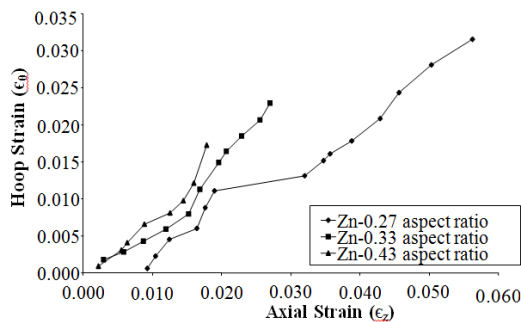


Figure 1: Axial Strain (εz) Versus Hoop Strain (εθ) for Zinc.

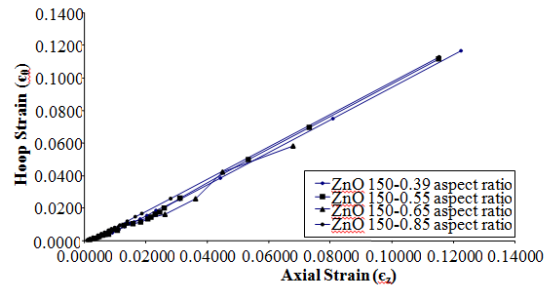


Figure 2: Axial Strain (εz) Versus Hoop Strain (εθ) for 150°C.

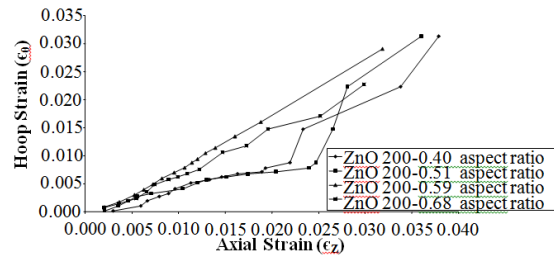


Figure 3: Axial Strain (εz) Versus Hoop Strain (εθ) for 200°C.

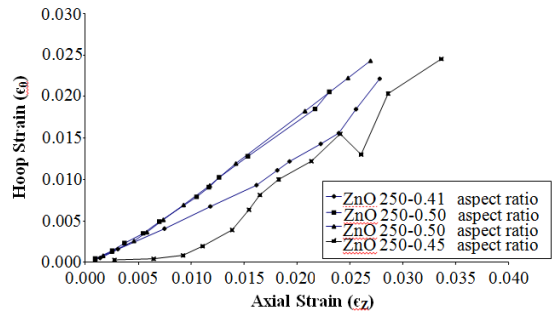


Figure 4: Axial Strain (εz) Versus Hoop Strain (εθ) for 250°C.

Plots between the true stress and true strain are shown in Figures 5 to 8. The stress value of preform increased with true strain. The true stress value improved in the sintered preform compared with pure Zinc. It indicates that lower oxidizing temperature may be suitable for getting Zinc-Zinc Oxide composite with higher performance. However, in Zinc-Zinc Oxide composite oxidized at 150°C, the slope of the curve was found to be the highest among the three different oxidizing temperatures (150°C, 200°C, and 250°C) which decreased with increase in oxidizing temperatures. Studies have further indicated that the true stress value was doubled in sintered preform when compared with pure Zinc.

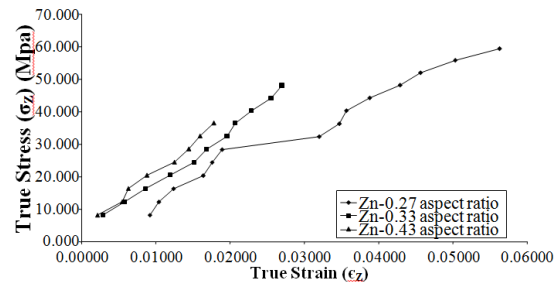
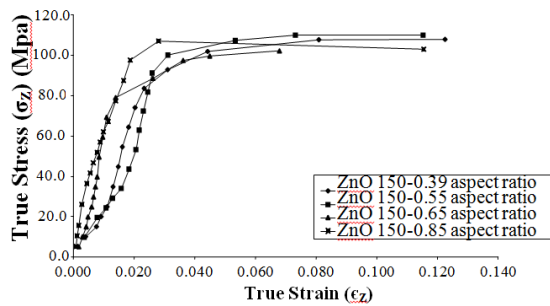
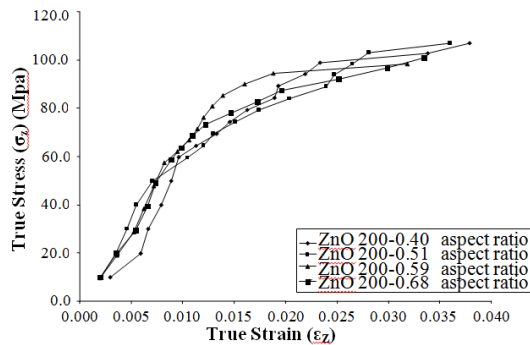
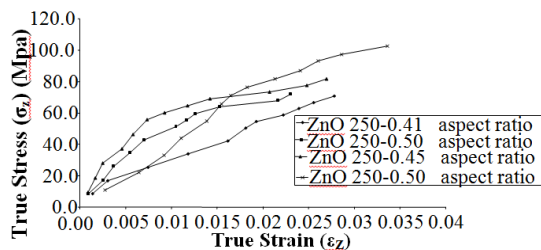


Figure 5: True Stress (σz) Versus True Strain (εz) for Zinc.

Figure 6: True Stress (σ_z) Versus True Strain (ϵ_z) for 150°C.Figure 7: True Stress (σ_z) Versus True Strain (ϵ_z) for 200°C.Figure 8: True Stress (σ_z) Versus True Strain (ϵ_z) for 200°C.

5. Conclusion

The major findings of the present investigations are:

- The rate of change of hoop strain with respect to the axial strain indicated high values for higher aspect ratios at low oxidizing temperature.
- The rate of change of true stress with respect to true strain was different for different aspect ratios.
- Higher aspect ratio had the maximum value of both true stress and true strain than lower aspect ratio in all sintered composites.
- Oxidized composite obtained at 150°C had the highest stress rate as well as strain rate compared with other two temperatures (viz., 200°C and 250°C).

These investigations have indicated that even though we have obtained Zinc-Zinc Oxide composite using low temperature, we did not obtain the composite of a very high strength. This indicates that we may have to conduct further studies to obtain Zinc-Zinc Oxide composite of sufficiently high strength to make it suitable for industrial applications.

References

- [1] J. Eliasson, R. Sandström, "Application of aluminium matrix composites". Key Engineering Materials, 104-107, 1995, 3-36.
- [2] P.S. Gilman, Journal Metallurgy, Vol. 43, No. 8, 1991, 7.
- [3] Y. Wu, Y. Zhang, X. Huang, J. Guo Ceram. Int., Vol. 27, 2001, 265-268.
- [4] P.K. Jena, E.A. Brocchi, M.S. Motta, "In-situ formation of Cu-Al₂O₃ nano-scale composites by chemical routes and studies on their microstructures". Materials Science and Engineering: A, Vol. 313, Issues 1-2, 2001, 180-186.
- [5] D.W. Lee, G.H. Ha, B.K. Kim, "Synthesis of Cu-Al₂O₃ nano composite powder". Scripta Materialia, Vol. 44, Issue 8, 2001, 2137-2140.
- [6] P.K. Jena, E.A. Brocchi, I.G. Solórzano, M.S. Motta, "Identification of a third phase in Cu-Al₂O₃ nanocomposites prepared by chemical routes". Materials Science and Engineering: A, Vol. 371, Issues 1-2, 25, 2004, 72-78.
- [7] C. Skoufadis, D. Panias, I. Paspaliaris, "Kinetics of boehmite precipitation from supersaturated sodium aluminate solutions". Hydrometallurgy, Vol. 68, No. 1, February, 2003, 57-68.
- [8] M.S. Motta, E.A. Brocchi, I.G. Solórzano and P.K. Jena, "Complementary microscopy techniques applied to the characterization of Cu-Al₂O₃ nanocomposites". FORMATEX Microscopy Book Series No. 2 - Current Issues on Multidisciplinary Microscopy Research and Education [ISBN (13): 978-84-609-6605-4/ (10): 84-609-6605-4] 2004, 215-223.
- [9] P. Ramakrishana, "Powder metallurgy-progress and opportunities". Proceedings of National Seminar on Powder Metallurgy-Opportunities for Engineering Industries, IIT Bombay, Vol. 1, 1985.
- [10] P.K. Jhonson, "P/M industry, trends, new technologies propel P/M growth". International Journal of Powder Metallurgy, Vol. 32, No. 2, 1996, 145-154.
- [11] R.J. Green, "A plasticity theory for porous solids". International Journal of Mechanical Science, Vol. 14, 1972, 205-224.
- [12] S. Shima, M. Oyane, "Plasticity theory of porous metals". International Journal of Mechanical Science, Vol. 18, 1976, 285-291.
- [13] T. Tabata, S. Maski, K. Hosokawa, "A yield function for forging of porous metals". International Journal of Powder Metallurgy, Powder Technology, Vol. 16, 1980, 149.
- [14] S.M. Doraivelu, H.L. Gegel, J.C. Malas, J.S. Gunasekera and J.F. Thomas, "A New Yield Function for Compressible P/M Materials". International Journal of Mechanical Science, Vol. 26, No. 9/10, 1984, 527-535.
- [15] H.K. Cho, J. Suh, K.T. Kim, "Densification of porous alloy steel preforms at high temperature". International Journal of Mechanical Science, Vol. 36, 1994, 317-328.
- [16] H.K. Cho, K.T. Kim, J.S. Kim, "Cold compaction of composite powders". Transactions on ASME, Journal of Engineering Materials and Technology, Vol. 122, 2000, 119-128.
- [17] K. Mori, S. Shima, K. Oskada, "Finite element method for the analysis of plastic deformation in porous metals". Bulletin of JSME, Vol. 23, No. 178, 1980, 516-522.
- [18] K.T. Kim, Y.S. Kwon, "Elastic plastic responses of porous iron under uniaxial strain cycling". Transactions on ASME, Journal of Engineering Materials and Technology, Vol. 115, 1993, 89-94.
- [19] K.T. Kim, "Elastic plastic strain hardening responses of porous metals". International Journal of Engineering Science, Vol. 27, 1989, 767-778.

Selection of Temperature Measuring Sensors Using the Analytic Hierarchy Process

T. Al-Hawari^{*a}, S. Al-Bo'ol^a, A. Momani^a

^aIndustrial Engineering Department, Jordan University of Science and Technology, Irbid 22110, Jordan

Abstract

This study presents an analytic hierarchy process (AHP) method to objectively select the best temperature sensor from among different alternative sensors in a certain industrial application. The underlying decision method based on AHP methodology, ranks temperature sensors with different features with a score resulting from the synthesis of relative preferences of each alternative with respect to the others at different levels considering independent evaluation criteria and sub-criteria. At each level, relative preferences of each candidate alternative with respect to the upper immediate level are calculated from pair-wise comparisons among the candidate alternative sensors with respect to a selected application. Pair-wise comparison matrices are compiled based on views of experts in this field. Seven alternative sensors were considered: the thermocouple, the thermister, the resistance temperature detector (RTD), the bimetallic strip thermometer, the mercury-in-glass thermometer, the optical disappearing filament pyrometer, and the liquid crystal display semi conductor thermometer (LCD). Three industrial applications were also considered: Automotives, Chemical Processes, and Heating, Ventilating and Air Conditioning. A case study is conducted which involves selecting the best sensor for an automotive catalytic converter. The thermocouple is found to be the most preferred sensor for this application with the largest score of 0.37849, the second ranked sensor is the RTD with a score of 0.34589, and the least preferred sensor is the thermister with a score of 0.27560. To test the robustness of the proposed work, a sensitivity analysis was conducted in which variations in the relative preferences of the alternative sensors against sub-criteria and criteria were employed.

© 2011 Jordan Journal of Mechanical and Industrial Engineering. All rights reserved

Keywords: Analytic Hierarchy Process; Temperature; Sensor

1. Introduction

Nowadays, we live in a highly competitive industrial environment that imposes stringent measures on product quality and uniformity. This calls for the employment of efficient and accurate process operations with a complete set of automated measurement sensors and control technologies. In this sense, process sensors are the devices that measure process variables, of which temperature in many cases is of high importance and indicative of process progress. The resulting data is used to control and monitor the process, and to take corrective actions if needed [1]. Additionally, process measurement enables better understanding of the process input and output variables and the various relationships that tie up these variables, which is a preliminary step for process improvement and optimization. The final result is reflected on cost minimization and profit maximization which is the final pursuit of an industrial company.

Temperature sensors selection and alternative sensors preferences are mostly based on subjective views and opinions of decision makers or experts in the sensors field. These views remain personal and subjective and may lead to erroneous judgments of the best sensor for a certain industrial application. These judgments vary from one expert to another and are not based on a systematic

approach of the evaluation process. On the other hand, the selection of the best sensor based on AHP, is a systematic way for the evaluation process. It is based on breaking down the decision problem of selecting the best sensor into smaller parts that represent the hierarchical structure levels and their components. These levels range from the lowest level, which is in this case the different alternatives that are to be assessed, to the top most level, which is the final goal; the selection of the best temperature sensor. In between the lowest and the top most levels, lie two levels representing the evaluative criteria and sub-criteria pertaining to sensors selection norms applied in industry. Starting from the lowest level, each alternative sensor is assessed against other alternatives with respect to each sub-criterion in the immediate subsequent level by means of pair-wise comparisons among the different alternatives. Each sub-criterion in the subsequent level is then pair-wise compared against other sub-criteria with respect to parent criterion in the third level; the criteria level. After that, each criterion in the third level is assessed against other criteria with respect to the top most level of the decision hierarchy; the final goal of choosing the best sensor. Finally, the different weights obtained for the different alternatives in the first level are aggregated and lumped together with weights obtained for the criteria and sub-criteria in the third and second levels to come up with overall final scores for different sensors against the overall problem objective. These overall scores are indicative of

* Corresponding author. e-mail: tarek321@hotmail.com

the relative preferences of the sensors against the overall goal. The best sensor with the largest score corresponds to the best (most preferred) sensor and the smallest score corresponds to the worst (least preferred) sensor, and values in between correspond to intermediate preferences.

2. Literature Review

Previous literature indicates the massive use of AHP methodology as a multi-criteria decision making tool in selecting from among nominated alternatives in many industrial fields. However the literature survey has not revealed any research conducted specifically on the selection of temperature sensors using AHP method, and here comes to the fore the importance of this study. Vaidya and Kumar [2] conducted research that overviewed different applications of the AHP method. In their paper, they referred to a total of 150 application papers such as; selection, evaluation, benefit-cost analysis, resource allocation, decision making, forecasting, medicine, QFD, social, political, manufacturing, engineering, education, industry, government, and others. Yurdakul [3] applied AHP as a strategic decision-making tool to justify machine tool, namely machining centers, selection. Analytic Network Process (ANP) method was also used in the same paper to account for calculation of the weights of the criteria due to interdependencies and interrelationships that exist among them. Pi-Fang et al [4] presented an AHP method for objectively selecting medical waste disposal firms in Taiwan based on the results of interviews with experts in the field. In their study, appropriate criteria weights based on AHP were selected to assess the effectiveness of medical waste disposal firms. The proposed AHP-based method offered a more efficient and precise means of selecting medical waste firms than subjective assessment methods, thus reducing the potential risks for hospitals. Che-Wei et al [5] studied and developed a manufacturing quality yield model for forecasting 12 in. silicon wafer slicing machine based on AHP framework. In their work, exponentially weighted moving average (EWMA) control charts were used to demonstrate and verify the feasibility and effectiveness of the proposed AHP-based algorithm. Okada, et al [6] applied AHP to irrigation project improvement. In their study, the work was divided into two parts. In the first part, a questionnaire survey was distributed among irrigation professionals to determine the most important evaluation factors in evaluating an irrigation project. The survey was then processed by the AHP method and local weights of evaluation factors were obtained. In the second part, these local weights were statistically analyzed and modeled by probability density functions. Results indicated that professionals give the first priority to water delivery services and that they consider the irrigation infrastructure of primary canals more important than that for secondary canals. Papalexandrou et al [7] applied AHP method for assessing liquid bio-fuels which are derived from agricultural crops and are a major feasible crude oil substitute in the European Union. Muralidhar et al [8] presented an improved methodology for information systems project selection using AHP. Bevilacqua and Braglia [9] applied AHP for selecting the best maintenance strategy for an important Italian oil refinery. Five possible alternatives were considered: preventive, predictive, condition-based, corrective and opportunistic maintenance.

Despite the fact that, the literature survey reveals a wide array of AHP applications, the survey does not reveal its use in evaluating temperature sensors selection. Research on temperature sensors was primarily concerned in proposing new temperature sensors fabrications that satisfy certain special demands and requirements. Vavra et al [10] proposed the use of Fe/Cr magnetoresistive sensors at temperatures below 2 K in the MilliKelvin temperature range. Hoa et al [11] studied electrical resistance drift of molybdenum disilicide (MoSi₂) thin film temperature sensors to study their thermo-resistance characteristics. Bianchi et al [12] discussed the properties, characteristics, applications and sensing principles of most of present-day integrated smart temperature sensors. A CMOS process-compatible temperature sensor developed for low-cost high-volume integrated Microsystems for a wide range of fields (such as automotive, oil prospecting, and biomedical applications) was also described. Han & Kim [13] developed a diode temperature sensor array (DTSA) for measuring the temperature distribution on a small surface with high resolution. The DTSA consisted of an array of 32x32 diodes (1024) for temperature detection in an 8mmx8mm surface area and was fabricated using the very large scale integration (VLSI) technique.

In the next section, the paper gives a brief introduction of the AHP method and the evaluative criteria used in selecting the best temperature sensor. A case study is then presented and the results are discussed. Sensitivity analysis is presented in the following section. The final section provides some concluding remarks.

3. AHP Method Theoretical Background

The analytic hierarchy process is a multi-criteria decision-making tool mostly used when a decision maker is faced with a problem involving multiple objectives and criteria. The method, which was developed by Thomas Saaty [14], has been widely applied to different decision making problems. AHP's widespread use may be considered as an evidence of the method's power and reliability among decision makers in dealing with different problems [15]. Typically, the decision maker will have an objective or multiple objectives that must be fulfilled and a group of candidate alternatives that are to be assessed. The alternatives, criteria, sub-criteria, and the objective are linked in a hierarchal structure and each forms a hierarchal level. Each component at a particular level is relatively pair-wise compared with its sister components with respect to the immediate upper level and weights of all components are determined and aggregated for upper levels. The final outcome of the method is a score for each alternative representing its relative preference towards the objective.

4. Method Application

Once the decision maker has identified the objective of the problem, the alternatives, the criteria and sub-criteria governing the comparison process, then the application of AHP becomes easy and can be described in terms of the following steps:

Step 1: The decision hierarchy is setup. The decision hierarchy will be made up of the objective level, the

criteria level, the sub-criteria level, and finally the alternatives level.

Table 1 shows the list of criteria and sub-criteria within each criterion that will be used as a basis for the comparison between the alternative sensors. There are four criteria: Static, Dynamic, Environmental, and Others. Static criterion refers to those characteristics that are inherent in the structure of the sensor such as the maximum and minimum operating temperatures for which the sensor is rated. This criterion comprises 11 sub-criteria represented by the symbols: CS1, CS2... CS11. Dynamic criterion refers to dynamic behavior of the sensor and mainly has to do with the sensor's response time which is

the time needed for the sensor to reach 63.2% of its steady state response following a step change in input temperature. This criterion comprises 3 sub-criteria represented by the symbols: CS12, CS13, and CS14. Environmental criterion refers, on the other hand, to the medium characteristics that the sensor is to be used in and the degree of suitability of a sensor in a certain medium, it comprises 5 sub-criteria represented by the symbols: CS15... CS19. Finally, Others criterion refers to miscellaneous sub-criteria defining the sensor's behavior, it consists of 4 sub criteria such as the cost sub-criterion.

Table 1: Criteria and sub-criteria factors used as basis for comparison between alternative sensors.

Criteria	Sub-Criteria
Static Criteria (C1)	Maximum Operating Temperature (CS1)
	Minimum Operating Temperature (CS2)
	Temperature Curve (CS3)
	Maximum Sensitivity Region (CS4)
	Self-Heating Issues (CS5)
	Long Term Stability and Accuracy (CS6)
	Typical Temperature Coefficient (CS7)
	Extension Wires (CS8)
	Long Wire runs from Sensor (CS9)
	Measurement Parameter (CS10)
	Temperature Measurement (CS11)
Dynamic Characteristics (C2)	Stimulation Electronics required (CS12)
	Typical Output Levels per Degree Celsius (CS13)
	Typical Fast Thermal Time Constant (CS14)
Environmental Parameters (C3)	Typical Small Size (CS15)
	Noise Immunity (CS16)
	Fragility-Durability Characteristics (CS17)
	High Thermal Gradient Environment (CS18)
	Corrosion Resistance (CS19)
Other Criteria (or Simply Others) (C4)	Point or Area Measurement (CS20)
	Manufacturing Variances (CS21)
	NIST Standards (CS22)
	Cost (CS23)

The best temperature sensor can then be selected and evaluated based on four evaluation criteria, twenty three

evaluation sub-criteria. Figure 1 shows the hierarchal structure for the temperature sensor selection problem for three alternative sensors.

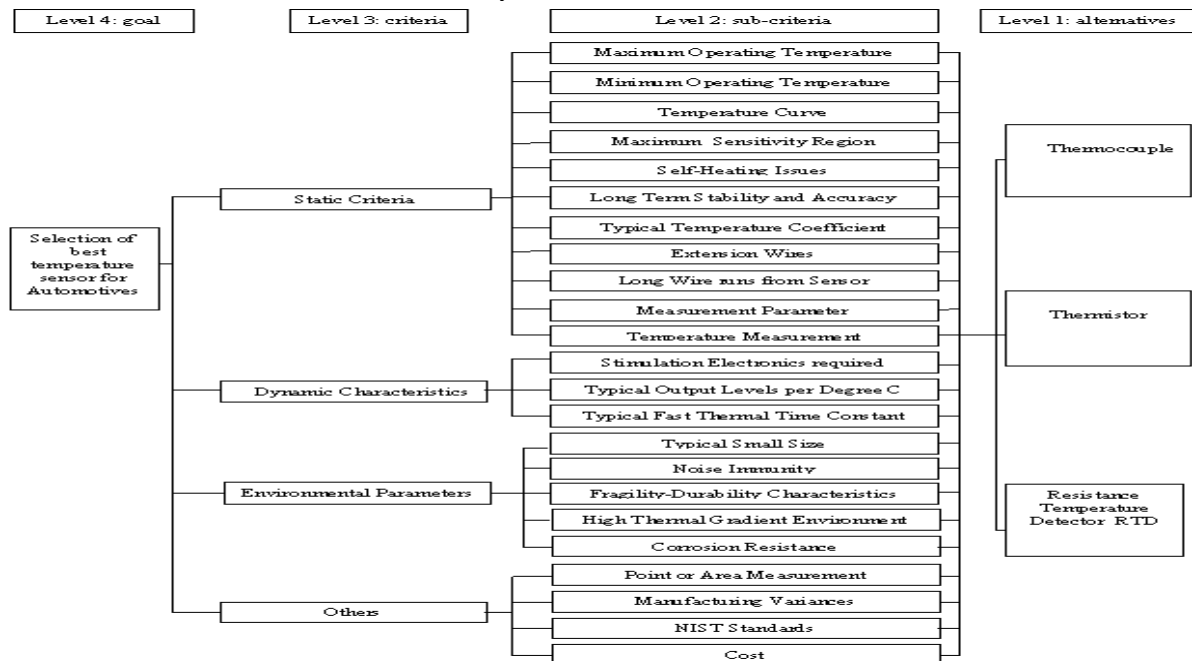


Figure 1: hierarchal structure for the temperature sensor selection problem.

Step 2: Pair-wise comparisons of the alternatives, sub-criteria, and criteria is performed. This is done to determine the weights of the different criteria and sub-criteria and also to determine how well the alternatives score on each sub-criterion and criterion. Values of relative importance (weights) throughout the whole hierarchy were taken from views of experts in the field of sensors. These values were collected and their averages were used. The weights of the different components in the hierarchal structure are aggregated throughout the whole hierarchy starting from the alternatives level through sub-criteria and criteria levels up to the objective level. Starting from the alternatives level, the relative importance of one alternative over the others with respect to the same sub-criterion in the decision hierarchy can be determined using Saaty's scale [16] shown in Table 2. According to Saaty, the relative weight of alternative i compared to alternative j with respect to the same sub-criterion can be obtained from a 9-point scale and assigned to the (i, j) th position of the pair-wise comparison matrix or judgment matrix.

Table 2: The pair-wise comparison scale.

Intensity of importance	Definition
1	Equally important
3	Weakly more important
5	Strongly more important
7	Very strongly more important
9	Extremely more important
2,4,6,8	Intermediate values between two adjacent judgments

In a more general form, let A_1, A_2, \dots, A_n be a set of n pairwise comparison matrices between criteria, sub-criteria and alternatives. Each matrix is composed of numerical weights that represent the evaluative judgments of experts of one component with respect to the others. The comparison of any two components such as criteria C_i and C_j is made using the question of the type: Of the two criteria which is more important and by how much. Saaty's scale is used to transform verbal judgments of the relative preference of one component to the other into numerical values representing the elements (a_{ij}) of the comparison matrices. The elements a_{ij} are governed by the following rules:

$$a_{ii} = 1, \forall i, a_{ij} > 0, a_{ji} = \frac{1}{a_{ij}}, \forall i, j \quad (1)$$

In the current study, comparison matrices were constructed for seven alternative sensors: the thermocouple, the thermister, the resistance temperature detector (RTD), the bimetallic strip thermometer, the mercury-in-glass thermometer, the optical disappearing filament pyrometer, and the liquid crystal display semiconductor thermometer (LCD). These matrices were constructed for 23 sub-criteria, and 4 criteria, for three different applications: Automotives, Chemical Processes, and HVAC. The matrices were compiled from the average values collected from different experts in the field of sensors. The outcomes of this step are 3 sets, one per application, of 23 matrices of the dimensions 7×7 representing relative preferences of the seven alternatives against each sub-criterion. In addition to, 3 sets of 4

matrices of the dimensions 11×11 , 3×3 , 5×5 , and 4×4 representing relative weights of the Static, Dynamic, Environmental, and Others sub-criteria towards their respective parents criteria, as well as, 3 sets of 4×4 matrices representing the criteria relative weights against the overall goal.

These sets of matrices are ideally capable of dealing with the selection of up to seven sensors simultaneously. However, depending on the restrictions that pertain to the industrial application in terms of temperature range, resolution, and response time the total number of candidate sensors can be reduced. The work proposed permits the extraction of the required entries from the matrices of each application depending on the number of alternatives considered.

Step 3: The comparison matrices are transformed into weights corresponding to the different components, i.e., criteria, sub-criteria and alternatives. The consistency in a decision maker's evaluations is then checked in terms of the consistency index CI and consistency ratio CR . Consider the following equation:

$$AW^T = \Delta W^T \quad (2)$$

Where A represents a pairwise comparison matrix, W is an unknown n -dimensional weight vector of each component and Δ is an unknown number. Saaty proposed a way to compute Δ and W by approximating Δ with Δ_{max} which represents the largest number for which a non trivial solution W exists for equation 2. This is only true, if the decision maker's judgments are consistent in which case Δ_{max} would be close to n . The consistency of the decision maker's judgments is measured by computing CI which is defined as:

$$CI = \frac{\Delta_{max} - n}{n - 1} \quad (3)$$

CR is defined in terms of CI and random index RI as:

$$CR = \frac{CI}{RI} \quad (4)$$

Values of RI for the appropriate values of n are found in literature [16]. A simple method described in [16] can be used to approximate Δ_{max} , W , CI and CR . The consistency of the decision maker is considered acceptable if CR is less than 0.1.

Step 4: the component weights are aggregated to obtain scores for the different alternatives towards the final objective and a decision is made.

Step 5: Sensitivity analysis is performed to examine the robustness of the selected alternative to changes in the judgments made by the decision maker. It can show the extent of change that can be made to the criteria or sub-criteria weights before the preferred alternative changes in favor of another alternative.

5. Case Study: Automotive Catalytic Converter

A case study is presented here to describe the AHP sensor selection procedure. AHP is applied to the selection of the best temperature sensor from among three alternatives: the thermocouple, the thermister, and the RTD in an automotive catalytic converter application. A catalytic converter is a device which chemically converts harmful exhaust gases, produced by the internal combustion engine as by-products of the fuel combustion process, into harmless carbon dioxide, water vapor, and nitrogen gas. The Automotive catalytic converter operates in the temperature range of 500 to 750 °C (773 - 1023 K). The resolution of industrial sensors employed practically for this application is 1% of the temperature range, i.e. (5-7.5) °C. The response time is 5-10 seconds. The relative weights that are related to these three sensors are extracted out of the automotives set of comparison matrices. The AHP method is then applied to find the best sensor.

6. Results

Selected judgment matrices are shown in Table 3, representing relative weights of the three sensor alternatives case study against selected sub-criteria, relative weights of selected sub-criteria against their respective parent criterion, and relative weights of the four criteria against the overall goal. It is shown that the best scoring sensor against the Time Constant sub-criterion is the thermocouple with a weight of 0.62323. This makes sense because the thermocouple is the fastest sensor among all three sensors while the RTD is the slowest one. The thermister, on the other hand, has moderate response time. The value of CR is $0.01578 < 0.1$ indicating consistent decision maker's comparisons. It can also be seen that the best scoring sensor against the Long Term Stability and Accuracy sub-criterion is the RTD with a weight of 0.63933. This can be explained based on the fact that, the RTD is the most accurate while the thermocouple is the least accurate of the three sensors. The thermister, on the other hand, retains moderate levels of accuracy. The value of CR 0.04663 is within acceptable limits.

Table 4 summarizes the three alternatives' weights with respect to the 23 sub-criteria, the 4 criteria weights with respect to the goal, the synthesis (aggregate) weight of the 23 sub-criteria towards the final goal, and the score of each alternative against each criterion. Table 4 shows

that the most important criterion in the selection of a temperature sensor in this case is the Static criterion with an overall score towards the goal of 0.53637. Static criterion pertains to those static qualities that are inherent in the sensor architecture and that relate to the basic technical characteristics which makeup a sensor. On the other hand, the score of the Environmental criterion is 0.22045, suggesting less importance. These weights match well with the view of experts who state that the choice of any temperature sensor is dictated by the technical qualities that the sensor has to meet on the first scale, and on the environmental considerations, or alternatively, the medium characteristics that the sensor will be placed in on the second scale. The Dynamic and Others criteria were the least important.

Values of the consistency index (CI) and the consistency ratio (CR) are listed in Table 5 for the matrices of the different components in the hierarchal structure. As can be seen these values are all within acceptable limits indicating consistency in decision maker's judgments.

Table 6 shows the final scores for the three temperature sensors for the case study, the thermocouple is the most preferred sensor with the largest score of 0.37849, the second ranked sensor is the RTD with a score of 0.34589, and the least preferred sensor is the thermister with a score of 0.27560. These results can be matched generally with views of experts in the field. The thermocouple is the simplest to install, the least expensive, the smallest in size, the most durable and reliable, the fastest, the least electronic circuits demanding. It retains reasonable accuracy and is good in many low accuracy applications, as is the case in the automotive catalytic converter, and does not experience any self heating. It is a point measurement sensor with well-established traceable NIST standards. The second best choice, the RTD, retains many of the good qualities that the thermocouple has, but it suffers from serious drawbacks such as: fragility, high cost, relatively slow response time, very low to low self heating issues, large size, and because it is an area measurement sensor it suffers from effects of high thermal gradients. Needless to say, the thermister comes last because of the many drawbacks it shares with the RTD in addition to the high level of self heating issues, and its non-standardized technical data owing to a larger amount of uncertainty in its measurements, and the manufacturing variances that accompany its use.

Table 3: Selected matrices representing relative weights of the three sensor alternatives against selected sub-criteria, relative weights of Environmental sub-criteria towards Environmental criterion, and relative weights of criteria towards the final goal for the case study in the automotive catalytic converter application.

Maximum Op.Temp. Jugement Matrix (CS1):							
	Thermocouple	Thermister	RTD		Thermocouple	Thermister	RTD
Thermocouple	1	3	1	Alternatives Weight Vector =	0.42857	0.14284	0.42857
Thermister	0.3333	1	0.3333	Consistency Index =	0		
RTD	1	3	1	Consistency Ratio =	0		
Long Term Stability and Accuracy Judgment Matrix (CS6):							
	Thermocouple	Thermister	RTD		Thermocouple	Thermister	RTD
Thermocouple	1	0.25	0.1667	Alternatives Weight Vector =	0.08695	0.27371	0.63933
Thermister	4	1	0.3333	Consistency Index =	0.02704		
RTD	6	3	1	Consistency Ratio =	0.04663		
Typical Fast Thermal Time Constant Judgment Matrix (CS14):							
	Thermocouple	Thermister	RTD		Thermocouple	Thermister	RTD
Thermocouple	1	3	4	Alternatives Weight Vector =	0.62322	0.23948	0.13728
Thermister	0.3333	1	2	Consistency Index =	0.00915		
RTD	0.25	0.5	1	Consistency Ratio =	0.01578		
Cost Judgment Matrix (CS23):							
	Thermocouple	Thermister	RTD		Thermocouple	Thermister	RTD
Thermocouple	1	1	6	Alternatives Weight Vector =	0.46153	0.46153	0.07693
Thermister	1	1	6	Consistency Index =	0		
RTD	0.1667	0.1667	1	Consistency Ratio =	0		
Criteria Matrix:							
	Static	Dynamic	Environ.	Others			
Static	1	4	3	4			
Dynamic	0.25	1	0.5	1			
Environ.	0.3333	2	1	2			
Others	0.25	1	0.5	1			
	Static	Dynamic	Environ.	Others			
Criteria Weight Vector =	0.53636	0.12159	0.22045	0.12159			
Consistency Index =	0.00686						
Consistency Ratio =	0.00762						
Environnemental Sub-Criteria Jugement Matrix:							
	CS15	CS16	CS17	CS18	CS19		
CS15	1	3	0.3333	4	0.25		
CS16	0.3333	1	0.25	3	0.2		
CS17	3	4	1	5	0.5		
CS18	0.25	0.3333	0.2	1	0.1667		
CS19	4	5	2	6	1		
Sensor Ranks							
0.37849							
0.2756							
0.34589							

Table 4: Weights of alternatives, sub-criteria, criteria and synthesis values for sub-criteria and the alternatives for the three sensors case study.

Criteria	Weights of Criteria	Sub-criteria	Weights of Sub-criteria	Synthesis Value	Thermocouple	Thermister	RTD
C1	0.53637	CS1	0.22119	0.11863	0.42858	0.14283	0.42858
		CS2	0.22119	0.11863	0.5	0.25	0.25
		CS3	0.05379	0.02885	0.25099	0.09602	0.65299
		CS4	0.09836	0.05275	0.06225	0.70131	0.23644
		CS5	0.09777	0.05244	0.65715	0.06825	0.2746
		CS6	0.1504	0.08067	0.086955	0.27371	0.63933
		CS7	0.05233	0.02806	0.09602	0.65299	0.25099
		CS8	0.03038	0.01629	0.07693	0.46154	0.46154
		CS9	0.01983	0.01063	0.19999	0.6	0.19999
		CS10	0.01452	0.00778	0.62322	0.13729	0.23948
		CS11	0.03355	0.01799	0.09642	0.28422	0.619360.619 0.61936
		Score of each alternative against first criterion			0.17481	0.15043	0.20743
C2	0.12159	CS12	0.16019	0.01947	0.62322	0.13728	0.23948
		CS13	0.10093	0.01227	0.46153	0.07693	0.46153
		CS14	0.73887	0.08983	0.62322	0.23948	0.13728
				Score of each alternative against second criterion			0.07378
C3	0.22045	CS15	0.15164	0.03342	0.53896	0.29726	0.16378
		CS16	0.08645	0.01905	0.09339	0.68529	0.22132
		CS17	0.28264	0.0623	0.65299	0.09602	0.25099
		CS18	0.04767	0.0105	0.68064	0.20141	0.11794
		CS19	0.43157	0.09513	0.08696	0.27371	0.63933
				Score of each alternative against third criterion			0.07557
C4	0.12159	CS20	0.1575	0.01915	0.53896	0.29726	0.16378
		CS21	0.07747	0.00941	0.09602	0.25099	0.65299
		CS22	0.22913	0.02786	0.44444	0.11111	0.44444
		CS23	0.53589	0.06519	0.46153	0.46153	0.07693
				Score of each alternative against fourth criterion			0.05369

Table 5: Consistency ratio and consistency index values for the three sensor alternatives, the criteria and sub-criteria matrices for the three sensors automotive case study.

Criteria	Sub-Criteria	CI	CR
Static Criterion	Maximum Operating Temperature	0	0
CI = 0.08281	Minimum Operating Temperature	0	0
CR= 0.05208	Temperature Curve	0.00918	0.01583
	Sensitivity	0.03622	0.06225
	Self-Heating Issues	0.02218	0.03824
	Long Term Stability and Accuracy	0.02705	0.04663
	Typical Temperature Coefficient	0.00918	0.01583
	Extension Wires	0	0
	Long Wire runs from Sensor	0	0
	Measurement Parameter	0.00915	0.01578
	Temperature Measurement	0.04333	0.07471
	Dynamic Characteristics	Stimulation Electronics required	0.00915
CI = 0.02722	Existence of Maximum Sensitivity Region	0	0
CR = 0.04694	Typical Fast Thermal Time Constant	0.00915	0.01578
Environmental Parameters	Typical Small Size	0.00459	0.00791
	Noise Immunity	0.0271	0.0271
CR = 0.05666	Fragility-Durability Characteristics	0.00918	0.01583
	High Thermal Gradient Environment	0.01235	0.02129
	Corrosion Resistance	0.02705	0.04663
Others	Point or Area Measurement	0.00459	0.00791
	Manufacturing Variances	0.00918	0.01583
CI = 0.03752	Standards exist	0	0
CR = 0.04169	Cost	0	0
	The four-criteria matrix:	CI = 0.00687	CR = 0.00763

Table 6: The software final results: the three sensors scores.

Sensor	Score	Rank
Thermocouple	0.37849	1
Thermister	0.2756	3
RTD	0.34589	2

7. Sensitivity Analysis

This section tackles the sensitivity analysis applied to the case study. Sensitivity analysis for any system of input and output dependent variables refers to intended variations in the input variables of the system for the purpose of monitoring changes in the output dependent variables. In any system, sensitivity analysis gives deeper understanding of the relationships that govern the system and allows for developing and optimizing the system and avoiding critical conditions which make the system unpredictable. In this paper five variations were made and the results studied: variations in the relative weights of an alternative with respect to the others in the 23 matrices, variations in the relative weight of the criteria and also in the sub-criteria, variation in the application, and variations in the number of alternatives that fit the case study application.

7.1. Case 1: Alternative Weights Variation:

In this section the relative weight of the RTD will be increased by 1 relative weight unit on Saaty's scale. This means adding 1 to each entry in all the 23 matrices where the RTD appears and the new scores of the alternatives are monitored and discussed. Table 7 shows the new scores of the alternative sensors for the case study.

It can be clearly seen that increasing the relative weights of the RTD alternative resulted in the dominance of the RTD over the thermocouple, i.e. the thermocouple was the most preferred sensor choice before the increase while the RTD became the most preferred after the increase was employed to the system. This reveals and confirms the challenging decision situation when the differences between the scores of alternatives obtained by AHP are small, in which case the decision maker cannot easily distinguish the preference of one alternative to the others, rather, the closely-scoring alternatives have almost the same preference.

Table 7: Case 1 Sensitivity Analysis results.

Sensor	Old Score	New score	New Rank
Thermocouple	0.37849	0.35457	2
Thermister	0.2756	0.24957	3
RTD	0.34589	0.39585	1

7.2. Case 2: Sub-criterion Relative Weights Variation:

In this case of sensitivity analysis the variation will be made to the Long Term Stability and Accuracy sub-criterion inside the Static criterion and the scores monitored. The relative weights of this sub-criterion among the 11 Static sub-criteria will be increased by a factor of 1 on Saaty's scale while the Static criterion overall score would remain unchanged to ensure that the change in the results is due to this sub-criterion effect. The procedure is merely to increase the whole values of the sixth row of the 11x11 Static sub-criteria matrix by one and the corresponding necessary changes in the reciprocals. The new scores of the three alternatives are shown in Table 8.

It can be clearly seen that although increasing the relative weights of the Long Term Stability and Accuracy sub-criterion by a factor of 1 has decreased the final score of the thermocouple alternative and has increased the final

score of the RTD alternative, it did not change the preferences (ranks) of the three alternatives and that the thermocouple remained the most preferred.

Table 8: Case 2 Sensitivity Analysis results.

Sensor	Old Score	New score	New Rank
Thermocouple	0.37849	0.37016	1
Thermister	0.2756	0.27616	3
RTD	0.34589	0.35368	2

7.3. Case 3: Dynamic Criterion Relative Weights Variation:

In this case, the relative weight of the Dynamic criterion is increased by a factor of 1 relative importance on Saaty's scale while the remaining criteria weights are kept unchanged. The results for this case are shown in Table 9.

It can be clearly seen that increasing the Dynamic criterion relative weight by a factor of 1 has increased the thermocouple final score and decreased the thermister and the RTD final scores, this is because the thermocouple scores the best on the response time sub-criterion. This change also made the preference of the thermocouple to the RTD more distinct. The thermocouple final score increased from 0.37849 to 0.39531 and the RTD score decreased from 0.34589 to 0.33446. The difference between the two alternatives before the change was 0.04403 has increased to 0.06085 giving more weight to the thermocouple's preference.

Table 9: Case 3 Sensitivity Analysis results.

Sensor	Old Score	New score	New Rank
Thermocouple	0.37849	0.39531	1
Thermister	0.2756	0.27022	3
RTD	0.34589	0.33446	2

7.4. Case 4: Changing the Application:

AHP is used in this case, to select from among the three sensors used in the case study based on the three different sets of matrices compiled for the three different applications: Automotives, Chemical Processes, and HVAC. The variations in the final scores of the alternatives are monitored. Table 10 shows the score of the three sensors against each application.

Results confirm the view of experts that not only does an alternative temperature sensor selection depend on its inherent characteristics but also it depends on the specific application and the peculiar environment (medium) the sensor is to be put in. The table also reveals the increased suitability of the RTD and the decreased suitability of the thermocouple to the HVAC application. The final score of the RTD in the HVAC application is very close to the thermocouple's score, suggesting that they are almost equally preferred in the HVAC application.

Table 10: Case 4 Sensitivity Analysis results.

Sensor	Automotives	Chemical Processes	HVAC
Thermocouple	0.37849	0.38179	0.35968
Thermister	0.2756	0.26806	0.2867
RTD	0.34589	0.35013	0.35362

7.5. Case 5: Increasing Number of Sensors:

In this case, the results are monitored upon introducing a new viable alternative sensor. In other words, scores for the three sensors case study are compared to those obtained when the pyrometer for example, is introduced. The scores for the four sensors are shown in Table 11. The pyrometer came in third place with a score of 0.25697. This score is comparable to that of the thermocouple and the RTD. The thermister on the other hand, remained the least preferred. All the original sensors' scores have decreased, but the decrease experienced by the thermocouple was the largest, about 29 %, this indicates that the introduction of the pyrometer was at the expense of the thermocouple to a larger degree than it was to the thermister and the RTD which both experienced a decrease in their final score of about 24 %.

Table 11: Case 5 Sensitivity Analysis results.

Sensor	Old Score	New score	% decrease (score)	New Rank
Thermocouple	0.37849	0.2691	29	1
Thermister	0.2756	0.20988	24	4
RTD	0.34589	0.26403	24	2
Pyrometer	-	0.25697	-	3

8. Conclusions

The paper shows how the AHP method enhances the evaluation process of selecting the best temperature sensor. This is because AHP relies on the breakdown of the decision problem into smaller components which are easily assessed and compared. The study also highlights the evaluative criteria and sub-criteria that relate to the selection of temperature sensors. The criteria with the highest weights through the hierarchy can be regarded as being the most important and critical in the evaluation process and can be lumped together in a bundle and may be used in a screening stage as a quick assessment measure. The ability of the AHP method to handle qualitative (verbal) as well as quantitative judgments is also shown. These judgments are transformed into measurable quantitative final scores for the purpose of ranking alternatives. These scores not only rank candidate alternative sensors, but also give a quantitative measure of the degree of dominance of one alternative over the others. This dominance or preference was further tested by means of sensitivity analysis to investigate to what degree the best alternative sensor remains dominant.

The results showed the robustness of the proposed work to the variations carried out in all cases of the sensitivity analysis except for the first case. The analysis shows that when the final scores are very close to each other, they can be regarded as equally preferred. If further distinction is needed, the experts' judgments should be reviewed or more experts can be consulted. Additionally, new criteria or sub-criteria can be introduced to further increase the distinction between alternatives. Finally, the application in which the sensor is to be used can be further investigated and weights can be adjusted accordingly.

References

- [1] D.M. Scott. Industrial Process Sensors. Boca Raton, Florida: CRC Press Taylor & Francis Group; 2008
- [2] O.S. Vaidya, S. Kumar, "Analytic hierarchy process: An overview of applications". European Journal of Operational Research, Vol. 169, No. 1, 2006, 1-29.
- [3] M. Yurdakul, "AHP as a strategic decision-making tool to justify machine tool selection". Journal of Materials Processing Technology, Vol. 146, No. 3, 2004, 365-376.
- [4] P-F. Hsu, C-R. Wu, Y-T. Li, "Selection of infectious medical waste disposal firms by using the analytic hierarchy process and sensitivity analysis". Waste Management, Vol. 28, No. 8, 2008, 1386-1394.
- [5] C-W. Chang, C-R. Wu, C-T. Lin, H-C. Chen, "An Application of AHP and sensitivity analysis for selecting the best slicing machine". Computers and Industrial Engineering, Vol. 52, No. 2, 2007, 296-307.
- [6] H. Okada, S.W. Styles, M.E. Grismer, "Application of the Analytic Hierarchy Process to irrigation project improvement. Part II. How professionals evaluate an irrigation project for its improvement". Agricultural Water Management, Vol. 95, No. 3, 2008, 205-210.
- [7] M.A. Papalexandrou, P.A. Pilavachi, and A.I. Chatzimouratidis, "Evaluation of liquid bio-fuels using the Analytic Hierarchy Process". Process Safety and Environmental Protection, Vol. 86, No. 5, 2008, 360-374.
- [8] K. Muralidhar, R. Santhanam, R.L. Wilson, "Using the analytic hierarchy process for information system project selection". Information and Management, Vol. 18, No. 2, 1990, 87-95.
- [9] N. Bevilacqua, M. Braglia, "The analytic hierarchy process applied to maintenance strategy selection". Reliability Engineering & System Safety, Vol. 70, No. 1, 2000, 71-83.
- [10] I.Vavra, J. Bydzovsky, K. Flachbart, J. Tejada, L. Kopera, E. Kovacova, K. Temst, Y. Bruynseraede, "Fe/Cr sensor for the MilliKelvin temperature range". Sensors and Actuators A: Physical, Vol. 91, No. 1, 2001, 177-179.
- [11] C.H. Ho, Y.H.C. Cha, S. Prakash, G. Potwin, H.J. Doerr, C.V. Deshpandey, R.F. Bunshah, & M. Zeller, "Electrical resistance drift of molybdenum silicide thin film temperature sensors". Thin Solid Films, Vol. 260, No. 2, 1995, 232-238.
- [12] R.A. Bianchi, F. Vinci Dos Santos, J.M. Karam, B. Courtois, F. Presseccq, S. Sifflet, "CMOS-compatible smart temperature sensors". Microelectronics Journal, Vol. 29, No. 9, 1998, 627-636.
- [13] I.Y. Han, S.J. Kim, "Diode temperature sensor array for measuring micro-scale surface temperatures with high resolution". Sensors and Actuators A: Physical, Vol. 141, No. 1, 2008, 52-58.
- [14] T.L. Saaty. The Analytic Hierarchy Process. New York: McGraw Hill; 1980.
- [15] P. Goodwin, G. Wright. Decision Analysis for Management Judgment. 2nd ed., West Sussex, England: John Wiley & Sons Ltd; 2000.
- [16] W.L. Winston. Operations Research. Applications and Algorithms, 3rd ed., Belmont, California: Wadsworth Publishing Company Inc; 1994.

Modeling of Weld Bead Geometry and Shape Relationships in Submerged Arc Welding using Developed Fluxes

Vinod Kumar^{*a}

^aCollege of Engineering, Punjabi University, Patiala, India

Abstract

To automate a welding process, which is the present trend in fabrication industry, it is essential that mathematical models have to be developed to relate the process variables to the weld bead parameters. Submerged arc welding (SAW) is characterized by its high reliability, deep penetration, smooth finish and high productivity especially for welding of pipes and boiler joints. In the present work mathematical models have been developed for SAW using developed fluxes. Response surface methodology has been used to predict critical dimensions of the weld bead geometry and shape relationships. The models developed have been checked for their adequacy and significance by using the F-test and the t-test, respectively. Main and interaction effects of the process variables on bead geometry and shape factors are presented in graphical form and using which not only the prediction of important weld bead dimensions and shape relationships but also controlling the weld bead quality by selecting appropriate process parameter values are possible.

© 2011 Jordan Journal of Mechanical and Industrial Engineering. All rights reserved

Keywords: Weld bead geometry; RSM; Design of Experiment

1. Introduction

Quality has now become an important issue in today's manufacturing world. Whenever a product is capable of conforming to desirable characteristics that suit its area of application, it is termed as high quality. Therefore, every manufacturing process has to be designed in such a way that the outcome would result in a high quality product. The present trend in the fabrication industries is the use of automated welding processes to obtain high production rates and high precision. To automate a welding process it is essential to establish the relationship between process parameters and weld bead geometry to predict and control weld bead quality [1]. Submerged arc welding (SAW) is preferred over other methods of welding of pipes and boilers because of its inherent qualities like easy control of process variables, high quality, deep penetration, smooth finish, capability to weld thicker sections and prevention of atmospheric contamination of weld pool [2]. With the growing emphasis on the use of automated welding systems, SAW is employed in semiautomatic or automatic mode in industry [3]. In such automated applications, a precise means of selection of the process variables and control of weld bead shape has become essential because mechanical strength of welds is influenced not only by the composition of the metal, but also by the weld bead shape [2, 3].

The weld bead shape is an indication of bead geometry. The acceptable or appropriate weld bead shape depends on factors such as line power which is the heat energy supplied by the arc to the base plate per unit length of weld, welding speed, joint preparation, etc. Hence,

study and control of weld bead shape is very much essential. To do this precise relationship between the process parameters and the bead parameters controlling the bead shape is to be established. This may be achieved by the development of mathematical expressions, which can be fed into a computer relating the weld bead dimensions to the important process control variables affecting these dimensions. Also, optimization of the process parameters to control and obtain the required shape and quality of weld beads is possible with these expressions.

In submerged arc welding approximately 10% -15% of the flux gets converted into very fine particles termed as flux dust before and after welding, due to transportation and handling. If welding is performed without removing these very fine particles from the flux, the gases generated during welding are not able to escape, thus it may result into surface pitting (pocking) and even porosity. On the other hand, if these fine particles are removed by sieving, the cost of welding will be increased significantly. And if this flux dust is dumped/ thrown, will create the pollution. Therefore to reduce the cost of welding and pollution, agglomerated fluxes have been developed [4] by utilizing wasted flux dust. The performance of the weldment obtained by using developed fluxes was checked by chemical analysis, radiography, mechanical and metallurgical tests; they showed good agreement with that of dictated by AWS for a perfect weld.

In the present study an attempt has been made to investigate the effect of using developed fluxes on different bead geometry parameters, including weld penetration shape factor, weld reinforcement form factor, through experiments based on design matrix. The analysis of variables (ANOVA) technique has been adopted to check the level and degree of the direct or interactive

* Corresponding author. e-mail: vk_verma5@rediffmail.com

effect of welding current, voltage, welding speed and flux basicity index on features of bead geometry and shape relationship. Response surface methodology has been applied to derive mathematical models that correspond to the welding phenomena using developed fluxes. Predictive equations have been used to represent graphically the effects of process parameters on various responses. No work so far has been performed which considers the four important process parameter used in this study using fluxes developed from waste flux dust.

2. Experimentation

The research work was planned to be carried out in the following steps [5]

- Selection of the important process control variables and finding their upper and lower limits
- Developing the design matrix
- Conducting the experiments as per the design matrix;
- Recording the response parameters
- Checking the significance of models and arriving at the final models
- Validation of models
- Presenting the direct and interaction effects of process parameters on bead geometry in graphical form
- Analysis of results.

2.1. Selection of process parameters and their working ranges:

Based on the effect on weld bead geometry, ease of control and capability of being maintained at the desired level, four independently controllable process parameters were identified namely, the open circuit voltage (A), current (B), welding speed (C) and Basicity Index (D). Trial runs were conducted by varying one of the process parameters at a time while keeping the rest of them at constant value [6]. The working range was fixed by inspecting the bead for a smooth appearance and the absence of visible defects. The upper and lower limits were coded as +1 and -1, respectively. The selected process parameters and their upper and lower limits together with notations and units are given in Table 1.

Table 1: Process control variables and their limits.

Parameters	Notations	Limits		
		-1	0	1
Voltage (volts)	A	32	35	38
Current (amperes)	B	375	425	475
Welding Speed (m/hr)	C	24	27	30
Basicity Index	D	0.6	0.9	1.2

2.2. Developing the design matrix:

Design of experiments is a powerful analysis tool analyzing the influence of process variables over some specific variable, which is unknown function of these

process variables. It is the process of planning the experiments that appropriate data can be analyzed by statistical methods, resulting in valid and objective conclusions. Statistical approval to experiment design is necessary if we wish to draw meaningful conclusions from the data [7].

In submerged arc welding, process parameters interact in a complicated manner that influences various features of quality characteristics of the weld bead. Quadratic response surface methodology is an efficient approach to represent these relationships through mathematical equations, [7]. The graphical representations of these equations serve as means for investigating main/direct as well as interaction effects of various process parameters on selected response(s). Application of this technique can be found in the reporting of [8-9]. The RSM was employed to quantify the relationship between the individual response factors and the input machining parameters of the following form:

$$Y = F(A, B, C, D) \quad (1)$$

Where, Y is the desired response and F is the response function or response surface. The approximation of Y has been proposed by fitting second-order polynomial regression model i.e. quadratic model [10] of the following form:

$$Y = a_0 + \sum_{i=1}^{i=4} a_i x_i + \sum_{i=1}^{i=4} a_{ii} x_i^2 + \sum_{i < j}^{i=4} a_{ij} x_i x_j \quad (2)$$

where, a_0 is constant and a_i , a_{ii} and a_{ij} respectively represent the coefficients of linear, quadratic and cross product terms. The x_i reveals the coded variables corresponding to the studied welding parameters. The coded variables x_i (1, 2, 3, and 4) are obtained from the following transformation equation:

$$x_1 = \frac{(A - A_0)}{\Delta A}, x_2 = \frac{(B - B_0)}{\Delta B}, x_3 = \frac{(C - C_0)}{\Delta C}, x_4 = \frac{(D - D_0)}{\Delta D} \quad (3)$$

Where x_1, x_2, x_3 and x_4 are the coded values of input parameters A, B, C and D respectively and A_0, B_0, C_0 and D_0 are the values of corresponding parameters at zero level. The terms $\Delta A, \Delta B, \Delta C$ and ΔD are the intervals of variation in A, B, C and D respectively.

The necessary data required for developing the response models have been collected by designing the experiments based on Box-Behnken Design (BBD) using state ease 6.0 version of design of experiment and by varying each numeric factor over three levels coded as -1, 0, and +1. The BBDs are available for 3 to 10 factors, which are formed by combining two-level factorial designs with incomplete block designs. This procedure creates designs with desirable statistical properties and more importantly, only a fraction of experiments are required, as compared to three-level factorial design [11-12]. The levels of four process parameters and experimental results are reported in Table 2. The values selected are well supported by earlier reported works.

Table 2: Design values and observed values of bead parameters.

Expt. Run No.	Process Parameters				Response factors				
	A Voltage (volts)	B Current (amperes)	C Welding Speed (m/hr)	D Basicity Index	W Bead Width (mm)	P Penetration (mm)	R Reinforcement (mm)	WPSF	WRF
1	1	-1	0	1	17.76	6.545	3.201	2.71352	5.54827
2	-1	0	0	0	17.24	7.349	4.043	2.3459	4.26416
3	0	0	0	1	17.81	6.735	3.345	2.64439	5.32436
4	0	-1	1	1	15.192	6.671	2.955	2.27732	5.14112
5	-1	0	0	-1	16.79	10.455	6.025	1.60593	2.78672
6	0	-1	0	0	17.48	6.389	2.382	2.73595	7.33837
7	0	0	0	1	17.2	6.17	3.245	2.78768	5.30046
8	0	1	-1	1	17.215	8.56	3.55	2.0111	4.8493
9	0	0	0	1	17.54	6.66	2.94	2.63363	5.96599
10	-1	0	-1	1	16.345	7.115	4.58	2.29726	3.56878
11	0	0	0	1	16.792	6.4	3.59	2.62375	4.67744
12	1	0	0	0	19.475	7.53	2.544	2.58632	7.65527
13	0	0	1	-1	15.812	8.75	4.392	1.80709	3.60018
14	0	0	1	0	16.99	6.525	3.01	2.60383	5.64452
15	0	1	0	-1	17.515	11.323	4.191	1.54685	4.17919
16	1	1	0	1	18.855	7.355	2.899	2.56356	6.50397
17	1	0	0	-1	18.985	9.285	3.22	2.0447	5.89596
18	0	1	0	0	17.865	7.895	3.135	2.26282	5.69856
19	0	1	1	1	16.2	6.6	3.165	2.45455	5.11848
20	-1	1	0	1	15.295	7.935	4.875	1.92754	3.13744
21	1	0	1	1	16.873	6.34	3.192	2.66136	5.28603
22	0	0	-1	0	19.355	7.835	3.45	2.47033	5.61014
23	-1	0	0	1	15.18	7.255	4.045	2.09235	3.75278
24	1	0	-1	1	20.44	6.99	3.565	2.92418	5.73352
25	-1	-1	0	1	15.56	7.025	3.49	2.21495	4.45845
26	0	0	-1	-1	17.905	11.07	4.906	1.61743	3.64961
27	0	0	0	1	17.042	6.7	3.205	2.54358	5.31732
28	0	-1	-1	1	17.365	6.32	3.475	2.74763	4.99712
29	0	-1	0	-1	16.63	8.272	4.005	2.0104	4.15231

2.3. Conducting the experiments as per the design matrix:

The experiments were conducted using Ador submerged arc-welding equipment.

- Electrode used: Grade C (AWS-5.17-80 EH -14)
- Work piece: Mild steel plates of 200× 75×12 mm size.
- Type of joint: bead on plate.
- Fluxes: Agglomerated developed fluxes
- Electrode-to-work angle: 90°

Twenty nine sets of bead on plates were laid down as per the design matrix by selecting trails at random. The chemical composition of base plate and electrode wire is given in Table 3.

Table 3: Chemical composition of base plate and electrode wire.

Element (%)	C	Mn	Si	S	P	Ni	Cr
Base Plate	0.23	0.4	0.13	0.04	0.06	0.07	0.11
Electrode Wire	0.07	1.9	0.1	0.03	0.02	Nil	Nil

2.4. Recording the responses and developing models from the data:

Two transverse specimens were cut from each welded plate. These specimens were prepared by the usual

metallurgical polishing methods and etched with 2% nital.

The profiles of the beads were traced by using optical profile projector. The response parameters namely penetration (P), reinforcement (R), width (W), weld penetration shape factor and weld reinforcement shape factor were measured. The shape relationships namely the weld penetration size factor (WPSF) which is the ratio of bead width to the height of penetration and the weld reinforcement form factor (WRF) which is the ratio of bead width to the height of reinforcement, were calculated. The observed values of W, P, R, WPSF and WRF are given in Table 2. The final models thus developed from the data are given below:

$$\text{Bead Width (W)} = + 18.28 + 1.23 \times A + 0.29 \times B - 1.06 \times C - 0.10 \times D + 0.20 \times A^2 - 0.54 \times B^2 - 0.29 \times C^2 - 0.90 \times D^2 + 0.34 \times A \times B - 0.60 \times A \times C + 0.19 \times A \times D + 0.29 \times B \times C - 0.097 \times B \times D + 0.052 \times C \times D$$

$$\text{Penetration (P)} = + 6.99 - 0.30 \times A + 0.95 \times B - 0.70 \times C - 1.53 \times D + 0.32 \times A^2 + 0.29 \times B^2 + 0.18 \times C^2 + 1.07 \times D^2 - 0.025 \times A \times B - 0.20 \times A \times C + 0.088 \times A \times D - 0.58 \times B \times C - 0.48 \times B \times D + 0.44 \times C \times D$$

$$\text{Reinforcement (R)} = + 2.94 - 0.91 \times A + 0.19 \times B - 0.24 \times C - 0.52 \times D + 0.40 \times A^2 - 0.15 \times B^2 + 0.22 \times C^2 + 0.85 \times D^2 - 0.42 \times A \times B + 0.041 \times A \times C + 0.41 \times A \times D + 0.034 \times B \times C + 4.071 \times B \times D + 0.012 \times C \times D$$

$$\text{WPSF} = + 2.62 + 0.22x_A - 0.19 x_B + 0.028 x_C + 0.38x_D - 0.098 x_A^2 - 0.16x_B^2 - 0.100x_C^2 - 0.35x_D^2 + 0.034 x_A x_B - 0.014 x_A x_C + 0.055 x_A x_D + 0.23x_B x_C + 0.062 x_B x_D - 0.086x_C x_D$$

$$\text{WRSF} = + 6.27 + 1.38 x_A - 0.22 x_B + 1.805E-003 x_C + 0.52x_D - 0.28 x_A^2 + 0.041x_B^2 - 0.48 x_C^2 - 1.47 x_D^2 + 0.57 x_A x_B - 0.16 x_A x_C - 0.33 x_A x_D + 0.031x_B x_C + 0.073 x_B x_D + 0.019 x_C x_D$$

2.5. Checking the significance of models:

ANOVA is a statistical technique, which can infer some important conclusions based on analysis of the experimental data. The method is very useful to investigate the level of significance of influence of factor(s) or interaction of factors on a particular response. The analysis of variance (ANOVA) test was performed to evaluate the statistical significance of the fitted quadratic models and factors involved therein for response factors W, P, R, WPSF and WRFF. In addition to this, the goodness of fit of the fitted quadratic model was also evaluated through Lack of fit test. The results obtained are summarized in Tables 4-9.

Table 4: ANOVA results for Bead Width (W).

Source	Sum of Squares	DF	Mean Square	F Value	Prob > F	Remarks
Model	45.5	14	3.25	29.7	<0.0001	significant
A	12.8	1	12.8	117	<0.0001	significant
B	0.73	1	0.73	6.68	0.02	significant
C	9.39	1	9.39	86	<0.0001	significant
D	0.18	1	0.18	1.63	0.22	not significant
A ²	0.25	1	0.25	2.32	0.15	not significant
B ²	1.86	1	1.86	17	0	significant
C ²	0.56	1	0.56	5.09	0.04	significant
D ²	3.57	1	3.57	32.7	<0.0001	significant
AB	0.46	1	0.46	4.23	0.06	not significant
AC	1.44	1	1.44	13.2	0	significant
AD	0.27	1	0.27	2.43	0.14	not significant
BC	0.34	1	0.34	3.07	0.1	not significant
BD	0.07	1	0.07	0.59	0.45	not significant
CD	0.02	1	0.02	29.7	<0.0001	not significant
Residual	1.52	14	0.1			
Lack of Fit	0.87	10	0.08	0.54	0.8	not significant
Pure Error	0.64	4	0.16			

Table 5: ANOVA results for Penetration (P).

Source	Sum of Squares	DF	Mean Square	F Value	Prob > F	Remarks
Model	54.66	14	3.9	48.99	<0.0001	significant
A	0.76	1	0.76	9.57	0.0079	significant
B	7.51	1	7.51	94.26	<0.0001	significant
C	4.1	1	4.1	51.47	<0.0001	significant
D	39.5	1	39.5	495.75	<0.0001	significant
A ²	0.68	1	0.68	8.49	0.0113	significant
B ²	0.53	1	0.53	6.7	0.0215	significant
C ²	0.21	1	0.21	2.62	0.1276	not significant
D ²	5.1	1	5.1	64.02	<0.0001	significant
AB	0	1	0	0.03	0.8619	not significant
AC	0.16	1	0.16	1.96	0.1835	significant
AD	0.05	1	0.05	0.68	0.4244	not significant
BC	1.34	1	1.34	16.76	0.0011	significant
BD	1.64	1	1.64	20.54	0.0005	significant
CD	1.351243	1	1.351243	16.95706	0.001	significant
Residual	1.12	14	0.08			
Lack of Fit	0.88	10	0.09	1.5	0.3692	not significant
Pure Error	0.23	4	0.06			

Table 6: ANOVA results for Reinforcement (R).

Source	Sum of Squares	DF	Mean Square	F Value	Prob > F	Remarks
Model	16.67	14	1.19	27.64	< 0.0001	significant
A	6.95	1	6.95	161.3	< 0.0001	significant
B	0.3	1	0.3	7.05	0.0188	significant
C	0.47	1	0.47	10.92	0.0052	significant
D	4.49	1	4.49	104.22	< 0.0001	significant
A ²	1.03	1	1.03	23.9	0.0002	significant
B ²	0.14	1	0.14	3.21	0.0947	not significant
C ²	0.33	1	0.33	7.57	0.0156	significant
D ²	3.17	1	3.17	73.52	< 0.0001	significant
AB	0.71	1	0.71	16.52	0.0012	significant
AC	6.56E-03	1	6.56E-03	0.15	0.7022	not significant
AD	1.19	1	1.2	27.71	0.0001	significant
BC	4.56E-03	1	4.56E-03	0.11	0.7498	not significant
BD	1.16E-04	1	1.16E-04	2.69E-03	0.9593	not significant
CD	1.02E-03	1	1.02E-03	0.024	0.8799	not significant
Residual	0.6	14	0.043			
Lack of Fit	0.38	10	0.038	0.69	0.7128	not significant
Pure Error	0.22	4	0.055			

Table 7: ANOVA results for WPSF.

Source	Sum of Squares	DF	Mean Square	F Value	Prob > F	Remarks
Model	4.02	14	0.29	29.3	< 0.0001	significant
A	0.42	1	0.42	42.72	< 0.0001	significant
B	0.31	1	0.31	31.64	< 0.0001	significant
C	0.01	1	0.01	0.69	0.4185	not significant
D	2.4	1	2.4	244.91	< 0.0001	significant
A ²	0.06	1	0.06	6.35	0.0245	significant
B ²	0.17	1	0.17	17.34	0.001	significant
C ²	0.06	1	0.06	6.56	0.0226	significant
D ²	0.55	1	0.55	55.77	< 0.0001	significant
AB	0	1	0	0.48	0.4988	significant
AC	0	1	0	0.09	0.7741	not significant
AD	0.02	1	0.02	2.18	0.1617	not significant
BC	0.21	1	0.21	21.31	0.0004	significant
BD	0.03	1	0.03	2.74	0.12	not significant
CD	0.05	1	0.05	5.22	0.0384	significant
Residual	0.14	14	0.01	0.14		
Lack of Fit	0.11	10	0.01	1.36	0.4123	not significant
Pure Error	0.03	4	0.01			

Table 8: ANOVA results for WRFF.

Source	Sum of Squares	DF	Mean Square	F Value	Prob > F	Remarks
Model	34.29	14	2.45	11.98	< 0.0001	significant
A	16.1	1	16.1	78.72	< 0.0001	significant
B	0.39	1	0.39	1.91	0.1886	not significant
C	0	1	0	0	0.9909	not significant
D	4.51	1	4.51	22.07	0.0003	significant
A ²	0.49	1	0.49	2.4	0.1436	not significant
B ²	0.01	1	0.01	0.05	0.8193	not significant
C ²	1.49	1	1.49	7.31	0.0171	significant
D ²	9.61	1	9.61	46.98	< 0.0001	significant
AB	1.3	1	1.3	6.34	0.0246	significant
AC	0.1	1	0.1	0.49	0.4964	not significant
AD	0.74	1	0.74	3.64	0.0772	not significant
BC	0	1	0	0.02	0.8919	not significant
BD	0.04	1	0.04	0.18	0.6754	not significant
CD	0	1	0	0.01	0.9138	not significant
Residual	2.9	14	0.2			
Lack of Fit	2	10	0.2	0.98	0.5583	not significant
Pure Error	0.8	4	0.2			

Table 9: Model summary statistics for Response Bead Geometry Parameters.

Bead geometry parameters	Std. Dev.	Mean	C.V. (%)	PRESS	(R ²)	Adjusted (R ²)	Predicted (R ²)	Adequate Precision (AP)
W	0.33	17	1.91	7.28	0.967	0.935	0.845	22.143
P	0.28	7.59	3.72	5.09	0.98	0.96	0.908	25.087
R	0.21	3.61	5.75	2.75	0.965	0.93	0.841	24.08
WPSF	0.099	2.34	4.24	0.71	0.967	0.934	0.829	18.614
WRF	0.452	5.01	9.03	12.08	0.923	0.846	0.675	15.638

All the fitted models are found to be significant. Since for all the responses, the probability of F (Prob. > F) are observed to be less than 0.0001. In other words, there is only a 0.01% chance that "Model F-Value" larger than those reported in Tables 4a and 5a could occur due to noise. The values of "Prob > F" less than 0.05 observed for some factors involved in model equations, indicate that the contribution of these terms to the model is significant. On the other hand, the value of "Prob > F" greater than 0.10 indicates that the impact of model terms are not significant.

2.6. Validation of models:

To test the accuracy of the models in actual applications, conformity test runs were conducted by assigning different values for process variables within their working limits. Specimens were cut from the conformity test plates and their bead profiles were traced. All bead dimensions were measured. The percentage of errors, which give the deviation of predicted results of responses from the actual measured values, were also calculated and presented in Table 10. It is found from the table that the average error for all models is less than 3%.

Table 10: Comparison of actual and predicted values of weld bead parameters.

S. No.	Process variables in coded form				Predicted values of bead parameters			Actual values of bead parameters			% Error		
	A	B	C	D	W	P	R	W	P	R	W	P	R
1	1	-1	0	1	17.83	6.48	3.24	17.29	6.54	3.3	-3.02	1	1.85
2	0	0	0	1	17.28	6.53	3.27	17.63	6.51	3.19	2.02	-0.003	-2.44
3	-1	0	-1	1	16.17	7.3	4.66	16.63	7.12	4.62	2.87	-2.46	-3
4	1	1	0	1	18.89	7.37	2.79	18.87	7.39	2.82	-0.1	0.27	1.07
5	0	-1	0	0	17.45	6.33	2.6	17.57	6.51	2.67	0.68	2.84	2.69
6	0	1	0	0	18.03	8.23	2.98	18.12	7.99	3.06	0.49	-2.91	3

3. Analysis of results and discussion:

The mathematical models developed above can be employed to predict the geometry of weld bead and shape relationships for the range of parameters used in the investigation by substituting their respective values in coded form. Based on these models, the main and the interaction effects of the process parameters on the bead geometry were computed and plotted as depicted in Figs. 1-13. The results show the general trends between the cause and effect.

3.1. Direct effects of process variables on bead geometry:

Fig.1 shows effect of process parameters on bead width. It is apparent that bead width increases with for all values of open circuit voltage. As shown in Fig. 1 bead width (W) increases from 17.24 to 19.70 mm with the increase in open circuit voltage from 32 to 38 volts. It can be attributed to the increase in arc length with the increase in open circuit voltage, which in turn results in spreading of the arc cone at its base which results in more melting of work piece instead of penetrating the plate. This extension in bead width causes corresponding reduction in penetration and reinforcement. In fact excessive increase in voltage can result in nearly flat bead. Bead width increases from 17.44 to 18.03 mm with increase in welding current from 375 to 475 amperes. This effect is due to increase in heat input and the weight of the weld metal deposited [13]. These factors contribute to increase in weld pool size and consequently increase the bead

width. As shown in Fig.1, Weld bead width decreases steadily with the increase in welding speed. The bead width decreases from 19.04 to 16.92 with increase in welding speed from 24 to 30 m/hr. This negative effect of speed on W is due to the fact that when speed increases, the thermal energy transmitted to the base plate from the arc or line power per unit length of the weld bead decreases and less filler metal is deposited per unit length of weld bead, resulting in thinner and narrower weld bead. Hence, at lower travel speeds, the weld bead is larger in mass, whereas at higher travel speeds, it is lesser in mass. If speed decreases, the bead becomes wider, flatter and smoother [14]. It can be explained on the basis of decrease in metal deposited rate and heat input with the increase in welding speed. The bead width increases from 17.44 to 18.04 mm with change in current from 375 to 475 amperes. The combined effect of these factors results in decrease in bead width with the increase in welding speed. The effect of basicity index on bead width is not significant.

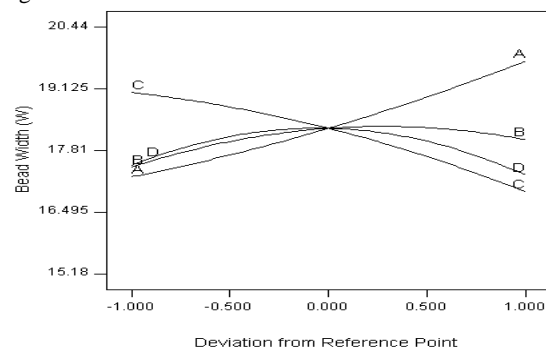


Figure 1: Effect of process parameters on bead width.

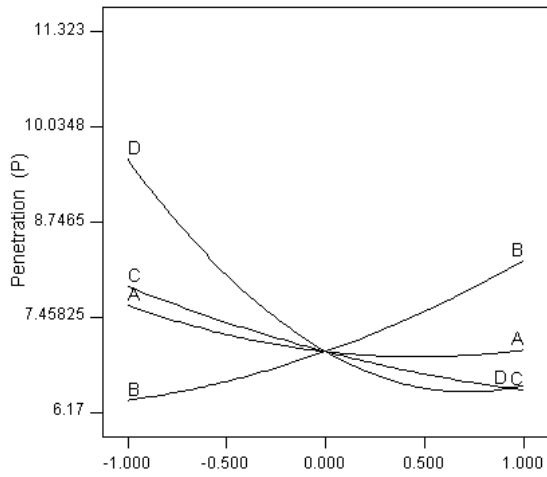


Figure 2: Effect of process parameters on Penetration.

As shown in Fig.2, the penetration (P) increases from 6.33 to 8.22 mm with the increase in welding current from 375 to 475 amperes. Increase in current gives rise to enhanced line power per unit length of the weld bead and higher current density, causing larger volume of the base material to melt and hence, deeper penetration. As current increases the temperature and hence the heat content of the droplets increases, which results in more heat being transferred to the base material. Increase in current also increases momentum of the droplets, which on striking the weld pool causes a deeper penetration. An increase in welding current, with other variables remaining constant, results in increased depth of penetration and weld width, increased deposition rate and increased weld bead size and shape at a given cross-section. It is also attributed to the increase in digging power of the arc with the increase in welding current. As the current increases, the intensity of the arc and hence the digging power of the arc and penetration increases. As depicted in Fig.3, the penetration decreases from 7.86 to 6.47 mm with the increase in welding speed from 24 to 30 m/hr. This could obviously be due to the reduced line power per unit length of weld bead as speed increases. Also, at higher welding speeds, the electrode travels faster and covers more distance per unit time. The combined effects of lesser line power and faster electrode travel speed results in decreased metal deposition rate per unit length of weld bead [12]. It is also attributed to decrease in heat input, metal deposition rate and digging power of the arc with the increase in welding speed resulting in decrease in weld metal penetration. From Fig.3, P decreases from 7.61 to 7.01 when open circuit voltage increases from 32 to 38 volts. This is obviously due to the fact that the increase in voltage results in increased arc length and spreading of arc cone at its base which results in more melting of work piece surface instead of penetrating the plate. In fact, excessive increase in voltage can result in nearly flat bead. Flux basicity also influences the penetration. It is observed from Fig.3, the higher value of penetration i.e 9.59 mm is obtained with using low basicity index flux (0.7), because low basicity index fluxes have high viscosity which enhances the tendency of heat concentration in the narrow zone and hence high penetration. This is consistent with the study conducted by Gupta [15].

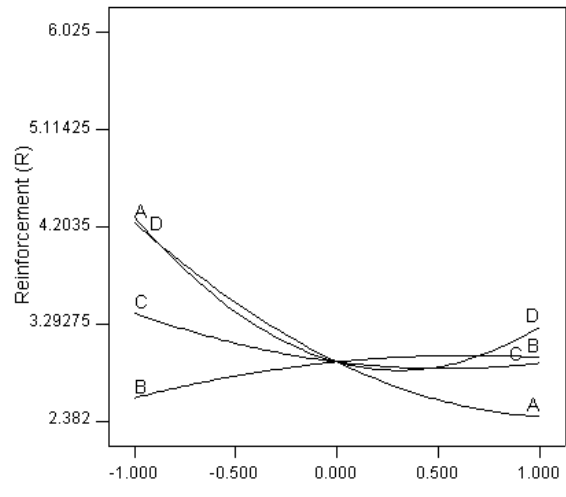


Figure 3: Effect of process parameters on Reinforcement.

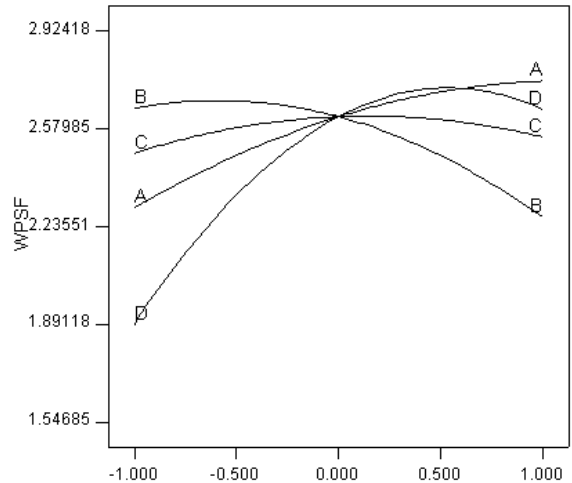


Figure 4: Effect of process parameters on WPSF.

From Fig. 3 it is observed that the reinforcement (R) decreases with the increase in open circuit voltage and welding speed and increase with the increase in welding current. Reinforcement decreases with increase in basicity index due to similar reasons as described for penetration. It is seen from this graph that reinforcement decreases from 4.24 to 2.42 mm with change of voltage from 32 to 38 volts, and decreases from 3.39 to 2.92 mm when welding speed increases from 24 to 30 m/hr. When current changes from 375 to 475 amperes, it changes from 2.59 to 2.97 mm. Its value increases from 4.29 to 3.26 mm with increase in basicity index from 0.6 to 1.2. The reasons for these changes are due to same reasons as described in preceding section for penetration.

Fig.4 and Fig. 5 shows Weld penetration shape factor (WPSF) increases from 2.37 to 2.67 and with the increase in open circuit voltage from 32 to 38 volts and weld reinforcement form factor WRF increases from 4.78 to 7.02 with increase of open circuit voltage from 32 to 38 volts. This positive effect of voltage on both the factors is due to the following reasons. Bead width (W) increases almost steadily but P and R decrease little as voltage increases from -1 to +1 limit as discussed already. Hence,

they increase steadily as voltage increases. WPSF decreases when current increases, but it remains nearly constant from 375 to 400 amperes and it decreases from 2.61 to 2.44 (Fig.5) when current changes from 375 to 475 amperes. This could be due to reason that WPSF which is the ratio of W/P, decreases when current changes from 400 ampere to 475 amperes, because rate of increase of P is more than that of W with in this range of current. It is also observed in Fig.5 that WPSF increases 1.82 to 2.42 with increase of basicity index from 0.6 to 1.2. It is seen from Fig.6 that WRFF decreases from 4.05 to 5.23 with increase of basicity index from 0.6 to 1.2. These results can be explained with the help of effects of welding variables on weld width, penetration and reinforcement respectively.

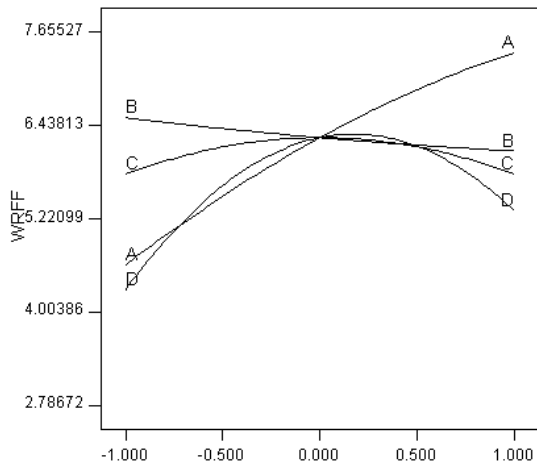


Figure 5: Effect of process parameters on WRFF.

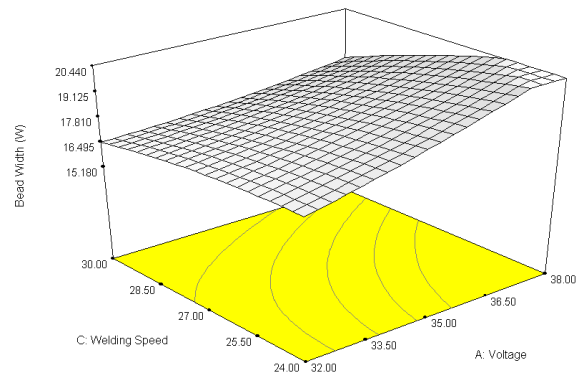


Figure 6: Interaction effect of voltage and speed on bead width.

3.2. Interaction effects of process variables on bead geometry:

3.2.1. Interaction effects on bead width (W) and penetration (P):

It is apparent from Fig. 6 showing interaction of open circuit voltage and welding speed on W that the increase in voltage increases W for all values of speed. The bead width increases from 17.40 to 21.07 mm and from 16.49 to 17.75 mm with the increase in voltage from 32 to 38 volts, at the welding speed 24 and 30 m/hr respectively. It shows that the increasing trend of bead width with the increase in open circuit voltage decreases with the increase in welding speed. It is due to the fact that open circuit voltage has a positive effect whereas welding speed has negative effect on bead width. Therefore the combined effect of these

parameters causes the decrease in increasing trend of bead width with the increase in open circuit voltage.

From the response surface plot in Fig.7, it is evident that P increases with the increase in welding current for all values of welding speed. It shows that the weld metal penetration increases from 6.63 to 9.67 mm and from 6.38 to 7.12, with increase in current, at the welding speed of 24 to 30 m/hr respectively. The rate of increase in P with the increase in current decreases gradually as speed increases. These effects on P are due to the reasons that current has positive effect but speed has a negative effect on P as discussed already in the direct effects of current and speed on P. It is found that at lower values of speed, the positive effect of current on P is stronger but at higher values of speed, the negative effect of speed on P is stronger. This is also consistent with the findings of Rayes [16]. From the contour surface, it is noted that P is maximum (about 9.67 mm) when current and speed are at their maximum (+1) and minimum (-1) limits, respectively, and the lowest value of P (about 6.004 mm) is obtained when current and speed are at their minimum and maximum limits, respectively. From Fig.8 it is observed that penetration increases from 8.45 to 11.31 mm and from 6.38 to 7.28, with increase in current, at the basicity index of 0.6 and 1.2 respectively. It is evident form Fig.10 that penetration decreases form 10.91 to 8.63 and from 6.97 to 6.45 with increase in welding speed from low basicity index to its higher value. These results can be explained with the help of effects of welding variables such as welding speed and basicity index penetration.

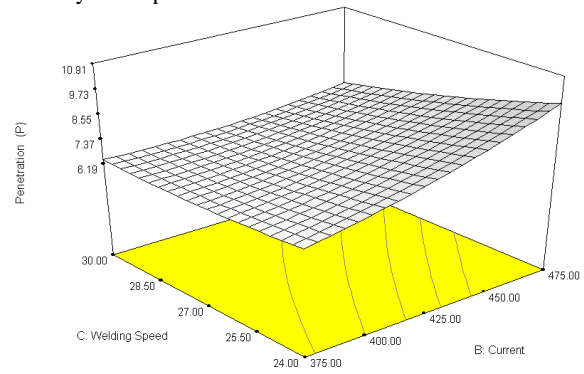


Figure 7: Interaction effect of current and speed on penetration.

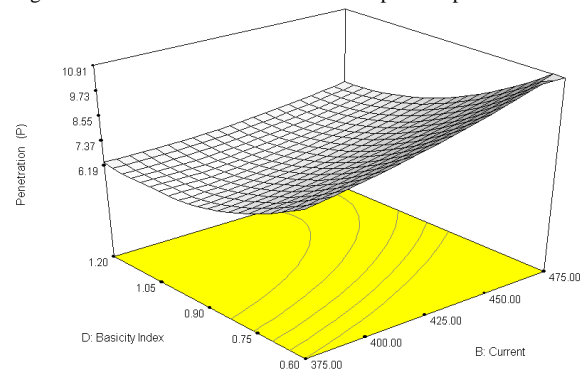


Figure 8: Interaction effect of current and basicity index on penetration.

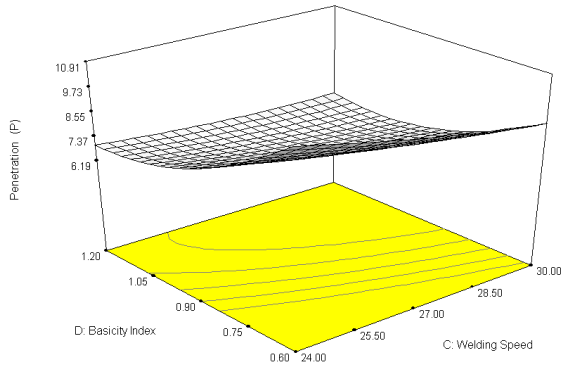


Figure 9: Interaction effect of speed and on basicity index on Penetration.

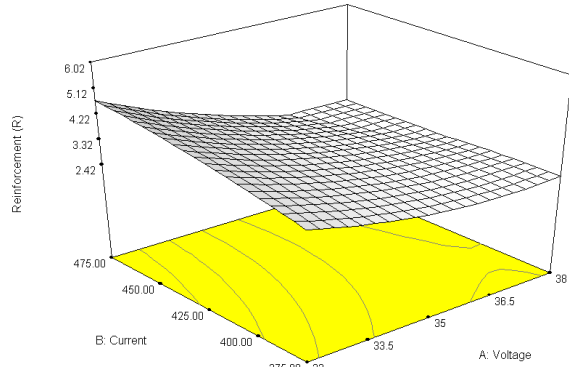


Figure 10: Interaction effect of voltage and current on Reinforcement.

3.2.2. Interaction effects on reinforcement (R), WPRF and WPSF:

It is observed in Fig.10 and 11 that reinforcement decreases with the increase in voltage, when the current changes from 375 to 475 amperes and it also decreases with voltage from low basicity index to its higher value. These interaction effects can be explained on the basis of effect of voltage, current and basicity index on reinforcement. Voltage has positive effect on reinforcement whereas current has negative effect on reinforcement. The negative effect is dominant while considering the interaction of voltage and current. Reinforcement decreases with increase in voltage from 32 to 38 volts, for all values of current.

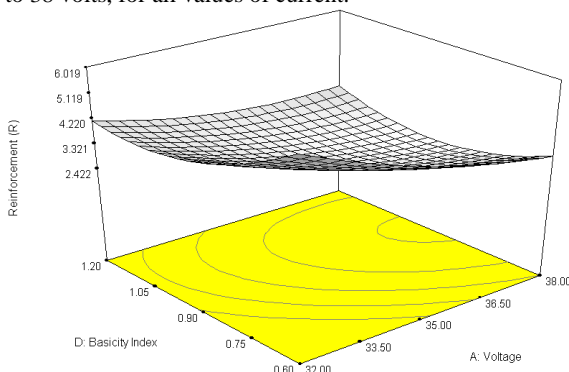


Figure 11: Interaction effect of voltage and basicity index on reinforcement.

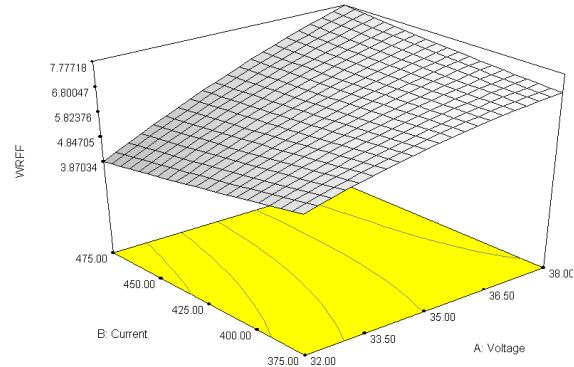


Figure 12: Interaction effect of voltage and current on WRRF.

Fig.12 shows the interaction effect of voltage and current on WRRF. It is evident from these graphs that WRRF increases for all values of current when voltage increases from 32 to 38 volts. But the increasing trend of WRRF is more at higher value of current i.e. at 475 amperes that that at 375 amperes. This is due to fact that $WRRF = W/R$, W increases with increase of voltage and nearly remains constant with change of current whereas R decreases with increasing voltage and increases with increase of current [17]. Thus voltage has positive effect on WRRF whereas current has negative effect on WRRF. This increasing trend of WRRF at higher current is due to more positive effect of voltage on WRRF. This can also be explained on the basis of effects of voltage and current on bead width and reinforcement. The interaction effects of welding speed and basicity index on WPSF can also be explained due to the effect of welding speed and basicity index on bead width and penetration (Fig. 13).

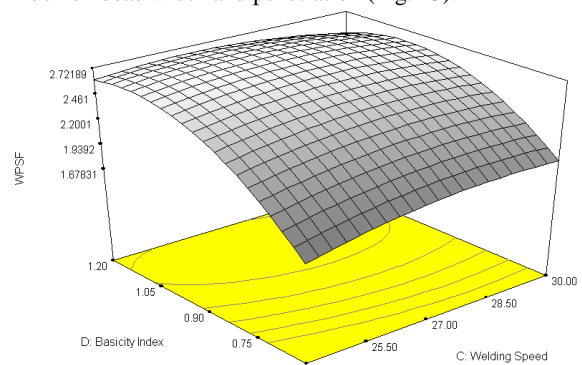


Figure 13: Interaction effect of Speed and basicity on WPSF.

4. Conclusion

In the present study, detailed experimentation and analyses have been carried out in order to emphasize the extent of utilizing developed flux prepared from waste flux dust in the conventional SAW, on different bead geometry parameters like: weld penetration shape factor, weld reinforcement form factor, bead width, penetration and reinforcement. The important parameters, which significantly affect these bead quality characteristics, have also been identified by ANOVA technique. Within limitations of the present work, the following conclusions are summarized as follows:

- Response surface methodology Box-Behnken Design (BBD) can be employed easily for developing mathematical models for predicting important weld

bead dimensions and shape relationships within the optimal range of process control variables for SAW.

- The models developed can be employed easily in automated or robotic welding in the form of a program, for obtaining the desired weld bead dimensions.
- Out of the four process variables considered, welding current had a significant positive effect but welding speed had an appreciable negative effect on most of the important bead parameters. Penetration (P) increased by 2 mm with the increase in welding current from 375 to 475 amperes whereas penetration decreased by about 1.4 mm with the increase in welding speed from 24 to 30 m/hr. The bead width decreased by 2.12 mm with increase in welding speed from 24 to 30 m/hr. Reinforcement decreased from 3.39 to 2.92 mm when welding speed increases from 24 to 30 m/hr, but when current changed from 375 to 475 amperes, it value increased from 2.59 to 2.97 mm.
- Open circuit voltage had a negative effect on penetration, but more significant negative effect was observed on reinforcement. Voltage had a significant positive effect on bead width, weld penetration size factor and weld reinforcement form factor.
- The interaction of welding current and speed had an appreciable effect on penetration and penetration size factor, but this interaction had not any significant effect on bead width and reinforcement form factor. Penetration increased with the increase in current for all values of welding speed but this increasing rate of the penetration with the increase in B gradually decreased with the increase in C.
- The interaction of voltage and current had significant effect on reinforcement and weld reinforcement form factor effect as compared to its effect on other response parameters. Reinforcement decreased with the increase in voltage for all values of current whereas WRFF increased with voltage for all current values. Positive effect of voltage was more dominant in WRFF as compared to negative effect of current for the trends in case of WRFF, whereas reverse is the case for reinforcement. This increasing trend of WRFF at higher current was due to more positive effect of voltage on WRFF.

Thus it is seen that with in the present experimental domain, using the developed flux prepared from waste flux dust had no adverse effect on bead geometry. Detailed experimentation on the effect of developed flux on mechanical properties and metallurgical characteristics of the weldment to be rigorously done. If the outcomes becomes positive, then developed flux prepared this way can be recommended to use as an alternative to fresh flux in practical situations to yield 'waste to wealth'.

Acknowledgment

The authors wish to thank Thapar University, Patiala and Punjab Engineering College Chandigarh for providing the facilities for carrying out the experiments in undertaking this work.

References

- [1] Parmer R S. Welding Processes and Technology. New Delhi: Khanna Publishers; 1992.
- [2] Houldcroft PT. Submerged Arc Welding. second ed., Cambridge, England: Abington Publishing; 1989.
- [3] Brien RL. Welding Handbook. vol.2, 8th edition, Miami, U.S.A: American Welding society; 1978.
- [4] Vinod. K, N. Mohan , J.S. Khamba, "Development of cost effective agglomerated fluxes from waste flux dust for submerged arc welding" . Proceedings of World Congress on Engineering, , Imperial College, London, 2009.
- [5] N. Murugan, R.S. Parmer, S.K. Sud, "Effect of submerged arc process variables on dilution and bead geometry in single wire surfacing". J. Mater. Process. Technol, Vol.37, 1993, 767-780.
- [6] V.K. Gupta, R.S. Parmer, "Fractional factorial technique to predict dimensions of the weld bead in automatic submerged arc welding". J. Inst. Eng. (India), Vol. 70, 1989, 67-86.
- [7] Myers R, Montgomery D. Response surface methodology. New York: John Wiley & Sons; 2004.
- [8] S. Datta, A. Bandyopadhyay, P.K. Pal , "Quadratic response surface modeling for prediction of bead geometry in submerged arc welding". Indian Weld J, Vol. 38, No.4, 2006, 33-43
- [9] S. Datta, M. Sundar, A. Bandyopadhyay, P.K. Pal, G. Nandi, S.C. Roy, "Statistical modeling for predicting bead volume of submerged arc butt welds". Australas Weld J, Vol. 51(2), 2006, 39-47.
- [10] Horng. Jenn. Tsong, Liu. Nun. Ming, Ko. Ta. Chiang. "Investigating the machinability of hardfield steel in hard turning with Al₂O₃/TiC mixed ceramic tool based on response surface methodology". J. Mater. Process. Technol, Vol. 208, 2008, 532-541.
- [11] G.E.P. Box, D.W. Behnken, "Some new three level designs for the study of quantitative variables". Technometrics, Vol.2, 1960, 455-475.
- [12] Box GEP, Hunter WG, Hunter JS. Statistics for experimenters: an introduction to design, data analysis, and model building. New York: John Wiley & Sons; 1976.
- [13] V. Gunuraj, N. Murgun, "Application of response surface methodology for predicting weld bead quality in submerged arc welding of pipes". Journal of material processing technology, Vol.88, 1999, 266-275.
- [14] Olson D L, Dixon R, Liby AL. Welding Theory and Practice. North-Holland Publication; 1990.
- [15] S.R. Gupta, P.C. Gupta, "Investigate into flux consumption in submerged arc welding". Indian welding journal, Vol. 21, No. 3, 1988, 365-369.
- [16] M. El. Rayes, "The influence of various hybrid welding parameters on bead geometry". Welding Journal, Vol. 85, No.5, 2004, 147s-155s.
- [17] S. Datta, A. Bandhopadhayaay, P.K. Pal, "Modeling and optimization of features of bead geometry including percentage dilution in submerged arc welding using mixture of fresh and fused flux". International Journal of advanced Manufacturing Technology, Vol. 36, No.11, 2008, 1080-1090.

Appendix

Notations

- P: Penetration
 RSM: Response surface methodology
 R: Reinforcement
 W: Bead width
 WPSF: Weld penetration size factor
 WRFF: Weld reinforcement form factor

Experimental Energy Study for Domestic Hot Water Storage Tanks

N. Beithou^{*a}, M. Abu Hilal^b

^aDepartment of Mechanical and Industrial Engineering, Applied Science University, 11931, Amman, Jordan

^bDepartment of Mechanical Engineering, An-Najah National University, Nablus, Palestine

Abstract

In the last decade, energy and water become the most important commodities as the world is suffering from a critical shortage in water and energy. Researchers are working hard on renewable energy, and energy saving. In this paper, an experimental study of the usable energy for domestic hot water storage tank was performed. Different supply features and different flow rates have been considered. To save energy in the storage tank, the turbulent mixing must be eliminated. In this study a cover over the supply lines was imposed. It has been found that the cover for the side supply feature improves the temperature distributions in the tank. For the bottom supply feature investigations indicated important improvement in the total usable hot water. Approximately 17% saving in usable hot water was achieved by using a round curved cover on the bottom supply line. The achieved saving in energy and hot water will help in reducing the consumed energy in residential buildings and thus keep us in a better environment.

© 2011 Jordan Journal of Mechanical and Industrial Engineering. All rights reserved

Keywords: Water Supply; Domestic Storage Tank; Hot Water Management; Energy Saving; Usable energy

1. Introduction

Recently, world starts suffering from critical shortage in energy. Most of the countries are non-oil producing countries that imports their energy from other countries. The significant increase in demand for energy by several emerging nations has driven the global energy consumption to unprecedented levels. As a result, the cost of energy has reached new levels and is expected to continue to rise. The ramifications of this large increase in energy cost, will pose serious challenges to the economies of most developing nations. Recently, the energy consumption for the residential sector in Jordan has jumped to 30% of the total consumed energy in the country [1]. This impose a heavy load on the national researchers to minimize the energy consumption in the residential buildings. Minimizing heat losses and reducing hot water consumption were the goals of different researchers over the past years. Therefore, different residential hot water systems, use patterns, and loads are investigated in [3,5,7,8,10]. Other researches studied insulation to reduce heat losses in the HWST [6,11]. Special heat exchangers were considered by Industrial Technology to recover the energy wasted during usage.

The studies were not limited to thermal insulation and reduction of water losses, many researchers attached the problem from managerial directions, such as water and water resources management in Abu-Dhabi [16], the role of women and modern water supply systems [9], water management practices [4], and demand side management [17]. Experimental analyses of hot water behavior in static mode of a full scale domestic electric HWST [13,18] have been done for different heating and cooling periods. The analyses reveal that thermal stratification is mainly

dependent on the initial water temperature. The dynamic mode of HWST was analyzed by N. Beithou [12] and J. F. Seara et al. [14]. They analyzed different inlets and outlets of practical interest, and they proposed to use certain features to minimize the thermal stratification.

As creating new resources of water and clean energy is a hard task, some efforts were directed toward conservation and managing the available resources. Actually conservation of resources can be defined as more efficient or effective use of resources.

This study is directed to more effective use of the available energy in the HWST. Firstly it investigates deeply the hot water temperature variations within the HWST for two different supply features: bottom and side supply. Secondly the study proposes to eliminate the expected turbulent mixing by introducing a simple cover on the supply lines, then analyzes the resulting temperature distributions in both cases and concluded the best solution.

2. Experimental Test Rig

Available HWSTs in the market suffer from scientific support as shown in Figure 1., they engorge turbulent mixing of cold water with the available hot water in the HWST that reducing the delivered amount of usable hot water.

* Corresponding author. e-mail: nabil@asu.edu.jo

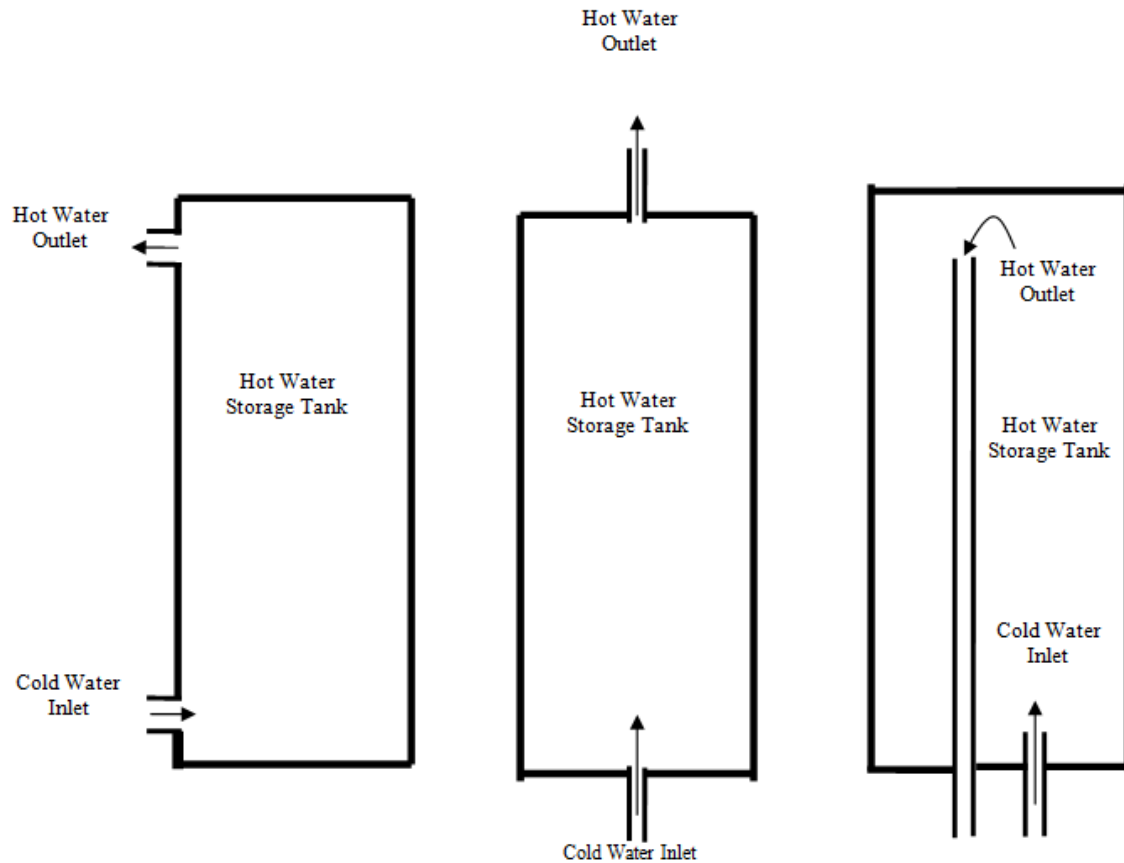


Figure 1: Features of hot water storage tanks in markets.

In the literature, scientists noticed the abovementioned problem. They tried to propose different solutions such as double hot water tanks, where the cold water enters the cooler tank and hot water leaves the hotter tank thus allowing mixing but with a lower temperature differences. Another solution was proposed by introducing a membrane to separate cold water from the hot water ASHRAE [2]. The proposed techniques seem to be costly and difficult to be implemented specially in the developing countries. Simpler and practical ideas were proposed by

investigating the supply features of the DHWST [14, 15]. Jose' et. al. [14] constructed a tank with different supply features to study dynamically the operation of a domestic hot water storage tank as shown in Figure 2.(a). The supply feature i2 was found to be the best of the investigated supply lines. On the other hand, Lana et. al.[15] investigated experimentally and numerically the thermal stratification in a solar domestic hot water system as shown in Figure 2.(b).

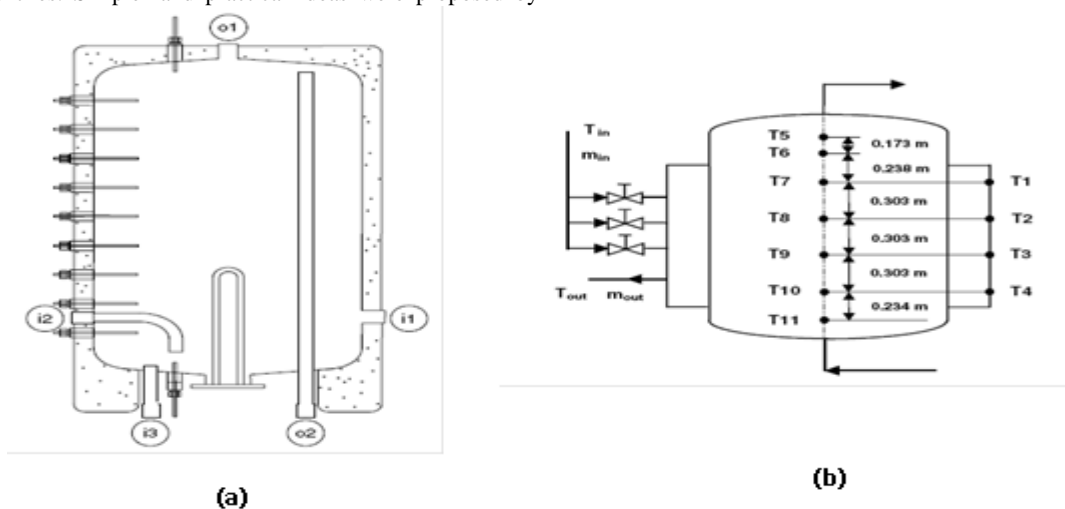


Figure 2: Schematic diagrams of proposed test HWST (a) Jose, [14] and (b) Lana [15].

In this study and aiming to eliminate the turbulent mixing between cold and hot water, the supply features were studied for both: side and bottom supply. Then simple practical covers over the supply lines have been imposed to minimize the mixing effects as shown in Figure 3.

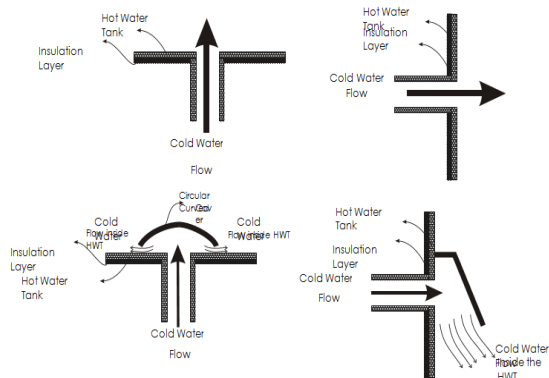


Figure 3: Supply features with the proposed cover.

In order to analyze and investigate the nature of hot water temperature variations within the HWST, data on the variation of the hot water temperatures should be collected under the different variable conditions. To achieve these data, an experimental rig has been constructed as shown in Figure 4. This rig consists of hot water reservoir, cold water reservoir, water pump, flow meter, hot water storage tank, and Data Acquisition System (DAS) (Lab-View software). The DAS automatically collect the temperatures from the storage tank at different times and positions then stores them in a separate excel file.

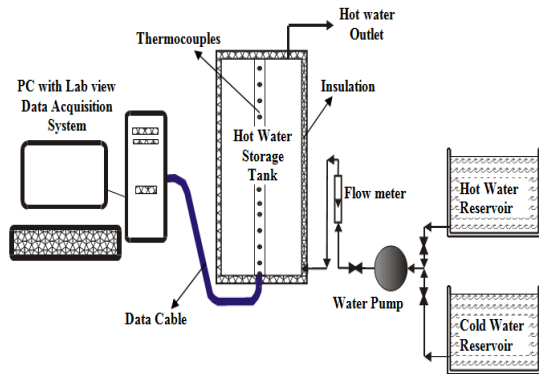


Figure 4: Schematic diagram for the experimental rig.

In the experiments performed, hot water is filled into the HWST from the hot water reservoir, circulated until having a uniform temperature of 62 °C inside the tank; then the cold water is pumped from the cold water reservoir at a specific flow rate into the HWST through the supply line, either from side or bottom of the tank and mixed with the hot water, the temperature-changes resulting from the mixing process are then recorded for analyses purposes.

The dimensions of the HWST are listed in Table 1. This tank has a total capacity of 108 liters and is provided with 15 thermocouples mounted at the middle of the HWST to record the temperatures throughout the tank. Different supply flow rates were considered to understand the effect of flow rates on the mixing and heat transfer between the hot and cold water inside the HWST.

Table 1: Dimensions of the hot water storage tank.

Hot Water Storage Tank	
Height	0.78 m
Internal diameter	0.42 m
Number of thermocouples	15
Distance between thermocouples	0.05 m
Insulation thickness	0.04 m
Tank total capacity	0.108 m ³

3. Experiments Performed

In this study, bottom and side supply lines were considered. Experiments were performed for different low and high flow rates and for covered and uncovered supply lines.

3.1. Side Supply Feature: Without Cover:

The side supply feature was considered to understand the mixing nature of cold and hot water if no cover is used. Different flow rates were executed in this part. The temperatures all over the HWST were collected and then plotted in order to find the influence of the considered flow rates on the temperature distributions in the tank versus time. Experiments were done first for flow rates of 1.9, 3.5, and 10 L/min without using a cover on the supply line.

In the plotted figures the most left curve represents the lowest thermocouple, whereas the most right curve represents the highest thermocouple, the distance between each two thermocouples is 5 cm. Figure 5. shows the temperature distributions for the 15 thermocouples located inside the HWST for the case of uncovered supply line with flow rate 1.9 L/min. It indicates smooth temperature distributions from the first to the last thermocouples in the tank.

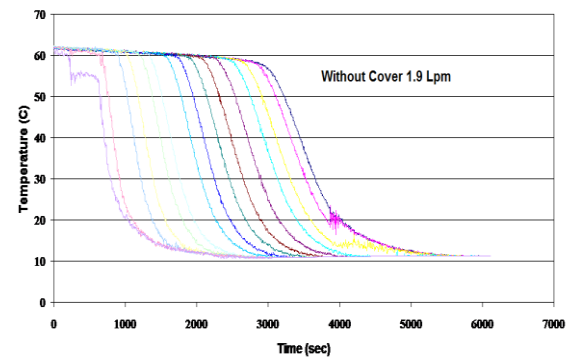


Figure 5: Temperature distributions of the 15 thermocouples versus time. Side supply without cover. Flow rate = 1.9 L/min.

In this study a minimum usable hot water temperature of 42 oC is selected. With such a usable temperature a total amount of 100 Liters was achieved.

The flow rate of cold water is then increased up to 3.5 L/min. The obtained data are plotted in Figure 6. The figure shows smooth temperature distributions in the tank as the previous case, but a total usable hot water of about 95 Liters was achieved.

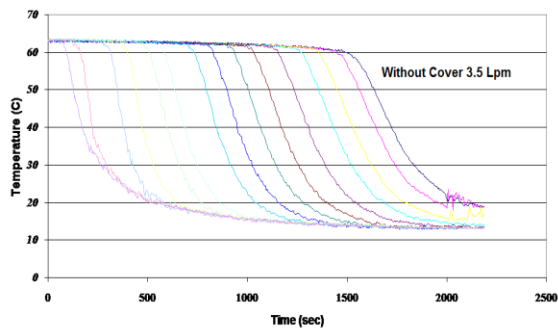


Figure 6: Temperature distributions of the 15 thermocouples versus time. Side supply without cover. Flow rate = 3.5 L/min.

Finally, the cold water flow rate was increased up to 10 L/min. The obtained data were plotted in Figure 7.

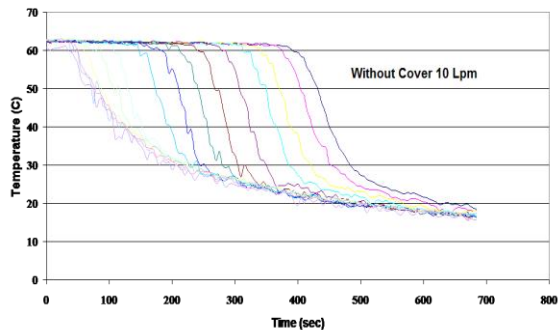


Figure 7: Temperature distributions of the 15 thermocouples versus time. Side supply without cover. Flow rate = 10 L/min.

It is obvious from the figure that as the flow rate increases, the temperature distributions start having fluctuations which affect the total usable hot water from the hot water tank. For instance, the 10 L/min cold water flow rate reduces the usable hot water capacity down to 70 liters.

3.2. Bottom Supply Feature: Without Cover:

Most of the tanks in the market implement the bottom supply feature because it is easy for manufacturing. In order to investigate this supply feature, experiments were performed for flow rates of 3, 6, and 9 L/min without using a cover on the supply line. The temperatures all over the HWST were collected and then plotted to find the influence of the considered flow rates on the temperature distributions in the tank versus time.

Figure 8 shows the temperature distributions for the case of 3 L/min. flow rate without cover. Compared with the side supply feature, higher fluctuations were observed and lower total usable hot water was obtained. This behavior becomes clearly noticeable as the flow rate increases. Figures 9 and 10 show the temperature distributions for 6 and 9 L/min, respectively. It is obvious that the temperatures become highly fluctuating and the usable hot water is reduced dramatically. This emphasizes the bad effects of using bottom supply feature, especially for high flow rates.

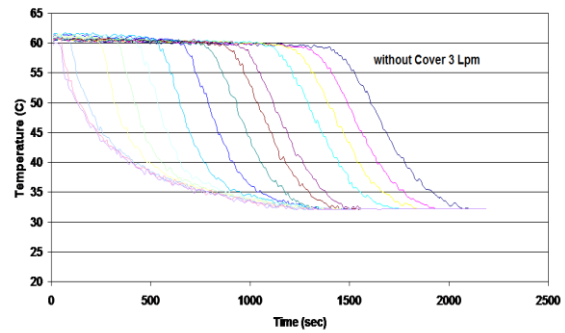


Figure 8: Temperature distributions of the 15 thermocouples versus time. Bottom supply without cover. Flow rate = 3 L/min.

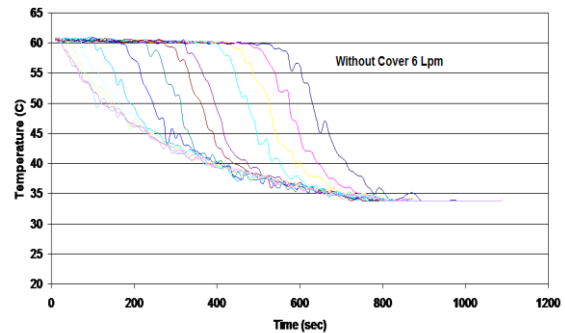


Figure 9: Temperature distributions of the 15 thermocouples versus time. Bottom supply without cover. Flow rate = 6 L/min.

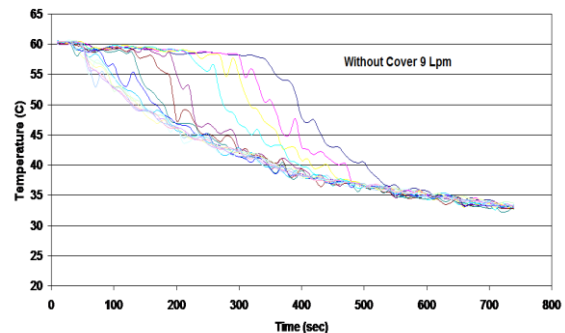


Figure 10: Temperature distributions of the 15 thermocouples versus time. Bottom supply without cover. Flow rate = 9 L/min.

Figure 11 shows the total usable hot water versus cold water flow rate for side and bottom supply features. The figure indicates that the side supply feature yields better results than bottom supply feature in the case of uncovered supply lines.

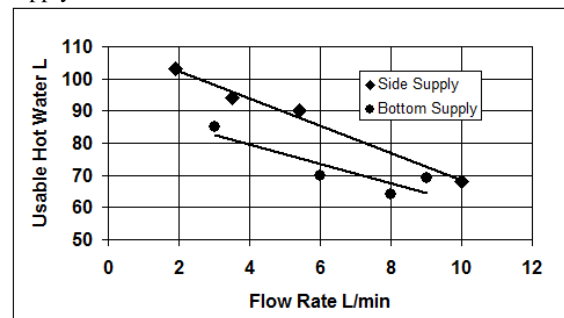


Figure 11: Total usable hot water versus cold water flow rate for bottom and side supply of cold water.

3.3. Side Supply Feature: With Cover:

As noted above, the bottom supply feature reduces dramatically the amount of usable hot water. This is mainly because of the turbulent mixing between cold and hot water inside the tank. Jose´ et. al. noted this problem, they constructed a tank with different supply features to study the operation of a domestic hot water storage tank. The supply feature i2 [figure 2.(a)] was found to be the best from the investigated supply lines, as it introduces the water to the bottom of the storage tank; this has mainly improved the amount of the usable hot water especially for the medium flow rates. In high flow rates the water will clash with the bottom of the tank and splash upward again. As the main purpose of this study is not to limit consumer with low flow rates, a simple practical covers were imposed on the supply lines to distribute the supplied water at high flow rates in a uniform manner. The side supply line was covered with a plate to forbid the water from flowing upward after sticking the far side of the tank. Figure 12. represents the temperature distributions all over the tank for cold water flow rate 3 L/min.

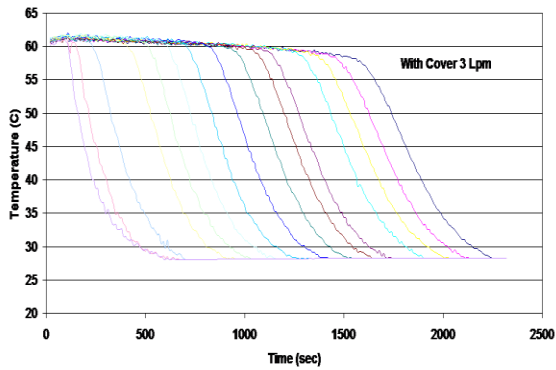


Figure 12: Temperature distributions of the 15 thermocouples versus time. Side supply with cover. Flow rate = 3 L/min.

By comparing the related figures for side supply with and without cover Figures 6, and 12 it is noted that the curves become smoother whereas the amount of the usable hot water supply does not show distinguished differences.

Figure 13, and 14 show temperature distributions for side supply line with cover, for cold water flow rates of 6 and 15 L/min respectively.

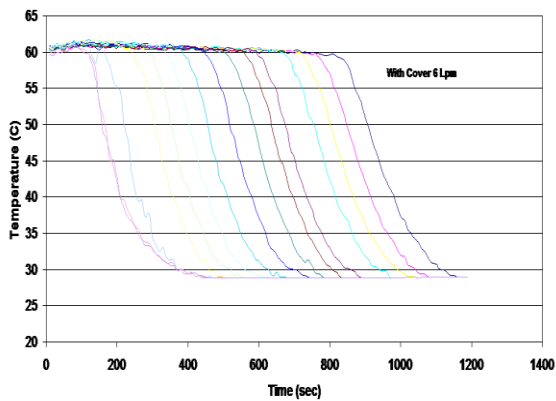


Figure 13: Temperature distributions of the 15 thermocouples versus time. Side supply with cover. Flow rate = 6 L/min.

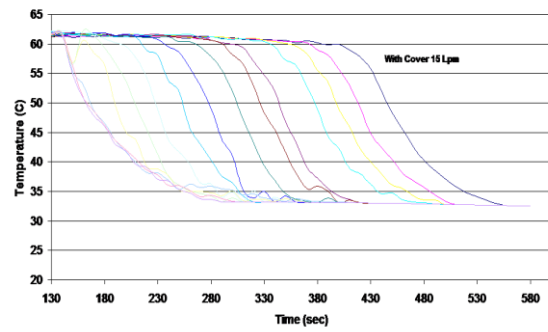


Figure 14: Temperature distributions of the 15 thermocouples versus time. Side supply with cover. Flow rate = 15 L/min.

It was very interesting to notice the differences between the related figures 13 and 14. As the flow rate increases the used cover over the supply line eliminated the fluctuations in the temperature distributions even for the high flow rates. This results in slightly higher amounts of usable hot water as shown in Figure 15 and the more important uniform supply temperatures.

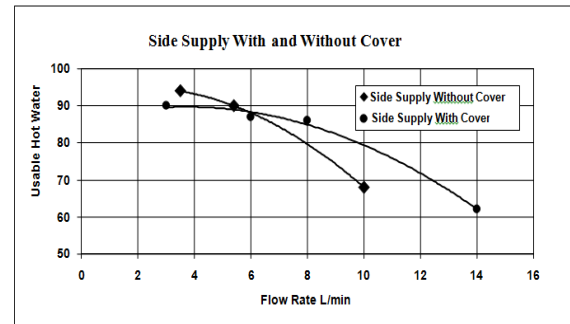


Figure 15: Usable hot water versus cold water flow rate for side supply feature.

3.4. Bottom Supply Feature: With Cover:

The bottom supply feature is considered to be easier in the manufacturing process, but it has extremely bad effects of the total usable energy in the HWST. Aiming to overcome the bad effects of high flow rates and to distribute the water smoothly and horizontally as much as possible, a round curved cover (like a cone) has been imposed on the bottom supply line. Experiments were performed for different flow rates of, 3, 6, and 9 L/min. The obtained temperature distributions are plotted in Figures 16, 17, and 18, respectively.

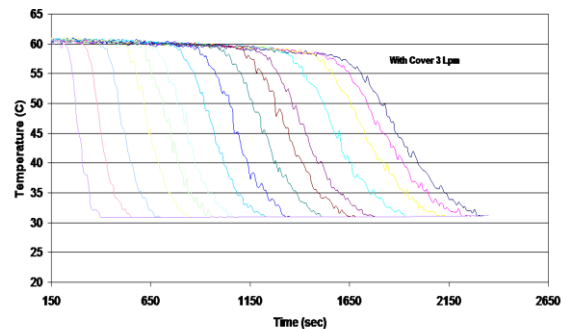


Figure 16: Temperature distributions of the 15 thermocouples versus time. Bottom supply with cover. Flow rate = 3 L/min.

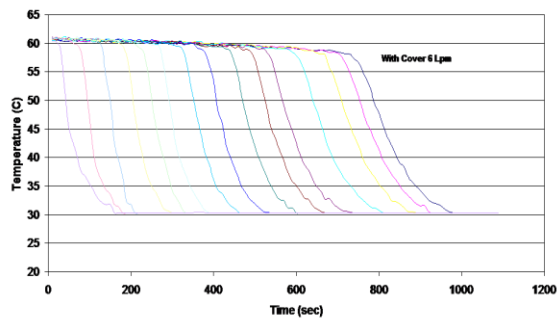


Figure 17: Temperature distributions of the 15 thermocouples versus time. Bottom supply with cover. Flow rate = 6 L/min.

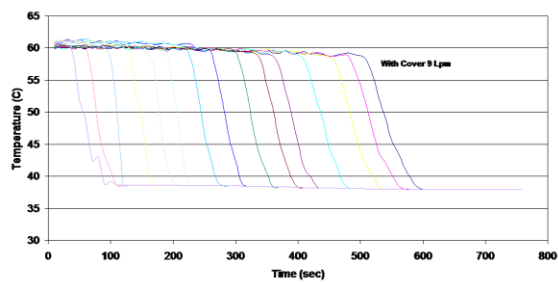


Figure 18: Temperature distributions of the 15 thermocouples versus time. Bottom supply with cover. Flow rate = 9 L/min.

Figure 16 represents temperature distributions for the covered bottom supply line with flow rate of 3 L/min. In this figure the temperature distributions for the 15 thermocouples do not show smoother curves than that in the uncovered case; that's because of the low flow rate. The distinct improvement for this flow rate lie in the total usable hot water; the uncovered case delivered 85 liters hot water whereas the covered case delivered 91 liters.

An important notice is observed in the curves for the temperature distributions of medium and high flow rates. Comparing figures 9 and 10 for the uncovered bottom flow with figures 17 and 18 for the covered bottom flow show the big improvement in the temperature distributions, that is fluctuations in side the HWST have been eliminated. Figure 18 for covered bottom flow [9 L/min] shows very smooth temperatures inside the tank and prove that water in the tank moves in laminate manner. This motion of the cold water without mixing with hot water in the HWST is the main target of this research.

Figure 19 shows the total usable hot water versus flow rate for both covered and uncovered bottom supply. The covered bottom supply delivered a noticeable increase in the usable hot water, with almost no variation with flow rate. In this way the problem of using high flow rates could be eliminated, and consumer can no more worry about the used flow rate.

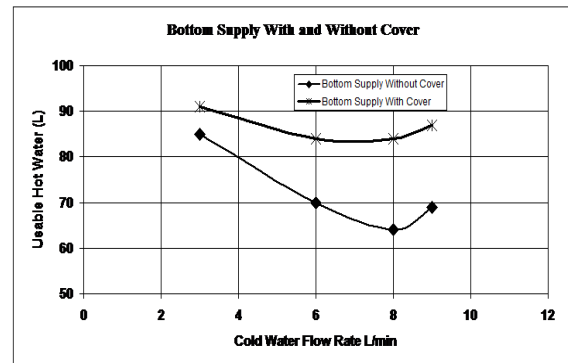


Figure 19: Usable hot water versus cold water flow rate.

Furthermore, figure 19 shows the amount of hot water saved by using the round cover on the bottom supply line. At 9 L/min the uncovered feature delivered approximately 69 liters, whereas the covered feature delivered 87 liters, with approximately 17% saving. The achieved saving in energy and hot water will help in reducing the consumed energy in residential buildings, and thus keep us in a better environment.

To eliminate completely the effects of turbulent mixing, a current study for a domestic hot water tank with a porous layer is under investigation see Figure 20.

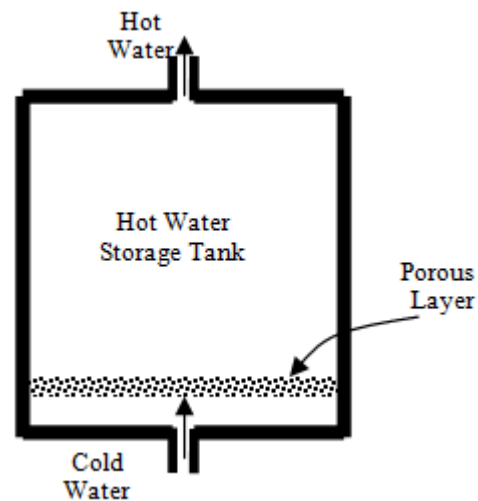


Figure 20: Domestic Hot Water Tank with a Porous Layer.

4. Conclusions

World these days suffers from critical shortage in water and energy. The reduction in water usage and energy consumption is one of the main goals of researchers. In this paper, an experimental study of the usable energy for domestic hot water storage tank was performed. Different experiments with different supply features and different flow rates have been performed. The temperature distributions for the side and bottom supply features were analyzed. To eliminate the turbulent mixing, covers over the supply lines were imposed. It has been found that the cover for the side supply feature improves the temperature distribution in the tank, but it does not show a distinguished improvement on the amount of usable hot water. As the bottom supply feature is easier in manufacturing, the investigations indicated important improvement in the total usable hot water. For 3 L/min

flow rate, the uncovered case resulted in 85 liters hot water whereas the covered case supplied 91 liters. More over, at 9 L/min the uncovered feature gave approximately 69 liters whereas the covered feature gave 87 liters, with approximately 17% saving. The achieved saving in energy

and hot water will help in reducing the consumed energy in residential buildings, and thus keep us in a better environment. To eliminate completely the effect of turbulent mixing, a current study for a domestic hot water tank with a porous layer is under investigation.

References

- [1] Al-Rawabdeh, "Role of Amman Chamber of Industry in Energy Field", German-Jordanian Workshop, 12th -14th October 2009 Amman-Jordan.
- [2] ASHRAE. Heating Ventilation and Air Conditioning Applications. ASHRAE, Inc., 1995.
- [3] K. T. Papakostas, N. E. Papageorgiou, B. A. Sotiropoulos, " Residential Hot Water Use Patterns in Greece", Solar Energy; VOL. 54, ISSUE 6, 1995, 369-374.
- [4] S. Ahmed, B. Hoque, A. Mahmud, ' Water management practices in rural and urban homes: a case study from Bangladesh on ingestion of polluted water', Public Health, Vol. 112, 1998, 317-321.
- [5] J. Wiehagen, J. L. Sikora, " Performance Comparison of Residential Hot Water Systems" NAHB Research Center, Upper Marlboro, Maryland, NREL/2003.
- [6] L. Barta, "Energy Conservation of Domestic Hot Water Distribution Systems", 27th International Symposium CIB W62 Water Supply and Drainage for Buildings, September 17-20, Portoroz, Slovenia, 2001.
- [7] H. Takata, S. Murakawa, D. Nishina, Y. Koshikawa, "An Analysis on the Load of Hot Water Consumption in the Apartment Houses", 27th International Symposium CIB W62 Water Supply and Drainage for Buildings, September 17-20, Portoroz, Slovenia, 2001.
- [8] T. Merrigan, " Residential Conservation Demonstration Program: Domestic Hot Water", Florida Solar Energy Center, Cape Canaveral (USA), Technical Report, 2001 May 13.
- [9] N. Singh, P. Bhattacharya, G. Jacks, J. Gustafsson, ' Women and Modern Domestic Water Supply Systems: Need for a Holistic Perspective', Water Resources Management, Vol. 18, 237-248, 2004.
- [10] Sezai, L. Aldabbagh, U. Atikol, H. Hacisevki, "Performance Improvement by using Dual Heaters in a Storage-type Domestic Electrical Water-Heater", Applied Energy, Vol. 81, 291-305, 2005.
- [11] N. Altuntop, Z. Kilik, V. Ozceyhan, O. Kincay, ' Effect of water inlet velocity on thermal stratification in a mantled hot water storage tank', Int. J. Energy Res., Vol. 30, 163-176, 2006.
- [12] N. Beithou, " Heat Transfer Aspects in Bottom Flow Mixing of Cold Water and Hot Water in Domestic Hot Water Storage Tank", Journal of Mechanical Engineering, Vol. 57, No. 1, 34-45, 2006.
- [13] Jose´ Ferná´ndez-Seara, Francisco J. Uhl´a, Jaime Sieres, " Experimental analysis of a domestic electric hot water storage tank. Part I: Static mode of operation", Applied Thermal Engineering, Vol. 27, 129-136, 2007.
- [14] Jose´ Ferná´ndez-Seara, Francisco J. Uhl´a, Jaime Sieres, ' Experimental analysis of a domestic electric hot water storage tank. Part II: Dynamic mode of operation', Applied Thermal Engineering, Vol. 27, 137-144, 2007.
- [15] L. Kenjo, Ch. Inard, D. Caccavelli, ' Experimental and numerical study of thermal stratification in a mantle tank of a solar domestic hot water system', Applied Thermal Engineering, Vol. 27, 1986-1995, 2007.
- [16] E. S. Al-Katheeri, 'Towards the Establishment of Water Management in Abu Dhabi Emirate', Water Resour Manage, Vol. 22, 205-215, 2008.
- [17] R. Rankin, P.G. Rousseau, ' Demand side management in South Africa at industrial residence water heating systems using in line water heating methodology', Energy Conversion and Management, Vol. 49, 62-74, 2008.
- [18] Daniel Setrak Sowmya, Racine T.A. Prado, ' Assessment of energy efficiency in electric storage water heaters', Energy and Buildings, Vol. 40, 2128-2132, 2008.



الجامعة الهاشمية



المملكة الأردنية الهاشمية

المجلة الأردنية
للمهندسة الميكانيكية والصناعية

JJIMOE

مجلة علمية عالمية محكمة

<http://jjmie.hu.edu.jo/>

ISSN 1995-6665

المجلة الأردنية للهندسة الميكانيكية والصناعية

مجلة علمية عالمية محكمة

المجلة الأردنية للهندسة الميكانيكية والصناعية: مجلة علمية عالمية محكمة تصدر عن عمادة البحث العلمي و الدراسات العليا في الجامعة الهاشمية بالتعاون مع صندوق دعم البحث العلمي في الأردن.

هيئة التحرير

رئيس التحرير

الأستاذ الدكتور موسى محسن

قسم الهندسة الميكانيكية، الجامعة الهاشمية، الزرقاء، الأردن.

الأعضاء

الأستاذ الدكتور أيمن المعاينة

الأستاذ الدكتور بلال العكش

الأستاذ الدكتور نسيم سواقد

الأستاذ الدكتور عدنان الكيلاني

الأستاذ الدكتور محمد النمر

الأستاذ الدكتور علي بدران

مساعد رئيس هيئة التحرير

الدكتور أحمد الغندور

فريق الدعم

تنفيذ وإخراج

المهندس حسن البعباع

المحرر اللغوي

الدكتور عبدالله جردات

ترسل البحوث إلى العنوان التالي:

رئيس تحرير المجلة الأردنية للهندسة الميكانيكية والصناعية

عمادة البحث العلمي والدراسات العليا

الجامعة الهاشمية

الزرقاء - الأردن

هاتف : 00962 5 3903333 فرعي 4147

Email: jjmie@hu.edu.jo

Website: www.jjmie.hu.edu.jo